



**Milena Ceccopieri da Rocha**

**Investigation of organic geochemical proxies  
as indicators of paleotemperature in the  
south-eastern Brazilian continental margin**

**Tese de Doutorado**

Thesis presented to the Programa de Pós-graduação em Química of PUC-Rio in partial fulfillment of the requirements for the degree of Doutor em Química.

Advisor: Prof. Renato da Silva Carreira

Co-advisor: Prof<sup>a</sup>. Angela de Luca Rebello Wagener

Rio de Janeiro  
February 2019

All rights reserved

## Milena Ceccopieri da Rocha

The author is a Chemistry technician from the Instituto Federal de Educação, Ciência e Tecnologia (IFRJ) and graduated in Oceanography from Universidade do Estado do Rio de Janeiro (2012). She holds a Master's Degree in Chemistry from PUC-Rio (2014) with emphasis in marine organic geochemistry.

### Bibliographic data

Ceccopieri da Rocha, Milena

Investigation of organic geochemical proxies as indicators of paleotemperature in the south-eastern Brazilian continental margin / Milena Ceccopieri da Rocha; advisor: Renato da Silva Carreira; co-advisor: Angela de Luca Rebello Wagener. – Rio de Janeiro: PUC-Rio, Departamento de Química, 2019.

191 f.: il. color. ; 30 cm

1. Tese (doutorado) – Pontifícia Universidade Católica do Rio de Janeiro, Departamento de Química.

Inclui referências bibliográficas

1. Química – Teses. 2. alquenona. 3. GDGT. 4. diol de cadeira longa. 5. Holoceno. I. Carreira, Renato da Silva. II. Pontifícia Universidade Católica do Rio de Janeiro. Departamento de Química. III. Título.

CDD: 540

## Acknowledgements

First of all, I would like to thank my advisor Renato Carreira, for all the guidance and support, for trusting and believing my work and for always teaching me to value my research. Thank you for all the advices, revisions and scientific talks. Second, I want to thank my co-adviser Angela Wagener, for the words of encouragement since the masters, for all the shared experience and for always being available when I needed. Further, I must thank my German adviser Gesine Mollenhauer, for giving me the opportunity to explore a new lab, for the trust deposited on me since the beginning, for all the knowledge that was shared and for being an inspiration inside and outside the academic environment.

I would like to thank Letícia Lazzari (Gugu) for lending me the Rio de Janeiro sediment core, for helping me with the TOC analysis, for making the lab atmosphere always funnier and for the best cococo-orientation anyone could have. Many many thanks to Ivy, for always being available in and outside the lab, for the countless conversations, for the brownies with coffee in the afternoon and for joining my crazy adventures in our “wonderful city” without hesitating. Thanks to Letícia Luz, for being the best doctoral companion anyone could possibly have, for the complicity, support and encouragement with the thesis, and, of course, for the short breaks at the nearest bar. Thanks to Carlos, for always being supportive and willing to help with the nerdy things in the R software or the equipments. Thanks also to Livia, for helping with the SPM samples, for sharing knowledge about the Campos Basin region and for being cheerful. To the other LabMAM friends (Lilian, Scott, Wellington, Renato, Ricardo, Camila, Otoniel, Eline and Giulia), I am very thankful for all the cooperation, friendship and good laughs, which made my days in the lab always happier.

I also like to thank the entire lab group at U.Bremen/AWI, specially to Jens and Maria, for giving me full support in the lab, and also to Eunmi, Célia, Vera, Liz, Sarah and Shuwen, for sharing the lab and the office with me and making me feel welcome. Each of you contributed to my short period in Bremen/Bremerhaven to be the most productive and fun (I still hope someday we finish our choreography of the ~GDGT dance~). Really, you guys are the best! I would also like to thank Enno Schefuß and Ralf Kreutz for the support with the sediment extractions at Marum.

Thanks to Ana Albuquerque, Douglas Lessa and the geochemistry lab group at UFF for the Cabo Frio sediment core and all the work and shared data involving these samples.

Thanks to Afonso Paiva, Ilson Silveira, Aberto Figueiredo and João Regis for the study area figures that were kindly designed.

Thanks to Fatima, for a few more years of patience and friendship.

Thanks to PUC-Rio, CNPq and DAAD for the financial support. To Petrobras for the samples under the Habitats and Upwelling projects, and to the Brazilian Navy for the sampling in the Rio de Janeiro shelf. This study was financed in part by the Coordenação de Aperfeiçoamento de Pessoal de Nível Superior – Brasil (CAPES) – Finance Code 001.

Thanks to the great physical oceanographers and friends Gui, Kaji, Jessica and Flavinha, who contributed to this thesis by running codes in Matlab/Python and giving me support with the instrumental data, and also to Dudu and Stella, who have always been supportive. Thank you all for more than 10 years of friendship.

Thanks to Ana Cecília and Amanda, oceanography gifts from USP that the organic geochemistry life gave me, for being amazing friends and great mentors.

Thanks to Cris and Zé in Rio, and Margaretha and Heiko in Bremen, for being the best hosts I could wish for.

Thanks to all my friends outside academia, who are more than essential in my life, for always making everything easier and sometimes showing interest in my work even without understanding what I have been doing in the past 4.5 years.

Thanks to my 19 pet siblings for being instant mood boosters every time I get a chance to visit them.

Thanks to Gabriel, my home office partner, for always being by my side, encouraging me to write when I wanted to procrastinate and to procrastinate when I had already written too much. Thank you for the amazing cooking, for taking care of me and for keeping me sane.

And last but not least, I would like to express my deepest gratitude to my family, for always being there for me no matter what, for being the coolest family ever, for never stop spoiling me, and for inspiring me and given me the basis to pursuit awesome things in life.

## Abstract

Ceccopieri da Rocha, Milena; Carreira, Renato da Silva (Advisor); Wagener, Angela de Luca Rebello (Co-advisor). **Investigation of organic geochemical proxies as indicators of paleotemperature in the south-eastern Brazilian continental margin.** Rio de Janeiro, 2019. 191p. Tese de Doutorado - Departamento de Química, Pontifícia Universidade Católica do Rio de Janeiro.

The reconstruction of past sea surface temperature (SST) using organic geochemical proxies has been a central theme of paleoclimatic research in recent years. Paleotemperature variability determinations in the South Atlantic are of great interest given the SST role in the global heat transport, but still requires further studies. The Cabo Frio Upwelling System (CFUS) is a particularly interesting study area for being a western boundary upwelling system subject to several peculiar oceanographic processes. This thesis aims at using organic geochemical proxies as indicators of paleotemperature, namely: the alkenone unsaturation index ( $U_{37}^{K'}$ ), the tetraether index ( $TEX_{86}^H$ ) and the long-chain diols index (LDI) as registered in sediments in the south-eastern Brazilian continental margin. The methylation of branched tetraether index (MBT') and the cyclization of branched tetraether index (CBT) were also tested as potential indicators of continental mean annual air temperature (MAAT) and soil pH. There are two focuses: (i) to investigate the applicability of  $U_{37}^{K'}$ ,  $TEX_{86}^H$  and MBT'/CBT proxies under local and regional environmental conditions in the Campos Basin region using 53 surface sediments; (ii) to use a multiproxy approach ( $U_{37}^{K'}$ ,  $TEX_{86}^H$  and LDI) to reconstruct the paleotemperature during the Holocene period from two sediment cores located in the shelves adjacent to Cabo Frio and Rio de Janeiro. The results reveal that  $U_{37}^{K'}$  and  $TEX_{86}^H$  are suitable temperature proxies for paleoclimate studies in regional scale in the SE Brazilian continental margin. Exceptions in the form of strong negative biases between reconstructed and observed mean annual SST (World Ocean Atlas 2013) were observed in the southern portion of the Campos Basin and highlight that, on a local scale, the effects of upwelling must be taken in consideration when applying these proxies to the same region. Regarding the MBT'/CBT proxies, the results for most of the marine sediments agree with the upper range of soil pH and lower range of MAAT found in the adjacent drainage basin. However, the spatial distribution of the branched GDGTs points to the

existence of different sources and post-depositional effects, e.g. selective degradation and *in situ* production, that compromise the applicability of these proxies to the marine sediments in the Campos Basin, especially more offshore. When applying the  $U_{37}^{K'}$ ,  $TEX_{86}^H$  and LDI proxies to reconstruct the SST for the past 14.5 kyr in the Rio de Janeiro core and 7.1 kyr in the Cabo Frio core, the variations observed agreed with several pre-existing paleoclimatic data for the same region and period. In the Rio de Janeiro shelf, a distinct phase before 7.5 cal kyr BP coincides with the period when the sea level was low and gradually increased. In the Cabo Frio shelf, the transition between mid- and late Holocene is well marked by a warming in SST- $U_{37}^{K'}$  and SST-LDI, probably related to a more intense Brazil Current (BC) activity over the shelf, whereas temp- $TEX_{86}^H$  showed an opposite cooling trend that may be a result of the subsurface upwelling of the cold South Atlantic Central Waters. A decrease in reconstructed temperatures after ca 2.5 kyr BP may be related to the establishment of the CFUS to modern conditions. Differences between Rio de Janeiro and Cabo Frio can be explained by the local instabilities of the BC near de CFUS region. Overall, for the entire covered period in both sediment cores, SST-LDI was warmer, SST- $TEX_{86}^H$  was clearly biased towards colder subsurface temperatures and SST- $U_{37}^{K'}$  was the most affected by the sea level variation and BC flow. The differences between the proxies' signal provided valuable information about the local paleoceanographic changes during the Holocene period, contributing to the paleoclimatology studies in the south-eastern Brazilian margin.

## Keywords

Alkenone; GDGT; long chain diol; Holocene.

## Resumo

Ceccopieri da Rocha, Milena; Carreira, Renato da Silva (Orientador); Wagener, Angela de Luca Rebello (Co-orientadora). **Investigação de marcadores geoquímicos orgânicos como indicadores de paleotemperatura na margem continental sudeste brasileira.** Rio de Janeiro, 2019. 191p. Tese de Doutorado - Departamento de Química, Pontifícia Universidade Católica do Rio de Janeiro.

A reconstrução da temperatura da superfície do mar (TSM) através de *proxies* geoquímicos orgânicos tem sido um tema central das pesquisas paleoclimáticas nos últimos anos. Determinações da variabilidade da paleotemperatura no Atlântico Sul são de grande interesse dado o papel da TSM no transporte de calor global, mas este tema ainda requer estudos mais aprofundados. O sistema de ressurgência de Cabo Frio (SRCF) representa uma área de estudo particularmente interessante por ser um sistema de ressurgência de contorno oeste sujeito a vários processos oceanográficos peculiares. Este projeto tem como objetivo a utilização de *proxies* geoquímicos orgânicos como indicadores de paleotemperatura, tais como: o índice de insaturação das alquenonas ( $U_{37}^{K'}$ ), o índice dos tetraéteres ( $TEX_{86}^H$ ) e o índice dos díois de cadeia longa (LDI) registrados em sedimentos da margem continental sudeste brasileira. Também foram testados os índices de metilação e de ciclização dos tetraéteres ramificados (MBT e CBT) como indicadores da temperatura média anual do ar (TMAA) e do pH do solo. O presente trabalho possui dois focos: (i) investigar a aplicabilidade dos índices  $U_{37}^{K'}$ ,  $TEX_{86}^H$  e MBT'/CBT considerando as condições ambientais locais e regionais observadas na região da Bacia de Campos utilizando 53 amostras de sedimento superficiais; (ii) aplicar uma abordagem *multi-proxy* ( $U_{37}^{K'}$ ,  $TEX_{86}^H$  e LDI) para reconstruir a paleotemperatura durante o período do Holoceno a partir de dois testemunhos sedimentares localizados nas plataformas adjacentes a Cabo Frio e Rio de Janeiro. Os resultados revelam que  $U_{37}^{K'}$  e  $TEX_{86}^H$  são *proxies* de temperatura adequados para estudos paleoclimáticos em escala regional na margem continental do sudeste brasileiro. Exceções na forma de desvios negativos entre a TSM média anual reconstruída e observada (World Ocean Atlas 2013) foram observados na porção sul da região estudada e ressaltam que, em escala local, os efeitos da ressurgência devem ser levados em consideração ao aplicar esses *proxies* na mesma região. Em relação aos índices MBT'/CBT, os

resultados se encaixam na faixa superior do pH do solo e na faixa inferior da TMAA encontrados na bacia de drenagem adjacente para a maioria das amostras. No entanto, a distribuição dos GDGTs ramificados apontam para a existência de diferentes fontes e efeitos pós deposicionais, e.g. degradação seletiva e produção *in situ*, que comprometem a aplicabilidade desses *proxies* nos sedimentos marinhos na Bacia de Campos. Ao aplicar os *proxies*  $U_{37}^{K'}$ ,  $TEX_{86}^H$  e LDI na reconstrução da temperatura para os últimos 14,5 kyr no testemunho do Rio de Janeiro e 7,1 kyr no testemunho de Cabo Frio, as variações observadas estão em acordo com diversos dados paleoclimáticos pré-existentes para a mesma região e período. Na plataforma do Rio de Janeiro, uma fase distinta antes de 7,5 cal kyr BP coincide com o período em que o nível do mar se encontrava baixo e passou a aumentar gradualmente. Na plataforma de Cabo Frio, a transição entre o Holoceno médio e o tardio é bem marcada pelo aumento na TSM- $U_{37}^{K'}$  e da TSM-LDI provavelmente relacionados a uma atividade mais intensa da Corrente do Brasil (BC) sobre a plataforma, enquanto a temp- $TEX_{86}^H$  apresentou uma tendência oposta de resfriamento que pode ser um resultado da ressurgência das Águas Centrais do Atlântico Sul em subsuperfície. Uma diminuição na temperatura reconstruída após cerca de 2,0 cal kyr BP pode ser explicada pelo estabelecimento do SRCF às condições modernas. Diferenças entre o Rio de Janeiro e Cabo Frio provavelmente estão relacionadas às instabilidades locais da CB próximo à região do SRCF. De forma geral, para o período investigado em ambos os testemunhos, a TSM-LDI mostrou-se mais quente, a TSM- $TEX_{86}^H$  obteve uma clara tendência a temperaturas mais frias de subsuperfície e a TSM- $U_{37}^{K'}$  foi a mais afetada pela variação no nível do mar e pelo fluxo da CB. As diferenças entre os *proxies* forneceram informações valiosas sobre as mudanças paleoceanográficas locais durante o Holoceno, contribuindo para os estudos paleoclimáticos na margem sudeste do Brasil.

## Palavras-chave

Alquenona; GDGT; diol de cadeia longa; Holoceno.

## Kurzfassung

Ceccopieri da Rocha, Milena; Carreira, Renato da Silva (Erstgutachter); Wagener, Angela de Luca Rebello (Zweitgutachter). **Organisch-geochemische Proxies als Paläotemperatur-Indikatoren am südöstlichen Kontinentalrand von Brasilien.** Rio de Janeiro, 2019. 191p. Tese de Doutorado - Departamento de Química, Pontifícia Universidade Católica do Rio de Janeiro.

Die Rekonstruktion Oberflächenwassertemperaturen in der Vergangenheit mit organisch-geochemischen Proxies ist in den vergangenen Jahren ein wichtiges Thema der Paläoklimaforschung gewesen. Die Rekonstruktion von Paläotemperaturvariabilität im Südatlantik ist hierbei in Anbetracht der wichtigen Rolle der Ozeane im globalen Wärmetransport von zentraler Bedeutung, erfordert jedoch noch weiterführende Untersuchungen. Das Auftriebssystem von Cabo Frio ist in diesem Zusammenhang wegen seiner speziellen Lage auf der westlichen Seite eines Ozeanbeckens und der damit zusammenhängenden besonderen ozeanographischen Prozesse ein interessantes Arbeitsgebiet. Diese Arbeit hat zum Ziel, die organisch-geochemischen Proxies  $U_{37}^{K'}$  (Alkenon-Untersättigungs-Index),  $TEX_{86}^H$  (Tetraether-Index an sogenannten GDGTs, Glycerol Dialkyl Glycerol Teteraether) und LDI (Langkettige-Diole-Index) aufgezeichnet in Sedimenten des südöstlichen brasilianischen Kontinentalrands zu verwenden. Zudem wurden die Indices MBT' und CBT, die die Methylierung bzw. Zyklisierung verzweigter GDGTs quantifizieren, als Proxies für die Jahresmitteltemperatur an Land und für den pH-Wert der Böden getestet. Der Fokus der Arbeit liegt hierbei einerseits darauf i) die Anwendbarkeit der Proxies  $U_{37}^{K'}$ ,  $TEX_{86}^H$ , MBT'/CBT im unter den lokalen und regionalen Umwelteinflüssen des Campos Bessens auf Grundlage von 53 Oberflächensedimentproben zu überprüfen und ii) eine sogenannte „multi-proxy“ Rekonstruktion der Paläoumweltbedingungen anhand der  $U_{37}^{K'}$ ,  $TEX_{86}^H$  und LDI Proxies an zwei Sedimentkernen vom Schelf vor Cabo Frio und Rio de Janeiro zu erstellen. Es zeigt sich, dass sich sowohl  $U_{37}^{K'}$  als auch  $TEX_{86}^H$  für regionale Paläoumweltstudien am südöstlichen brasilianischen Kontinentalrand eignen. Ausnahmen in Form von starken negativen Abweichungen zwischen rekonstruierter und instrumentell beobachteter (World Ocean Atlas 2013) Oberflächenwassertemperatur treten im südlichen Teil des Campos Beckens auf und zeigen, dass sehr lokal die Auswirkungen von Auftrieb bei der einer regionalen

Anwendung dieser Proxies berücksichtigt werden müssen. Die Ergebnisse der MBT'/CBT Proxies an marinen Sedimenten stimmen mit den Gegebenheiten an Land weitgehend überein, wobei die pH-Rekonstruktionen im oberen Bereich der Beobachtungen im angrenzenden Einzugsgebiet liegen, während die Rekonstruktion der Jahresmitteltemperatur an Land zu den niedrigeren Werten der Beobachtungen neigen. Die räumliche Verteilung der verzweigten GDGTs in deutet zudem auf unterschiedliche Quellen sowie diagenetische Effekte wie selektiven Abbau und in-situ Produktion von verzweigten GDGTs hin, die die Anwendbarkeit der MBT'/CBT Proxies an marinen Sedimenten des Campos Beckens, insbesondere in den küstenfernen Regionen, einschränken. Die Rekonstruktion der Paläo-Oberflächenwassertemperaturen mithilfe von  $U_{37}^{K'}$ ,  $TEX_{86}^H$  und LDI für die letzten 14.5 kyr vor Rio de Janeiro und für die letzten 7.1 kyr vor Cabo Frio ergab eine Variabilität, die mit Ergebnissen aus mehreren vorherigen paläoklimatischen Studien für die Region übereinstimmt. Auf dem Schelf vor Rio de Janeiro kann eine Phase vor 7.5 kyr deutlich vom Rest der Zeitreihe unterschieden werden, während derer der Meeresspiegel niedriger war und allmählich anstieg. Auf dem Schelf vor Cabo Frio ist der Übergang vom mittleren ins späte Holozän von deutlichen Anstiegen der  $U_{37}^{K'}$ - und LDI-basierten Temperaturrekonstruktionen geprägt, die wahrscheinlich mit der Intensivierung des Brasilstroms auf dem Schelf in Verbindung stehen. Im Gegensatz dazu verzeichnet die  $TEX_{86}^H$ -basierte Temperaturrekonstruktion eine deutliche Abkühlung, die das Ergebnis von verstärktem Auftrieb von kaltem südatlantischem Zentralwasser sein kann. Eine Abnahme der rekonstruierten Temperaturen nach 2.5 kyr vor heute deutet auf die Etablierung moderner Bedingungen im Cabo Frio Auftriebssystem hin. Unterschiede zwischen den Temperaturrekonstruktionen für die Regionen Cabo Frio und Rio de Janeiro können mit lokaler Instabilität des Brasil-Stroms im Bereich des Cabo Frio Auftriebssystems zusammenhängen. Insgesamt sind über die gesamte Untersuchungsperiode die Temperaturrekonstruktionen auf Grundlage von LDI am wärmsten, die auf  $TEX_{86}^H$  basierenden von kälteren Temperaturen in etwas größeren Wassertiefen beeinflusst und diejenigen auf Grundlage von  $U_{37}^{K'}$  am stärksten von Meeresspiegeländerungen und Variabilität im Brasil-Strom betroffen. Diese Unterschiede zwischen den einzelnen Proxies liefern wertvolle Informationen über die lokalen paläozeanographischen Veränderungen während des Holozäns und somit einen Beitrag zum Verständnis des Paläoklimas am südöstlichen brasilianischen Kontinentalrand.

## **Schlüsselwörter**

Alkenon; GDGT; Langkettige-Diole; Holozän.

## Table of contents

Chapter 1 Introduction	22
1.1. General introduction	22
1.1.1. Global climate and the reconstruction of paleotemperature	22
1.1.2. Organic geochemical proxies	24
1.1.3. Proxies uncertainties and the multiproxy approach	34
1.1.4. Paleoclimatology in the South Atlantic during the Holocene period	36
1.2. Study area	38
1.2.1. Geomorphology	38
1.2.2. Hydrodynamics	39
1.2.3. Sedimentology	41
1.3. Research background and thesis motivation	43
1.4. Objectives of this thesis	45
1.5. Thesis outline	45
Chapter 2 Experimental	47
2.1. Sampling	47
2.1.1. Surface sediments	47
2.1.2. Sediment cores	47
2.2. Geochronology of the sediment cores	49
2.3. TOC and $\delta^{13}\text{C}$ analysis of the sediment cores	50
2.4. Lipids extraction and separation	51
2.5. Alkenone analysis and $U_{37}^{K'}$ index	52
2.6. GDGT analysis, $\text{TEX}_{86}^H$ , MBT', CBT and BIT indices	53
2.7. Long chain diol analysis and LDI index	54
2.8. Instrumental data	54
Chapter 3 On the application of alkenone- and GDGT-based temperature proxies in the south-eastern Brazilian continental margin	56
Chapter 4 Branched GDGTs and the associated MBT' and CBT proxies in surface sediments from the south-eastern Brazilian continental margin	84

Chapter 5 Holocene sea water temperature variations in the south-eastern Brazilian shelf inferred from organic proxies in sediments ( $U_{37}^K$ , $TEX_{86}^H$ and LDI)	100
Chapter 6 Conclusions	125
References	127
Supplementary data	158

## List of Figures

Figure 1.1: Alkenones structures.	24
Figure 1.2: (a) World Ocean Atlas 2013 (WOA13) statistical annual mean SST and the locations of the core top samples (n = 518) used for the global calibration of $U_{37}^{K'}$ (black and white dots). The white dots (n = 147) represent the samples used in the eastern South Atlantic (Müller et al., 1998). (b) Relation between the $U_{37}^{K'}$ and the annual mean SST for the eastern South Atlantic and (c) for the global dataset (Müller and Fischer, 2004).	26
Figure 1.3: GDGTs structures and the correspondent ion masses ( $m/z$ ).	27
Figure 1.4: (a) World Ocean Atlas 2013 (WOA13) statistical annual mean SST and the locations of the core top samples (n = 426) used for the global calibration of $TEX_{86}$ (black dots). (b) Relation between the $TEX_{86}$ and the annual mean SST. Red and blue dots represent the Red Sea and the samples with SST cooler than 3 °C, respectively (Kim et al., 2010).	30
Figure 1.5: Long chain diol structures.	33
Figure 1.6: (a) World Ocean Atlas 2013 (WOA13) statistical annual mean SST and the locations of the core top samples (n = 162) used for the global calibration of LDI (black dots). (b) Relation between the LDI and the annual mean SST (Rampen et al., 2012).	34
Figure 1.7: Schematic characterization of the circulation in the Subtropical South Atlantic Ocean (modified from Peterson and Stramma, 1991, designed by Ilson Silveira).	39
Figure 1.8: (a) SST and (b) surface chlorophyll concentration obtained by satellite (MODIS sensor, Aqua satellite) in the year 2007 for the Southwestern Atlantic (designed by Afonso Paiva).	41
Figure 1.9: Grain size of the surface sediments in the south-eastern Brazilian margin (unpublished sediment grain size data provided by Alberto Figueiredo, personal communication; designed by João R. dos Santos Filho).	43

Figure 2.1: Location of the surface (0-2 cm) sediment sampling stations in the Campos Basin (black dots), the sediment core CF10-09A in the Cabo Frio shelf and the RJ13-01C in the Rio de Janeiro shelf (red circles). 48

Figure 2.2: Flow chart of the laboratory procedures. 55

Figure 3.1: Location of the core top (0-2 cm) sediment sampling stations from the Habitats Project (a). Each transect (A, B, G, H and I) is divided by isobaths as follows: 1, 25 m; 2, 50 m; 3, 75 m; 4, 100 m; 5, 150 m; 6, 400 m; 7, 700 m; 8, 1000 m; 9, 1300 m; 10, 1900 m; 11, 1900 m and 12, 3000 m. Color map (b) shows the peak upwelling conditions and the meandering of the Brazil Current with SST taken from the Modis Aqua satellite, and the location of the two sections (c) and (d). The sections illustrate the intrusion of the South Atlantic Central Water under non-upwelling and coastal upwelling conditions, respectively, with water temperatures taken from the World Ocean Database (Boyer et al., 2013). Seasonal depth profiles of water temperature (e-h) taken from the World Ocean Atlas 2013 (Locarnini et al., 2013). Each profile corresponds to the nearest interpolated gridboxes of the stations according to the symbol colors of the stations: blue (around Cabo Frio), gray (transects A and B) and black (transects G, H, and I), as marked on the study area map (a). 60

Figure 3.2: Contents of (a) total alkenones per gram TOC ( $\mu\text{g gTOC}^{-1}$ ), (b) total isoGDGTs per gram TOC ( $\mu\text{g gTOC}^{-1}$ ), (c) total brGDGTs per gram TOC ( $\mu\text{g gTOC}^{-1}$ ), and (d) BIT index. PSR = Paraíba do Sul River; CST = Cabo de São Tomé; CF = Cabo Frio. The letters A-I represent the transects. 67

Figure 3.3: SST estimates based on  $U_{37}^{K'}$  proxy using South Atlantic core-top calibrations (Müller et al., 1998) for (a) annual mean; (b) austral summer (Jan-Mar), (c) austral autumn (Apr-Jun), (d) austral winter (Jul-Sep) and (e) austral spring (Oct-Dec). Differences between SST- $U_{37}^{K'}$  estimates and SST (WOA13) for (f) annual mean; (g) austral summer (Jan-Mar), (h) austral autumn (Apr-Jun), (i) austral winter (Jul-Sep) and (j) austral spring (Oct-Dec). 68

Figure 3.4: (a) SST- $\text{TEX}_{86}$  relationship and (b) RI- $\text{TEX}_{86}$  relationship in the global core-top sediments presented in Kim et al. (2010) (grey dots) and in the core-top sediments from the present study (red dots). 69

Figure 3.5: Temperature estimates based on  $\text{TEX}_{86}^{\text{H}}$  using (a) SST calibration (Kim et al., 2010) and (b) subsurface calibration for 0-200 m (Kim et al., 2012). Differences between reconstructed and climatological mean (WOA13) temperatures for (c)  $\text{TEX}_{86}^{\text{H}}$  surface temperature estimates minus annual mean SST and (d)  $\text{TEX}_{86}^{\text{H}}$  subsurface temperature estimates minus annual mean depth-integrated (100-200 m) temperature. 70

Figure 3.6: Depths of agreement between estimated (Kim et al., 2010, 2012) and climatological mean temperatures (WOA13) from 0-200 m depth along the isobaths. Dots represent the water depth of optimal agreement and dashed lines represent minimum and maximum water depth in which the residuals are within the standard error of estimates for surface (black) and subsurface (grey) calibrations. 78

Figure 4.1: Chemical structure of brGDGTs and crenarchaeol with the correspondent ion masses ( $m/z$ ). 87

Figure 4.2: (a) Map of the Campos Basin with locations of the surface (0-2 cm) sediment sampling stations. Each transect (A, B, G, H and I) was sampled on isobaths as follows: 1, 25 m; 2, 50 m; 3, 75 m; 4, 100 m; 5, 150 m; 6, 400 m; 7, 700 m; 8, 1000 m; 9, 1300 m; 10, 1900 m; 11, 1900 m and 12, 3000 m. (b) Map showing the three drainage basins adjacent to the Campos Basin and their main rivers. (c) Mean annual air temperature, (d) annual precipitation (Fick and Hijmans, 2017) and (e) pH of the 30 cm topsoil (FAO/IIASA/ISRIC/ISS-CAS/JRC, 2012) in the three drainage basins. PSR = Paraíba do Sul River drainage basin; RJ = coastal drainages of the State of Rio de Janeiro; ES = coastal drainages of the Espírito Santo State. 88

Figure 4.3: Contents of (a) total brGDGTs ( $\mu\text{g gTOC}^{-1}$ ), and (b) crenarchaeol ( $\mu\text{g gTOC}^{-1}$ ), (c) BIT index; (d) CBT-derived pH (Weijers et al., 2007b; Peterse et al., 2012), (e) MBT' (Peterse et al., 2012) and (f) MBT'/CBT derived MAAT in the Campos Basin surface sediments (Weijers et al., 2007b; Peterse et al., 2012). The total brGDGT and crenarchaeol normalized by the TOC were not determined in sample H1 because the TOC content of this sample was below quantification limit, but the contents in the sediment were comparable to sample H2 (Supplementary Table S4.1). 92

Figure 4.4: Relative abundance of the brGDGTs for each transect and sampling depth in the Campos Basin. 93

Figure 4.5: Distribution of groups using Ward's hierarchical cluster analysis based on the brGDGTs relative abundance. See text for details. 96

Figure 5.1: Map with location of the sediment core sampling stations and grain size of the surface sediments in the south-eastern Brazilian margin (unpublished sediment grain size data provided by Alberto Figueiredo, personal communication; designed by João R. dos Santos Filho). 104

Figure 5.2: Variation in the (a) TOC (%); (b) bulk  $\delta^{13}\text{C}$  (‰); (c) total isoGDGT and total alkenone contents ( $\mu\text{g gTOC}^{-1}$ ); (d) BIT index; and (e) temperature estimates based on  $U_{37}^K$ ,  $TEX_{86}^H$  and LDI ( $^{\circ}\text{C}$ ) along the RJ13-01C core. The vertical dashed lines represent the depositional phases as proposed by Lazzari et al. (2018), based on sedimentary processes, geochemical and geophysical properties. 109

Figure 5.3: Variation in the (a) TOC (%); (b) bulk  $\delta^{13}\text{C}$  (‰) (Ana L. S. Albuquerque, personal communication); (c) total isoGDGT and total alkenone contents ( $\mu\text{g gTOC}^{-1}$ ); (d) BIT index; and (e) temperature estimates based on  $U_{37}^K$ ,  $TEX_{86}^H$  and LDI ( $^{\circ}\text{C}$ ) along the CF10-09A core. The vertical dashed lines represent the depositional phases as proposed by Lessa et al. (2016) based on planktonic foraminifera. 112

Figure 5.4: Annual mean and seasonal depth profiles of water temperature (1955-2012) corresponding to the nearest interpolated  $0.25^{\circ}$  grid box taken from the World Ocean Atlas 2013. Dashed grey lines correspond to the proxy-estimated temperatures for the core-top sample from the present work. 115

## List of tables

Table 2.1: Information of the surface sediment samples of the Campos Basin.	48
Table 2.2: Information of the sediment core samples.	50
Table 3.1: Information and results of alkenone, GDGT and bulk analyses from the surface sediment samples of the Campos Basin (n.d. = not determined).	71
Table 3.2: Calibrations used for SST- $U_{37}^{K'}$ and temp- $TEX_{86}^H$ estimates and their relationship with the instrumental temperatures obtained from the WOA13.	76

## List of Abbreviations

$\Delta R$  – reservoir effect  
AMOC – Atlantic Meridional Overturning Circulation  
AMS – accelerator mass spectrometry  
ASE – accelerated solvent extraction system  
BC – Brazil Current  
BIT – Branched and Isoprenoid Tetraether  
brGDGTs – branched glycerol dialkyl glycerol tetraethers  
BSTFA – N,O-bis(trimethylsilyl)trifluoroacetamide  
CAPES – Coordination for the Improvement of Higher Education Personnel  
CBT – cyclization of branched tetraether index  
CFUS – Cabo Frio upwelling system  
CNPq – National Council for Scientific and Technological Development  
cren – crenarchaeol  
cren' – crenarchaeol regio-isomer  
CW – Coastal Water  
DAAD – German Academic Exchange Service  
DWBC – Deep Western Boundary Current  
ENSO – El Niño Southern Oscillation  
GC-FID – gas chromatography with a flame ionization detector  
GC-TOF-MS – gas chromatography-time of flight mass spectrometry  
GDGTs – glycerol dialkyl glycerol tetraethers  
HPLC-MS – high performance liquid chromatography coupled to mass spectrometry  
HPLC-APCI-MS – high performance liquid chromatography-atmospheric pressure chemical ionization-mass spectrometry  
IEAPM – Instituto de Estudos do Mar Almirante Paulo Moreira  
IPL – intact polar lipids  
IRMS – isotope ratio mass spectrometer  
IPCC – Intergovernmental Panel on Climate Change  
IWBC – Intermediate Western Boundary Current  
isoGDGTs – isoprenoid glycerol dialkyl glycerol tetraethers  
ITCZ – Intertropical Convergence Zone  
kyr – thousand years

cal kyr BP – calibrated thousand years before present  
LDI – long-chain diol index  
LGM – last glacial maximum  
LIA – Little Ice Age  
Ma – million years before present  
MAAT – mean annual air temperature  
MARUM – Center for Marine Environmental Sciences (University of Bremen)  
MBT – methylation of branched tetraether index  
MBT' – simplified methylation of branched tetraether index  
MC – Malvinas Current  
MCA – Medieval Climatic Anomaly  
MI – methane index  
MIS – marine isotope stage  
NADW – North Atlantic Deep Water  
NBC – North Brazil Current  
OEA – Organic Elemental Analyzer  
OM – organic matter  
PSR – Paraíba do Sul River  
PUC-Rio – Pontifícia Universidade Católica do Rio de Janeiro  
RI – ring index  
SACW – South Atlantic Central Waters  
SACZ – South Atlantic Convergence Zone  
SAMS – South American Monsoon System  
SASH – South Atlantic Subtropical High  
SIM – single ion monitoring  
SPM – suspended particulate matter  
SST – sea surface temperature  
TEX<sub>86</sub> – tetraether index  
TEX<sub>86</sub><sup>H</sup> – tetraether index for high temperatures  
TEX<sub>86</sub><sup>L</sup> – tetraether index for low temperatures  
TOC – total organic carbon  
TW – Tropical Waters  
U<sub>37</sub><sup>K</sup> – alkenone unsaturation index  
U<sub>37</sub><sup>K'</sup> – simplified alkenone unsaturation index  
WOA09 – World Ocean Atlas 2009  
WOA13 – World Ocean Atlas 2013

“There is no unique picture of reality.”  
Stephen Hawking

# Chapter 1

## Introduction

### 1.1. General introduction

#### 1.1.1. Global climate and the reconstruction of paleotemperature

The oceans play a fundamental role in global climate due to the capacity to store large amounts of heat and redistribute it from low to high latitudes (Rahmstorf, 2002; Ganachaud and Wunsch, 2003). The interplay between atmosphere and oceans is complex and involves several processes, e.g., release of stored heat from the ocean to the atmosphere, effect of the atmospheric wind patterns in ocean currents, and influence of air temperatures on sea surface temperature (SST) (Rahmstorf, 2002). The ocean also interacts with the atmosphere by exchanging gases, influencing its greenhouse gas content. The increase in atmospheric CO<sub>2</sub> causes a positive flux of this gas into the ocean, which can influence, together with ocean's physical and chemical properties, the marine biogeochemical cycles on a global scale (Rahmstorf, 2002; IPCC, 2007).

According to IPCC (2007), climate change is defined as a “change in the state of the climate that can be identified (e.g., by using statistical tests) by changes in the mean and/or the variability of its properties, and that persists for an extended period, typically decades or longer.” Global warming has become evident from the observation of increases in global average air and ocean temperatures, which leads to melting of ice sheets and rising of global average sea level. Several studies have suggested human activities, including burning of fossil fuels, industrialization and deforestation, as the main causes of increasing greenhouse gases in the atmosphere and the consequent rise in air and ocean water temperatures on a global scale. The potential impact of human activities on present and future climate has increased the interest in understanding the climate of the past. To investigate and predict future climate changes, the reconstruction and evaluation of past climate changes over longer time scales in a good resolution becomes necessary (IPCC, 2007).

Paleoclimatology studies are an important contribution to current climate modeling because it can reveal the sensitivity of the climate system and the frequency at which the climate changes may occur in the future (Schilman et al., 2001). The Quaternary period (2.6 Ma up to present) is characterized by periodic glaciations. The last glacial maximum (LGM, about 20 kyr BP) has been one of the main objects of interest in paleoclimatic studies in the last decades because it is the most recent period with a climate state much different from the present (Rahmstorf and Feulner, 2013). The Quaternary is divided in two periods: the Pleistocene (2.6 Ma to 11.7 kyr BP) and the Holocene (11.7 kyr BP to the present) (Cohen et al., 2013). To understand the natural variability behind anthropogenic climate change, it is important to focus on the climate of the more recent past (Mayewski et al., 2004). The Holocene studies made possible to evaluate the climatic variability during the current interglacial phase, in which the current climatic conditions have developed (Rohling et al., 2002).

The SST variation is a crucial factor to paleoclimatic research because it can provide information about the oceanic and atmospheric dynamics that are related to spatial and temporal variation of climatic processes. As the instrumental record of global surface temperature only began in the mid-19<sup>th</sup> century (IPCC, 2007), temperature reconstructions using proxies records have been a central theme of paleoclimatic research in recent years. A climate indicator is a local record that, if interpreted using chemical, physical and biological principles, may represent climate-related environmental parameters and act as evidence for long-term past climatic changes. Proxies can be applied on several environmental records, such as pollen, tree rings, speleothems, corals, marine and lake sediments and ice cores (IPCC, 2013).

The recent increase in the number of proxy-reconstructed paleotemperature data with a higher resolution and wider spatial coverage can improve today's climate models. The several proxies proposed along the last two or three decades to reconstruct paleotemperature from marine sedimentary record can be divided into two groups, according to the inorganic or organic fossil record considered. The inorganic proxies include  $\delta^{18}\text{O}$  (Urey, 1947; Erez and Luz, 1983) and Mg/Ca ratio (Nürnberg et al., 1996) of planktonic foraminifera and are based on the thermodynamic behavior of isotopes and elements during calcification depending on the local temperature. This type of determination can yield uncertainties related to the depth inhabited by the species, the preservation of the shells, carbonate concentrations and  $\delta^{18}\text{O}$  composition of seawater (Spero et al., 1997).

The organic paleotemperature proxies are based on the ability of several microorganisms to adjust the stability of their cell membranes to local temperature variations through changes in the structures of specific lipid compounds during cell formation (Ray et al., 1971; Oshima and Miyagawa, 1974). Those organic molecules derived from a specific animal or vegetal metabolic process and whose structure are preserved (or can be traced back to its original composition), are known as molecular biomarkers (Meyers, 2003; Peters et al., 2004). The  $U_{37}^K$  index from alkenones was the first organic proxy developed to reconstruct past SST (Brassell et al., 1986; Prah and Wakeham, 1987). Later, two other organic proxies for SST reconstruction were proposed: the  $TEX_{86}$ , based on glycerol dialkyl glycerol tetraethers (GDGTs) with 86 carbon atoms (Schouten et al., 2002), and, more recently, the LDI (long-chain diols index), based on long-chain diols  $C_{28}$  1,13-diol,  $C_{30}$  1,13-diol and  $C_{30}$  1,15-diol (Rampen et al., 2012). The GDGTs can also be used in marine sediments to reconstruct the soil pH and the mean annual air temperature (MAAT) of the adjacent continent (Weijers et al., 2006b). The application of each of these organic geochemical proxies in paleoclimatic studies will be discussed in detail in the following section.

### 1.1.2. Organic geochemical proxies

#### 1.1.2.1. Alkenones and the $U_{37}^{K'}$ index

The alkenones are long-chain ketones (from  $C_{37}$  to  $C_{39}$ ) having 2 to 4 unsaturations in their structures (Figure 1.1). They were first discovered in deep-sea sediments from the Walvis Ridge by Boon et al. (1978) and later identified by Leeuw et al. (1980). Alkenones are synthesized by haptophyte algae, mainly the marine coccolithophores *Emiliana huxleyi* and *Gephyrocapsa oceanica* (Volkman et al., 1980, 1995), and are ubiquitous in marine sediments worldwide (Brassell et al., 1986). The *E. huxleyi* species is particularly abundant and has populated the surface of oceanic waters since the middle Pleistocene (Meyers, 1997).

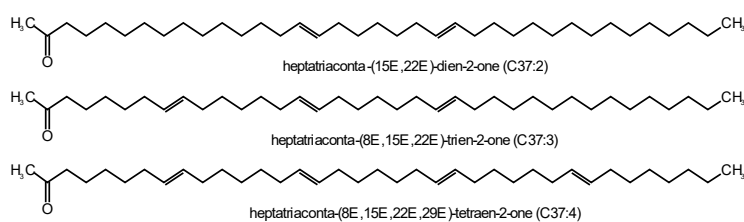


Figure 1.1: Alkenones structures.

The role of alkenones on haptophyte physiology is still unclear, but experimental evidence show changes in the alkenone composition of these organisms in a way that, as water temperature decreases, the number of unsaturations of alkenones structures increases (Brassell et al., 1986; Prahl and Wakeham, 1987). Based on this principle, the alkenone unsaturation index  $U_{37}^K$  (Equation 1-1) was first developed by Brassell et al. (1986) through empirical equations that provided a linear relationship between di-, tri- and tetra-unsaturated alkenones ( $C_{37:2}$ ,  $C_{37:3}$  and  $C_{37:4}$ , Figure 1.1) and the growth temperature of the cultivated algae. Later, Prahl and Wakeham (1987) developed the  $U_{37}^{K'}$  (Equation 1-2), a simplified index without the  $C_{37:4}$  because of its distribution restricted at high latitudes.

$$U_{37}^K = \frac{(C_{37:2}-C_{37:4})}{(C_{37:2})+(C_{37:3})+(C_{37:4})} \quad (1-1)$$

$$U_{37}^{K'} = \frac{(C_{37:2})}{(C_{37:2})+(C_{37:3})} \quad (1-2)$$

The use of a specific compound ratio as a temperature proxy requires the development of an adequate calibration. In the case of  $U_{37}^{K'}$ , the first calibration was performed by cultivating *E. huxleyi* in the laboratory, where a good correlation between the calculated index and the controlled temperatures was observed (Equation 1-3) for temperatures between 8 and 25 °C, with an accuracy of less than 0.5 °C (Prahl and Wakeham, 1987). Further studies with surface sediments and particulate material have confirmed the linearity between  $U_{37}^{K'}$  and SST (Conte and Eglinton, 1993; Prahl et al., 1993; Sikes and Volkman, 1993; Rosell-Melé et al., 1995a; Sikes et al., 1997; Sonzogni et al., 1997; Müller et al., 1998). Müller et al. (1998), for example, analyzed alkenones in 149 surface sediment samples and developed a regional calibration for tropical to subpolar eastern South Atlantic (Equation 1-4; Figure 1.2a,b). The authors also established a global calibration with data from a total of 370 sites between 60°S and 60°N in the Atlantic, Indian, and Pacific Oceans (Equation 1-5; Figure 1.2a,c) and found a strong linearity between  $U_{37}^{K'}$  values and global SST annual average for temperatures between 0 and 29 °C, with an error of  $\pm 1.5$  °C. Later, a study developed by Benthien and Müller (2000) with surface sediment samples collected in the western South Atlantic (between 5 °N and 50 °S) showed a good correlation between the temperatures calculated through the calibration of Müller et al. (1998) and the annual mean SST for regions north of 32 °S.

$$T (^{\circ}\text{C}) = \frac{U_{37}^{K'} - 0.043}{0.033} \quad (1-3)$$

$$T (^{\circ}\text{C}) = \frac{U_{37}^{K'} - 0.069}{0.033} \quad (1-4)$$

$$T (^{\circ}\text{C}) = \frac{U_{37}^{K'} - 0.044}{0.033} \quad (1-5)$$

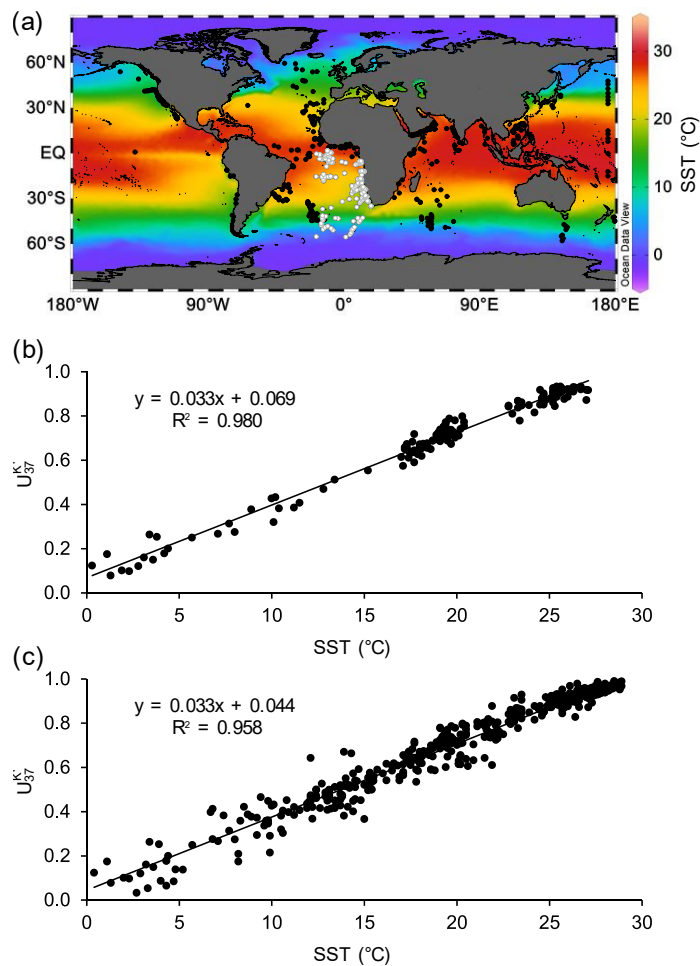


Figure 1.2: (a) World Ocean Atlas 2013 (WOA13) statistical annual mean SST and the locations of the core top samples ( $n = 518$ ) used for the global calibration of  $U_{37}^{K'}$  (black and white dots). The white dots ( $n = 147$ ) represent the samples used in the eastern South Atlantic (Müller et al., 1998). (b) Relation between the  $U_{37}^{K'}$  and the annual mean SST for the eastern South Atlantic and (c) for the global dataset (Müller and Fischer, 2004).

The  $U_{37}^{K'}$  is largely used because it shows a strong linear relationship with SST and can be determined easily with high precision. However, its use is limited in tropical areas at temperatures above 28 °C, where the tri-unsaturated alkenones can be below the detection limit (Kim et al., 2008) and in polar oceans, where alkenone-producing coccolithophorids do not occur (Sikes and Volkman, 1993).

Moreover, they generally cannot be used in sediments older than 6 million years (Bard, 2001).

### 1.1.2.2.

#### GDGTs and the TEX<sub>86</sub>, MBT, CBT and BIT indices

GDGTs are lipids present in the cell membranes of Archaea and bacteria. These molecules occur in the environment in the isoprenoid (isoGDGTs) and branched (brGDGTs) forms, whose structures are shown in Figure 1.3. The Archaea domain can be divided into two groups: Crenarchaeota (Marine “Group I”), which was later renamed as Thaumarchaeota, and Euryarchaeota (Marine “Group II”). The isoGDGTs are produced by a variety of Archaea, which are mainly comprised by acyclic or cyclic biphytane core lipids (Sinninghe Damsté et al., 2000). Crenarchaeol is a specific isoGDGT of Thaumarchaeota and was initially associated only with non-thermophilic marine organisms of this group. BrGDGTs are generally attributed to soil bacteria (Sinninghe Damsté et al., 2000), possibly Acidobacteria, recently described as acidophilic (Sinninghe Damsté et al., 2002).

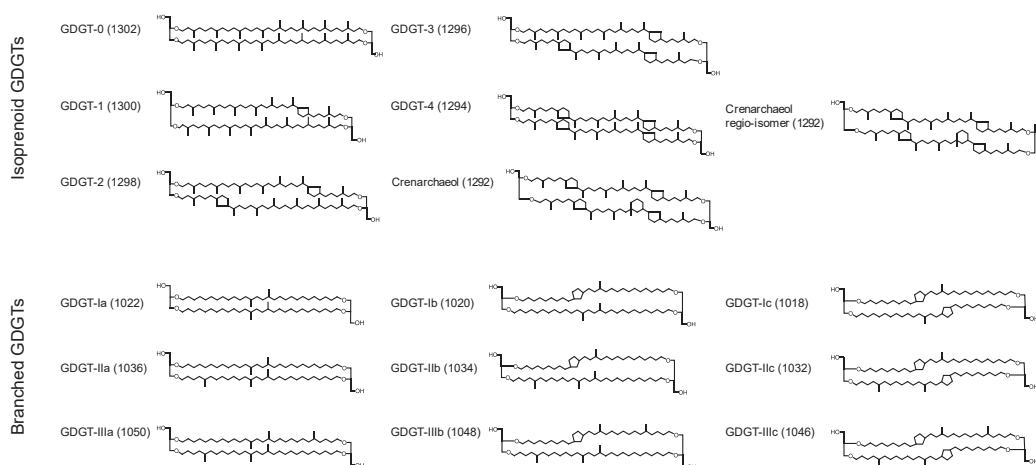


Figure 1.3: GDGTs structures and the correspondent ion masses ( $m/z$ ).

Organisms of the Archaea domain were initially detected and isolated from extreme environments. Thus, the first characterizations of the lipids present in their membranes were made from extremophiles cultures. After the first isolation and characterization of the archaeol, a diphytanyl glycerol diether, from a culture of *Halobacterium cutirubrum* (Kates et al., 1963), several studies were conducted in order to investigate new lipids and the isoprenoid glycerol ethers were found to be the main constituents of these organisms. The first discovered tetraether was a saturated GDGT extracted from thermoacidophilic Archaea (Langworthy, 1977).

After the discovery that the Archaea domain is also widely distributed in the water column and marine sediments (DeLong, 1992), the research on Archaea lipids focused on these non-extreme environments, resulting in the identification of several other tetraether structures, notably the isoGDGTs (Hoefs et al., 1997; Schouten et al., 2000).

Thaumarchaeota represents the main source of isoGDGTs and have a wide distribution in the oceans, representing up to 20% of picoplankton (Karner et al., 2001). They produce GDGTs with a wide variety of structures containing cyclopentane rings ( $n = 0$  to 4), and also the crenarchaeol (cren) and its regioisomer (cren'), with four cyclopentane rings and one cyclohexane (Sinninghe Damsté et al., 2002). Mesocosm studies with Thaumarchaeota showed that the increase in number of cyclopentane moieties in the GDGTs of the membrane lipids of these organisms changes in response to temperature (Wuchter et al., 2004). This physical adaptation occurs because compounds with cyclopentane rings have a higher melting point and their presence increase the stability of the cell membrane at higher temperatures (Gliozzi et al., 1983).

By measuring the relative contribution of GDGTs in a marine sediment sample, it is possible to determine the temperature the organisms thrive and, consequently, produced their membranes. By analyzing a globally distributed group of more than 200 marine surface sediment samples, Schouten et al. (2002) developed the  $\text{TEX}_{86}$  index (Equation 1-6), which considers the isoprenoid compounds GDGT-1, GDGT-2, GDGT-3 and cren' and correlates linearly with the annual mean SST (Equation 1-7). The GDGT-0 and Crenarchaeol are excluded from the equation, since the first one occurs in many other Archaea groups in addition to Thaumarchaeota (Koga et al., 1993b), and the second is much more abundant than the other GDGTs and does not show a strong correlation with the SST (Schouten et al., 2002; Kim et al., 2010). This index reflects mainly annual mean temperature variations between 0 and 30 °C, as would be expected for the Brazilian coast.

$$\text{TEX}_{86} = \frac{\text{GDGT-2} + \text{GDGT-3} + \text{cren}'}{\text{GDGT-1} + \text{GDGT-2} + \text{GDGT-3} + \text{cren}'} \quad (1-6)$$

$$T \text{ (}^\circ\text{C)} = \frac{\text{TEX}_{86} + 0.27}{0.015} \quad (1-7)$$

In the past decade, a few calibration models have been proposed to improve SST calculation from  $\text{TEX}_{86}$  values. Most of them use linear regression to construct the calibration model from a spatially constant relationship between modern marine surface sediments and observed instrumental SST (Schouten et

al., 2002; Kim et al., 2008, 2010; Liu et al., 2009). The global calibration developed by Schouten et al. (2002) was improved by Kim et al. (2008) with a larger data set of surface sediments ( $n = 287$ ). In this new calibration (Equation 1-8), a linear correlation between  $\text{TEX}_{86}$  and annual mean SST was observed for a temperature range between 5 and 30 °C. However, below 5 °C the  $\text{TEX}_{86}$  values become less sensitive to the variation of temperature in a way that the temperatures become overestimated in the polar regions' samples. Unreasonably high estimated SST are also observed for some low-latitude sites (Kim et al., 2008). In an attempt to solve this problem, Liu et al. (2009) developed a nonlinear alternative calibration using the inverse  $\text{TEX}_{86}$  value (Equation 1-9).

$$T (\text{°C}) = 56.2 (\text{TEX}_{86}) - 10.78 \quad (1-8)$$

$$T (\text{°C}) = -16.3 \left( \frac{1}{\text{TEX}_{86}} \right) + 50.5 \quad (1-9)$$

Based on the finding that the concentration of crenarchaeol regio-isomer correlates more strongly with SST at high temperatures, Kim et al. (2010) suggested the need for two different logarithmic calibrations for different temperature ranges:  $\text{TEX}_{86}^L$  for SST below 15 °C (Equations 1-10 and 1-11) and  $\text{TEX}_{86}^H$  for SST above 15 °C (Equations 1-12 and 1-13). The authors analyzed 116 new sediment samples, most of which from polar regions, and combined with other previously published core-top data, including Red Sea samples analyzed by Trommer et al. (2009), totalizing a global dataset of 426 samples (Figure 1.4a). It was observed that, like the samples of the polar regions, the samples of the Red Sea also behave different from the others (Figure 1.4b), probably because the population of Thaumarchaeota present different responses to the temperature when subjected to extreme salinity conditions (Trommer et al., 2009). Thus, the authors decided to exclude the data from the Red Sea and from the polar oceans from the global core-top dataset in this new calibration (Kim et al., 2010).

$$\text{TEX}_{86}^L = \log \left( \frac{\text{GDGT-2}}{\text{GDGT-1} + \text{GDGT-2} + \text{GDGT-3}} \right) \quad (1-10)$$

$$T (\text{°C}) = 67.5 (\text{TEX}_{86}^L) + 46.9 \quad (1-11)$$

$$\text{TEX}_{86}^H = \log(\text{TEX}_{86}) \quad (1-12)$$

$$T (\text{°C}) = 68.4 (\text{TEX}_{86}^H) + 38.6 \quad (1-13)$$

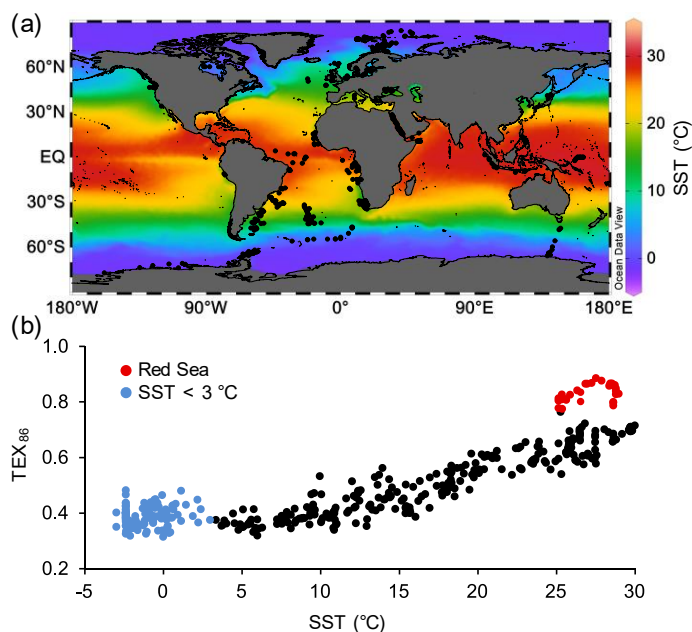


Figure 1.4: (a) World Ocean Atlas 2013 (WOA13) statistical annual mean SST and the locations of the core top samples ( $n = 426$ ) used for the global calibration of  $\text{TEX}_{86}$  (black dots). (b) Relation between the  $\text{TEX}_{86}$  and the annual mean SST. Red and blue dots represent the Red Sea and the samples with SST cooler than  $3\text{ }^{\circ}\text{C}$ , respectively (Kim et al., 2010).

Motivated by the fact that the depth of GDGTs production may vary in function of regional oceanographic dynamics, and that the availability of data used in global calibrations varies strongly from a region to another (Figure 1.4a), Tierney and Tingley (2014) recently proposed a new calibration model. The authors used a Bayesian regression approach that allows model parameters to vary as a function of space, which leads to larger uncertainties at locations that are data-poor.

The development of a new high performance liquid chromatography coupled to mass spectrometry (HPLC-MS) technique for the analysis of isoGDGTs made possible to also detect the brGDGTs (Hopmans et al., 2000). While the isoGDGTs are generally attributed to the aquatic environments, the brGDGTs are most likely produced by anaerobic and heterotrophic bacteria present in peat and soil (Pancost and Sinninghe Damsté, 2003; Weijers et al., 2006a, 2007b). Hence, the brGDGTs may be potentially used in the evaluation of terrestrial organic matter (OM) inputs into the marine environment as an alternative to the tracers derived from higher plants (Hopmans et al., 2004). The precise origin of the brGDGTs remains uncertain, but there is evidence that they are most likely produced by Acidobacteria (Weijers et al., 2009; Sinninghe Damsté et al., 2011, 2014).

In addition to the common source assignment of brGDGTs to terrestrial sources, recent studies suggest that these compounds may be produced not only in soil and peat, but also in aquatic systems, such as lakes (Damsté et al., 2009; Tierney et al., 2010), rivers (Zhu et al., 2011; Yang et al., 2013) and the marine environment (Peterse et al., 2009; Zhu et al., 2011; Hu et al., 2012; Zell et al., 2014a, 2014b). The brGDGTs can even be found in hot spring microbial mats (Schouten et al., 2007b).

The brGDGTs can vary in the degree of methylation (from 4 to 6 methyl groups) and cyclization (up to 2 cyclopentane rings) of its structures (Figure 1.3) (Weijers et al., 2006b, 2007b). The predominance of one or other form of brGDGTs, due to the different environmental conditions, is necessary to maintain the cellular structure and its vital functions. To investigate the factors that could be affecting the distribution of brGDGTs in different environments, Weijers et al. (2006b) analyzed 134 soil samples globally distributed in 90 regions. The authors found that the presence of cyclic brGDGTs in the lipid membranes of the organisms is related to the pH of the terrestrial material, while the degree of methylation of the brGDGTs is associated with both soil pH and mean annual air temperature (MAAT). Based on this relation, the authors developed the indices CBT (cyclization of branched tetraether, Equation 1-14) and MBT (methylation of branched tetraether, Equation 1-15) and proposed specific calibrations to reconstruct the soil pH (Equation 1-16) and the MAAT (Equation 1-17) to be applied in paleoenvironmental studies at different scales of geological time.

$$CBT = -\log\left(\frac{GDGT-Ib + GDGT-IIb}{GDGT-Ia + GDGT-IIa}\right) \quad (1-14)$$

$$MBT = \frac{GDGT-Ia + GDGT-Ib + GDGT-Ic}{\Sigma[\text{all branched GDGTs}]} \quad (1-15)$$

$$pH = -\frac{(CBT - 3.33)}{0.38} \quad (1-16)$$

$$MAAT = \frac{MBT - 0.122 - 0.187(pH)}{0.020} \quad (1-17)$$

Recently, Peterse et al. (2012) re-examined the calibrations for both indices with an extended data set of 287 globally distributed surface soils and a different statistical approach. The authors found that in 63% of the soils, only seven of the nine most common brGDGTs were detected and proposed a new simplified MBT' index (Equation 1-18) excluding the GDGT-IIIb and GDGT-IIIc isomers, and new calibrations for both pH (Equation 1-19) and MAAT (Equation 1-20) reconstruction.

$$MBT' = \frac{GDGT-Ia + GDGT-Ib + GDGT-Ic}{GDGT-Ia + GDGT-Ib + GDGT-Ic + GDGT-IIa + GDGT-IIb + GDGT-IIc + GDGT-IIIa} \quad (1-18)$$

$$\text{pH} = 7.9 - 1.97 \times \text{CBT} \quad (1-19)$$

$$\text{MAAT} = 0.81 - 5.67 \times \text{CBT} + 31.0 \times \text{MBT}' \quad (1-20)$$

When applied to marine sediments, in areas with a relatively high amount of soil OM input (Peterse et al., 2009), the MBT'/CBT proxy usually corresponds well with the MAAT and soil pH of the river drainage basin area (Weijers et al., 2007b; Rueda et al., 2009). However, the above-mentioned marine *in situ* production can interfere with the use of the MBT'/CBT proxies.

Based on the fact that brGDGTs occur predominantly in the terrestrial environment, while crenarchaeol would be the dominant GDGT in the marine environment, Hopmans et al. (2004) proposed the Branched and Isoprenoid Tetraether (BIT) index (Equation 1-21), a ratio between the branched and the isoprenoidal compounds (brGDGTs/isoGDGTs) applied to determine the contributions of terrestrial organic matter in aquatic environments. The BIT index is close to 1 in the terrestrial environment and near to 0 in offshore marine sediments and a gradient decrease from river to ocean is usually observed (Hopmans et al., 2004; Herfort et al., 2006b). It is important to highlight that the BIT index might not correlate well with other terrigenous biomarkers (Huguet et al., 2007b; Walsh et al., 2008) because of their exclusive presence in soil organic matter (Weijers et al., 2006b).

$$\text{BIT} = \frac{\text{GDGT-I} + \text{GDGT-II} + \text{GDGT-III}}{\text{GDGT-I} + \text{GDGT-II} + \text{GDGT-III} + \text{cren}} \quad (1-21)$$

The BIT index may also serve as a valuable parameter to verify the reliability of the TEX<sub>86</sub> index. A common issue with the use of the TEX<sub>86</sub> in the reconstruction of the SST is the potential contribution of terrestrial organic matter containing isoGDGTs derived from Thaumarchaeota (Sinninghe Damsté et al., 2012) and other Archaea present in the soil (Weijers et al., 2006b). When mixed with isoGDGTs produced *in situ* in the marine environment, these terrigenous isoGDGTs can interfere with the TEX<sub>86</sub> values and generate significant biases in the reconstructed SST. The BIT index consists of a very useful tool to evaluate the bias caused in TEX<sub>86</sub> by allochthonous isoGDGTs contribution. Zhu et al. (2011), for example, observed a better correlation between the TEX<sub>86</sub> and the SST in the Yangtze River after exclusion of sediment samples with BIT values higher than 0.2.

### 1.1.2.3. Long chain diols and the LDI

Long chain alkyl diols are composed of an alkyl chain containing two hydroxyl groups, one bound on the first carbon and another in the middle of the chain (Figure 1.5). They were first identified in the Black Sea (de Leeuw et al., 1981) and later a wide variety of these lipids were found in Quaternary sediments, from low to high latitudes, with the size of the chains ranging from C<sub>24</sub> to C<sub>36</sub> and the second hydroxyl group positioned between C<sub>11</sub> and C<sub>19</sub> (Versteegh et al., 1997, 2000).

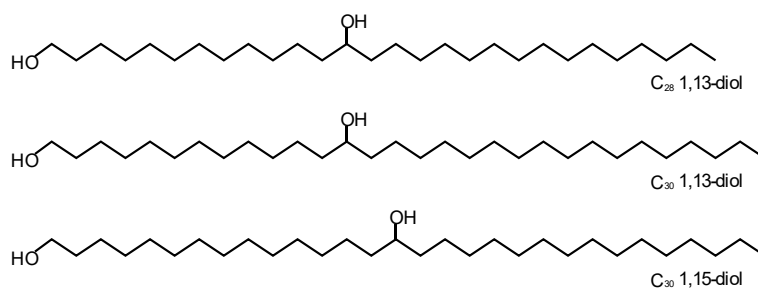


Figure 1.5: Long chain diol structures.

Previous studies have already suggested a potential application of long chain 1,14-diols in climate reconstruction (e.g. Rampen et al., 2008, 2009), but at first little was known about the relationship between 1,13 and 1,15-diols and environmental parameters and their potential application as paleoclimatic proxies as well. Versteegh et al. (2000) were the first to point out that the ratio between C<sub>30</sub> and C<sub>32</sub> long chain 1,15-diols was related to salinity, with higher contributions of C<sub>32</sub> 1,15-diol in areas that had a higher riverine input or upwelling conditions.

More than a decade later, Rampen et al. (2012) analyzed the distribution of long-chain diols in a large set of surface sediments collected worldwide, most of them from the Atlantic Ocean, and compared these data with environmental parameters of the overlying surface waters, such as temperature, salinity and nutrient concentration. The authors observed a significant correlation between the annual mean SST and the compounds C<sub>28</sub> 1,13-diol, C<sub>30</sub> 1,13-diol and C<sub>30</sub> 1,15-diol (Figure 1.5). These compounds are ubiquitous in a comprehensive set of marine surface sediments and have been reported to be produced by eustigmatophytes algae (Volkman et al., 1992, 1999; Gelin et al., 1997; Méjanelle et al., 2003). From this correlation, Rampen et al. (2012) proposed the LDI (long chain diol index, Equation 1-22) as a new paleotemperature proxy and its first calibration for marine surface sediments (Figure 1.6, Equation 1-23) for a temperature range between -3 and 27 °C, with a standard error of ± 2 °C.

$$\text{LDI} = \frac{(C_{301,15\text{-diol}})}{(C_{281,13\text{-diol}}) + (C_{301,13\text{-diol}}) + (C_{301,15\text{-diol}})} \quad (1-22)$$

$$T \text{ (}^\circ\text{C)} = \frac{\text{LDI} - 0.095}{0.033} \quad (1-23)$$

By analyzing a 43 kyr sediment core collected in the South-eastern Atlantic, near the Congo River outflow, Rampen et al. (2012) observed that the LDI shows variation patterns, similarly to other SST proxies, that can be linked to known climate events. This suggests a promising application of LDI as a new proxy for paleotemperature. However, other studies revealed that the records of eustigmatophyte algae in the marine environment are rare and the composition of the long chain diols in these algae do not coincide with that of the marine sediments (Volkman et al., 1992; Versteegh et al., 1997; Rampen et al., 2012). Thereby, the actual role of eustigmatophyte algae in producing these compounds and their interaction with other parameters in the marine environment remains uncertain.

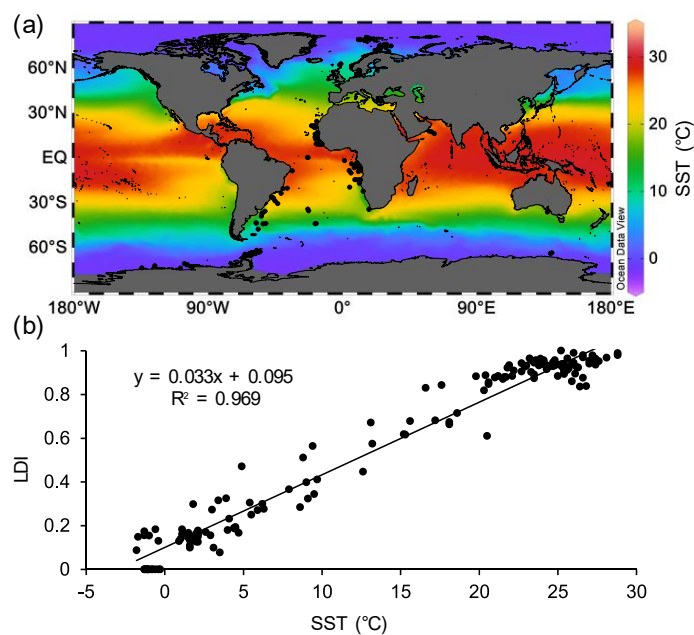


Figure 1.6: (a) World Ocean Atlas 2013 (WOA13) statistical annual mean SST and the locations of the core top samples ( $n = 162$ ) used for the global calibration of LDI (black dots). (b) Relation between the LDI and the annual mean SST (Rampen et al., 2012).

### 1.1.3. Proxies uncertainties and the multiproxy approach

As with any biomarker, the organic geochemical SST proxies carry inherent uncertainties that might affect the accuracy of estimates and cause misinterpretation of the paleotemperature variations. Although these proxies are

calibrated against annual mean SST using core top sediments, the global calibrations inevitably contain associated errors that must be considered when using the proxy in a regional scale. Biases between the proxy based estimates and the actual temperatures were observed in several studies (e.g., Ternois et al., 1997; Herfort et al., 2006a; Leider et al., 2010; Prah et al., 2010; Lopes dos Santos et al., 2013; Chen et al., 2014) and could be related to parameters other than growth temperature, such as seasonal production and preferential depth habitats of the source organisms (Sikes et al., 1997; Prah et al., 2001; Herfort et al., 2006a; Popp et al., 2006; Huguet et al., 2007a; Lee et al., 2008), pre- or post-depositional lateral transport (Benthien and Müller, 2000; Mollenhauer et al., 2007; Kim et al., 2009), influence of nutrients and light (Epstein et al., 1998; Versteegh et al., 2001; Prah et al., 2003) or even preferential degradation of a specific compound used in the proxy (Conte et al., 1992; Gong and Hollander, 1999).

A reliable estimation of paleotemperatures is essential to improve the understanding of past climate variations. The application of different paleotemperature proxies on different records can improve the confidence in large scale past climate reconstruction (Mann et al., 1998; IPCC, 2007). For a single marine sediment record, it is possible that each of the proxies may provide different signals associated with their particular uncertainties. Lopes dos Santos et al. (2013), for example, applied multiple SST proxies to a sediment core from the Murray Canyons area offshore Australia and observed that the LDI seems to be related to the SST of the austral summer, the  $\text{TEX}_{86}^H$  with the SST of the austral winter and the  $U_{37}^{K'}$  to the annual mean SST. Regarding the depth habitat, some studies suggest that GDGTs are mainly exported from subsurface waters rather than surface waters, as the  $\text{TEX}_{86}$  reconstructed temperatures usually agree better with colder temperatures measured between 40 and 150 m, while the  $U_{37}^{K'}$  and LDI better reflect the SST (Huguet et al., 2007a; Lopes dos Santos et al., 2010; Chen et al., 2014). Based on the biases and uncertainties associated with each of the organic geochemical proxies for SST presented so far, the application of multiple proxies to the same samples is often required to bring more insights regarding these biases and improve understanding of the proxies' uncertainties and local limitations, thereby enabling a more precise paleotemperature reconstruction.

#### 1.1.4. Paleoclimatology in the South Atlantic during the Holocene period

The Holocene was considered a relatively stable period, marked by less intense climatic variations when compared to the glacial periods (Mayewski et al., 2004). Nevertheless, recent high-resolution paleoclimatic records have shown that the Holocene presents larger and more frequent climatic variations than was previously thought, including changes in scales of hundreds to thousands of years (O'Brien et al., 1995; Alley et al., 1997; Bond, 1997, 2001; Mayewski et al., 2004). Mayewski et al. (2004), for example, made a compilation of ~50 globally distributed paleoclimatic records and reported at least six rapid changes, most of them characterized by cooling at the poles, dryness in the tropics and significant changes in atmospheric circulation.

The reconstruction of paleotemperature during the Holocene shows significant long-term trends in the SST variation that clearly mark the period (Kim et al., 2004). Among the climatic oscillations that characterize the Holocene, the Little Ice Age (LIA) and the Medieval Climatic Anomaly (MCA) are the best-known examples on scales of hundreds of years. The LIA occurred in the period between 0.55 and 0.25 cal kyr BP and is characterized by lower temperatures in the Northern Hemisphere (Mann et al., 2009). It is believed to be the more recent among the climate fluctuations events, known as the Bond Events, that took place during the Holocene with a cyclicity of ~1.5 kyr (Bond, 1997, 2001), probably caused by a decrease in solar irradiance and a weakening in the thermohaline circulation (Bond, 2001; Wanner et al., 2011). The MCA occurred earlier, between 1.0 and 0.7 kyr BP, characterized by relatively higher temperatures in some regions of the Northern Hemisphere. It was probably caused by a higher solar irradiance and lesser volcanic activity (Crowley, 2000; Mann et al., 2009; Diaz et al., 2011), and marked by a tendency for La Niña-like conditions in the tropical Pacific (Mann et al., 2009).

Climatic variations during the Holocene in the South Atlantic Ocean receive much less attention and is not constrained as it is for the North Atlantic, especially on the western margin of the South Atlantic (Mahiques et al., 2007; Pivel et al., 2013). The lack of studies for the Holocene with good time-scale resolution raise uncertainties about the evolution and the occurrence of important climatic events in the South Atlantic during this period (Lessa et al., 2016).

The Atlantic Meridional Overturning Circulation (AMOC) is considered the central mechanism of heat transport between the two hemispheres across the

Atlantic Ocean (Buckley and Marshall, 2016 and references therein). Abrupt changes in the AMOC dynamics have been considered an important factor in the climatic variations along the Holocene (Menary et al., 2012). The Brazil Current (BC) and the North Brazil Current (NBC) play an important role in the South Atlantic upper level circulation (Peterson and Stramma, 1991). There is evidence suggesting alternations in the strengths of these two western boundary currents resulted in significant climatic events which affected the AMOC magnitude (Arz et al., 1999; Chiessi et al., 2014). Chiessi et al. (2014), for example, observed that positive (negative) anomalies in SST and  $\delta^{18}\text{O}$  relate to a stronger (weaker) BC and a weaker (stronger) AMOC. These authors also observed that periods of strong BC synchronize with periods of weak NBC, negative anomalies of SST in the high latitudes of the North Atlantic and positive anomalies of rainfall over the Southeastern South America.

Paleotemperature oscillations in South Atlantic SST may also be related to variations in the dynamics of the South Atlantic Convergence Zone (SACZ), the South American Monsoon System (SAMS) and, therefore, the south-eastern South American climate (Zhou and Lau, 1998; Robertson and Mechoso, 2000; Liebmann and Marengo, 2001; Carvalho et al., 2004; Chaves and Nobre, 2004). From a compilation of 120 paleoclimatic records, Prado et al. (2013b) observed a less intense precipitation in eastern South America during the mid-Holocene relative to the late Holocene, relating this feature to a low austral summer insolation (Prado et al., 2013a). Bender et al. (2013) demonstrated that paleoclimatic changes during the Holocene were related to changes in the intensity and periodicity of the El Niño Southern Oscillation (ENSO) in the Southern Hemisphere. Wainer et al. (2014) observed changes in the position and intensity of the South Atlantic Subtropical High (SASH) that altered the precipitation regime over South America during the cooling events of the northern hemisphere in 12.9-11.6 cal kyr BP and 8.6-8.0 cal kyr BP. In general, the climate changes identified during the Holocene in South America are mostly related to conditions of more or less humidity (Mahiques et al., 2007; Cordeiro et al., 2008; Bender et al., 2013; Prado et al., 2013b; Razik et al., 2013; Wainer et al., 2014).

## **1.2. Study area**

### **1.2.1. Geomorphology**

The Cabo Frio and Rio de Janeiro continental shelves are located in the arc-shaped sector of the southeastern Brazilian upper margin, that extends from Cabo de Santa Marta in the south (28°30'S–49°00'W) to Cabo Frio in the north (23°00'S–42°00'W). The continental shelf in this sector has a width ranging from 73 to 231 km and declivity between 1:656 and 1:1333. The shelf break is located between 120 and 180 m water depth. The isobaths approach the coast towards the Cabo Frio region in the north, where the shelf is narrower (Mahiques et al., 2004). The platform in this region is crossed by narrow, shallow and long channels, which generally reach the shelf break and favor sediment transport to deeper regions. The most evident ones are the Cabo Frio, Rio de Janeiro, Ilha Grande, Cananéia and Itajaí channels (Zembruski, 1979).

The Campos Basin extends farther north of Cabo Frio, located between 20.5°S (Vitoria High) and 24°S (Cabo Frio High), with an area of more than 100,000 km<sup>2</sup> (Viana et al., 1998). The water column is up to 3,000 m, with depths of more than 200 m in more than 70% of its area (Carminatti and Scarton, 1991). The continental shelf width is on average 100 km, and the shelf break is usually located at water depths around 80 to 130 m in the north-south direction. The slope has an averaged depth gradient and width of 2.5° and 40 km, respectively (Viana et al., 1998). A major topographic feature in the slope is the presence of eleven major U-shaped canyons in the central and southern portions of the basin exhibiting the following characteristics: heads starting from 115 to 1022 m water depths, lengths from 9.5 to 42.5 km and average widths of the submarine valleys from 1.0 to 8.0 km (de Almeida and Kowsmann, 2016). The slope is bordered to the east by the São Paulo plateau, a low declivity area (0 to 2°) that extends from 2000 to 3500 m depth, where the canyons converge into a more expressive drainage system (Viana et al., 1998; de Almeida and Kowsmann, 2016).

The northern area of the basin is influenced by the Paraíba do Sul River (Razik et al., 2015) and the slope base is shallower (1500 m water depth) than in the south (2000 m) due to the development of a submarine cone connected to the Almirante Camara submarine canyon (Brehme, 1993). The Paraíba do Sul River is considered a medium-sized river, with a length of 1145 km and a catchment area

of 55,400 km<sup>2</sup>, crossing three of the most industrialized Brazilian states: Minas Gerais, São Paulo and Rio de Janeiro (Carvalho et al., 2002). Events of coastal upwelling are observed in the southern portion of the basin, as will be presented in further details later.

### 1.2.2. Hydrodynamics

The water circulation pattern on the southeastern Brazilian margin (Figure 1.7) is mainly controlled by the flow of BC, formed at 10°S as a branch of the South Equatorial Current and is highly influenced by the Subtropical Gyre and the South Atlantic High (Peterson and Stramma, 1991). At approximately 36°S, the BC converges with the Malvinas Current (MC) flowing northwards from the Argentinean shelf. The ocean surface processes in the southern Brazilian continental shelf are then characterized by the interaction between northward flows of the cold and low salinity sub-Antarctic waters from the Argentinean shelf, which are mixed with Rio de la Plata and Patos Lagoon discharge, as well as with the southward flow of the BC that transport hot and saline tropical waters (Lima et al., 1996).

The BC plays an important role in southward heat transport in the southwest Atlantic, whose variability affects the intensity of the South America Monsoon System (SAMS), which, in turn, is responsible for precipitation in most of the South American continent (Robertson and Mechoso, 2000; Cruz et al., 2005; Zhang and Delworth, 2005; Chiessi et al., 2009). According to Chiessi et al. (2014), positive SST anomalies have been correlated with increased precipitation over the northern sector of southeastern South America.

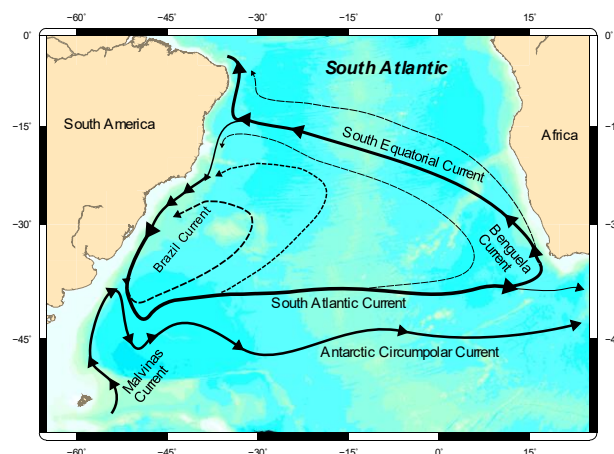


Figure 1.7: Schematic characterization of the circulation in the Subtropical South Atlantic Ocean (modified from Peterson and Stramma, 1991, designed by Ilson Silveira).

The BC flows southward following the 200 m isobath and transports Tropical Waters (TW) from the tropical South Atlantic in its upper levels and South Atlantic Central Waters (SACW) between 200 and 700 m water depths (Campos et al., 2000). Meandering in the BC flow is caused by changes in the coastline orientation. These meanders frequently develop and form strong cyclonic and anticyclonic frontal eddies, inducing the intrusion of SACW onto the shelf break (Campos et al., 2000; Silveira et al., 2000). Particularly in the Cabo Frio region, the sudden change in the shoreline orientation associated with the prevailing NE winds is responsible for an intermittent surface upwelling of the SACW (Figure 1.8a) (Rodrigues and Lorenzetti, 2001; Castelao and Barth, 2006). The Cabo Frio upwelling system (CFUS) is therefore characterized by a cold SST anomaly during the beginning of the austral summer, when the intense NE winds associated with the South Atlantic high-pressure cell exerts its highest influence on local hydrodynamics (Valentin, 1984a; Rodrigues and Lorenzetti, 2001; Franchito et al., 2008). The summer period also corresponds to the rainy season in SE Brazil and, consequently, an increase in the continental runoff to the coastal waters is observed (Mahiques et al., 2004). In contrast, during the austral winter, the NE winds are weaker and the frequency of cold front SW winds is higher, which inhibits the surface upwelling of SACW and increases the influence of warm surface waters transported by the BC (Valentin et al., 1987; Lessa et al., 2014).

In summary, the water mass structure of the CFUS is composed of three main water masses: the surface oligotrophic, warm and salty TW, flowing offshore carried by the BC; the colder and nutrient-rich SACW, which is almost constantly located at the shelf bottom; and the low salinity, warmer, Coastal Water (CW), which results from the dilution of oceanic waters with continental fresh water inputs (Mahiques et al., 2004). The SACW intrusions onto the shelf increase nutrient concentrations and enhance the rates of primary production in the CFUS to  $>0.5 \text{ gC m}^{-2} \text{ d}^{-1}$  (Brandini et al., 2018 and references therein; Figure 1.8b). Consequently, the regional fisheries (Matsuura, 1996) and the export of biomass to adjacent areas (Lorenzetti and Gaeta, 1996) are also enhanced. This scenario contrasts with the overall oligotrophic conditions ( $<0.04 \text{ gC m}^{-2} \text{ d}^{-1}$ ) in adjacent continental shelf and open waters dominated by warm TW (Marone et al., 2010; Suzuki et al., 2015; Brandini et al., 2018).

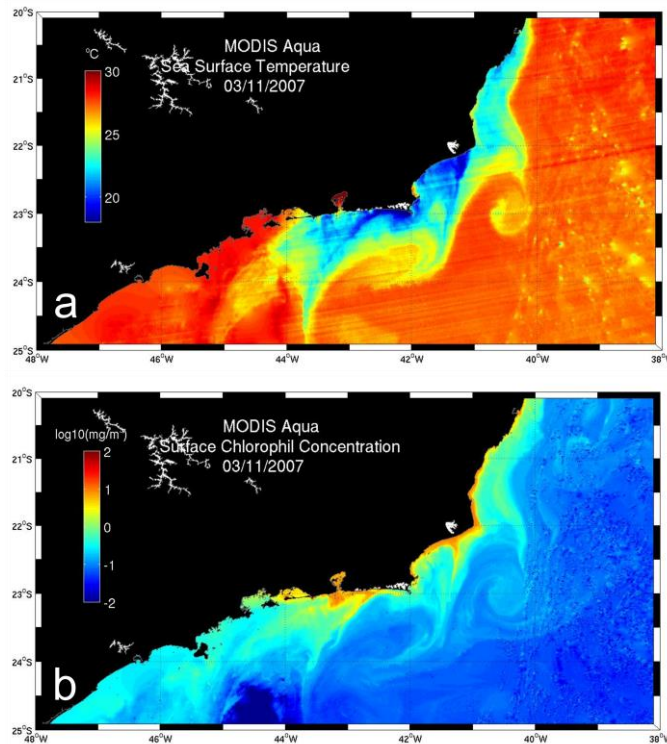


Figure 1.8: (a) SST and (b) surface chlorophyll concentration obtained by satellite (MODIS sensor, Aqua satellite) in the year 2007 for the Southwestern Atlantic (designed by Afonso Paiva).

### 1.2.3. Sedimentology

Overall, sedimentation patterns on the Brazilian continental shelf are defined by the interaction between sediment source, hydrodynamic processes and sea-level oscillations in a way that modern sedimentary deposits are concentrated in the inner and middle shelf, whereas relict and carbonate sediment deposits are concentrated on the outer shelf (Figueiredo Jr. et al., 2016 and references therein). During the last regressive event at the end of the Late Pleistocene, the shelf was exposed to intense erosion and, therefore, dissected by fluvial valleys that led to the direct deposition of sediments on the slope (Kowsmann and Costa, 1979; Viana et al., 1998).

The sedimentation dynamics varies along the south-eastern Brazilian platform, resulting in different sedimentation rates from one location to another, according to the shelf and slope morphologies and the BC meandering (Mahiques et al., 2002; Sanders et al., 2014). According to Mahiques et al. (2004), the sedimentation rates in the south-eastern Brazilian shelf and upper slope can vary from 5 to 660 mm kyr<sup>-1</sup> and is strongly related to the primary productivity, to the

continental input and to the flow of the BC. The areas of lower sedimentation rates in the south-eastern Brazilian upper margin are correlated with the main flux of the BC, whereas pelagic processes associated with meandering of the BC and upwelling events create higher rates of sedimentation, as observed in the CFUS region (Mahiques et al., 2004). Terrigenous sediment is supplied by small to medium size rivers, with the Paraíba do Sul River being the highest contributor (Viana et al., 1998; Razik et al., 2015).

Mahiques et al. (1999) proposed a division of the south-eastern Brazilian inner shelf (<100 m depth) in two sectors, as a function of distinct sedimentary, geomorphological and organic matter features. To the south of São Sebastião Island, in the State of São Paulo (23.76°S and 45.41°W), there is an increase in the clay content with depth due to a more effective action of the wave's energy on the bottom in the shallower areas. This hydrodynamic action prevents the deposition of fine sediment and organic matter, causing a depositional gradient towards the shelf break. In this portion, the highest organic carbon contents occurs close to the 100 m isobath. Our region of interest is located northward of São Sebastião Island (Figure 1.9), where, even though the clay contents are lower than those observed in the south, the geomorphological complexity significantly attenuates the hydrodynamic energy, favoring the deposition of fine sediments and organic matter, with presence of bioclastic sediment between the isobaths of 75 and 200 meters (Mahiques et al., 2004; Figure 1.9).

In the Cabo Frio shelf, the upwelling events increase sedimentation rates and contribute to enhanced organic matter accumulation in the sediment (Mahiques et al., 2002). Continental inorganic and organic matter delivered by the Paraíba do Sul River, whose discharge ranges from 110 to 2600 m<sup>3</sup> s<sup>-1</sup> over the year (Carvalho et al., 2002), must also be considered. Another potential source of materials to the CFUS is the coastal plume formed by waters from Guanabara (Albuquerque et al., 2014).

Transport of suspended particulate material and/or resuspended sediments on the Cabo Frio shelf is basically controlled by wind-driven circulation (NE trade winds) and by coastal currents on the inner shelf, by cross-shelf upwelled coastal waters on the mid-shelf and by the meandering of the internal front of the BC on the outer shelf (Mendoza et al., 2014 and references therein).

The distribution of sediment types in the Campos Basin is heterogeneous and complex. Lithoclastic sediments predominate in the inner and mid continental shelf whereas bioclastic and biolithoclastic sediments are found in the mid and outer shelf in the southern portion of the basin and also to the north in the shallow

areas nearby the Itapemirim River (Figueiredo Jr. et al., 2016). Fine-grained and silty-clay sediments with high contents of total organic carbon (TOC) are observed to the south of Cabo Frio (Figure 1.9; Yoshinaga et al., 2008; Cruz et al., 2013; Sanders et al., 2014), possibly as a result of high primary production in the water under the influence of upwelling and local hydrodynamics (i.e., eddies and lateral transport processes; Sanders et al., 2014). This ‘mud bank’ near Cabo Frio has a high potential of recording past biogeochemical and oceanic variability at elevated time resolution (Cordeiro et al., 2014). Bulk  $\delta^{13}\text{C}$  values observed by Sanders et al. (2014) indicate predominance of marine-derived organic carbon in this area.

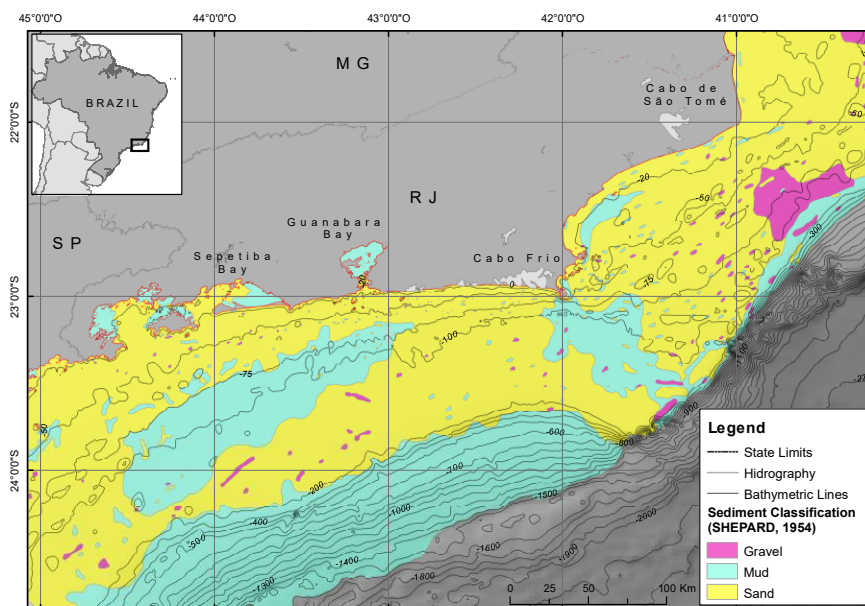


Figure 1.9: Grain size of the surface sediments in the south-eastern Brazilian margin (unpublished sediment grain size data provided by Alberto Figueiredo, personal communication; designed by João R. dos Santos Filho).

### 1.3. Research background and thesis motivation

A greater knowledge of paleotemperature variability in the South Atlantic is of great interest given the role of SST in the global heat transport. Despite this aspect, such studies in the south-western portion of the Atlantic are scarce when compared to the south-eastern counterpart or to the northern basin of the Atlantic Ocean (Leduc et al., 2010; McGregor et al., 2015). In this context, the continental shelf along the State of Rio de Janeiro is a particularly interesting area to study in the SW Atlantic because of unique characteristics along the Brazilian coast, including: (i) eutrophic conditions supported by upwelling and orthogonal intrusion into the photic zone of nutrient-rich waters – which contrasts with an overall

oligotrophic condition in the tropical Brazilian shelf; (ii) a complex and dynamic current system that favor the accumulation of OM-rich sediments in the inner and mid-shelf; (iii) enhanced sedimentation ratios nearby Cabo Frio resulting in areas with great potential to archive paleoceanographic variability since the late Pleistocene in a high temporal resolution. Because of these aspects, the upwelling system of Cabo Frio is usually a target area for paleoceanographic reconstructions in Brazil (Mahiques et al., 2004; Nagai et al., 2009; Gyllencreutz et al., 2010; Cruz et al., 2013; Cordeiro et al., 2014; Lessa et al., 2016), but the same is not true on a regional scale along the Rio de Janeiro's shelf (Lazzari et al., 2018).

Paleotemperature indicators based on data obtained from foraminifera (Pivel et al., 2013; Chiessi et al., 2014; Lessa et al., 2014, 2016; Santos et al., 2014) and alkenones (Mahiques et al., 2005; Rühlemann and Butzin, 2006; Magalhães, 2010; Cordeiro et al., 2014; Evangelista et al., 2014; Lourenço et al., 2017b) in marine sediments have already been considered in Brazil. However, GDGT and long-chain diol determinations are rare in the country (Chiessi et al., 2015; Crivellari et al., 2018) and the current global calibrations have almost no contribution from south-eastern Atlantic sediment samples (Kim et al., 2008, 2010; Liu et al., 2009; Pearson et al., 2011; Rampen et al., 2012; Lü et al., 2014; Tierney and Tingley, 2014).

The establishment of a direct correlation between the indication of SST based on a particular ratio among selected molecules in surface sediments and the actual instrumental SST – in other words, the proxy calibration – is an essential aspect in the chemical (organic or inorganic) proxy approach. The main issue here is the spatial and seasonal variation that may occur in this relation, and thus the knowledge of the potential influence of oceanographic processes upon the production of the organic molecules considered in the proxies (i.e., GDGTs, alkenones or diols) is essential to constrain the proxy performance and extrapolate local data to regional or even global scales. The best approach to cope with this issue is to estimate the temperature from surface sediment samples from the study area of interest using the pre-existing calibrations and compare it with the instrumental SST (Benthien and Müller, 2000; Leider et al., 2010; Chen et al., 2014). The bias between the proxy-based estimates and instrumental temperatures may provide information about parameters affecting the proxies other than growth temperature and whether or not the proxy should be applied for downcore reconstructions in the region of interest.

The data scarcity of proxy calibration using sediment samples from the south-eastern continental margin, particularly for GDGTs and diols motivated an

initial work in this thesis to change this scenario. Based on these results, a multiproxy approach was considered to investigate paleoceanographic variability during the Holocene as registered in sediment cores from representative regions in the continental shelf along the State of Rio de Janeiro.

#### **1.4. Objectives of this thesis**

The present thesis aims at using organic geochemical proxies as indicators of paleotemperature as registered in shelf sediments of the south-eastern Brazilian continental margin, with two foci: (i) to test the applicability of the selected proxies under the local and regional environmental conditions of the study area in the present; (ii) to apply a multiproxy approach to reconstruct the paleotemperature during the Holocene period using two sediment cores retrieved from the Cabo Frio and Rio de Janeiro shelves.

The specific goals are:

- Investigate the applicability and the uncertainties of the  $U_{37}^{K'}$  and  $TEX_{86}^H$  proxies in the SST reconstruction in the study region by analyzing surface sediments from the Campos Basin shelf and slope;
- Investigate the applicability and the uncertainties of the MBT'/CBT proxies in the reconstruction of the soil pH and MAAT of the adjacent continent by analyzing surface sediments from the Campos Basin;
- Apply three organic geochemical proxies ( $U_{37}^{K'}$ ,  $TEX_{86}^H$  and LDI) to reconstruct the paleotemperature in the south-eastern Brazilian margin during the Holocene using two sediment cores collected from the continental shelf at Cabo Frio and Rio de Janeiro;
- Compare the data obtained in the present study with the previous results observed by Lessa et al. (2016) and Lazzari et al. (2018) for the Cabo Frio and the Rio de Janeiro sediment cores, respectively.

#### **1.5. Thesis outline**

Chapter 2 provides detailed information on the experimental part of the thesis including the applied analytical methods. Chapters 3 to 5 present a discussion of the results in the form of three first-author manuscripts having in mind the objectives addressed in section 1.4.

Chapter 3 describes the applicability of  $U_{37}^{K'}$  and  $TEX_{86}^H$  as ocean temperature proxies in the Campos Basin (SE Brazilian shelf). The reconstructed temperatures obtained from 53 surface sediments along cross-margin transects were compared with the modern temperatures from WOA13 and the biases observed were related to potential non-thermal factors, such as seasonality, depth habitat of the source organisms and lateral transport of particles. The results contribute to the general understanding for the use of organic geochemical paleotemperature proxies and reveal that, even though  $U_{37}^{K'}$  and  $TEX_{86}^H$  are suitable for paleoclimate studies, local oceanographic processes must be considered.

In chapter 4, the brGDGTs in marine surface sediment records are used to evaluate soil organic matter input by rivers into the marine environment and reconstruct the MAAT and soil pH of the nearby land using MBT' and CBT proxies from 51 stations in the Campos Basin. A comparison between the reconstructed parameters and the instrumental data from the adjacent drainage basins was made to evaluate the influence of local features (e.g. selective degradation and *in situ* production) on the MBT' and CBT proxies. Our results contribute to the understanding of the MBT'/CBT proxies' applicability to marine sediments and, more specific, to the studied region.

In chapter 5, a multiproxy approach ( $U_{37}^{K'}$ ,  $TEX_{86}^H$  and LDI) was considered to reconstruct the paleotemperature during the last 14.5 kyr in two sediment cores retrieved from the Cabo Frio and Rio de Janeiro shelves. The study first discusses the agreement observed between the proxy-based temperatures reconstructed for the core-top samples of each core and the modern observed temperatures from WOA. Thereafter, the variation of the reconstructed temperatures throughout the Holocene period is interpreted based on previous paleoclimate records. The differences between the two locations and between the proxies' response to the local environmental factors are fully discussed. The results contribute to the understanding of the paleoclimatic changes during the Holocene in the south-eastern Brazilian margin.

Overall, the thesis demonstrates the complexity behind the pre- and post-depositional processes that may complicate the use of alkenone- and GDGT-based temperature proxies in the Campos Basin region and describes the importance of applying multiple organic geochemical proxies ( $U_{37}^{K'}$ ,  $TEX_{86}^H$  and LDI) in marine sediment records retrieved from two different regions under distinct hydrodynamic settings in order to obtain more information about the local paleoceanographic changes.

## **Chapter 2**

### **Experimental**

#### **2.1.**

##### **Sampling**

##### **2.1.1.**

###### **Surface sediments**

The surface sediment samples were collected as part of the Habitats Project (CENPES/PETROBRAS) in 2008 and 2009 along 5 cross-margin transects (A, B, G, H and I; Figure 2.1) across the Campos Basin. A total of 53 sampling stations were distributed along the transects on twelve isobaths at depths of 25, 50, 75, 100, 150, 400, 700, 1000, 1300, 1900, 2500 and 3000 m. Sediments were collected with a large adapted Van Veen sampler at the continental shelf stations and with an adapted box corer at the slope stations. Samples represent the top 2 cm layer of the sediment and are a composite of three deployments of the sampler.

##### **2.1.2.**

###### **Sediment cores**

The 403 cm long sediment core CF10-09A was collected from the Cabo Frio continental shelf at 23.20°S and 41.74°W (Figure 2.1) from aboard the R/V Ocean Surveyor in January 2010 as a part of the Upwelling Project (UFF and Petrobras Geochemistry Network). The core was collected from 117 m depth using a piston corer. The core was sectioned at 1 cm intervals and stored at 4 °C in the Paleoenvironmental Studies Laboratory (Geochemistry Department, UFF).

The 160 cm long sediment core RJ13-01C was recovered from the Rio de Janeiro continental shelf at 23.40°S and 43.33°W from aboard the Brazilian Navy Vessel AV.Pq.Oc. Diadorim, in December 2013. The core was collected at the 100 m isobath with a polycarbonate tube using a piston corer sampler. The cores were sectioned at 1 cm intervals and stored at 4 °C in the Marine and Environmental Studies Laboratory (Chemistry Department, PUC-Rio) until analysis.

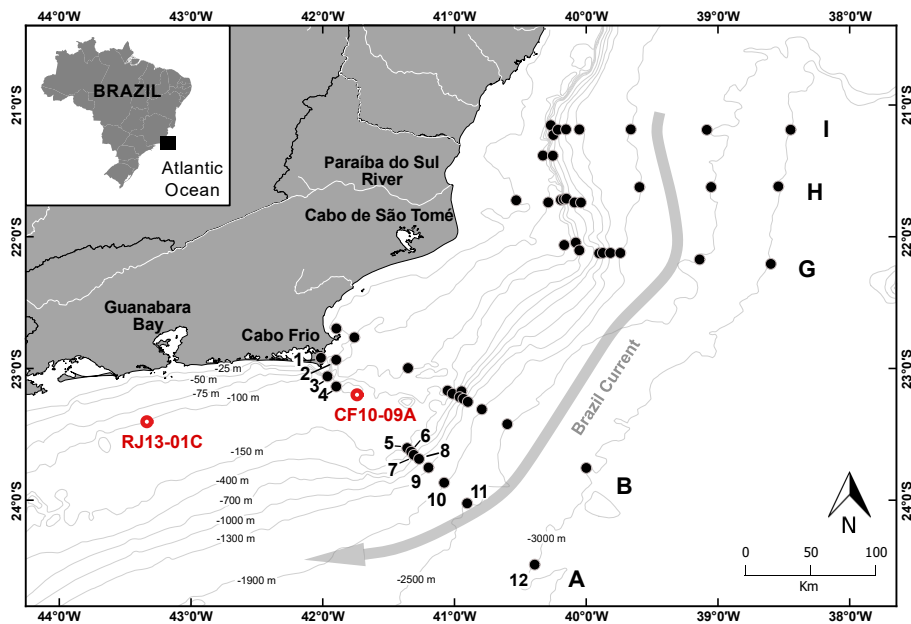


Figure 2.1: Location of the surface (0-2 cm) sediment sampling stations in the Campos Basin (black dots), the sediment core CF10-09A in the Cabo Frio shelf and the RJ13-01C in the Rio de Janeiro shelf (red circles).

Table 2.1: Information of the surface sediment samples of the Campos Basin.

Station (0-2 cm)	Latitude (°S)	Longitude (°W)	Water depth (m)	Location
A01	22.9193	42.0141	25	shelf
A02	22.9346	41.8979	50	shelf
A03	23.0603	41.9643	75	shelf
A04	23.1373	41.8976	100	shelf
A05	23.6047	41.3587	150	shelf
A06	23.6327	41.3284	400	upper slope
A07	23.6561	41.3089	700	upper slope
A08	23.6867	41.2693	1000	upper slope
A09	23.7527	41.1972	1300	upper slope
A10	23.8675	41.0784	1900	down slope
A11	24.0241	40.9037	2500	down slope
A12	24.4893	40.3912	3000	down slope
B1	22.6968	41.8966	25	shelf
B2	22.7643	41.7598	50	shelf
B3	22.9970	41.3526	75	shelf
B4	23.1683	41.0521	100	shelf
B5	23.1919	41.0142	150	shelf
B6	23.1734	40.9467	400	upper slope
B7	23.2176	40.9606	700	upper slope
B8	23.2307	40.9324	1000	upper slope
B9	23.2535	40.8987	1300	upper slope
B10	23.3104	40.7925	1900	down slope

Station (0-2 cm)	Latitude (°S)	Longitude (°W)	Water depth (m)	Location
B11	23.4227	40.5990	2500	down slope
B12	23.7554	39.9995	3000	down slope
G03	22.0631	40.1670	75	shelf
G04	22.0443	40.0793	100	shelf
G05	22.1033	40.0521	150	shelf
G07	22.1258	39.9018	700	upper slope
G08	22.1227	39.8733	1000	upper slope
G09	22.1231	39.8164	1300	upper slope
G10	22.1232	39.7408	1900	down slope
G11	22.1727	39.1391	2500	down slope
G12	22.2063	38.5986	3000	down slope
H1	21.7234	40.5316	25	shelf
H2	21.7393	40.2881	50	shelf
H3	21.7200	40.1923	75	shelf
H4	21.7154	40.1713	100	shelf
H5	21.7109	40.1504	150	shelf
H6	21.7398	40.0888	400	upper slope
H7	21.7402	40.0398	700	upper slope
H10	21.6233	39.5956	1900	down slope
H11	21.6227	39.0516	2500	down slope
H12	21.6184	38.5413	3000	down slope
I02	21.3836	40.3289	50	shelf
I04	21.1534	40.2689	100	shelf
I05	21.3848	40.2534	150	shelf
I06	21.2278	40.2499	400	upper slope
I07	21.1872	40.2149	700	upper slope
I08	21.1850	40.1533	1000	upper slope
I09	21.1858	40.0522	1300	upper slope
I10	21.1850	39.6611	1900	down slope
I11	21.1883	39.0843	2500	down slope
I12	21.1875	38.4481	3000	down slope

## 2.2. Geochronology of the sediment cores

The geochronology of the sediment core CF10-09A was determined by Lessa et al. (2016). Dating relied on  $^{14}\text{C}$  measurements on the organic matter from 13 samples using accelerator mass spectrometry (AMS) in the Arizona AMS Facility (University of Arizona, USA). The AMS  $^{14}\text{C}$  ages were calibrated using the Calam software (Blaauw, 2010) and the Marine09 curve (Reimer et al., 2009). The reservoir effect ( $\Delta R$ ) considered for the region was  $8 \pm 17$  years (Angulo et al., 2005), proposed for the south and south-eastern Brazilian continental margin. The

Clam software created a statistical chronological model and the ages that represented the highest probability in the confidence interval were used in the paleotemperature reconstruction. According to Lessa et al. (2016), the CF10-09A core encompasses a time range of 1.1–7.1 cal kyr BP, with uncertainties between 0.15 and 0.33 kyr.

The geochronology of the sediment core RJ13-01C was determined by Lazzari et al. (2018) and is based on four  $^{14}\text{C}$  dates of planktonic foraminifera (*Globigerinoides ruber*) determined by AMS in the Laboratory of Ion Beam Physics (ETH Zurich, Switzerland). The foraminifera were cleaned following the Barker et al. (2003) procedure and the fraction  $>125\ \mu\text{m}$  was considered. The AMS  $^{14}\text{C}$  ages were calibrated using the OxCal online program (Ramsey and Lee, 2013) and the Marine13 curve (Reimer et al., 2013). The  $\Delta R$  considered for the region was  $-127 \pm 67$  years (Macario et al., 2015). The first centimeters of the RJ13-01C core were also dated by the  $^{210}\text{Pb}$  method by Lazzari et al. (2018) using instrumental gamma ray emission method for  $^{210}\text{Pb}$  (46,5 keV),  $^{214}\text{Pb}$  (351 keV) and  $^{137}\text{Cs}$  (661 keV) using a high purity germanium detector (Canberra GCW 4023S) in Professor Edward Boyle's lab (Massachusetts Institute of Technology, USA). According to these age models, the RJ13-01C core covers a period of 0.3–14.5 cal kyr BP (Lazzari et al., 2018).

Table 2.2: Information of the sediment core samples.

Station	Latitude (°S)	Longitude (°W)	Water depth (m)	Location	Length (cm)	Age (cal kyr BP)	Reference
CF10-09A	23.20	41.74	117	Cabo Frio shelf	403	1.1–7.1	Lessa et al. (2016)
RJ13-01C	23.40	43.33	100	Rio de Janeiro shelf	160	0.3–14.5	Lazzari et al. (2018)

### 2.3.

#### TOC and $\delta^{13}\text{C}$ analysis of the sediment cores

The sediment was freeze-dried and homogenized. Dry sediment samples were weighed (10 mg for TOC and 0.5 mg for  $\delta^{13}\text{C}$ ) in silver capsules, acidified with a HCl solution ( $1\ \text{mol L}^{-1}$ ) and heated at  $100\ ^\circ\text{C}$  to remove carbonate. The capsules were kept at this temperature for 6 h. TOC (%) was determined using a Flash 2000 model Organic Elemental Analyzer (OEA, Thermo Scientific). The quantification was based on a calibration curve of aspartic acid (C = 39.09 %). An intermediate amount of the aspartic acid standard (0.2 mg) was analyzed as an

unknown sample throughout the sequence for every 10 samples to monitor the calibration. The instrumental accuracy was verified through the analysis of the standard reference material NIST 1941B (Organics in Marine Sediments), which has a TOC content of  $2.99 \pm 0.24$  %. The TOC of the reference material analyzed 3 times within the sequence was  $3.07 \pm 0.05$  %. To determine the analytical reproducibility, 27 out of the total of 174 samples were analyzed in duplicate, and 8 in triplicate. The average standard deviation of these analyses was  $\pm 0.03$  %.

The carbon isotopic composition ( $\delta^{13}\text{C}$ ) of the bulk organic matter was determined using a Flash 2000 model OEA coupled to Delta V isotope ratio mass spectrometer (IRMS, Thermo Scientific) system. Three pulses of the reference gas ( $\text{CO}_2$ ), previously calibrated with the IAEA USGS40 standard material, were introduced at the beginning of each analysis. The  $\delta^{13}\text{C}$  was calculated according to the value of the third pulse, and the values reported as the average of two injections. Only the results with a deviation of less than 0.4 ‰ were accepted.

## **2.4. Lipids extraction and separation**

The surface samples were extracted and fractionated in Dr. Enno Schefuß's Laboratory (MARUM, University of Bremen, Germany) and in Prof. Gesine Mollenhauer's Laboratory (Department of Geosciences, University of Bremen, Germany), respectively. The sediment core samples were extracted and fractionated in the Marine and Environmental Studies Laboratory (PUC-Rio) by reproducing the same method, as described below.

An aliquot of 5 g ( $\pm 0.001$  g) of dry sediment for the top-core samples and the core CF10-09A was extracted, whereas for the RJ13-01C core a higher mass of sediment was necessary, because of the low TOC contents of these samples: 10 g ( $\pm 0.001$  g) from the top down to 99 cm, and 30 g ( $\pm 0.001$  g) for the samples from 101 to 160 cm in the core. Sediment was extracted by an accelerated solvent extraction system (ASE 200, Dionex) with a mixture of dichloromethane:methanol (9:1, v:v) at a temperature of 100 °C and a pressure of 1000 psi. Before extraction, 1000 ng of  $\text{C}_{19}$ -ketone and 1000 ng of  $\text{C}_{46}$ -GDGT were added as internal standards. The bulk lipid extracts were concentrated by rotary evaporation and saponified for 2h at 80 °C with 1 mL of KOH (0.1 M) in methanol: $\text{H}_2\text{O}$  (9:1; v:v). Neutral lipids were recovered in hexane with 3 successive extractions. The neutral extract was fractionated in 3 fractions of different polarity using silica gel column chromatography, as follows: *n*-alkane fraction using 4 mL of hexane; alkenone

fraction using 4 mL of dichloromethane:hexane, 2:1 (v:v); and the polar fraction, containing the GDGTs and long chain diols, using 4 mL of dichloromethane:methanol, 1:1 (v:v). The column was a Pasteur pipette filled with 4 cm of the silica gel previously deactivated with 1 % H<sub>2</sub>O. The fractions were dried under a stream of nitrogen at 40 °C.

The alkenone fraction was re-dissolved in hexane to be analyzed by gas chromatography with a flame ionization detector (GC-FID). The polar fraction was re-dissolved in n-hexane:isopropanol 99:1 (v:v), filtered 3 times using a 0.45 µm PTFE filter, re-dried, weighted, and re-dissolved again in n-hexane:isopropanol 99:1 (v:v) to a final concentration of 2 mg mL<sup>-1</sup> (Schouten et al., 2009) for further analysis of the GDGTs by high performance liquid chromatography-atmospheric pressure chemical ionization-mass spectrometry (HPLC-APCI-MS). After the GDGTs analyses, the remaining polar fraction was dried and derivatized by adding 100 µL of acetonitrile and 100 µL of N,O-bis(trimethylsilyl)trifluoroacetamide (BSTFA) and heating the mixture at 80 °C for 1h, for the analysis of the long chain diols using gas chromatography–time of flight mass spectrometry (GC–TOF-MS).

The analyses of the lipid fractions were performed in Prof. Gesine Molenhauer's Laboratories: in the Department of Geosciences (Bremen University, Germany) for the surface sediments and in the Alfred Wegener Institute (Bremerhaven, Germany) for the sediment cores.

## 2.5.

### Alkenone analysis and $U_{37}^{K'}$ index

The alkenone analyses were performed in an Agilent model 7890A GC-FID system, equipped with a Agilent J&W DB-5ms column (60 m x 0.25 mm x 0.25 µm), using the following instrumental conditions: (i) He as carrier gas at a flow rate of 2.0 mL min<sup>-1</sup>; (ii) initial oven temperature at 60 °C and hold of 1 min; temperature ramp of 20 °C min<sup>-1</sup> up to 150 °C and then of 6 °C min<sup>-1</sup> up to 320 °C, with a final hold of 35 min at this temperature. The di- and tri-unsaturated C<sub>37</sub> alkenones (C<sub>37:2</sub> and C<sub>37:3</sub>) were identified based on the retention times of a reference standard and quantified by peak integration relative to the internal standard C<sub>19</sub>-ketone, which was also used to evaluate the recovery of the method.

The  $U_{37}^{K'}$  was calculated using the equation described by Prahl and Wakeham (1987, Equation 1-2) and SST values were estimated using the global core top calibration of Müller et al. (1998, Equation 1-4) for the tropical to subpolar eastern South Atlantic.

## 2.6. GDGT analysis, $\text{TEX}_{86}^{\text{H}}$ , MBT', CBT and BIT indices

GDGTs were analyzed on an Agilent 1200 series HPLC system coupled via APCI to a single quadrupole mass spectrometer (Agilent 6120 MSD), using a method slightly modified from Hopmans et al. (2000). Separation occurred in a Prevail Cyano column (Grace, 3  $\mu\text{m}$ , 150 mm x 2.1 mm) at a temperature of 30 °C. After injection of the sample (20  $\mu\text{L}$ ) on the column and a 5 min isocratic elution with mobile phase A (hexane:2-propanol:chloroform; 98:1:1) at a flow rate of 0.2 mL  $\text{min}^{-1}$ , the proportion of mobile phase B (hexane:2-propanol:chloroform; 89:10:1) was increased in a linear gradient to 10% within 20 min, and thereafter to 100% within 10 min. After each analysis, the column was cleaned by back flushing for 5 min at a flow of 0.6 mL  $\text{min}^{-1}$  and re-equilibrated with solvent A (10 min, flow 0.2 mL  $\text{min}^{-1}$ ).

The GDGTs were identified using single ion monitoring (SIM) as described by Schouten et al. (2007). The ions ( $m/z$ ) monitored were 1302, 1300, 1298, 1296, 1292 for isoGDGTs, 1050, 1048, 1046, 1036, 1034, 1032, 1022, 1020, 1018 for brGDGTs (Figure 1.3) and 744 for the  $\text{C}_{46}$ -GDGT standard. Concentrations were calculated relative to the peak area of the internal standard ( $\text{C}_{46}$ -GDGT). The lack of appropriate standards hampered the evaluation of individual response factors of the different  $\text{C}_{86}$  GDGTs relative to the  $\text{C}_{46}$  standard, therefore reported concentrations should be considered semi-quantitative.

$\text{TEX}_{86}$  proxy was calculated according to Schouten et al. (2002, Equation 1-6) converted to  $\text{TEX}_{86}^{\text{H}}$  (Equation 1-12) and to SST estimates (Equation 1-13) using the calibration proposed by Kim et al. (2010) for high temperatures (from 15 to 30 °C). The CBT and the simplified MBT' indices were calculated according to Weijers et al. (2007) and Peterse et al. (2012), respectively, using the Equations 1-14 and 1-18. The calculation of pH and MAAT were performed based on the global soil calibrations proposed by Peterse et al. (2012), using Equations 1-19 and 1-20. The BIT index was calculated according to Hopmans et al. (2004), using the Equation 1-21.

To determine the analytical reproducibility of the HPLC-APCI-MS analyses, 2 of the surface sediment samples and 9 of the sediment core samples were randomly selected to be injected in triplicate. The average reproducibility of the temp- $\text{TEX}_{86}^{\text{H}}$  estimates was 0.43 °C for the surface sediment samples and 0.20 °C for the sediment cores.

## 2.7. Long chain diol analysis and LDI index

The long-chain diols were identified in a GC-TOF-MS system consisting of a Leco Pegasus III (Leco Corp., St. Joseph, MI) interfaced to an Agilent model 6890 GC, equipped with a Restek Rtx-1MS column (10 m x 0.25 mm x 0.14  $\mu\text{m}$ ) with a 5m integrated precolumn, using the conditions described by Hefter (2008), as follows: (i) He as carrier gas at a flow rate of 0.8 mL min<sup>-1</sup>; (ii) GC oven initially held at 60 °C for 1 min, and then heated at a temperature ramp of 50 °C min<sup>-1</sup> up to 250 °C and then of 30 °C min<sup>-1</sup> up to 310 °C, with a final hold of 2 min at this temperature, resulting in an analysis time of 8.8 min. The electron impact ion source is operated at a temperature of 220 °C and is connected to the GC by a heated transfer line set to 280 °C. The pressure in the flight tube of the TOF-MS was  $2 \times 10^{-7}$  Torr. The compounds were identified using characteristic fragment ions (Versteegh et al., 1997): *m/z* 299 (C<sub>28:0</sub> 1,14-diol), *m/z* 313 (C<sub>28:0</sub> 1,13- and C<sub>30:0</sub> 1,15-diols), *m/z* 327 (C<sub>28:0</sub> 1,12-, C<sub>30:1</sub> and C<sub>30:0</sub> 1,14-diols) and *m/z* 341 (C<sub>30:0</sub> 1,13-diol). The relative abundance among the diols was determined by integration of the chromatographic peaks. Since no specific internal standard was added, the long chain diol results will be only expressed in terms of temperature reconstruction.

The LDI index was calculated (Equation 1-22) and converted to SST (Equation 1-23) using the calibration described by Rampen et al. (2012).

## 2.8. Instrumental data

To verify the applicability of the U<sub>37</sub><sup>K'</sup> and TEX<sub>86</sub><sup>H</sup> proxies in the Campos Basin region, the calculated SST based on the surface sediment samples was compared with instrumental observations taken from the World Ocean Atlas 2013 (WOA13, Locarnini et al., 2013). Each result was compared with the annual and seasonal observed mean (from 1955 to 2012) corresponding to the nearest interpolated 0.25° gridbox. For the MBT'/CBT proxies, the calculated MAAT and soil pH were compared with the data taken from the WorldClim 2 (Fick and Hijmans, 2017) and the Harmonized World Soil Database (FAO/IIASA/ISRIC/ISS-CAS/JRC, 2012), respectively.

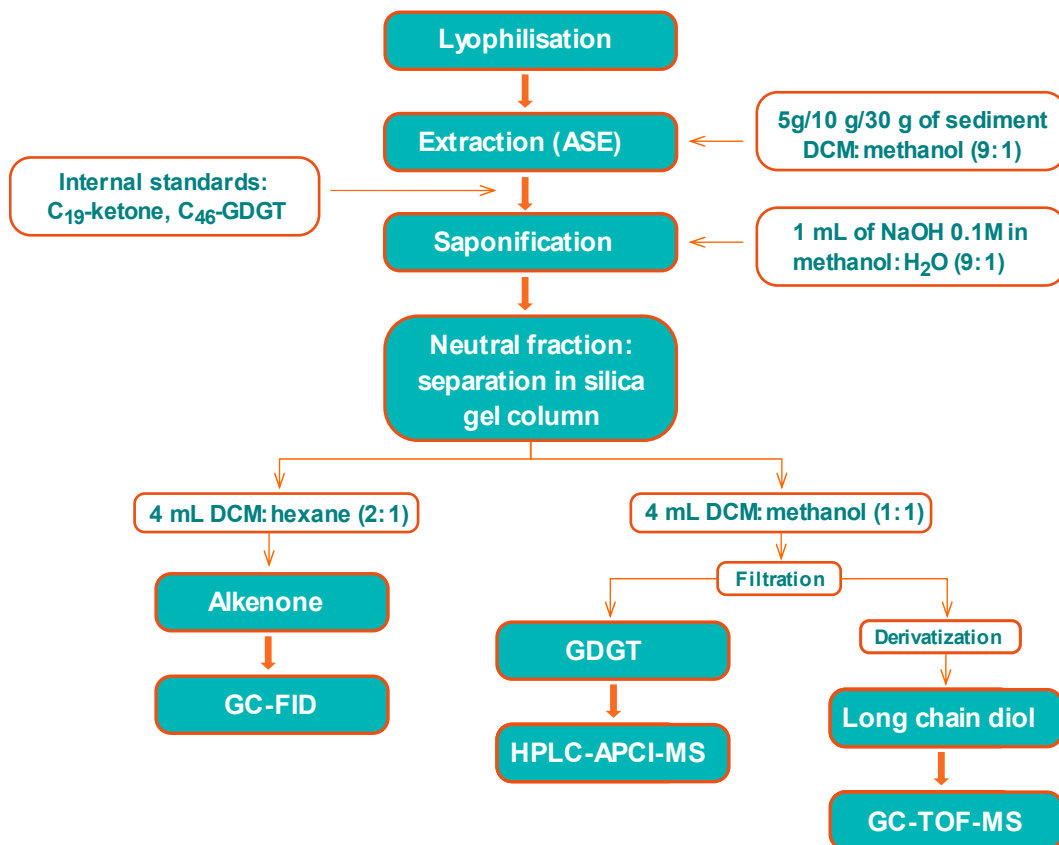


Figure 2.2: Flow chart of the laboratory procedures.

## Chapter 3

# On the application of alkenone- and GDGT-based temperature proxies in the south-eastern Brazilian continental margin

Milena Ceccopieri, Renato S. Carreira, Angela L. R. Wagener, Jens Hefter, Gesine Mollenhauer

*Published in Organic Geochemistry*

### Abstract

The applicability of two organic geochemical proxies ( $U_{37}^{K'}$  based on alkenones and  $TEX_{86}^H$  based on glycerol dialkyl glycerol tetraethers) for ocean temperatures was investigated on a regional scale in the SE Brazilian continental margin (Campos Basin) using 53 core-top sediments. In 71% of the samples for  $U_{37}^{K'}$  and 85% for  $TEX_{86}^H$  the estimated annual mean sea surface temperature (SST) is comparable to the climatological annual mean data, with deviations within the calibration error. The surface  $TEX_{86}^H$  estimates reflects the surface mixed layer, while the depth-integrated (0-200 m)  $TEX_{86}^H$  estimates showed better agreement with temperatures at 100–200 m depth. In addition, the SST- $U_{37}^{K'}$  results were more consistent (73% of the samples) using a winter rather than annual mean calibration. This seasonal effect might be ascribed to an increase in the abundance of Haptophytes in the region under winter conditions. Exceptions for these general trends were observed for both proxies as a strong cold bias in reconstructed temperature in few samples in the southern portion of the studied region, which may be related to (i) a predominant subsurface habitat of Thaumarchaeota combined with enhanced primary production and flux of particles during upwelling and (ii) alkenones being laterally transported from adjacent colder waters. Effects of river input of terrestrially sourced GDGTs on  $TEX_{86}^H$  are not evident. Overall, our findings show that  $U_{37}^{K'}$  and  $TEX_{86}^H$  are suitable temperature proxies for paleoclimate studies in regional scale in the SE Brazilian continental margin, but on a local scale the effects of upwelling must be taken in consideration.

### 3.1. Introduction

The most common organic-geochemical proxy currently in use to infer past sea surface temperatures is the  $U_{37}^{K'}$  (Brassell et al., 1986; Prahl and Wakeham, 1987) based on the relative abundance of di- and tri-unsaturated alkenones ( $C_{37:2}$  and  $C_{37:3}$ ), which are mainly produced by haptophyte algae and are particularly abundant in the *coccolithophore* *Emiliana huxleyi* (Volkman et al., 1980; Brassell et al., 1986; Prahl and Wakeham, 1987). More recently, the  $TEX_{86}$  index was developed based on the relative distribution of isoprenoidal glycerol dialkyl glycerol tetraethers (isoGDGTs) with 86 carbon atoms (Schouten et al., 2002), a group of compounds found abundantly in marine Thaumarchaeota (Sinninghe Damsté et al., 2000).

The major challenge in the proxy-approach is the capacity of making accurate assignments between the value of a particular proxy obtained from the sedimentary record and the environmental variable intended to be reconstructed. The lipid-based proxy-SST relationship can be obtained by comparison of instrumental SST and proxy data from modern marine sediments distributed globally (Sikes et al., 1991, 1997; Müller et al., 1998; Schouten et al., 2002; Conte et al., 2006; Kim et al., 2008, 2010; Liu et al., 2009) and/or mesocosm experiments (Prahl and Wakeham, 1987; Prahl et al., 1988; Volkman et al., 1995). In the past two decades, several calibration studies using core-top sediments proposed models to improve SST calculation from  $U_{37}^{K'}$  (Müller et al., 1998; Conte et al., 2006; Tierney and Tingley, 2018) and  $TEX_{86}$  values (Kim et al., 2008, 2010; Liu et al., 2009; Tierney and Tingley, 2014). Kim et al. (2010), for example, proposed two different logarithmic calibrations –  $TEX_{86}^L$  and  $TEX_{86}^H$  – to be used for water temperatures below and above 15 °C, respectively.

Nonetheless, several studies still report biases between the SST estimates and instrumental temperatures for both proxies. The parameters other than growth temperature of the source organisms that may impair proxy performance include: (i) seasonal production and preferential depth habitats of the source organisms (Prahl et al., 2001; Herfort et al., 2006a; Huguet et al., 2007a; Lee et al., 2008; Leider et al., 2010); (ii) lateral transport of sediments (Benthien and Müller, 2000; Mollenhauer et al., 2007; Kim et al., 2009); (iii) differential resistance to bacterial degradation of a particular molecule (Conte et al., 1992; Gong and Hollander, 1999); and (iv) influence of nutrients and light (Epstein et al., 1998; Versteegh et al., 2001; Hurley et al., 2016). In addition, as isoGDGTs are produced by a large

group of archaea, different archaeal communities may influence the  $\text{TEX}_{86}$  parameter dependent on environmental conditions (e.g., Schouten et al., 2012; Basse et al., 2014; Elling et al., 2015). One example is the anaerobic oxidation of methane by mesophilic Euryarchaeota, characterized by a large production of GDGTs with 1–3 cyclopentane rings (Pancost et al., 2001; Blumenberg et al., 2004), whose presence and potential to interfere with  $\text{TEX}_{86}$  can be investigated by the Methane Index (MI, Zhang et al., 2011). Methanogenic archaea can also affect the  $\text{TEX}_{86}$  proxy by their exclusive production of GDGTs with no cyclopentane rings, which can be potentially identified by a higher input of GDGT-0 relative to crenarchaeol (Koga et al., 1993a; Blaga et al., 2009). Moreover, the input of terrigenous organic material containing isoGDGTs may bias the  $\text{TEX}_{86}$  signal on continental shelves under the influence of river discharge (Weijers et al., 2006b). The Branched and Isoprenoid Tetraether (BIT) index, proposed by Hopmans et al. (2004) to determine the relative contributions of terrigenous organic matter (OM) in aquatic environments, is commonly applied to evaluate potential  $\text{TEX}_{86}$  biases caused by allochthonous isoGDGT contributions. Considering that branched GDGTs (brGDGTs) are generally attributed to soil bacteria, while crenarchaeol would be the dominant GDGT in the marine environment, the BIT index can be near to 0 in sediments from the open ocean and around 1 in inner continental systems (Hopmans et al., 2004). However, even though the brGDGTs sources are predominantly terrestrial, it has been shown that they can also be derived from *in situ* production in the marine environment (Peterse et al., 2009; Zhu et al., 2011; Hu et al., 2012; Zell et al., 2014b, 2014a), which can complicate the BIT index. An alternative tool to evaluate the effect of parameters other than temperature on  $\text{TEX}_{86}$  estimates is the weighted number of cyclopentane rings proposed by Zhang et al. (2015) as the Ring Index (RI). According to the authors, deviations from the global RI- $\text{TEX}_{86}$  relationship may indicate that the GDGT distributions are influenced by non-thermal factors.

Considering the factors described above, regional oceanographic influences on both  $U_{37}^{K'}$  and  $\text{TEX}_{86}$  proxies can lead to a proxy-temperature relationship different from the globally averaged values. In some specific regions, Thaumarchaeota may present different responses to temperature when subjected to particular or extreme conditions (Kim et al., 2010). In the Red Sea, for example,  $\text{TEX}_{86}$  data behave differently when compared to the open ocean (Trommer et al., 2009; Kim et al., 2010). This may be related to the presence of a singular Crenarchaeotal population, adapted to the extreme local salinity conditions, that responds differently to sea water temperature variations (Qian et al., 2010).

Limitations in the  $\text{TEX}_{86}$  applicability were also found in polar regions, related to a lower proxy sensitivity to the variation of temperature below 5 °C (Kim et al., 2008, 2010). Calibrations that have been developed until now for both alkenones and GDGTs (Müller et al., 1998; Schouten et al., 2002; Conte et al., 2006; Kim et al., 2008, 2010; Tierney and Tingley, 2014, 2018) include relatively few data from sites in the south-western Atlantic. Moreover, while downcore variation in alkenones have been used for paleotemperature reconstructions in subtropical south-western Atlantic (Mahiques et al., 2005; Rühlemann and Butzin, 2006; Magalhães, 2010; Cordeiro et al., 2014), GDGT-based temperature reconstructions in this region have not been published yet.

The Campos Basin is characterized by the presence of a western boundary upwelling system, a relatively low river input and a complex pattern of OM deposition. As the Southwest Atlantic in general and the Brazilian margin in particular are interesting target sites for paleoclimate studies reconstructing past ocean temperatures, the applicability of the organic geochemical proxies  $U_{37}^{K'}$  and  $\text{TEX}_{86}^H$  on a regional scale needs to be investigated in further detail. In this study we analyzed alkenones and GDGTs in core top sediments collected along cross-margin transects (25 m to 3000 m water depths) in the Campos Basin and compared the reconstructed water temperatures based on the  $U_{37}^{K'}$  and  $\text{TEX}_{86}^H$  proxies to the objectively analyzed mean temperatures as provided by the World Ocean Atlas 2013 (WOA13, Locarnini et al., 2013).

### **3.2. Study area and regional setting**

The Campos Basin (Figure 3.1) is located between 20.5°S (Vitoria High) and 24°S (Cabo Frio High), with an area of more than 100,000 km<sup>2</sup>. The average width of the continental shelf is 100 km, whereas the water depth at the shelf-break varies from 80 m to 130 m going from north to the south. The slope has an average gradient and width of 2.5° and 40 km, respectively (Viana et al., 1998). The circulation on the south-eastern Brazilian Shelf is mainly controlled by the Brazil Current (BC), which flows southward along the most external part of the continental shelf (Peterson and Stramma, 1991). The Intermediate Western Boundary Current (IWBC) flows in the opposite direction underlying the BC along the continental slope (500-1,200 m depth). Below the IWBC, the slower Deep Western Boundary Current (DWBC) flows towards the pole (Reid, 1989; Boebel et al., 1999; Stramma and England, 1999; Schmid et al., 2000).

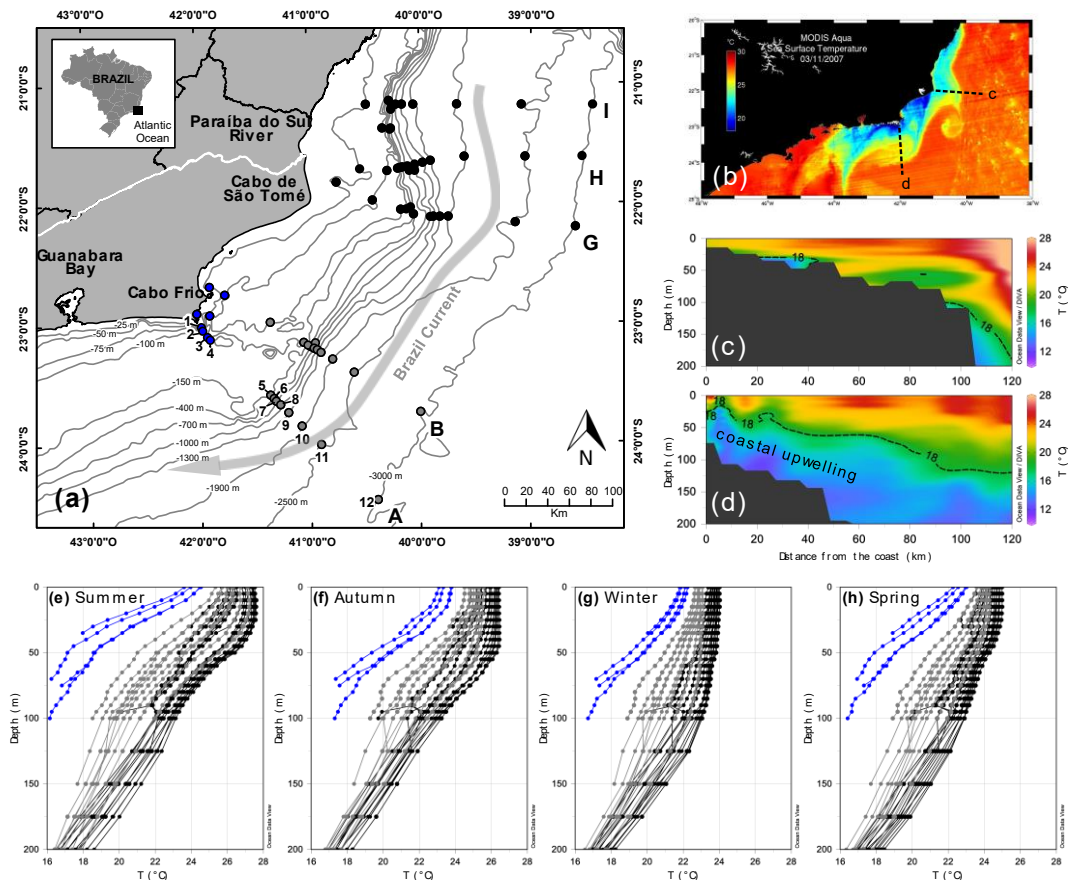


Figure 3.1: Location of the core top (0-2 cm) sediment sampling stations from the Habitats Project (a). Each transect (A, B, G, H and I) is divided by isobaths as follows: 1, 25 m; 2, 50 m; 3, 75 m; 4, 100 m; 5, 150 m; 6, 400 m; 7, 700 m; 8, 1000 m; 9, 1300 m; 10, 1900 m; 11, 1900 m and 12, 3000 m. Color map (b) shows the peak upwelling conditions and the meandering of the Brazil Current with SST taken from the Modis Aqua satellite, and the location of the two sections (c) and (d). The sections illustrate the intrusion of the South Atlantic Central Water under non-upwelling and coastal upwelling conditions, respectively, with water temperatures taken from the World Ocean Database (Boyer et al., 2013). Seasonal depth profiles of water temperature (e-h) taken from the World Ocean Atlas 2013 (Locarnini et al., 2013). Each profile corresponds to the nearest interpolated gridboxes of the stations according to the symbol colors of the stations: blue (around Cabo Frio), gray (transects A and B) and black (transects G, H, and I), as marked on the study area map (a).

The BC transports the oligotrophic warm Tropical Water (TW,  $T > 20\text{ }^{\circ}\text{C}$ ) in its upper levels and the nutrient-rich and cold South Atlantic Central Water (SACW,  $T < 20\text{ }^{\circ}\text{C}$ ) between 200 and 700 m. The coastal region is occupied by the Coastal Water (CW), which has a temperature range similar to the TW, but lower salinity due to the fluvial input (Campos et al., 2000; Silveira et al., 2000; Castro Filho et al., 2017). The changes in the coastline orientation affect the BC flow, resulting in the formation of meandering and strong cyclonic and anticyclonic frontal eddies,

which induces the mid-shelf and shelf-break upwelling of SAWC into the euphotic zone (Campos et al., 2000; Silveira et al., 2000). Those meanders can be clearly observed by satellite SST image (MODIS sensor, Aqua satellite, Figure 3.1b) near Cabo de São Tomé and Cabo Frio.

In the Cabo Frio coast, the coastal morphology associated with prevailing NE winds is responsible for the offshore Ekman transport of surface waters (CW and TW) that result in an intermittent coastal upwelling of SACW (Rodrigues and Lorenzetti, 2001; Castela and Barth, 2006). Even though occurring all year round, the coastal upwelling is seasonally variable. During austral summer and spring, when NE winds are usually more intense, the SACW advances towards the coast (Figure 3.1e,h). This process can be traced by the 18 °C isotherm position at 15–25 m depth off Cabo Frio (Figure 3.1d). By contrast, during the austral autumn and winter, the NE winds are weaker and the frequency of cold front SW winds is higher. Thus, the 18 °C isotherm retreats to 45–55 m depth and the influence of warm surface waters from the BC in the region increases (Valentin et al., 1987; Franchito et al., 2008; Cerda and Castro, 2014; Figure 3.1f,g). Less intense coastal upwelling can be observed near Cabo de São Tomé, especially during summer, which may extend as an independent filament southwestward reaching the outer shelf off Cabo Frio (Rodrigues and Lorenzetti, 2001; Figure 3.1b).

The thermohaline structure in the Campos Basin shelf is defined by the degree of intrusion of the TW and the SACW towards the coast and on the extension and physical characteristics of the CW. In the southern portion (south of Cabo de São Tomé), the volume of SACW is relatively large in the bottom layers (Figure 3.1d), while in the northern portion (Figure 3.1c) the TW generally prevails (Castro Filho et al., 2017). The subsurface presence of SACW on the shelf enriches the water column with nutrients, contrasting with the overall oligotrophic conditions in adjacent continental shelf and open waters dominated by warm TW (Souza et al., 2011; Suzuki et al., 2015). This enrichment significantly affects the productivity of regional fisheries (Matsuura, 1996) and also contributes to the fertilization and the export of biomass to southwestern adjacent areas (Lorenzetti and Gaeta, 1996). The period of intermittent upwelling events also corresponds to the rainy season in SE Brazil and, consequently, to an increase of the terrigenous flux to the coastal waters (Mahiques et al., 2004).

The Paraíba do Sul River, located in the northern part of the Campos Basin (Figure 3.1a) is a medium-sized river with discharges between 110 m<sup>3</sup> year<sup>-1</sup> (winter) and 2600 m<sup>3</sup> year<sup>-1</sup> (summer) but even so it is considered the main source

of terrigenous materials to the shelf (Carvalho et al., 2002). The influence of the Paraíba do Sul plume is observed on a regional scale over the continental shelf, as demonstrated by isotopic markers (Souza et al., 2010), production and export of OM to sediments (Carreira et al., 2015), dissolved black carbon (Dittmar et al., 2012) and metals (Lacerda et al., 1993; Carvalho et al., 2002; Araujo et al., 2017), among others. Most of the river's discharged suspended sediment is transported southward by the BC (Gyllencreutz et al., 2010).

Sediment transport patterns in the southern basin near Cabo Frio on the inner shelf is controlled by wind-driven circulation (NE trade winds) and by coastal current remobilization and transport, whereas sediment dispersal on the outer shelf is dominated by the meandering of the internal front of the BC (Mahiques et al., 2002). On the mid-shelf the sediment transport is primarily controlled by cross-shelf upwelled coastal waters (Belem et al., 2013). The contribution of material to the southern part of the Campos Basin from Guanabara Bay, at a distance of more than 150 km from Cabo Frio, cannot be ruled out (Albuquerque et al., 2014).

### **3.3. Material and methods**

#### **3.3.1. Sampling**

The core-top sediments were collected as part of the Habitats Project (CENPES/PETROBRAS) in 2008 and 2009 along 5 cross-margin transects (A, B, G, H and I; Figure 3.1a, Table 3.1) across the Campos Basin. The sampling stations along each transect were distributed on twelve isobaths at depths of 25, 50, 75, 100, 150, 400, 700, 1000, 1300, 1900, 2500 and 3000 m. Undisturbed sediments were collected with an adapted Van Veen sampler at the continental shelf stations and with a box corer at the slope stations. Samples represent the top 2 cm layer of the sediment and are a composite of three deployments of the sampler.

#### **3.3.2. Lipid extraction and separation**

An aliquot of 5 g ( $\pm 0.01$  g) of freeze-dried and homogenized sediment was extracted by an accelerated solvent extraction system (ASE 200, Dionex) with a mixture of dichloromethane:methanol (9:1, v:v) at a temperature of 100 °C and a

pressure of 1000 psi. Before extraction, known amounts of C<sub>19</sub>-ketone and C<sub>46</sub>-GDGT were added as internal standards (samples from transects B and H only C<sub>46</sub>-GDGT was added). The bulk extracts were concentrated by rotary evaporation and saponified for 2h at 80 °C with 1 mL of KOH (0.1 M) in methanol:H<sub>2</sub>O (9:1; v:v). Neutral lipids were recovered in *n*-hexane and further fractionated using silica gel column chromatography as follows: *n*-alkane fraction using *n*-hexane; alkenone fraction using dichloromethane:*n*-hexane, 2:1 (v:v); and GDGT fraction using dichloromethane:methanol, 1:1 (v:v). The fractions were dried under a stream of nitrogen at 40 °C. The alkenone fraction was re-dissolved in *n*-hexane and analyzed by gas chromatography with a flame ionization detector (GC-FID). The GDGT fraction was filtered using a 0.45 µm PTFE filter, weighed, and re-dissolved in *n*-hexane:isopropanol 99:1 (v:v) to a final concentration of 2 mg/mL (Schouten et al., 2009) for further analysis by high performance liquid chromatography-atmospheric pressure chemical ionization-mass spectrometry (HPLC-APCI-MS). The lipids extraction, separation and instrumental analysis were performed at the University of Bremen.

### 3.3.3.

#### Alkenone analysis and U<sub>37</sub><sup>K'</sup> index

The alkenone analyses were performed on an Agilent model 6870 GC-FID system, equipped with a Agilent J&W DB-5ms column (60m x 0.25mm x 0.25µm), using the following conditions: (i) He as carrier gas at a flow rate of 2.0 mL min<sup>-1</sup>; (ii) initial oven temperature at 60 °C and hold of 1 min; temperature ramp of 20 °C min<sup>-1</sup> up to 150 °C and then of 6 °C min<sup>-1</sup> up to 320 °C, with a final hold of 35 min at this temperature. The di- and tri-unsaturated C<sub>37</sub> alkenones (C<sub>37:2</sub> and C<sub>37:3</sub>) were identified based on the retention times of a reference standard and quantified by peak integration relative to the internal standard C<sub>19</sub>-ketone, which was also used to evaluate the recovery of the method.

The U<sub>37</sub><sup>K'</sup> was calculated using the equation described by Prahl and Wakeham (1987, Equation 3-1) and SST values were estimated using the annual mean core top calibration of Müller et al. (1998, Equation 3-2) for tropical to subpolar eastern South Atlantic. This calibration is suitable for temperatures between 0 and 27 °C, with a standard error of ±1.0 °C.

$$U_{37}^{K'} = \frac{(C_{37:2})}{(C_{37:2})+(C_{37:3})} \quad (3-1)$$

$$\text{SST} = \frac{U_{37}^{K'} - 0.069}{0.033} \quad (3-2)$$

SST- $U_{37}^{K'}$  values were also estimated using the seasonal (austral) calibration curves from Müller et al. (1998, Equation 3-6). Summer, winter and spring calibrations have a standard error of  $\pm 1.1$  °C. The autumn calibration has a standard error of  $\pm 1.0$  °C.

$$\text{Summer SST} = \frac{U_{37}^{K'} - 0.056}{0.031} \quad (3-3)$$

$$\text{Autumn SST} = \frac{U_{37}^{K'} - 0.080}{0.031} \quad (3-4)$$

$$\text{Winter SST} = \frac{U_{37}^{K'} - 0.129}{0.034} \quad (3-5)$$

$$\text{Spring SST} = \frac{U_{37}^{K'} - 0.099}{0.033} \quad (3-6)$$

### 3.3.4.

#### GDGT analysis and related indexes ( $\text{TEX}_{86}^H$ , BIT, MI and RI)

GDGTs were analyzed on an Agilent 1200 series HPLC system coupled via APCI to a single quadrupole mass spectrometer (Agilent 6120 MSD), using a method slightly modified from Hopmans et al. (2000). Separation was achieved on a Prevail Cyano column (Grace, 3 $\mu$ m, 150mm x 2.1mm) at a temperature of 30 °C. After injection of the sample (20  $\mu$ L) on the column and a 5 min isocratic elution with mobile phase A (*n*-hexane:2-propanol:chloroform; 98:1:1) at a flow rate of 0.2 mL/min, the proportion of mobile phase B (*n*-hexane:2-propanol:chloroform; 89:10:1) was increased in a linear gradient to 10% within 20 min, and thereafter to 100% within 10 min. After each analysis, the column was cleaned by back flushing for 5 min at a flow of 0.6 mL/min and re-equilibrated with solvent A (10 min, flow 0.2 mL/min).

The identification of GDGTs was performed using single ion monitoring (SIM) as described by Schouten et al. (2007). The ions (*m/z*) monitored were 1302, 1300, 1298, 1296, 1292 for isoGDGTs, 1050, 1048, 1046, 1036, 1034, 1032, 1022, 1020, 1018 for brGDGTs and 744 for the  $\text{C}_{46}$ -GDGT standard. Contents were calculated relative to the peak area of the internal standard ( $\text{C}_{46}$ -GDGT). The lack of appropriate standards hampered the evaluation of individual response factors of the different  $\text{C}_{86}$  GDGTs relative to the  $\text{C}_{46}$  standard, therefore reported contents should be considered semi-quantitative.

TEX<sub>86</sub> proxy was calculated according to Schouten et al. (2002, Equation 3-7) and converted to SST estimates using the calibrations (Equation 3-8,9) proposed by Kim et al. (2010) for high temperatures from 15 to 30 °C, with a standard error of ±2.5 °C.

$$\text{TEX}_{86} = \frac{\text{iGDGT-2} + \text{iGDGT-3} + \text{cren}'}{\text{iGDGT-1} + \text{iGDGT-2} + \text{iGDGT-3} + \text{cren}'} \quad (3-7)$$

$$\text{TEX}_{86}^{\text{H}} = \log(\text{TEX}_{86}) \quad (3-8)$$

$$T \text{ (}^\circ\text{C)} = 38.6 + 68.4 (\text{TEX}_{86}^{\text{H}}) \quad (3-9)$$

Temp-TEX<sub>86</sub><sup>H</sup> values were also calculated using the subsurface calibration from Kim et al. (2012, Equation 3-10). The calibration has a standard error of ±1.1 °C.

$$T \text{ (}^\circ\text{C)} = 30.7 + 54.7 (\text{TEX}_{86}^{\text{H}}) \quad (3-10)$$

BIT index was calculated according to Hopmans et al. (2004, Equation 3-11), MI was calculated after Zhang et al. (2011, Equation 3-12) and RI was calculated using the equation proposed by Zhang et al. (2015, Equation 3-13).

$$\text{BIT} = \frac{\text{bGDGT-I} + \text{bGDGT-II} + \text{bGDGT-III}}{\text{bGDGT-I} + \text{bGDGT-II} + \text{bGDGT-III} + \text{cren}} \quad (3-11)$$

$$\text{MI} = \frac{\text{iGDGT-1} + \text{iGDGT-2} + \text{iGDGT-3}}{\text{iGDGT-1} + \text{iGDGT-2} + \text{iGDGT-3} + \text{cren} + \text{cren}'} \quad (3-12)$$

$$\text{RI} = 0 \times (\text{iGDGT-0}) + 1 \times (\text{iGDGT-1}) + 2 \times (\text{iGDGT-2}) + 3 \times (\text{iGDGT-3}) + 4 \times (\text{cren}) + 4 \times (\text{cren}') \quad (3-13)$$

### 3.3.5. Climatological mean temperature data

To verify the applicability of each paleotemperature proxy applied in this study, the calculated temperatures based on surface sediment data were compared with the objectively interpolated mean temperature taken from the WOA13. The proxy-estimated temperatures were compared with the annual mean and seasonal temperatures (from 1955 to 2012) corresponding to the nearest interpolated 0.25° gridbox (Supplementary Table S3.2).

### 3.4. Results

#### 3.4.1. Alkenone and GDGT distributions

The distribution of both alkenones and GDGTs in the sediments are quite similar to other lipids analyzed in the Campos Basin (Oliveira et al., 2013; Cordeiro et al., 2018), with higher contents on the slope for all transects and in the middle of the shelf in the Cabo Frio upwelling system (CFUS) region, where accumulation of OM is observed. To compensate for the effect of the local circulation and sedimentation patterns on the distribution of these compounds, the contents were normalized to the total organic carbon (TOC) content reported by Cordeiro et al. (2018, Table 3.1).

The alkenones were quantified in the samples from transects A, G and I. The total content of the di- and tri-unsaturated  $C_{37}$  alkenones varied between 15 and 320  $\mu\text{g gTOC}^{-1}$  (Figure 3.2a). The GDGTs were determined in all samples (transects A, B, G, H and I). The total content of isoGDGTs varied between 7 and 319  $\mu\text{g gTOC}^{-1}$  (Figure 3.2b). A typical marine profile of the isoGDGTs distribution (Schouten et al., 2002) was observed in all samples with predominance of crenarchaeol (40-60% of total isoGDGT), followed by GDGT-0 (21-40% of total isoGDGT) and lower amounts of GDGT-1, GDGT-2, GDGT-3, and the crenarchaeol regio-isomer. The total brGDGTs contents varied from 5 to 30  $\mu\text{g gTOC}^{-1}$  with a rapid decrease from the coastal to the deeper waters (Figure 3.2c).

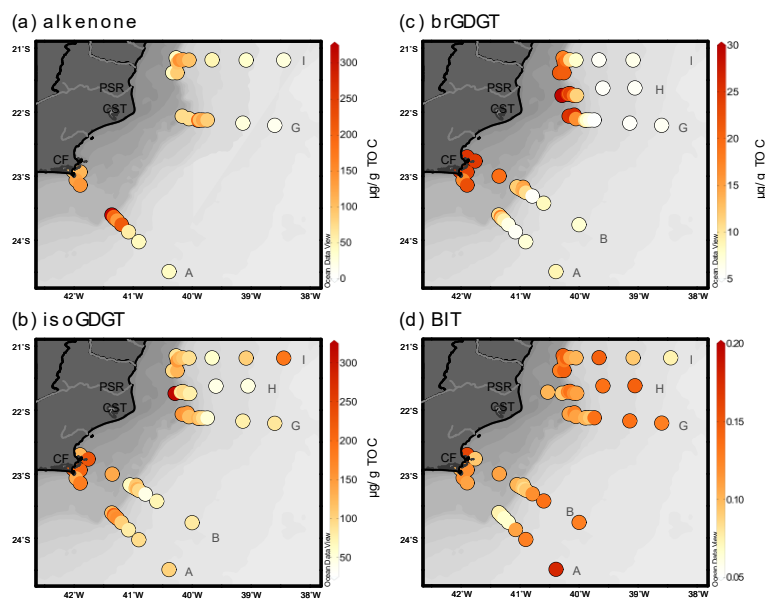


Figure 3.2: Contents of (a) total alkenones per gram TOC ( $\mu\text{g gTOC}^{-1}$ ), (b) total isoGDGTs per gram TOC ( $\mu\text{g gTOC}^{-1}$ ), (c) total brGDGTs per gram TOC ( $\mu\text{g gTOC}^{-1}$ ), and (d) BIT index. PSR = Paraíba do Sul River; CST = Cabo de São Tomé; CF = Cabo Frio. The letters A-I represent the transects.

### 3.4.2.

#### $U_{37}^{K'}$ and alkenone-based temperatures

The  $U_{37}^{K'}$  index varied between 0.70 and 0.95, resulting in a calculated SST using the annual mean Müller et al. (1998) calibration for South Atlantic (SST- $U_{37}^{K'}$  hereafter) ranging from 19.2 °C to 26.6 °C (Figure 3.3a, Table 3.1). SST- $U_{37}^{K'}$  ranges from 20.9-23.9°C at the shelf sites (A1-A4, B1-B4) located in the CFUS, which agree to previously reported data for the same region (Cordeiro et al., 2014). The lowest values are observed on transect B, with SST- $U_{37}^{K'}$  up to 5.3 °C lower compared to observed annual mean SST (Figure 3.3f).

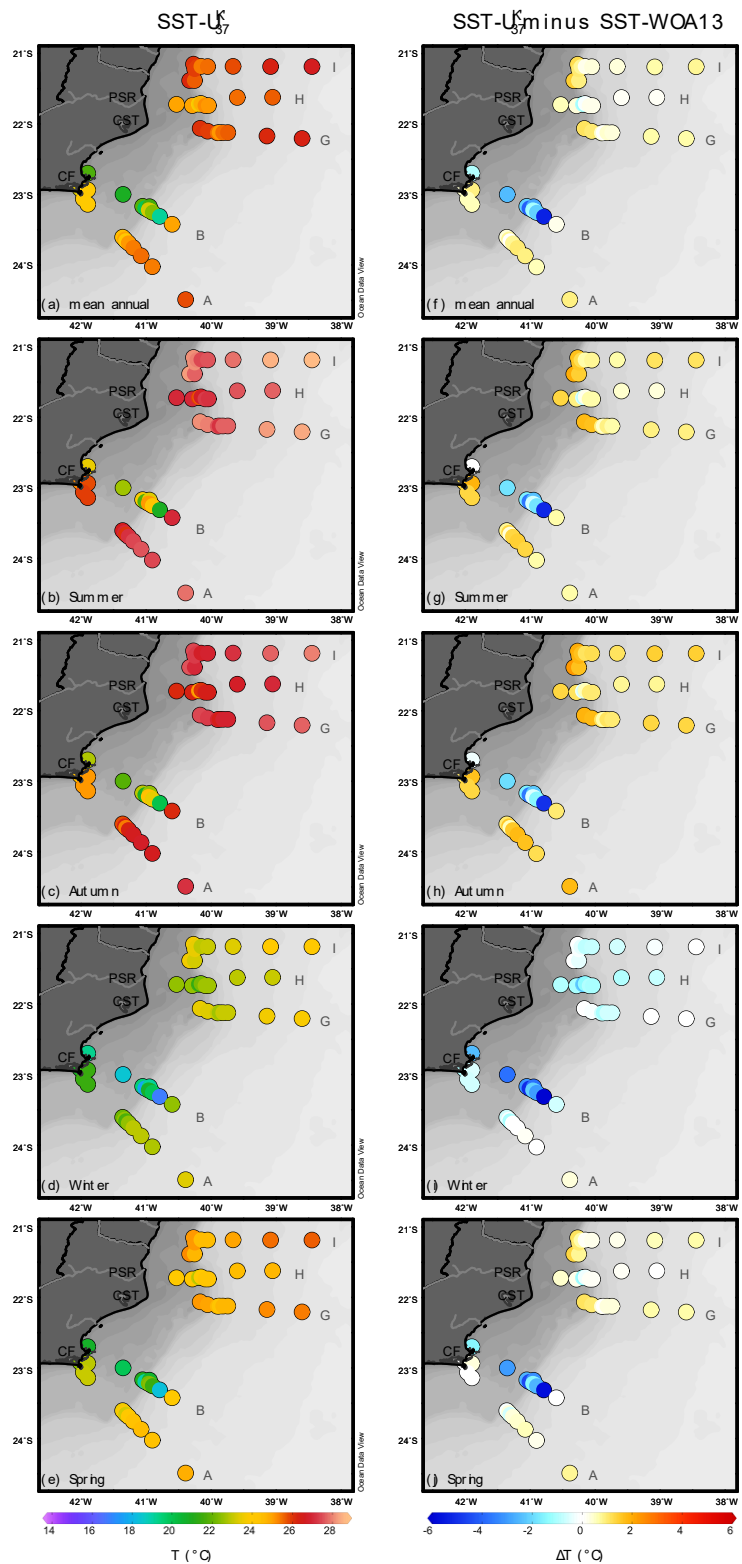


Figure 3.3: SST estimates based on  $U_{37}^{K'}$  proxy using South Atlantic core-top calibrations (Müller et al., 1998) for (a) annual mean; (b) austral summer (Jan-Mar), (c) austral autumn (Apr-Jun), (d) austral winter (Jul-Sep) and (e) austral spring (Oct-Dec). Differences between SST- $U_{37}^{K'}$  estimates and SST (WOA13) for (f) annual mean; (g) austral summer (Jan-Mar), (h) austral autumn (Apr-Jun), (i) austral winter (Jul-Sep) and (j) austral spring (Oct-Dec).

### 3.4.3. $\text{TEX}_{86}^{\text{H}}$ and GDGT-based temperatures

$\text{TEX}_{86}$  values varied between 0.49 and 0.68. A comparison of our  $\text{TEX}_{86}$  values and data used by Kim et al. (2010) as a function of the climatological annual mean SST highlights that the results of the present study fit within the global calibration curve (Figure 3.4a).

$\text{TEX}_{86}^{\text{H}}$ -based temperatures (temp- $\text{TEX}_{86}^{\text{H}}$ ) range from 17.4 °C to 27.3 °C (Figure 3.5a, Table 3.1) when the annual mean SST calibration is used (Kim et al., 2010). Lowest temp- $\text{TEX}_{86}^{\text{H}}$  are observed in near-coastal upwelling sites (transects A and B), with temperature estimates up to 5.3 °C lower compared to annual mean SST (Figure 3.5c) and 5.9 °C lower compared to SST- $U_{37}^{\text{K}'}$ .  $\text{TEX}_{86}^{\text{H}}$  estimations based on annual mean depth-integrated (0-200 m) calibration (Kim et al., 2012) present colder values between 13.8 °C and 21.7 °C (Figure 3.5b).

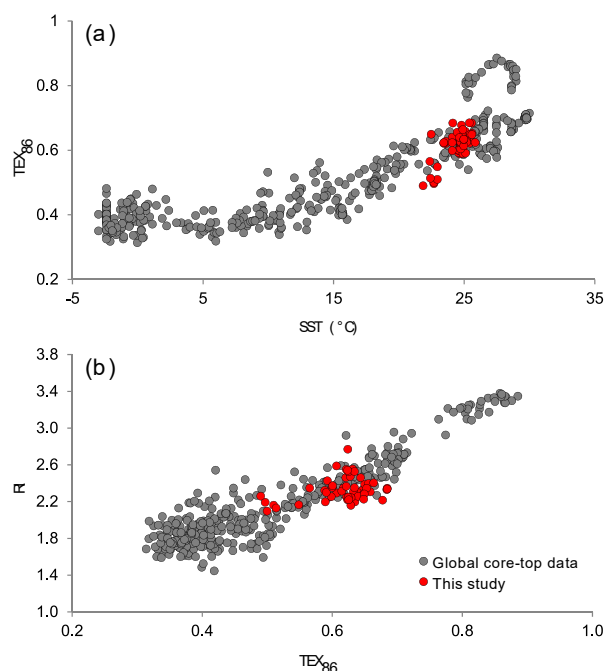


Figure 3.4: (a) SST- $\text{TEX}_{86}$  relationship and (b) RI- $\text{TEX}_{86}$  relationship in the global core-top sediments presented in Kim et al. (2010) (grey dots) and in the core-top sediments from the present study (red dots).

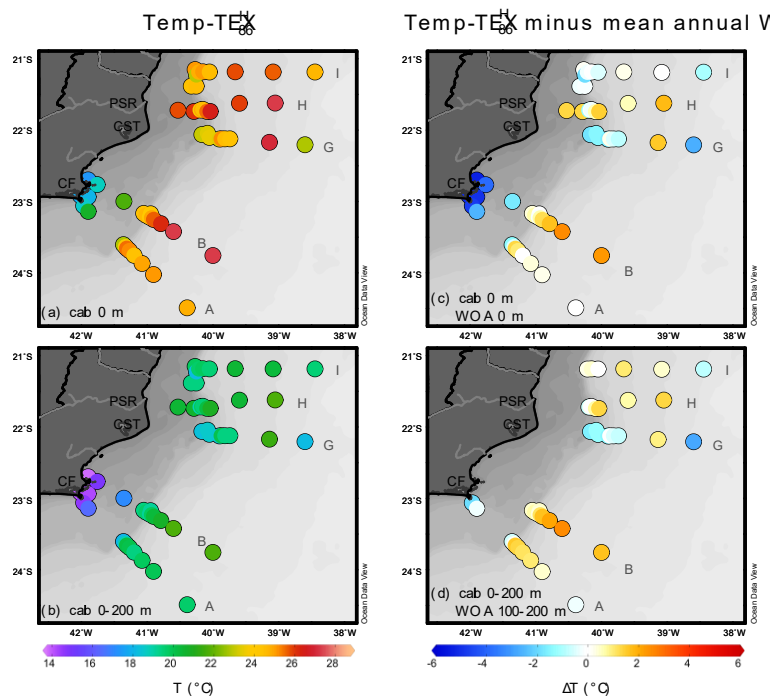


Figure 3.5: Temperature estimates based on  $\text{TEX}_{86}^H$  using (a) SST calibration (Kim et al., 2010) and (b) subsurface calibration for 0-200 m (Kim et al., 2012). Differences between reconstructed and climatological mean (WOA13) temperatures for (c)  $\text{TEX}_{86}^H$  surface temperature estimates minus annual mean SST and (d)  $\text{TEX}_{86}^H$  subsurface temperature estimates minus annual mean depth-integrated (100-200 m) temperature.

#### 3.4.4. BIT, GDGT-0/cren, MI and RI

The BIT value was  $\leq 0.20$  for all samples (except for station H12, the most offshore station on transect H), with a mean value of  $0.13 \pm 0.05$  (Table 3.1). No trend in the BIT values with distance was observed (Figure 3.2d). Due to the low content of isoGDGTs and the high BIT value of 0.46, the sample H12 was considered an outlier and excluded from the temperature calibration discussion. GDGT-0/cren ratios varied from 0.35 to 0.86. The MI ranged from 0.17 to 0.33, with lowest values found in the CFUS area. The RI varied from 2.10 to 2.77 and its correlation with  $\text{TEX}_{86}$  fit within the global RI- $\text{TEX}_{86}$  relationship for all samples (Figure 3.4b).

Table 3.1: Information and results of alkenone, GDGT and bulk analyses from the surface sediment samples of the Campos Basin (n.d. = not determined).

Station (0-2 cm)	Latitude (°S)	Longitude (°W)	Water depth (m)	Location	TOC <sup>a</sup> (%)	∑alkenones (µg gTOC <sup>-1</sup> )	∑isoGDGT (µg gTOC <sup>-1</sup> )	∑brGDGT (µg gTOC <sup>-1</sup> )	U <sup>K</sup> <sub>37</sub>	SST- U <sup>K</sup> <sub>37</sub> <sup>b</sup> (°C)	TEX <sub>86</sub>	Temp- TEX <sub>86</sub> <sup>Hc</sup> (°C)	BIT index	GDGT- 0/cren	MI	RI
A01	-22.9193	-42.0141	25	shelf	0.07	91.79	212.31	25.06	0.84	23.37	0.50	17.82	0.11	0.78	0.17	2.19
A02	-22.9346	-41.8979	50	shelf	0.17	111.06	207.63	23.64	0.86	23.87	0.50	18.00	0.13	0.86	0.22	2.10
A03	-23.0603	-41.9643	75	shelf	1.31	129.43	135.06	16.89	0.86	23.98	0.51	18.58	0.13	0.80	0.23	2.16
A04	-23.1373	-41.8976	100	shelf	1.36	139.43	183.07	22.68	0.86	23.94	0.55	20.75	0.12	0.81	0.23	2.17
A05	-23.6047	-41.3587	150	shelf	0.40	319.52	125.68	11.00	0.88	24.57	0.59	22.84	0.08	0.65	0.27	2.32
A06	-23.6327	-41.3284	400	slope	0.52	193.13	215.10	17.63	0.90	25.05	0.61	23.76	0.08	0.69	0.26	2.29
A07	-23.6561	-41.3089	700	slope	1.26	202.60	156.72	11.68	0.87	24.14	0.65	25.57	0.08	0.68	0.25	2.32
A08	-23.6867	-41.2693	1000	slope	1.01	136.61	166.43	9.46	0.90	25.09	0.64	25.29	0.07	0.70	0.26	2.30
A09	-23.7527	-41.1972	1300	slope	0.64	213.60	105.87	6.69	0.91	25.41	0.62	24.49	0.07	0.73	0.28	2.25
A10	-23.8675	-41.0784	1900	slope	0.68	59.72	81.30	5.79	0.91	25.53	0.63	24.96	0.12	0.76	0.29	2.22
A11	-24.0241	-40.9037	2500	slope	0.45	46.84	94.82	7.45	0.91	25.35	0.63	25.10	0.14	0.78	0.30	2.20
A12	-24.4893	-40.3912	3000	slope	0.29	43.96	102.78	8.88	0.92	25.81	0.63	24.81	0.20	0.81	0.33	2.16
B1	-22.6968	-41.8966	25	shelf	1.26	n.d.	126.13	25.04	0.79	21.74	0.49	17.41	0.18	0.71	0.19	2.26
B2	-22.7643	-41.7598	50	shelf	0.22	n.d.	228.97	24.55	n.d.	n.d.	0.51	18.80	0.10	0.83	0.22	2.13
B3	-22.9970	-41.3526	75	shelf	0.18	n.d.	139.24	19.41	0.76	20.90	0.57	21.66	0.12	0.64	0.22	2.35
B4	-23.1683	-41.0521	100	shelf	0.44	n.d.	67.27	11.93	0.79	21.92	0.62	24.45	0.11	0.54	0.26	2.46
B5	-23.1919	-41.0142	150	shelf	0.41	n.d.	63.49	11.93	0.73	19.95	0.63	24.76	0.11	0.53	0.27	2.47
B6	-23.1734	-40.9467	400	slope	1.64	n.d.	111.05	14.82	0.78	21.55	0.62	24.24	0.10	0.64	0.26	2.35
B7	-23.2176	-40.9606	700	slope	1.57	n.d.	111.80	14.06	0.84	23.23	0.61	24.15	0.10	0.67	0.25	2.31
B8	-23.2307	-40.9324	1000	slope	1.63	n.d.	131.16	14.69	0.84	23.26	0.63	24.99	0.09	0.68	0.27	2.31
B9	-23.2535	-40.8987	1300	slope	1.16	n.d.	97.60	10.92	0.81	22.40	0.65	25.74	0.10	0.70	0.29	2.29
B10	-23.3104	-40.7925	1900	slope	0.71	n.d.	45.84	5.52	0.70	19.19	0.66	26.18	0.13	0.69	0.27	2.31
B11	-23.4227	-40.5990	2500	slope	0.39	n.d.	73.46	8.53	0.89	25.00	0.68	27.31	0.15	0.67	0.27	2.33
B12	-23.7554	-39.9995	3000	slope	0.21	n.d.	83.84	7.70	n.d.	n.d.	0.68	27.33	0.14	0.65	0.28	2.35
G03	-22.0631	-40.1670	75	shelf	0.24	75.07	156.83	25.20	0.93	26.07	0.59	23.06	0.12	0.56	0.27	2.43
G04	-22.0443	-40.0793	100	shelf	0.28	n.d.	150.61	25.72	n.d.	n.d.	0.60	23.42	0.14	0.62	0.29	2.35
G05	-22.1033	-40.0521	150	shelf	0.20	76.05	117.89	16.59	0.93	25.95	0.60	23.45	0.12	0.60	0.29	2.37

Station (0-2 cm)	Latitude (°S)	Longitude (°W)	Water depth (m)	Location	TOC <sup>a</sup> (%)	∑alkenones (µg gTOC <sup>-1</sup> )	∑isoGDGT (µg gTOC <sup>-1</sup> )	∑brGDGT (µg gTOC <sup>-1</sup> )	U <sup>K</sup> <sub>37</sub>	SST- U <sup>K</sup> <sub>37</sub> <sup>b</sup> (°C)	TEX <sub>86</sub>	Temp- TEX <sub>86</sub> <sup>Hc</sup> (°C)	BIT index	GDGT- 0/cren	MI	RI
G07	-22.1258	-39.9018	700	slope	0.34	197.68	130.67	11.36	0.91	25.57	0.60	23.35	0.11	0.72	0.27	2.25
G08	-22.1227	-39.8733	1000	slope	0.79	101.55	113.25	8.05	0.90	25.16	0.64	25.33	0.11	0.73	0.28	2.26
G09	-22.1231	-39.8164	1300	slope	0.57	126.90	94.59	6.80	0.91	25.60	0.62	24.56	0.10	0.76	0.27	2.22
G10	-22.1232	-39.7408	1900	slope	0.59	88.47	53.80	5.22	0.92	25.64	0.62	24.47	0.15	0.62	0.27	2.37
G11	-22.1727	-39.1391	2500	slope	0.38	28.62	77.62	5.66	0.93	26.20	0.68	27.03	0.15	0.77	0.29	2.22
G12	-22.2063	-38.5986	3000	slope	0.12	15.36	87.70	5.99	0.94	26.32	0.59	22.88	0.14	0.79	0.24	2.20
H1	-21.7234	-40.5316	25	shelf	n.d.	n.d.	n.d.	n.d.	0.89	24.98	0.65	25.79	0.11	0.62	0.25	2.39
H2	-21.7393	-40.2881	50	shelf	0.27	n.d.	318.66	29.65	0.90	25.03	0.66	26.05	0.10	0.62	0.26	2.40
H3	-21.7200	-40.1923	75	shelf	0.37	n.d.	97.02	25.54	0.86	24.04	0.61	23.74	0.14	0.46	0.23	2.59
H4	-21.7154	-40.1713	100	shelf	0.32	n.d.	78.69	20.64	0.85	23.69	0.63	24.93	0.13	0.49	0.24	2.55
H5	-21.7109	-40.1504	150	shelf	0.32	n.d.	96.42	24.14	0.89	24.81	0.62	24.62	0.15	0.51	0.23	2.53
H6	-21.7398	-40.0888	400	slope	0.66	n.d.	96.30	18.87	0.90	25.21	0.64	25.52	0.13	0.56	0.25	2.46
H7	-21.7402	-40.0398	700	slope	0.92	n.d.	79.62	11.38	0.90	25.17	0.66	26.43	0.12	0.61	0.25	2.40
H10	-21.6233	-39.5956	1900	slope	0.54	n.d.	44.45	5.61	0.91	25.48	0.65	25.93	0.15	0.65	0.26	2.34
H11	-21.6227	-39.0516	2500	slope	0.26	n.d.	49.14	5.77	0.92	25.67	0.68	27.34	0.16	0.66	0.28	2.34
H12	-21.6184	-38.5413	3000	slope	0.08	n.d.	7.38	7.08	0.81	22.60	0.62	24.58	0.46	0.35	0.22	2.77
I02	-21.3836	-40.3289	50	shelf	0.34	46.21	98.52	21.43	0.93	26.20	0.62	24.47	0.14	0.49	0.24	2.55
I04	-21.1534	-40.2689	100	shelf	0.44	45.03	88.02	17.69	0.93	26.10	0.63	25.07	0.16	0.51	0.24	2.53
I05	-21.3848	-40.2534	150	shelf	0.61	91.21	128.72	20.94	0.92	25.69	0.62	24.56	0.16	0.50	0.23	2.54
I06	-21.2278	-40.2499	400	slope	1.36	98.22	150.97	21.24	0.93	25.98	0.59	22.97	0.14	0.67	0.29	2.30
I07	-21.1872	-40.2149	700	slope	1.13	145.59	127.31	18.98	0.93	25.97	0.63	24.82	0.16	0.74	0.27	2.24
I08	-21.1850	-40.1533	1000	slope	1.02	129.11	113.90	11.35	0.91	25.44	0.63	25.07	0.12	0.65	0.25	2.35
I09	-21.1858	-40.0522	1300	slope	0.87	99.72	91.09	7.93	0.91	25.56	0.62	24.61	0.11	0.74	0.27	2.25
I10	-21.1850	-39.6611	1900	slope	0.47	52.40	58.05	5.80	0.92	25.84	0.65	25.77	0.16	0.71	0.28	2.28
I11	-21.1883	-39.0843	2500	slope	0.24	38.06	104.44	6.44	0.94	26.41	0.65	25.73	0.10	0.75	0.30	2.23
I12	-21.1875	-38.4481	3000	slope	0.11	29.20	188.97	n.d.	0.95	26.59	0.63	24.66	0.08	0.75	0.27	2.22

<sup>a</sup> TOC (%) published by Cordeiro et al. (2018).

<sup>b</sup> SST-U<sub>37</sub><sup>K</sup> calculated with the calibration of Müller et al. (1998).

<sup>c</sup> Temp-TEX<sub>86</sub><sup>H</sup> calculated with the calibration of Kim et al. (2010).

## **3.5. Discussion**

### **3.5.1. Spatial distribution of alkenones and GDGTs**

The complex hydrodynamics of the Campos Basin directly influence the biogeochemistry of OM on a regional scale (Yoshinaga et al., 2008; Oliveira et al., 2013). Contents of both alkenones and isoGDGTs are higher in the southern portion of the Campos Basin when compared with the northern portion (Figure 3.2a,b) due to the high productivity in the Cabo Frio region caused by the upwelling of SACW. Thaumarchaeota are chemolithoautotrophic organisms that obtain energy from oxidizing ammonia regenerated from organic material of phytoplankton origin (Könneke et al., 2005; Hurley et al., 2016) and thereby tend to increase in abundance at high productivity environments. When comparing between the isobaths, alkenone contents in transect A were expressly higher on the outer shelf (150 m depth), where the influence of the upwelled waters is lower. By analyzing surface sediments across the Cabo Frio shelf, Cordeiro et al. (2014) also observed an increase in the TOC-normalized alkenones further offshore on the outer shelf. In a study on pigment signatures in the Campos Basin, Rodrigues et al. (2014) found that diatoms dominated the inner shelf region, whereas haptophytes and Prasinophyceae were predominant in the outer shelf and shelf-break regions over the dry season. Also, Yoshinaga et al. (2008) observed significantly higher concentrations of diatom derived lipids as compared to alkenones in the inner and mid-shelf in sediments from the CFUS region. Considering the existence of a complex ecological community in this coastal system (Valentin, 1984b; Gonzalez-Rodriguez et al., 1992), the higher alkenone content in sediments of the outer shelf may be related to a phytoplankton succession typically observed in upwelling systems. This is characterized by diatom prevalence in coastal upwelled waters and dense coccolithophorid communities found further offshore, towards the more nutrient depleted and stratified surface waters (Schiebel et al., 2004; Henderiks et al., 2012).

The highest isoGDGTs contents in the southern portion of the basin (transects A and B) were found in the continental shelf area directly affected by the coastal and shelf-break intrusion of the nutrient-rich SACW. This may be related to a higher Thaumarchaeota production and/or export as a response to the increased fertilization of the upper water column layer, as detailed below.

As expected, brGDGT contents are higher in the inner shelf samples and gradually decrease with the distance from the terrestrial sources in all transects. The same rapid land-sea decline is observed in other regions (Hopmans et al., 2004; Kim et al., 2006; Walsh et al., 2008; Zhu et al., 2011; Hu et al., 2012; Zell et al., 2014a, 2014b; Sinninghe Damsté, 2016) and is related to the fact that brGDGTs are primarily produced in soil, transported to the ocean by rivers and diluted from the river estuary to the open ocean (Hopmans et al., 2004).

### 3.5.2. Effects of the terrestrial input and methane metabolism upon GDGTs indices

The low BIT values ( $< 0.20$ ) suggest that all samples contain relatively low amounts of brGDGTs when compared to crenarchaeol and the contribution of terrestrial isoGDGTs may not be considered to interfere with the  $\text{TEX}_{86}^{\text{H}}$  marine signal. However, the BIT index presents a better correlation with the crenarchaeol ( $R = 0.36$ ) than with the brGDGTs contents ( $R = 0.04$ ). As the BIT index is more influenced by crenarchaeol, it does not show the same land-sea decline observed for the brGDGTs and thus the BIT index should not be used as indicator for estimating riverine influence in the region. These results are consistent with the overall autochthonous nature of the sedimentary OM in the shelf and slope of Campos Basin (Yoshinaga et al., 2008; Oliveira et al., 2013; Carreira et al., 2015; Cordeiro et al., 2018).

To verify if the  $\text{TEX}_{86}^{\text{H}}$  signal may also be affected by members of archaea that participate in the methane cycle, the GDGT-0/crenarchaeol ratio and the MI were evaluated. Relatively higher GDGT-0/crenarchaeol ratios ( $>2$ ) can be indicative of significant contribution from methanogenic archaea (Blaga et al., 2009). Our GDGT-0/cren values are  $\leq 0.86$  (Table 3.1) and, therefore, suggest that the GDGT-0 in the Campos Basin may originate mainly from marine Thaumarchaeota. MI values between 0 and 0.3 are related to normal marine conditions, i.e., without anaerobic oxidation of methane by methanotrophic archaea (Zhang et al., 2011). The results reveal that only one sample (A12) has a MI  $>0.3$  (Table 3.1). However, the MI value of this sample is not expressly higher (0.33) and the temp- $\text{TEX}_{86}^{\text{H}}$  estimate agrees well with the observed SST ( $\Delta T = -0.07$ ; Supplementary Table S3.4), which means that the contribution of methanotrophic archaea can be considered negligible to bias the  $\text{TEX}_{86}$  signal in the study region. The agreement of our RI- $\text{TEX}_{86}$  results within the global RI- $\text{TEX}_{86}$

relationship (Figure 3.4b) support the assumption that the influence of non-temperature parameters on the  $\text{TEX}_{86}$  signal may be neglected.

### 3.5.3. Temperature calibrations and residuals

As the range of sea water temperature among the stations in the Campos Basin is relatively small, the present study does not intend to develop new local calibrations, but rather test the applicability of the pre-existing ones.  $\text{SST-U}_{37}^{K'}$  estimates will be discussed based on the annual mean and seasonal calibrations of Müller et al. (1998) for the eastern South Atlantic and respectively compared with annual mean and seasonal SST from WOA13 (Figure 3.3, Table 3.2).  $\text{Temp-TEX}_{86}^H$  estimates will be discussed based on the global SST calibration of Kim et al. (2010) for high temperatures and on the global subsurface (0-200 m) temperature calibration from Kim et al. (2012), and respectively compared with the annual mean SST and depth-integrated water temperatures from WOA13 (Figure 3.5, Table 3.2). These calibrations were found to be more suitable to the geographic location of the study area. Other annual mean global calibrations were also tested for both proxies (Schouten et al., 2002; Conte et al., 2006; Kim et al., 2008, 2010; Liu et al., 2009; Tierney and Tingley, 2014, 2018) and revealed qualitatively similar discrepancies when compared to the WOA13 temperatures (Supplementary Table S3.5), with colder/warmer biases varying systematically even for the non-linear calibrations (Kim et al., 2010; Tierney and Tingley, 2014, 2018). Quantitatively, however, the biases variation among the calibrations tested were either very expressive or very slightly, depending on the sample. The preference was to use the calibration methods that showed a better fit and the highest number of proxy-estimated temperatures within the calibration error was the criteria considered to define a particular calibration to estimate seawater temperatures.

Previous studies on surface sediments from the South Atlantic (e.g., Benthien and Müller, 2000; Cordeiro et al., 2014) showed a strong correlation between the estimated temperatures using the global calibration of Müller et al. (1998) and the annual mean SST for the region influenced by the BC. For  $\text{TEX}_{86}^H$ , however, there is only sparse data from the western South Atlantic, which are included in the global core-top calibrations (Figure 3.4a, Kim et al., 2008, 2010). When compared with the annual mean SST-WOA13 (Figure 3.5c, Table 3.2), most of the  $\text{temp-TEX}_{86}^H$  estimated with the global SST calibration (85%) remain within

the calibration error (Kim et al., 2010) in the Campos Basin region. For the annual mean SST- $U_{37}^{K'}$  (Figure 3.3f, Table 3.2), 71% of the estimated temperatures agree with the annual mean SST-WOA13. A significant discrepancy is observed in two main areas of the southern portion of the basin: the coastal upwelling region and the outer shelf and slope of transect B, where cold bias can be observed for the  $TEX_{86}^H$  and  $U_{37}^{K'}$  temperatures, respectively. The transects from the northern area, located outside the CFUS (transects G, H and I), however, showed minor deviations from the expected value, except for the sample closest to the Paraíba do Sul River (transect H, 25 m depth), which presented a warm discrepancy for both proxies. Discrepancies between the two proxies have been reported in several previous studies (e.g., Huguet et al., 2006b; Leider et al., 2010; Lopes dos Santos et al., 2013; Chen et al., 2014) which the authors usually attribute to the combined factors that control productivity of the organisms synthesizing the compounds used as proxies and environmental factors such as water circulation patterns, sedimentation processes and degradation of OM. These biases will be discussed in further detail in the next sub-sections.

Table 3.2: Calibrations used for SST- $U_{37}^{K'}$  and temp- $TEX_{86}^H$  estimates and their relationship with the instrumental temperatures obtained from the WOA13.

Calibration	Reference	Standard error	Instrumental temperature (WOA13)	Pearson correlation (r)	Samples within the error (%)	<i>n</i>
<i>U<sub>37</sub><sup>K'</sup></i>						
Annual mean South Atlantic (0 m)	Muller et al., 1998	1.0	annual mean SST	0.63	71	49
Summer South Atlantic (0-10 m)	Muller et al., 1998	1.1	summer SST	0.64	51	49
Autumn South Atlantic (0-10 m)	Muller et al., 1998	1.0	autumn SST	0.63	22	49
Winter South Atlantic (0-10 m)	Muller et al., 1998	1.1	winter SST	0.62	73	49
Spring South Atlantic (0-10 m)	Muller et al., 1998	1.1	spring SST	0.57	69	49
<i>TEX<sub>86</sub><sup>H</sup></i>						
Global calibration (0m)	Kim et al., 2010	2.5	annual mean SST	0.77	85	52
Global calibration (0-200 m)	Kim et al., 2012	2.2	annual mean depth-integrated (0-200 m)	0.80	68	41
Global calibration (0-200 m)	Kim et al., 2012	2.2	annual mean depth-integrated (100-150 m)	0.51	93	41
Global calibration (0-200 m)	Kim et al., 2012	2.2	annual mean depth-integrated (100-200 m)	0.76	95	41

### 3.5.3.1. Depth habitats of the source organisms

In general,  $U_{37}^{K'}$  reconstructed annual mean temperatures seem to agree better with observed SST than  $\text{temp-TEX}_{86}^H$ , despite the biases observed in transect B (Figure 3.3f and Figure 3.5c, Table 3.2). As Haptophytes are photoautotrophic algae thriving in the photic zone (Prahl and Wakeham, 1987; Conte and Eglinton, 1993),  $U_{37}^{K'}$  reflects very likely the temperature in the upper 6 to 75 m of the water column in the working area (Rodrigues et al., 2014). On the other hand,  $\text{TEX}_{86}$ -based temperatures need a more careful interpretation regarding the water depth in which the source organisms are thriving. Even though most of the global calibrations are based on the correlation between  $\text{TEX}_{86}$  and annual mean SST, it is known that Thaumarchaeota grow at different depths in the water column. According to Karner et al. (2001), although widely distributed, Thaumarchaeota tend to achieve their maximum abundance around <250 m, with relative increase occurring between 100 and 150 m in the open ocean. Several studies suggest that GDGTs are mainly exported to the sediments from subsurface waters at ca. 40-150 m depth (Huguet et al., 2007a; Lee et al., 2008; Lopes dos Santos et al., 2010; Kim et al., 2012; Chen et al., 2014). It is believed that the sedimentary  $\text{TEX}_{86}$  signal is primarily derived from the upper part of the water column due to the existence of an active food web that generates fast sinking large particles (e.g., fecal pellets and marine snow) (McCave, 1984; Wuchter et al., 2005). This may be related to a possible predominant habitat below the mixed layer (Lee et al., 2008; Lopes dos Santos et al., 2010), where the  $\text{NH}_4^+$  regenerated from organic detritus derived from primary producers is more available to the ammonia-oxidizing archaea (Könneke et al., 2005; Beman et al., 2010; Pitcher et al., 2011a).

In the South Atlantic off Brazil, rates of assimilation of nitrogen indicate that the primary production is dominated by regenerated production (Metzler et al., 1997). To verify if the  $\text{TEX}_{86}^H$  signal recorded in the marine sediments of the Campos Basin relates better to the subsurface temperatures than the SST, the temperatures estimated with the surface and subsurface calibrations (Kim et al., 2010, 2012) were compared with the WOA13 temperatures for all available depths from 0 to 200 m. The water depths that showed the lowest deviations between estimated and observed temperatures and the minimum and maximum water depths where the residual fits within the calibration error are shown in Figure 3.6. For most of the samples, the estimated surface  $\text{temp-TEX}_{86}^H$  (Kim et al., 2010) seems to show better agreement within the surface mixed layer, which is about 16-

55 m deep throughout the Campos Basin continental shelf (Suzuki et al., 2015; Figure 3.1e-h).

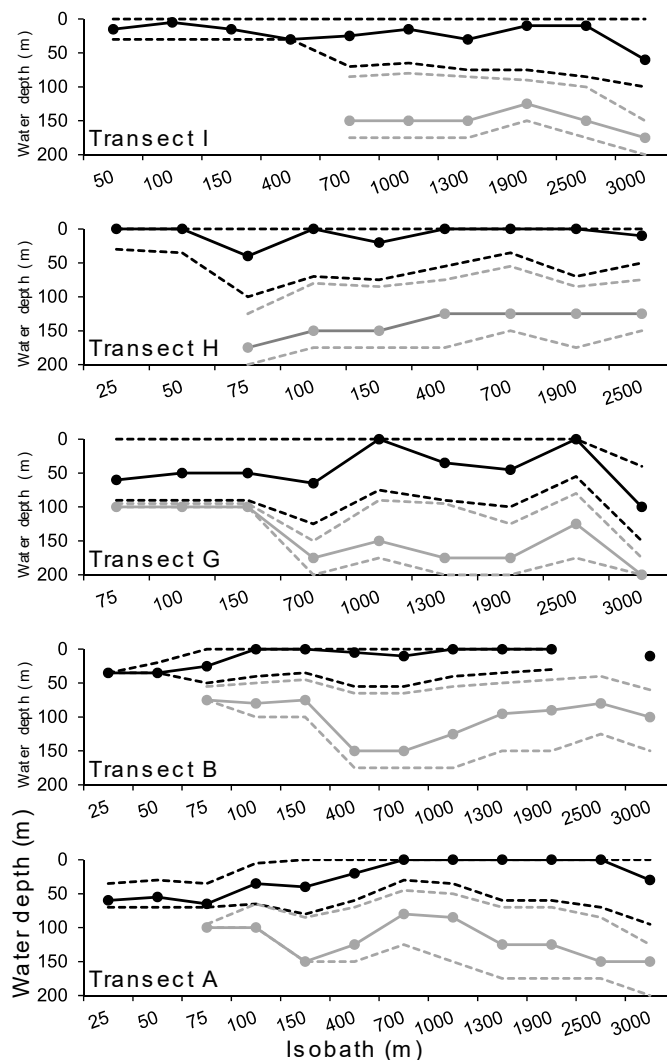


Figure 3.6: Depths of agreement between estimated (Kim et al., 2010, 2012) and climatological mean temperatures (WOA13) from 0-200 m depth along the isobaths. Dots represent the water depth of optimal agreement and dashed lines represent minimum and maximum water depth in which the residuals are within the standard error of estimates for surface (black) and subsurface (grey) calibrations.

In the coastal upwelling region (transect A, 25-75 m depth; transect B, 25-50 m depth; Figure 3.6), the agreement between 20 and 70 m depth, with an optimal fit from 35 to 65 m depth, suggest a predominant subsurface habitat for Thaumarchaeota in this area. Chen et al. (2014) suggest that  $\text{TEX}_{86}^H$  may often reflect temperatures from 30–50 m depth in the upwelling area off the Lesser Sunda Islands, while  $U_{37}^{K'}$  correlates well to SST. For the coastal upwelling stations, strong cold biases are observed between the surface calibration estimates and

observed annual mean SST (Figure 3.5c). The influence of the upwelling on the Thaumarchaeota production and  $\text{TEX}_{86}^{\text{H}}$  signal will be further discussed.

The estimated subsurface temp- $\text{TEX}_{86}^{\text{H}}$  (Kim et al., 2012) shows optimal agreement with the temperatures from water depths below the mixed layer (75 to 200 m depth, Figure 3.6). In view of the observed results from Figure 3.6, the  $\text{TEX}_{86}^{\text{H}}$  estimated subsurface temperatures were tested against the annual mean WOA13 depth-integrated temperatures (Kim et al., 2008) from 0–200 m, 100-150 m and 100-200 m (Table 3.2). A strong linear correlation ( $r = 0.80$ ) was found for the 0–200 m water depth, however, the best agreement is observed between 100-200 m (Figure 3.5d), with a higher number of samples within the calibration error (95 %). The inner-shelf stations with water depths below 100 m were not considered for the subsurface calibration.

### 3.5.3.2.

#### Seasonality of the source organisms

In general, both  $U_{37}^{\text{K}'}$  and  $\text{TEX}_{86}^{\text{H}}$  proxies in surface sediments show a strong relationship with annual mean SST, a prerequisite for the development of the several above mentioned global calibrations. However, it has been reported that the abundances of prymnesiophyte algae and Thaumarchaeota are seasonal (Murray et al., 1998; Wuchter et al., 2006; Pitcher et al., 2011b; Rosell-Melé and Prah, 2013) and both proxies can be biased toward the temperature of the high production periods (e.g., Harada et al., 2006; Herfort et al., 2006; Yamamoto et al., 2007, 2012; Turich et al., 2013; Chen et al., 2016; Park et al., 2018).

Satellite observations indicate blooms of the coccolithophore *Emiliana huxleyi* on the shelf and shelf break off the south-eastern coast of South America during the late austral spring and summer (Brown and Podestá, 1997). In the Campos Basin region, Rodrigues et al. (2014) observed predominance of pigments associated with haptophytes in the outer shelf and shelf break during the dry season, i.e. August and September. To test if the  $U_{37}^{\text{K}'}$  signal may be biased due to seasonality, seasonal SST- $U_{37}^{\text{K}'}$  estimates were compared to seasonal SST-WOA13. Our results show that, in terms of number of samples within the calibration error,  $U_{37}^{\text{K}'}$ -temperatures agree better with observed SST using the winter calibration (from July to September, Figure 3.3g-j, Table 3.2), which corresponds to the period of the maximum abundance of haptophytes observed in the region (Rodrigues et al., 2014). Studies in the northeastern Atlantic (Rosell-Melé et al., 1995b), Adriatic Sea (Leider et al., 2010) and Mediterranean Sea (Emeis et al.,

2000) also observed a better relation of  $U_{37}^{K'}$  with winter temperatures, reflecting a higher haptophyte production during the colder season for these regions.

Thaumarchaeotal abundance and GDGTs fluxes to the sediments can be higher in certain periods of the year, usually associated with nutrient enrichment of surface waters (Wuchter et al., 2005). In the North Sea, for example, the  $TEX_{86}$  signal registered in sediments reflected winter temperatures, which is the season with higher abundance of Thaumarchaeota (Herfort et al., 2006a). However, only annual mean calibrations are available for  $TEX_{86}^H$  and our results for surface temp- $TEX_{86}^H$  de facto show better agreement with the annual mean SST rather than with the seasonal SST. An exception to this observation is the colder bias observed in the southern portion of the basin for the  $TEX_{86}^H$ -reconstructed temperatures in the coastal stations, which are probably related to the seasonal peak of upwelling events.

### 3.5.3.3.

#### **Influence of hydrodynamics on the source organisms**

In the southern region, the CFUS area has a very peculiar oceanographic setting not considered in global calibrations that may complicate the lipid-based temperature reconstruction. Temp- $TEX_{86}^H$  are up to 5.3 °C lower than the annual mean SST in the first isobaths of transects A and B, where the coastal upwelling is located. A similar cold-bias in the  $TEX_{86}$  signal was found for other upwelling areas (e.g., Kim et al., 2008; Lee et al., 2008; Chen et al., 2014). Because Thaumarchaeota may be more abundant in certain periods of the year, temperature biases based on  $TEX_{86}$  signal are likely to occur in the high production season (Wuchter et al., 2005; Herfort et al., 2006a). The intrusion of the SACW on the Cabo Frio shelf is responsible for an increase in nutrient availability and a decrease in temperature of the water column (Souza et al., 2011; Suzuki et al., 2015). For being an intermittent process, the colder temperatures of peak upwelling in austral summer are likely smoothed by the spatial (gridded data sets) and temporal (annual and seasonal statistical mean values) resolution of the climatological mean temperature from WOA13. The WOA13 data therefore likely overestimate the true temperatures at the sites affected by upwelling. Thus, other than a possible subsurface habitat for Thaumarchaeota in the coastal upwelling region (Figure 3.6), the colder  $TEX_{86}^H$  signal in relation to the annual mean SST could be caused by a higher Thaumarchaeota production during the cooler

upwelling events as a response to the increased fertilization of the upper layer (Lee et al., 2008).

However, marine Thaumarchaeota are generally considered more abundant in surface waters when the primary production is low (Murray et al., 1998; Wuchter et al., 2005; Herfort et al., 2006a). Taking into account that Thaumarchaeota cells are too small to sink through the water column, GDGTs can only reach the sediment after aggregation with phytoplankton and other suspended matter, i.e. marine snow or fecal pellets (Huguet et al., 2006a). Alternatively, instead of an actual increase in Thaumarchaeota abundance and GDGT production itself, the TEX<sub>86</sub> signal could be primarily controlled by the increase in surface phytoplankton production and a subsequent increased amount of aggregates, which could, in turn, increase the GDGT flux and a seasonally increased export efficiency to the sediment during the upwelling events (Wuchter et al., 2005; Huguet et al., 2007a; Kim et al., 2008).

Phytoplankton blooming during a coastal upwelling event at Cabo Frio is dominated by diatoms (Coelho-Souza et al., 2017) and responsible for the development of a zooplanktonic community characterized by high abundance and low diversity of species (Valentin and Moreira, 1978; Valentin and Monteiro-Ribas, 1993). The high zooplanktonic grazing rates are the main cause of a decrease in phytoplankton biomass after the upwelling (Valentin and Moreira, 1978; Gonzalez-Rodriguez et al., 1992). Thereby, the zooplankton plays an important role in the vertical flux of phytoplankton-derived OM to the surface sediments of the CFUS by increasing the production of aggregates (Yoshinaga et al., 2008). The cold temp-TEX<sub>86</sub><sup>H</sup> may actually reflect colder waters from peak coastal upwelling conditions because of a more efficient export of GDGTs to the sediment during these events.

In contrast, the SST-U<sub>37</sub><sup>K'</sup> are in agreement with the annual mean SST and do not reflect the low temperatures during peak upwelling in the CFUS samples. A plausible scenario to explain the difference between the two proxies is the above-mentioned typical phytoplankton succession, where the alkenone producers are outcompeted by the diatoms during the upwelling events, while the export of GDGTs is generally tied to diatom-dominated fluxes as previously suggested by Mollenhauer et al. (2015). Thereby, the dominance of diatoms during peak upwelling could support the GDGT fluxes and restrict the alkenone production at the same time.

Another peculiar feature can be observed for transect B in the shelf-break and slope samples (from 150 to 1900 m depth) with SST-U<sub>37</sub><sup>K'</sup> up to 5.9 °C lower

compared to annual mean SST, while temp-TEX<sub>86</sub><sup>H</sup> agrees well with annual mean SST (Figure 3.5a,c). There is evidence from compound specific radiocarbon analyses that GDGTs are more labile than alkenones and better reflect local conditions, whereas alkenones are usually more affected by lateral transport (Mollenhauer et al., 2007; Shah et al., 2008). The alkenones deposited on the outer shelf and upper slope near transect B may be reflecting colder temperatures of adjacent colder waters, as they are more susceptible to lateral transport, while the GDGTs register local temperature signals. In the same samples of this transect considered here, higher contents of TOC (Oliveira et al., 2013) and lipids (Cordeiro et al., 2018) relative to the adjacent transects were observed and attributed to the lateral transport from shallow shelf waters to the upper slope. However, the source area where the advected material originates and the reason why the adjacent transect A is not affected are not clear and further evidence is still necessary to constrain this hypothesis.

### 3.6. Conclusions

The estimated annual mean SST calculated by the two proxies in surface sediments in cross-margin transects samples agreed well (71% for U<sub>37</sub><sup>K'</sup> and 85% for TEX<sub>86</sub><sup>H</sup>) with the interpolated annual mean SST from WOA13, with minor deviations that are within the calibration error. Overall, the subsurface and seasonal calibrations also showed strong correlations for TEX<sub>86</sub><sup>H</sup> and U<sub>37</sub><sup>K'</sup>, respectively. While the temp-TEX<sub>86</sub><sup>H</sup> using the surface calibration (Kim et al., 2010) reflects the surface mixed layer, the subsurface temp-TEX<sub>86</sub><sup>H</sup> using the depth-integrated calibration for 0-200 m (Kim et al., 2012) agrees with the observed depth-integrated temperatures at 100-200 m (95% of the estimates, not including the inner shelf samples). In relation to the seasonal calibrations, SST-U<sub>37</sub><sup>K'</sup> shows a better agreement with SST-WOA13 for winter (73% of the estimates), which may be related to a maxima abundance of haptophytes in the region during this period.

However, the proxy-based temperature estimates are biased towards colder temperatures in two main southern areas: the CFUS inner-shelf and the outer shelf and slope of transect B. In the CFUS inner-shelf area, the cold-biased TEX<sub>86</sub><sup>H</sup> record is probably caused by the coastal SACW intrusion that increases the fertilization and primary production leading to a maximum export and/or a predominant subsurface habitat of Thaumarcheota in comparison to the

oligotrophic adjacent waters. In the transect B, the cold-biased  $U_{37}^{K'}$  signal may be caused by lateral transport, but further investigation regarding the advected material origin is needed.

Besides showing agreement between reconstructed and observed SST for most samples, the colder offsets observed for a few samples located inside or near the CFUS area show that care must be taken when using both  $U_{37}^{K'}$  and  $TEX_{86}^H$  in paleoclimate studies in the Campos Basin. Our results reinforce that alkenone and GDGT ratios are correlated with annual mean SST, but  $U_{37}^{K'}$  and  $TEX_{86}^H$  proxies still contain uncertainties and limitations that must be considered when applied to areas with exceptional oceanographic settings.

### **Acknowledgements**

The authors thank PETROBRAS (Brazilian Petroleum Company) for providing samples under the Habitats project. This study is funded in part by the Coordenação de Aperfeiçoamento de Pessoal de Nível Superior – Brasil (CAPES) – Finance Code 001. M. Ceccopieri thanks the National Council for Scientific and Technological Development (CNPq, grant 142451/2015-0), CAPES (grant PDSE 88881.134877/2016-01) and the German Academic Exchange Service (DAAD, short-term grant 2015/91591964) for her PhD scholarships. R. S. Carreira was supported by research fellowships from CNPq (grant 309347/2017-3) and CAPES (grant 88881.121009/2016-01). The research was partially funded by CNPq (process 402459/2012-1). Our thanks to Ralph Kreutz and Dr. Enno Schefuß (MARUM, University of Bremen) for assistance with the sediment extractions, to Dr. Maria Winterfeld, Eunmi Park and Dr. Amanda Spera for the support in the laboratory, and to Prof. Afonso Paiva for the satellite map. Thanks also go to three anonymous reviewers for their constructive and stimulating comments, which helped to improve the manuscript.

## Chapter 4

### Branched GDGTs and the associated MBT' and CBT proxies in surface sediments from the south-eastern Brazilian continental margin

Milena Ceccopieri, Renato S. Carreira, Angela L. R. Wagener, Jens Hefter, Gesine Mollenhauer

*In preparation for Frontiers in Earth Sciences*

#### Abstract

Branched glycerol dialkyl glycerol tetraethers (brGDGTs) in marine sediment records can be used to infer inputs of terrigenous organic matter and also to reconstruct the mean annual air temperature (MAAT) and soil pH of the nearby land areas using the methylation of branched tetraethers (MBT') and cyclization of branched tetraethers (CBT) indices. In this study, we considered these proxies obtained from 51 core-top sediments collected in the Campos Basin (southeast Brazil) and compared these data with instrumental data of MAAT and soil pH measured in the adjacent drainage basins. The Paraíba do Sul River is confirmed as the main source of brGDGTs to the study region. The results for most of the marine sediments fit in the upper range of soil pH and lower range of MAAT found in the adjacent drainage basin. However, selective compound degradation and *in situ* production of brGDGTs clearly seems to exert an additional influence on the proxies obtained here. The first effect leads to a decrease of both the CBT-based pH and MBT'/CBT-based MAAT values with distance from the coast, and the latter resulted in an overestimation of the CBT-based pH and MBT'/CBT-based MAAT in the mid and outer shelf.

#### 4.1. Introduction

Glycerol dialkyl glycerol tetraethers (GDGTs) are lipids present in the cell membranes of Archaea and bacteria that occur in the environment in the isoprenoid (isoGDGTs) and branched (brGDGTs) forms (Schouten et al., 2013b). While the isoGDGTs are most likely to occur in the aquatic and terrestrial environments, the brGDGTs are attributed to anaerobic and heterotrophic bacteria present in peat and soil (Pancost and Sinninghe Damsté, 2003; Weijers et al., 2006a, 2007b). Therefore, to evaluate the input and distribution of terrigenous OM in the continental margin, the brGDGTs can be used as alternative proxies to the more common tracers derived from higher plants (Hopmans et al., 2004).

BrGDGT structures vary in the degree of methylation (4-6) and cyclization (up to 2 cyclopentane rings) (Weijers et al., 2006a, 2007, Figure 4.1). The relative abundance of the individual forms of brGDGTs in the lipid membranes varies as a function of different environmental conditions, which is necessary to maintain the bacterial cellular structure and its vital functions. Weijers et al. (2007) found a significant correlation between the cyclic brGDGTs and the pH of the terrestrial material, and between the methylation of the brGDGTs and both soil pH and the mean annual air temperature (MAAT), leading to the definition of the cyclization of branched tetraethers (CBT) and methylation of branched tetraethers (MBT) indices. The MBT was later simplified by Peterse et al. (2012) to the MBT' index. Both indices are widely used in paleoenvironmental studies to evaluate soil pH and MAAT, based on specific calibrated equations. When applied to marine sediments, brGDGT-reconstructed MAAT usually corresponds well with the nearby land (Weijers et al., 2007b; Rueda et al., 2009) in areas with a relatively high amount of terrestrial OM input (Peterse et al., 2009). However, even though the brGDGTs are predominantly terrigenous, it was demonstrated that they can also derive from *in situ* production in the marine realm (Peterse et al., 2009; Zhu et al., 2011; Hu et al., 2012; Zell et al., 2014b, 2014a), which may constrain the use of the MBT'/CBT proxies.

The BIT index (Hopmans et al., 2004) was proposed to infer the contributions of soil OM to the ocean. It is based on the ratio of the continentally-derived brGDGTs and the marine crenarchaeol, an isoprenoid GDGT produced by Thaumarchaeota. In addition to the characterization of soil OM, the BIT index also provides information about the applicability of the GDGT-derived proxies in a particular region (Zhu et al., 2011). As there is evidence for limited terrestrial

sources of crenarchaeol, confidence in the BIT values requires evaluation of the relative contributions of allochthonous and autochthonous sources to the total isoprenoid GDGTs, which are derived from archaea, in continental margin sediments (Weijers et al., 2006b).

The Campos Basin, in the south-eastern Brazilian continental margin, is influenced by large to meso-scale hydrodynamic fronts (Brandini et al., 2018) resulting in diverse pelagic and benthic ecosystems with latitudinal and bathymetrical gradients, which make this region of great ecological and biogeochemical significance (Falcão et al., 2017). A coastal and shelf break upwelling system at Cabo Frio (~23° S; Figure 4.2a) results in one of the highest rates of primary production in the Brazilian margin, with ranges from 0.04 to 0.45 mgC m<sup>-2</sup> d<sup>-1</sup> on the shelf (Gonzalez-Rodriguez et al., 1992; Metzler et al., 1997; Brandini et al., 2014), contrasting with the overall oligotrophic conditions along the margin caused by the influence of the nutrient-poor Brazil Current (Silveira et al., 2017). The occurrence of these zones of enhanced primary production results in a predominance of autochthonous OM in the basin's sediments on a regional scale (Yoshinaga et al., 2008; Carreira et al., 2010; Cordeiro et al., 2018), a scenario also favored by a relatively low input of allochthonous OM (Carreira et al., 2015). The major contributor to continentally-derived materials to the Campos Basin is the Paraíba do Sul river, located to the north of the basin (Figure 4.2a), as evidenced by isotopic and molecular markers (Souza et al., 2010; Albuquerque et al., 2014; Carreira et al., 2015), dissolved black carbon (Dittmar et al., 2012) and metals (Lacerda et al., 1993; Carvalho et al., 2002; Araujo et al., 2017). Even though the Paraíba do Sul River plays a minor role as source of material to the global oceans when compared to other rivers, the influence of Paraíba do Sul River is relevant on a regional scale (Carvalho et al., 2002).

Here we considered crenarchaeol and the brGDGTs found in core-top sediments collected along cross-margin transects (25-3000 m water depths) in the Campos Basin (Figure 4.2a). The aims were to evaluate the applicability of the GDGT-based proxies to marine sediments of the basin, to reconstruct the soil pH and MAAT of the adjacent continental areas, and to contribute for the characterization of the OM in the region.

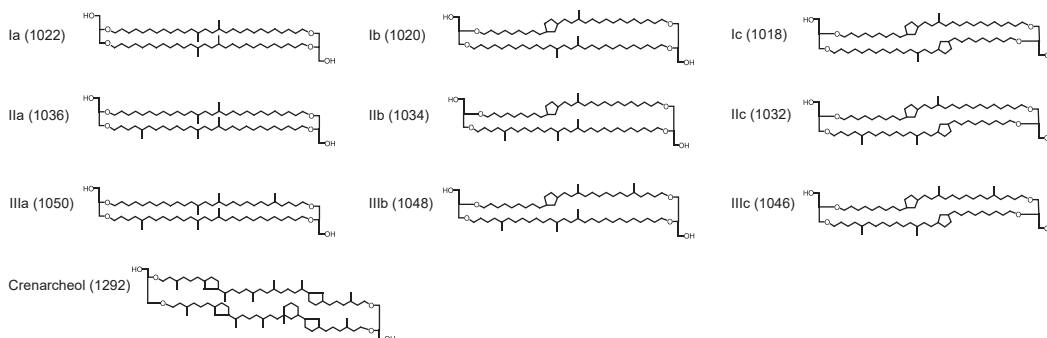


Figure 4.1: Chemical structure of brGDGTs and crenarchaeol with the correspondent ion masses ( $m/z$ ).

## 4.2. Study area

The Campos Basin (Figure 4.2a) extends over an area of 100,000 km<sup>2</sup>, in the south-eastern Brazilian continental margin between 20.5°S (Vitoria High) and 24°S (Cabo Frio High). The continental shelf has an average width of 100 km and the shelf break water depth varies from 80 m in the northern area to 130 m in the south. The slope, marked by the presence of several submarine canyons and channels, extends over 40 km with an average gradient of 2.5 ° (Viana et al., 1998).

The circulation in the Campos Basin is mainly controlled by the BC, formed at 10°S as a branch of the South Equatorial Current (Peterson and Stramma, 1991). The BC flows southward following the 200 m isobath and transports the oligotrophic warm Tropical Waters in its upper levels and the nutrient-rich and cold South Atlantic Central Water (SACW) between 200 and 700 m (Campos et al., 2000). In the southern portion of the basin, south of Cabo de São Tomé (22°S), changes in the coastline orientation affects the BC flow, resulting in the formation of strong cyclonic and anticyclonic frontal eddies. Those features induce the intrusion of SACW into the photic zone on the shelf break and the uppermost slope (Campos et al., 2000; Calado et al., 2010). Near Cabo Frio, wind-driven intrusions of SACW occur through the Ekman system during austral spring and summer, when NE winds prevail (Rodrigues and Lorenzetti, 2001; Castelao and Barth, 2006).

In the northern Campos Basin, the Paraíba do Sul River (Figure 4.2), a medium sized river with approximately 1,145 km of extension, flows into the ocean and is the major source of terrestrial material to the basin. The river drains an area of 55,400 km<sup>2</sup> (Figure 4.2b,c,d,e), crossing three of the most industrialized states of Brazil: Minas Gerais, São Paulo and Rio de Janeiro (Carvalho et al., 2002).

Other rivers bring in additional terrigenous material to the Campos Basin throughout the coastal drainage basins of Rio de Janeiro and Espírito Santo States (Figure 4.2b) but drain much smaller catchments than the Paraíba.

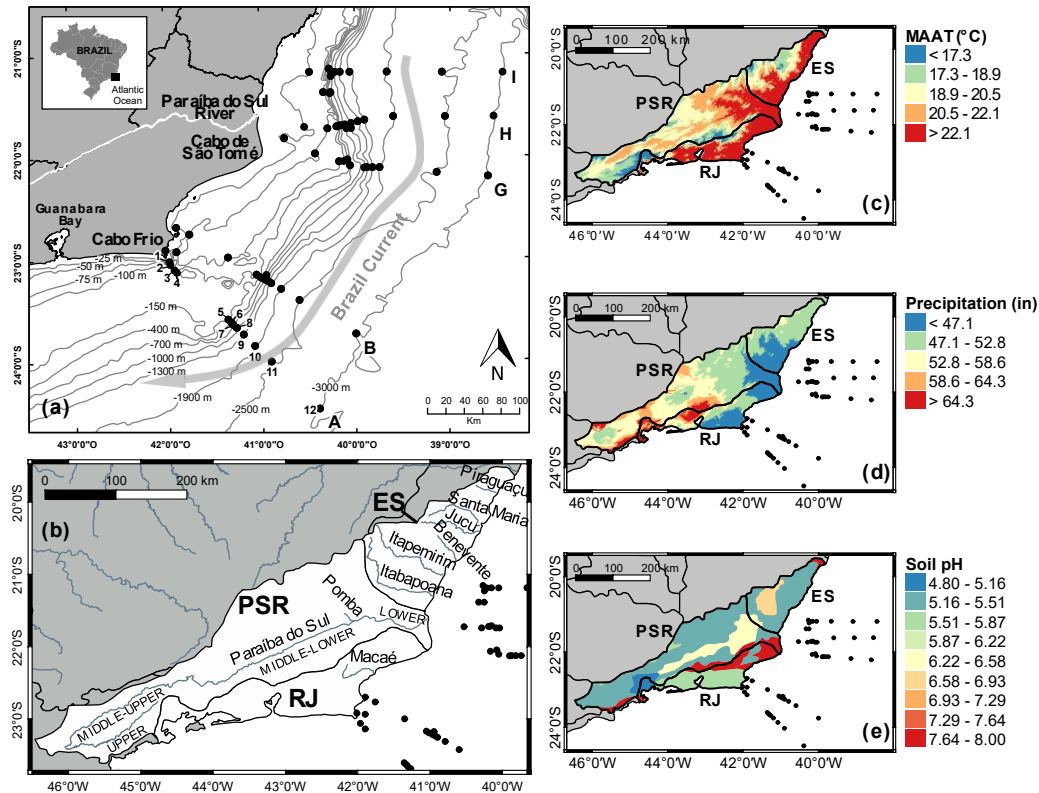


Figure 4.2: (a) Map of the Campos Basin with locations of the surface (0-2 cm) sediment sampling stations. Each transect (A, B, G, H and I) was sampled on isobaths as follows: 1, 25 m; 2, 50 m; 3, 75 m; 4, 100 m; 5, 150 m; 6, 400 m; 7, 700 m; 8, 1000 m; 9, 1300 m; 10, 1900 m; 11, 1900 m and 12, 3000 m. (b) Map showing the three drainage basins adjacent to the Campos Basin and their main rivers. (c) Mean annual air temperature, (d) annual precipitation (Fick and Hijmans, 2017) and (e) pH of the 30 cm topsoil (FAO/IIASA/ISRIC/ISS-CAS/JRC, 2012) in the three drainage basins. PSR = Paraíba do Sul River drainage basin; RJ = coastal drainages of the State of Rio de Janeiro; ES = coastal drainages of the Espírito Santo State.

The climate in the Paraíba do Sul River drainage area is subtropical with a well-defined precipitation regime. The MAAT varies from 10.1 °C in the upper basin to 24.1 °C (Figure 4.2b) in the lower basin, with an average of 20.1 °C (Fick and Hijmans, 2017). The average rainfall in the river basin is 54.2 inches year<sup>-1</sup> (Figure 4.2d) with higher precipitation in the upper and middle sectors of the drainage basin (maxima of 91.0 inches year<sup>-1</sup>) and less humidity in the lower basin (minimum of 39.3 inches year<sup>-1</sup>, Fick and Hijmans, 2017). Half of the annual rainfall occurs between November and January, while the period between June and August is the

driest of the year (Carvalho and Torres, 2002; Dittmar et al., 2012). Several studies in the Paraíba do Sul River have shown a strong dependence of the river water discharge and transported material on the rainfall regime (Carvalho et al., 2002; Souza and Knoppers, 2003; Souza et al., 2010; Figueiredo et al., 2011; Ovalle et al., 2013). A maximum river flow of  $4380 \text{ m}^3 \text{ s}^{-1}$  is observed during the rainy season, when more than 80% of the total annual load is transported, decreasing to  $180 \text{ m}^3 \text{ s}^{-1}$  in the dry season (Carvalho et al., 2002; Souza et al., 2010).

The vegetation in the drainage area of the Paraíba do Sul River is approximately 70% pastures, 27% agriculture and reforestation areas, and only 3% of the original Atlantic Forest (Ovalle et al., 2013), which is distributed over small patches (Dittmar et al., 2012). The river serves as an important water source for agriculture, industry and human use for approximately 13 million people and 5000 industries especially in the State of Rio de Janeiro (Ovalle et al., 2013), but also receives back the waste, generally without efficient treatment (Carvalho et al., 2002). Most of the industries are located in the middle and upper basin sectors, while extensive sugarcane plantations occupy the lower basin (Dittmar et al., 2012; Ovalle et al., 2013).

The texture of the soil along the Paraíba do Sul River basin is mainly silt/clay, with predominance of clay and sand/clay in the upper basin and clay/sand and clay/silt organic sediments (turf) in the flood-plain areas (Carvalho and Torres, 2002). The soil pH varies from 4.8 in the river's upper basin to 8.0 in the lower basin. The average soil pH across the entire drainage area adjacent to the Campos Basin is 6.1 (Figure 4.2e; FAO/IIASA/ISRIC/ISS-CAS/JRC, 2012).

### **4.3. Material and methods**

#### **4.3.1. Sampling**

Surface sediment samples (0-2 cm) were collected from 5 cross-shelf transects (A, B, G, H and I) along 12 isobaths (25, 50, 75, 100, 150, 400, 700, 1000, 1300, 1900, 2500 and 3000 m) in the Campos Basin as a part of the Habitats Project (CENPES/PETROBRAS) in 2008 and 2009 (Figure 4.2a). Undisturbed sediments were collected with an adapted large volume Van Veen sampler at the continental shelf stations and with a box corer at the slope stations.

### 4.3.2. Lipid extraction and GDGTs analysis

Fractions of about 5 g ( $\pm 0.01$  g) of freeze-dried and homogenized samples were extracted by use of an accelerated solvent extraction system (ASE 200, Dionex), with a mixture of dichloromethane:methanol 9:1 (v:v) at a temperature of 100 °C and a pressure of 1000 psi. A known amount of C<sub>46</sub>-GDGT was added as internal standard prior to the extraction. The volume of the bulk extracts was rotary evaporated under vacuum and saponified for 2h at 80 °C with 1 mL of KOH (0.1 M) in methanol:H<sub>2</sub>O (9:1; v:v). The extracts were fractionated into three polarity fractions using silica gel column chromatography. The polar fraction containing the GDGTs was obtained by eluting with dichloromethane:methanol 1:1 (v:v) and dried under a stream of nitrogen at 40 °C.

The GDGT fractions were filtered to remove particles and analyzed using an Agilent 1200 series high performance liquid chromatography system coupled via an atmospheric pressure chemical ionization interface to an Agilent 6120 mass spectrometry (HPLC–APCI-MS), with a method slightly modified from Hopmans et al. (2000). The GDGTs were separated on a Prevail Cyano column (Grace, 3 $\mu$ m, 150mm x 2.1mm) maintained at a temperature of 30 °C. After injection of the sample on the column (20  $\mu$ L), the compounds were eluted isocratically in mobile phase A (hexane:2-propanol:chloroform; 98:1:1) at a flow rate of 0.2 mL min<sup>-1</sup>, followed by an increase with a linear gradient in the proportion of mobile phase B (hexane:2-propanol:chloroform; 89:10:1) to 10% within 20 min, and thereafter to 100% within 10 min.

The identification of the GDGTs was performed using single ion monitoring (SIM) as described by Schouten et al. (2007). The ion masses (m/z) monitored were 1050, 1048, 1046, 1036, 1034, 1032, 1022, 1020, 1018 for brGDGTs, 1292 for crenarchaeol and 744 for the C<sub>46</sub>-GDGT standard. Contents were calculated by comparing the peak areas of the GDGTs analyzed relative to the peak area of the internal standard (C<sub>46</sub>-GDGT). Due to the lack of appropriate standards, the individual response factors of the analyzed C<sub>86</sub>-GDGTs relative to the C<sub>46</sub>-GDGTs standard was not evaluated and the reported contents should be considered semi-quantitative.

### 4.3.3. Calculation of CBT, MBT' and BIT indices

The BIT index was calculated according to Hopmans et al. (2004), using the Equation 4-1 as follows:

$$\text{BIT} = \frac{\text{Ia} + \text{IIa} + \text{IIIa}}{\text{Ia} + \text{IIa} + \text{IIIa} + \text{cren}} \quad (4-1)$$

The CBT and the simplified MBT' indices were calculated according to Weijers et al. (2007) and Peterse et al. (2012), respectively, using the Equations 4-2 and 4-3, below:

$$\text{CBT} = -\log\left(\frac{\text{Ib} + \text{IIb}}{\text{Ia} + \text{IIa}}\right) \quad (4-2)$$

$$\text{MBT}' = \frac{\text{Ia} + \text{Ib} + \text{Ic}}{\text{Ia} + \text{Ib} + \text{Ic} + \text{IIa} + \text{IIb} + \text{IIc} + \text{IIIa}} \quad (4-3)$$

The calculation of pH and MAAT were performed based on the global soil calibrations proposed by Peterse et al. (2012), using Equations 4-4 and 4-5, respectively:

$$\text{pH} = 7.9 - 1.97 \times \text{CBT} \quad (4-4)$$

$$\text{MAAT} = 0.81 - 5.67 \times \text{CBT} + 31.0 \times \text{MBT}' \quad (4-5)$$

## 4.4. Results

### 4.4.1. GDGT distribution and BIT index

The bulk contents of total brGDGTs showed a geographic distribution similar to the total isoGDGTs (Ceccopieri et al., 2018) and to other lipid biomarkers analyzed in the Campos Basin sediments (Oliveira et al., 2013; Cordeiro et al., 2018). Higher contents of total brGDGTs were found in the slope samples in all transects and in the middle shelf samples of the CFUS region, which are areas where preferential accumulation of OM was already demonstrated (Oliveira et al., 2013; Albuquerque et al., 2014; Cordeiro et al., 2018).

Based on the sediment TOC contents reported by Cordeiro et al. (2018), the total brGDGTs contents varied from 5 to 30  $\mu\text{g gTOC}^{-1}$ , with a sharply decreasing gradient in contents from the coastal to deeper waters (Figure 4.3a). The relative contribution of the analyzed brGDGTs (Figure 4.4) showed that the isomers without cyclopentane rings in the structure (Ia, IIa and IIIa) are the most

abundant for almost all the samples. With a few exceptions, especially in the inner- and mid-shelf areas, the relative abundance of the isomers with no rings increased with distance from the coast. The content of crenarchaeol varied between 21 and 153  $\mu\text{g gTOC}^{-1}$  (Figure 4.3b) and higher values were measured in the Cabo Frio costal upwelling area and in the proximities of the Paraíba do Sul River mouth. BIT index values ranged from 0.07 to 0.20 with no clear bathymetric gradient and only the low values from the slope samples of transect A is noticeable (Figure 4.3c).

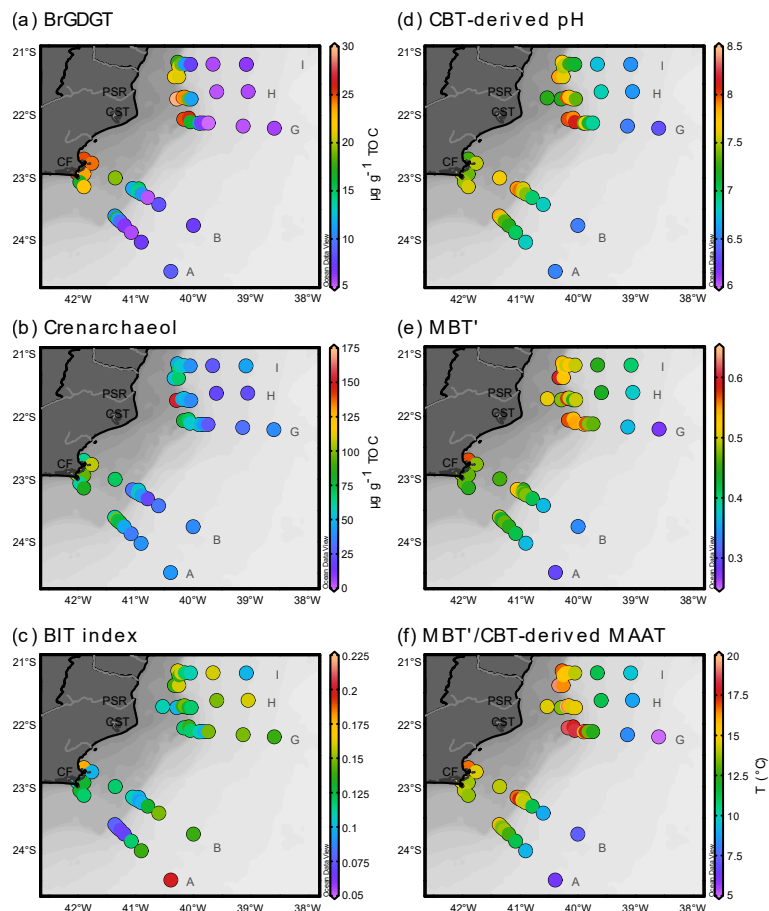


Figure 4.3: Contents of (a) total brGDGTs ( $\mu\text{g gTOC}^{-1}$ ), and (b) crenarchaeol ( $\mu\text{g gTOC}^{-1}$ ), (c) BIT index; (d) CBT-derived pH (Weijers et al., 2007b; Peterse et al., 2012), (e) MBT' (Peterse et al., 2012) and (f) MBT'/CBT derived MAAT in the Campos Basin surface sediments (Weijers et al., 2007b; Peterse et al., 2012). The total brGDGT and crenarchaeol normalized by the TOC were not determined in sample H1 because the TOC content of this sample was below quantification limit, but the contents in the sediment were comparable to sample H2 (Supplementary Table S4.1).

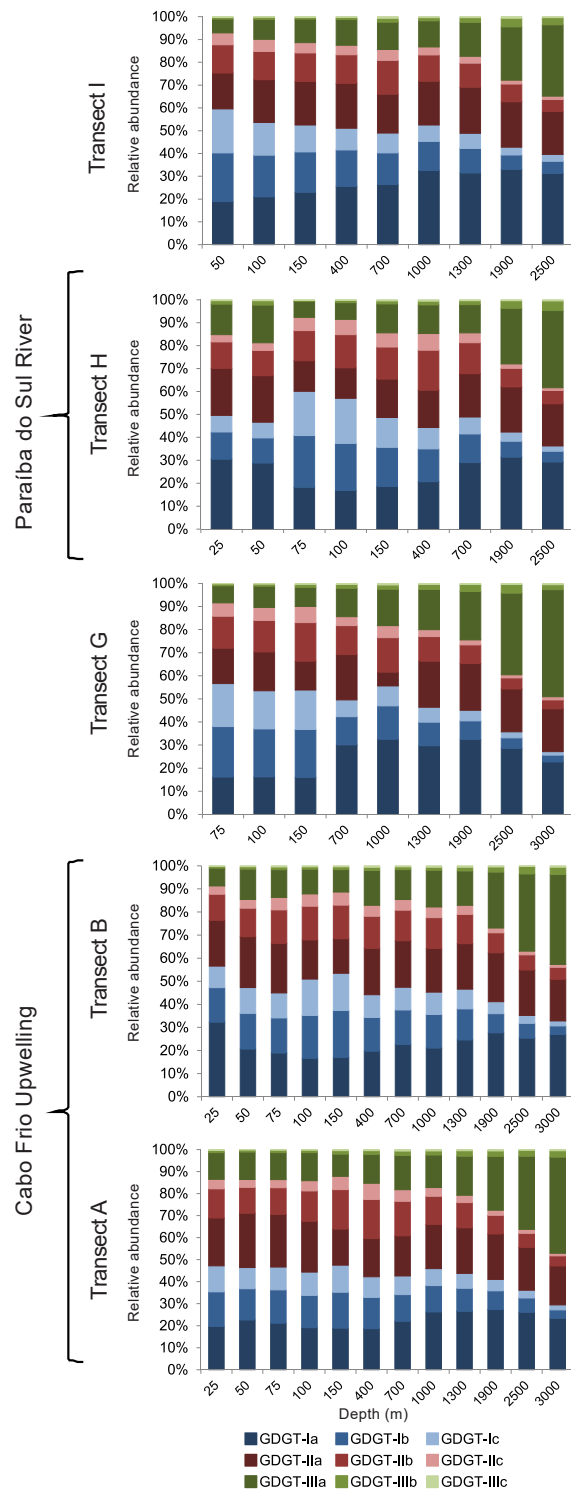


Figure 4.4: Relative abundance of the brGDGTs for each transect and sampling depth in the Campos Basin.

#### **4.4.2. CBT and MBT' indices**

The CBT values varied between  $-0.12$  and  $0.78$ , resulting in a CBT-based estimated pH range from  $6.4$  to  $8.1$  with an average of  $7.4 \pm 0.46$  (Figure 4.3d). The MBT' ranged from  $0.28$  to  $0.60$  (Figure 4.3e), resulting in MBT'/CBT-based estimated MAAT varying from  $5.0$  to  $19.9$  °C (Figure 4.3f) with an average of  $14.0 \pm 3.4$  °C. The lowest values for both pH and MAAT were found for the slope samples ( $> 400$  m depth) and the highest values are in the mid and outer shelf (75 to 150 m depth).

#### **4.5. Discussion**

##### **4.5.1. Sources and fate of GDGTs in the marine environment**

Because of their production in soils and further dilution with marine-derived material, a decreasing concentration gradient in brGDGTs is commonly observed along the river-estuary-coastal ocean continuum (Hopmans et al., 2004; Kim et al., 2006; Walsh et al., 2008; Zhu et al., 2011; Hu et al., 2012; Zell et al., 2014a, 2014b; Sinninghe Damsté, 2016). Consistent with this trend, the brGDGTs contents in the Campos Basin are higher in the inner shelf samples (depth  $< 75$  m) and gradually decrease towards deeper stations on the slope and rise in all transects (Figure 4.3a). Two samples with the highest brGDGTs contents are close to the Paraíba do Sul River mouth (25 and 50 m depths, transect H), which confirm the role of this river as the main source of these compounds to the Campos Basin. In addition, relatively high contents of brGDGTs were also found near the Cabo Frio coast (transects A and B). This is consistent with the potential transport of allochthonous OM from small rivers and the Paraíba do Sul River by coastal currents (Albuquerque et al., 2014).

Regarding the distribution of the brGDGTs isomers, a general trend of decreasing contribution of the isomers with one or two cyclopentane rings (i.e., Ib, IIb, IIIb and Ic, IIc and IIIc) can be seen in the upper slope samples (Figure 4.4). At deeper stations (1900-3000 m water depths), the no-cyclopentane moiety isomers (Ia, IIa and IIIa) represent more than 70% of the total brGDGTs. This suggests a higher relative rate of degradation of the brGDGTs with cyclopentane rings, which may be attributed to a lower stability of carbon bonds in the cyclic structure (Wiberg, 1986). Two samples enriched in brGDGTs close to the Paraíba do Sul

River mouth stand out (Supplementary Table S4.2), in which the acyclic compounds were the most abundant even at these shallow stations, possibly reflecting a local influence of the river discharge.

Our data also revealed in the mid- and outer shelf samples of all transects a predominance of cyclic over acyclic brGDGTs, especially for the II and III compounds, when compared to the river-influenced samples close to the Paraíba do Sul River (Figure 4.4). A higher abundance of cyclic brGDGTs in marine sediments, when compared to the counterpart distribution in fluvial sediments, has been attributed to *in situ* production of cyclic brGDGTs under elevated pH of marine waters (Peterse et al., 2009; Zhu et al., 2011; Hu et al., 2012; Zell et al., 2014b, 2014a; Sinninghe Damsté, 2016). Zell et al. (2014b) proposed an indicator of recent *in situ* marine production of cyclic brGDGTs based on marine samples from the Amazon shelf. Notwithstanding specific data for brGDGTs composition of fluvial sediments from the Paraíba do Sul River drainage basin are still lacking, our data suggest the same process of marine production of brGDGTs is also occurring in the shelf of the Campos Basin. On the other hand, further offshore, on the shelf-break and slope, the brGDGTs distribution is likely influenced by selective degradation of cyclic compounds, as suggested above.

Based on the relative distribution of brGDGT, the samples were divided in four groups (Figure 4.5) using Ward's hierarchical clustering method (Ward, 1963). The different groups and their spatial distribution agree with the previous description of the observed distributional pattern, as follows: group 1 is composed by the coastal upwelling samples of transect A and B, and by the inner-shelf samples of transect I; group 2 represents all the samples that contains a predominance of cyclic over acyclic brGDGTs and are probably affected by *in situ* production; group 3 is characterized by the samples that are more influenced by the riverine input; group 4 includes the slope and rise samples (>1900 m) that contain a predominance of non-cyclic brGDGTs because of a possible preferential degradation of the cyclic compounds with increasing distance from the coast.

The BIT index represents the ratio between the sum of Ia, IIa and IIIa branched compounds and crenarchaeol, and provides information on soil OM contributions to the marine sediments. The BIT is expected to be near 0 in sediments from the open ocean and near 1 in soils (Hopmans et al., 2004), and thus a decreasing trend in the BIT values is usually observed with distance from the river mouth (Hopmans et al., 2004; Zell et al., 2014a, 2014b; Sinninghe Damsté, 2016). The data for the Campos Basin showed no such trend, as all samples exhibited low (<0.20) BIT values (Figure 4.3c). Similar behavior was

observed in several systems (Herfort et al., 2006b; Schmidt et al., 2010; Fietz et al., 2011; Smith et al., 2012) and were attributed to a higher influence of *in situ* production of crenarchaeol than the continental input of brGDGTs upon the BIT values, which in turn limit the application of this index to trace soil organic carbon in the ocean. In fact, the TOC-normalized crenarchaeol contents are higher at the shelf stations of both the transects influenced by upwelling (A and B) and by the Paraíba do Sul River flow (H and I). This process is favored by aggregation of the small cells of Traumarchaeota with phytoplankton and other suspended matter (Wuchter et al., 2005; Huguet et al., 2006a, 2007a; Kim et al., 2008), which seems to also occur in our study region as discussed in a related previous paper (Ceccopieri et al., 2018). More data on the composition of brGDGTs in soil and river suspended particle is necessary to better constrain the limitation of the BIT index in the Campos basin.

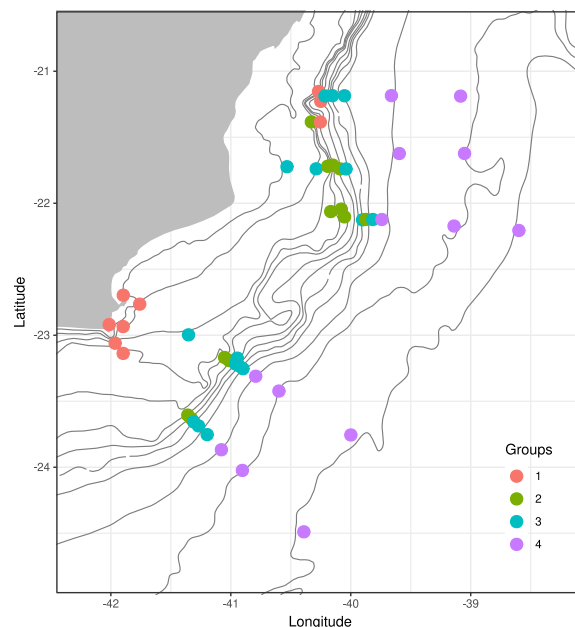


Figure 4.5: Distribution of groups using Ward's hierarchical cluster analysis based on the brGDGTs relative abundance. See text for details.

#### 4.5.2. Implications for CBT and MBT' indices in the Campos Basin sediments

The brGDGTs in the marine sediments were first assumed to represent an integrated signal of the entire river basin from where the soil brGDGTs derive (Weijers et al., 2007a). However, it has been shown that the reconstructed MAAT and soil pH can be biased towards a certain area and/or period of increased input

of brGDGTs to the river (Freymond et al., 2017). In addition, the hydrodynamics and microbial activity during fluvial transport might influence the distribution of brGDGTs along the river (Zell et al., 2013a, 2013b, 2014a, De Jonge et al., 2014b, 2016). These effects must be considered in the evaluation of whether or not the MBT'/CBT proxies reflect the MAAT and soil pH of the adjacent drainage basins.

The CBT-based pH values in the Campos Basin (6.4 to 8.1, Figure 4.3d) fit in the range of the topsoil pH measured along the Paraíba do Sul River, RJ and ES drainage basins (4.8 to 8.0, Figure 4.2e) for all the analyzed samples. The estimated pH of 7.2 for the samples H1 and H2, the nearest to the Paraíba do Sul River, seems to reflect the soil pH from the lower basin of this river. The magnitude of the Paraíba do Sul River flow and the associated transport of terrigenous/riverine materials is marked by a seasonal rainfall regime, with most of the precipitation measured in the summer in the middle-upper lands (Carvalho and Torres, 2002; Ovalle et al., 2013). Therefore, our data suggest that other factors, in addition to the flow regime, including erosional patterns along the river bank and intermediate storage of materials, may have a role on the final transport of terrigenous/riverine material along the Paraíba do Sul River drainage basin and final export to the coastal ocean. In addition, the evidences of *in situ* brGDGTs production affecting the samples clustered in the group 2 (Figure 4.5) also resulted in positive biased CBT-pH values.

The map of MBT'/CBT-based estimated MAAT for the Campos Basin shows a large range of values (5.0 to 19.9 °C; Figure 4.3f), which is not fully consistent with the instrumental MAAT available for the adjacent drainage basin (average = 20.7 °C; range = 9.3 and 24.1 °C; Figure 4.2c), but both negative and positive bias can be pointed out. Detailed comparison of such inconsistencies between estimated and instrumental MAAT is hindered because our analytical procedure does not separated the 5- and 6-methyl isomers of brGDGTs, which allows exclusion of potential production of riverine *in situ* brGDGTs and consequently reduce residual mean error of the global calibration for both the MAAT and pH (De Jonge et al., 2013, 2014a; Hopmans et al., 2016). Despite this limitation, a clear cross-shelf trend in the MBT'/CBT based values is observed, with MAAT estimates in the inner shelf samples (Figure 4.3f) with a lower bias compared to instrumental data (Figure 4.2e). Until more research is need to constrain the MBT'/CBT-based estimated MAAT, including collection of soil and river water samples in the catchment and the use of the new analytical protocol, our brGDGTs data and associated proxies provided useful information regarding

the transport and distribution of terrigenous biomarkers in the continental margin sediments of the studied region.

Finally, the MBT' and CBT proxies show an inverse gradient with distance from the coast (Supplementary Table S4.1), with the former slightly decreasing with depth whereas the latter increases abruptly seaward of the mid and outer shelf (>100 m depth). Schouten et al. (2013) compiled data from artificial maturation tests showing a similar trend with increasing water temperature, which was attributed to the lower stability of the brGDGTs containing cyclopentane moieties. Thus, distinct degradation rates among the groups of brGDGTs during the transport of OM in the river – shelf – deep ocean gradient may limit the applicability of the MBT' and CBT proxies with distance from the continental sources. This same effect was already previously observed for high latitude systems (Peterse et al., 2009) and our data support the same effect in sediments from a tropical – sub-tropical transition zone

#### **4.6. Conclusions**

The highest brGDGTs contents were found near the Paraíba do Sul River outflow, which confirms this river as the main source of soil brGDGTs to the study region. The BIT seems to be more strongly influenced by the contents of crenarchaeol rather than brGDGTs and no trend from coast to open ocean was observed, which limits the use of brGDGTs as proxy for input of soil organic carbon in the study region. The spatial heterogeneity observed for our brGDGTs highlights the existence of different sources and post-depositional effects that compromise the use of brGDGTs to reconstruct the soil pH and MAAT of the nearby land area.

Overall, our results show a strong variation in the estimated pH and MAAT along the cross-margin transects, which might be ascribed to selective degradation of the brGDGTs from the shallow to deep-waters as well as to *in situ* marine production of brGDGTs in the middle and outer shelf. Therefore, our data contribute to the general observation that the interpretation of brGDGTs-estimated MAAT and soil pH in marine sediments must consider the limitations of the proxies. Finally, analyses of soil and water samples from the Paraíba do Sul River drainage basin and the use of the new method to resolve the 5 and 6-methyl isomers could provide new insights of the possible *in situ* production of brGDGTs and contribute to a better understanding of the MBT'/CBT proxies' applicability to the region.

## Acknowledgements

The authors thank PETROBRAS (Brazilian Petroleum Company) for providing samples under the Habitats project. This study is funded in part by the Coordenação de Aperfeiçoamento de Pessoal de Nível Superior - Brasil (CAPES) - Finance Code 001. M. Ceccopieri thanks the National Council for Scientific and Technological Development (CNPq, grant 142451/2015-0), CAPES (grant PDSE 88881.134877/2016-01) and the German Academic Exchange Service (DAAD, short-term grant 2015/91591964) for her PhD scholarships. R. S. Carreira was supported by research fellowships from CNPq (grant 309347/2017-3) and CAPES (grant 88881.121009/2016-01). The research was partially funded by CNPq (process 402459/2012-1). Our thanks to Ralph Kreutz and Dr. Enno Schefuß (MARUM, University of Bremen) for assistance with the sediment extractions and to Prof. Carlos Massone for helping with the statistical analysis using software R.

## Chapter 5

### Holocene sea water temperature variations in the south-eastern Brazilian shelf inferred from organic proxies in sediments ( $U_{37}^{K'}$ , $TEX_{86}^H$ and LDI)

Milena Ceccopieri, Renato S. Carreira, Angela L. R. Wagener, Jens Hefter, Ana L. S. Albuquerque, Gesine Mollenhauer

*In preparation for Continental Shelf Research*

#### Abstract

A multi-proxy ( $U_{37}^{K'}$ ,  $TEX_{86}^H$  and LDI) approach using sediment cores from the shelf off Cabo Frio and Rio de Janeiro was considered to reconstruct the paleotemperature over the last 14.5 kyr off SE Brazil. The core-top estimates of temperature agree with the recent instrumental annual mean SST for two proxies ( $U_{37}^{K'}$  and LDI), whereas for  $TEX_{86}^H$  a negative bias was observed, especially in the Cabo Frio region. This disconformity in the  $TEX_{86}^H$  values seems to be related to the influence of upwelling and orthogonal intrusion of nutrient-rich and cold waters combined with subsurface habitat of Thaumarchaeota. Regarding the paleotemperature variation, the transition between mid- and late Holocene is well marked by a warming in SST- $U_{37}^{K'}$  and SST-LDI, probably related to a more intense Brazil Current (BC) activity over the shelf, whereas temp- $TEX_{86}^H$  showed an opposite cooling trend that may be a result of the subsurface upwelling of the cold South Atlantic Central Waters. The core off Rio de Janeiro presents a distinct phase before 7.5 cal kyr BP that is consistent with low sea level stands in the early Holocene. A decrease in reconstructed temperatures after ca 2.5 cal kyr BP in both records may be explained by the upwelling enhancement, more pronounced in Cabo Frio. Differences in the reconstructed temperatures between the two cores are observed, probably related to the local instabilities of the BC near de Cabo Frio upwelling system region. Notwithstanding, for the entire covered period in both sediment cores, SST-LDI correlate better with summer temperatures, SST- $TEX_{86}^H$  is clearly biased towards subsurface temperatures and SST- $U_{37}^{K'}$  was more affected by the sea level variations and/or the BC flow. Oscillations in SST- $TEX_{86}^H$  may be related to variations in the thermocline depth. Our data showed the influence of thermal and non-thermal effects upon performance of each paleotemperature proxy and these factors must be considered when using the same approach in other continental margins with similar influence as those observed in the SE Brazil shelf.

## 5.1. Introduction

All the temperature proxies have uncertainties that could affect the interpretation of the results. Although they are calibrated against annual mean SST using core top sediments, several studies observed biases that might be related to different seasonal production and/or depth habitats of the source organisms (e.g., Ternois et al., 1997; Herfort et al., 2006a; Leider et al., 2010; Prahl et al., 2010; Chen et al., 2014; Ceccopieri et al., 2018). For example, in a sediment core from the Murray Canyon (southeast Australia), Lopes dos Santos et al. (2013) observed a better agreement of LDI with the austral summer SST and  $\text{TEX}_{86}^{\text{H}}$  with the austral winter SST, while the  $\text{U}_{37}^{\text{K}'}$  better reflects the annual mean SST. In terms of the source depth, previous studies suggest that GDGTs are mainly exported to the sediments from subsurface waters rather than surface waters, as the  $\text{TEX}_{86}$ -based temperatures are more related to the temperatures measured between 40 and 150 m depth in the water column, usually at the chlorophyll maximum or the thermocline depths (Karner et al., 2001; Wuchter et al., 2005; Huguet et al., 2007a; Lee et al., 2008; Lopes dos Santos et al., 2010; Chen et al., 2014). The input of terrigenous organic material containing isoGDGTs can also bias the  $\text{TEX}_{86}$  signal on continental shelves under the influence of river discharge (Weijers et al., 2006b). The Branched and Isoprenoid Tetraether (BIT) index, proposed by Hopmans et al. (2004) to determine the relative contributions of soil organic matter in the marine environment, is commonly applied to evaluate potential  $\text{TEX}_{86}$  biases caused by terrigenous isoGDGT contributions. This BIT index can be close to 0 in sediments from the open ocean and near 1 in inner continental systems (Hopmans et al., 2004), as it relies on previous observations that brGDGTs are generally attributed to soil bacteria, while crenarchaeol would be the dominant GDGT in the marine environment. The application of multiple proxies to the same samples can bring more information regarding these biases and lead to the achievement of a more accurate paleotemperature reconstruction in a particular region (Lopes dos Santos et al., 2013; Becker et al., 2015; Rodrigo-Gámiz et al., 2015; Jonas et al., 2017). Moreover, the differences between the proxies can reveal additional paleoceanographic information.

Despite the recent increase in the number of paleoclimatic studies in the South Atlantic, the scarcity of high resolution records for the Holocene in comparison with the North Atlantic, especially in the western margin, leads to uncertainties about the events that marked the subtropical southwest Atlantic

variability during this period (Mahiques et al., 2007; Pivel et al., 2013; Lessa et al., 2016). SST anomalies during the Holocene can be related to variations in the strengthening of the Atlantic meridional overturning circulation (AMOC), to the dynamics of the South Atlantic Convergence Zone (SACZ), to the South American monsoon system (SAMS) and, hence, on the climate of south-eastern South America (Chiessi et al., 2014). Overall, the climate during the Holocene over the southeastern South America seems to have oscillated between periods of higher and lower humidity conditions (Mahiques et al., 2007; Cordeiro et al., 2008; Bender et al., 2013; Prado et al., 2013b; Wainer et al., 2014).

In the studied region, data obtained from foraminifera (Pivel et al., 2013; Chiessi et al., 2014; Lessa et al., 2014, 2016) and alkenones (Mahiques et al., 2005; Rühlemann and Butzin, 2006; Magalhães, 2010; Cordeiro et al., 2014; Evangelista et al., 2014) have been previously used in paleoclimatic studies. No information for GDGTs and long-chain diol in the same region is available. Here, we considered a multiproxy approach in two sediment cores retrieved off the Cabo Frio upwelling system (CFUS) and Rio de Janeiro shelves to reconstruct the paleotemperature during the last 14.5 kyr. The main goals were to investigate how each independent organic proxy ( $U_{37}^{K'}$ ,  $TEX_{86}^H$  and LDI) is affected by the local environmental conditions in these two different areas, compare with pre-existing data from both sediment cores (Lessa et al., 2016; Lazzari et al., 2018) and contribute to paleoceanographic and paleoclimatic studies in the south-western Atlantic.

## **5.2. Study area and oceanographic settings**

The Cabo Frio and Rio de Janeiro continental shelves are located in the northernmost portion of the south-eastern Brazilian continental margin (Figure 5.1) that extends from Cabo de Santa Marta in the south (28° 30' S, 49°00' W) to Cabo Frio in the north (23° 00' S, 42° 00' W). The continental shelf width in this sector varies from 73 to 231 km, with slope ratios between 1:656 and 1:1333 (Mahiques et al., 2004). The current system in the shelf is determined by the flow of the BC towards the south (Peterson and Stramma, 1991). The BC has a total thickness of 400-500 m and transport the nutrient-poor Tropical Water (TW,  $T > 20$  °C;  $S > 36$ ; core depth at 20 m depth) and the nutrient-rich South Atlantic Central Water (SACW,  $T = 6-20$  °C,  $S = 34.6-36$ ; core depth at 300 m) (Silveira et al., 2017).

In response to morphology and bathymetric variations along the coast, meandering and eddies of the BC are observed in the study region, causing the SACW intrusion onto the mid-shelf and shelf-break (Campos et al., 2000; Silveira et al., 2000). In addition, in the Cabo Frio region, an abrupt change in the coastline orientation associated with prevailing NE winds induces the intermittent coastal upwelling of SACW, which is more pronounced during the austral summer (Rodrigues and Lorenzetti, 2001; Castelao and Barth, 2006; Franchito et al., 2008). This period also corresponds to the rainy season in southeast Brazil and, consequently, to an increase in the flow of continental material to the coastal waters (Mahiques et al., 2004). The upwelled SACW – both near the coast and/or in the mid-shelf and shelf break – and its associated nutrients enhance the rates of primary production in these localities to  $>0.5 \text{ gC m}^{-2} \text{ d}^{-1}$ , which contrasts with the overall oligotrophic conditions ( $<0.04 \text{ gC m}^{-2} \text{ d}^{-1}$ ) observed along the southeastern Brazilian continental margin (Brandini et al., 2018 and references therein). Under fertilized conditions caused by SACW upwelling, the export of biomass to the oligotrophic adjacent continental shelf and offshore areas is observed (Lorenzetti and Gaeta, 1996; Marone et al., 2010).

The dynamics of sediment transport and accumulation on the shelf is coupled to bottom topography and hydrodynamic fronts, like the BC meandering, resulting in a complex and heterogeneous array of sedimentary provinces over the shelf and slope (Mahiques et al., 2002 and references therein). The sedimentation rates recorded in these distinct sedimentary provinces also varies largely, ranging from ca  $5 \text{ mm kyr}^{-1}$  on the lower slope up to  $184 \text{ mm kyr}^{-1}$  in the vicinity of the CFUS (Mahiques et al., 2002). The flow of the Paraíba do Sul River, located to the north of our study sites (Figure 5.1), is the main source of continental material in the region, but other smaller rivers also have to be considered (Razik et al., 2015). The terrestrial material delivered by these rivers is transported to the south and reaches the location of our cores (Gyllencreutz et al., 2010; Albuquerque et al., 2014). In addition, the Guanabara Bay may also contribute with dissolved and particulate matter to the shelf (Albuquerque et al., 2014). The modern surface sediment in this sector is composed of very thin siliciclastic sands and silts, while coarser sediments and carbonate gravel are generally derived from sediments deposited under low sea level conditions (Mahiques et al., 2002 and references therein).

The two cores were collected in two areas of fine sediment accumulation around the 100 m isobath between 23 and 23.5 °S (Figure 5.1). The core CF10-09A (117 m water depth) is representative of a large deposit of muddy sediments

near the CFUS. This deposit has been extensively studied in the last years with respect to the major physical and biogeochemical processes responsible for the accumulation of OM over the Holocene (Gyllencreutz et al., 2010; Souto et al., 2011; Cruz et al., 2013; Mendoza et al., 2014; Lessa et al., 2016), including past SST estimates using alkenones (Mahiques et al., 2005; Cordeiro et al., 2014; Evangelista et al., 2014; Lourenço et al., 2017b). The core RJ13-01C represents another muddy deposit – apparently not connected to that of CFUS – that extends as a relatively narrow belt along the 100 m isobath to the west (Figure 5.1). Information about the OM accumulation in this second mud belt is available to modern or very recently deposited sediments (Carreira et al., 2012; Lourenço et al., 2017a).

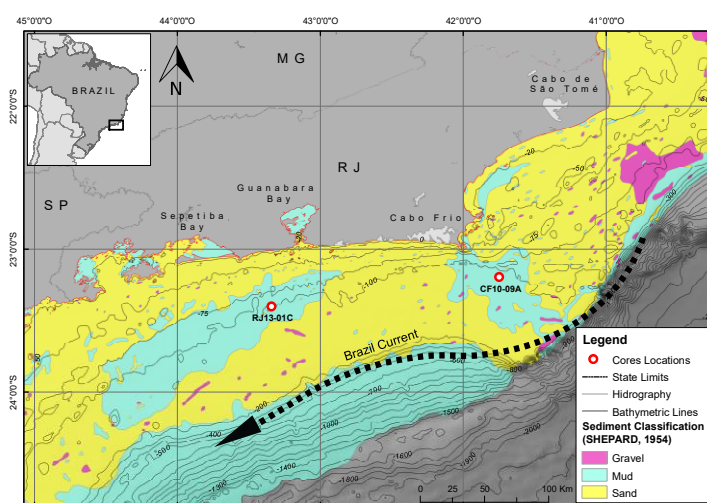


Figure 5.1: Map with location of the sediment core sampling stations and grain size of the surface sediments in the south-eastern Brazilian margin (unpublished sediment grain size data provided by Alberto Figueiredo, personal communication; designed by João R. dos Santos Filho).

### 5.3. Material and methods

#### 5.3.1. Sampling and geochronology

The sediment core RJ13-01C (23.40° S, 43.34° W, Figure 5.1), with 160 cm length, was recovered from the mid-shelf off Rio de Janeiro city, at 100 m depth onboard of the Brazilian Navy Vessel AV.Pq.Oc. Diadorim in December 2013. The geochronology was determined by Lazzari et al. (2018). The  $^{14}\text{C}$  dates in planktonic foraminifera (*Globigerinoides ruber*) from 4 samples were determined by

accelerator mass spectrometry (AMS). The conventional  $^{14}\text{C}$  ages were calibrated using the OxCal program (Ramsey and Lee, 2013) and the Marine13 curve (Reimer et al., 2013). The reservoir effect ( $\Delta R$ ) considered for the region was  $-127 \pm 67$  years (Macario et al., 2015). For the first centimeters of the RJ13-01C core,  $^{210}\text{Pb}$  dating was also performed by the gamma spectrometry method using a high purity germanium detector.

The sediment core CF10-09A, which is 403 cm long, was collected on the Cabo Frio continental shelf ( $23.20^\circ \text{ S}$ ,  $41.74^\circ \text{ W}$ , Figure 5.1) at 117 m water depth using the Ocean Surveyor vessel in January 2010. The geochronology of the core was determined and described in details by Lessa et al. (2016). In summary, it was performed by quantification of  $^{14}\text{C}$  in organic matter from 13 samples by AMS and the ages obtained were calibrated using the Clam software (Blaauw, 2010) and the Marine09 curve (Reimer et al., 2009). The  $\Delta R$  considered for the region was  $8 \pm 17$  years (Angulo et al., 2005).

### 5.3.2. Total organic carbon (TOC) and $\delta^{13}\text{C}$ analyses

The sediments were freeze-dried and weighed ( $10 \pm 0.1$  mg for TOC and  $0.5 \pm 0.01$  mg for  $\delta^{13}\text{C}$ ) directly in silver capsules. Carbonates were removed by acid treatment (HCl 0,1 M) and heating ( $100^\circ \text{ C}/6$  h). The contents of TOC (%) were determined in an organic elemental analyzer (Flash 2000, Thermo). Calibration was based on a calibration curve of aspartic acid (C = 39.09 %). An intermediate amount of the aspartic acid standard (0.2 mg) was analyzed as an unknown sample throughout the sequence for every 10 samples to monitor the calibration. The instrumental accuracy was verified using the NIST 1941B standard (Organics in Marine Sediments). The results of triplicate analyses in each sequence was  $3.07 \pm 0.05$  %, comparable to the certified value ( $2.99 \pm 0.24$  %). Replicate analyses of selected samples (27 in duplicate and 8 in triplicate from a total of 174 analyses) revealed an analytical precision of  $\pm 0.03\%$  of TOC.

The  $\delta^{13}\text{C}$  of the bulk OM for sediment core RJ13-01C was determined using isotope ratio mass spectrometry (Flash 2000 model OEA coupled to a Delta V IRMS, Thermo). Three pulses of the reference gas ( $\text{CO}_2$ ), previously calibrated with the IAEA USGS40 standard material, were introduced at the beginning of each analysis. The  $\delta^{13}\text{C}$  was calculated according to the value of the third pulse. The  $\delta^{13}\text{C}$  values are reported as the average of two injections. Only values that showed a standard deviation of less than 0.3‰ were accepted. The  $\delta^{13}\text{C}$  values for

sediment core CF10-09A were provided by Ana L. S. Albuquerque (personal communication).

### 5.3.3. Lipid extraction and separation

An aliquot of 5 g ( $\pm 0.001$  g) of freeze-dried and homogenized sediment was extracted for the core CF10-09A, whereas for the RJ13-01C core a higher mass of sediment was necessary, because of the low TOC contents of these samples: 10 g ( $\pm 0.001$  g) from the top down to 99 cm, and 30 g ( $\pm 0.001$  g) for the samples from 101 to 160 cm in the core. Sediments were extracted by an accelerated solvent extraction system (ASE 200, Dionex) with a mixture of dichloromethane:methanol (9:1, v:v) at a temperature of 100 °C and a pressure of 1000 psi. Before extraction, known amounts of C<sub>19</sub>-ketone and C<sub>46</sub>-GDGT were added as internal standards. The bulk extracts were concentrated by rotary evaporation and saponified for 2h at 80 °C with 1 mL of KOH (0.1 M) in methanol:H<sub>2</sub>O (9:1; v:v). Neutral lipids were recovered in hexane and further fractionated using silica gel column chromatography as follows: *n*-alkane fraction using hexane (stored); alkenone fraction using dichloromethane:hexane, 2:1 (v:v); and the polar fraction, containing the GDGTs and long chain diols, using dichloromethane:methanol, 1:1 (v:v). The fractions were dried under a stream of nitrogen at 40 °C. The alkenone fraction was re-dissolved in hexane and analyzed by gas chromatography with a flame ionization detector (GC-FID). The polar fraction was filtered using a 0.45  $\mu$ m PTFE filter, weighed, and re-dissolved in *n*-hexane:isopropanol 99:1 (v:v) to a final concentration of 2 mg mL<sup>-1</sup> (Schouten et al., 2013a) for further analysis of the GDGTs by high performance liquid chromatography-atmospheric pressure chemical ionization-mass spectrometry (HPLC-APCI-MS). After the GDGT analyses, the remaining polar fraction was dried and derivatized for the analysis of the long chain diols using gas chromatography–time of flight mass spectrometry (GC-TOF-MS).

### 5.3.4. Alkenone analysis and U<sub>37</sub><sup>K'</sup> index

The alkenone analyses were performed on an Agilent model 6870 GC-FID system, using the following conditions: (i) He as carrier gas at a flow rate of 2.0 mL min<sup>-1</sup>; (ii) initial oven temperature at 60 °C and hold of 1 min; temperature ramp of 20 °C min<sup>-1</sup> up to 150 °C and then of 6 °C min<sup>-1</sup> up to 320 °C, with a final hold of

35 min at this temperature. The di- and tri-unsaturated C<sub>37</sub> alkenones (C<sub>37:2</sub> and C<sub>37:3</sub>) were identified based on the retention times of a reference standard and quantified by peak integration relative to the internal standard C<sub>19</sub>-ketone, which was also used to evaluate the recovery of the method.

The  $U_{37}^{K'}$  was calculated using the equation described by Prahl and Wakeham (1987, Equation 5-1) and SST values were estimated using the global core top calibration of Müller et al. (1998, Equation 5-2) for tropical to subpolar eastern South Atlantic:

$$U_{37}^{K'} = \frac{(C_{37:2})}{(C_{37:2})+(C_{37:3})} \quad (5-1)$$

$$SST = \frac{U_{37}^{K'} - 0.069}{0.033} \quad (5-2)$$

### 5.3.5. GDGT analysis, TEX<sub>86</sub><sup>H</sup> and BIT indices

GDGTs were analyzed on an Agilent 1200 series HPLC system coupled via APCI to a single quadrupole mass spectrometer (Agilent 6120 MSD), using a method slightly modified from Hopmans et al. (2000). Separation was achieved on a Prevail Cyano column (Grace, 3 μm, 150 mm x 2.1 mm) at a temperature of 30 °C. After injection of the sample (20 μL) on the column and a 5 min isocratic elution with mobile phase A (hexane:2-propanol:chloroform; 98:1:1) at a flow rate of 0.2 mL min<sup>-1</sup>, the proportion of mobile phase B (hexane:2-propanol:chloroform; 89:10:1) was increased in a linear gradient to 10% within 20 min, and thereafter to 100% within 10 min. After each analysis, the column was cleaned by back flushing for 5 min at a flow of 0.6 mL min<sup>-1</sup> and re-equilibrated with solvent A (10 min, flow 0.2 mL min<sup>-1</sup>).

The identification of GDGTs was performed using single ion monitoring (SIM) as described by Schouten et al. (2007). The ions (*m/z*) monitored were 1302, 1300, 1298, 1296, 1292 for isoprenoid GDGTs (isoGDGTs), 1050, 1036, 1022 for branched GDGTs (brGDGTs) and 744 for the C<sub>46</sub>-GDGT standard. Concentrations were calculated relative to the peak area of the internal standard (C<sub>46</sub>-GDGT). The lack of appropriate standards hampered the evaluation of individual response factors of the different C<sub>36</sub>-GDGTs relative to the C<sub>46</sub>-GDGT standard, therefore reported concentrations should be considered semi-quantitative.

TEX<sub>86</sub> and BIT proxies are calculated according to Schouten et al. (2002, Equation 5-3) and Hopmans et al. (2004, Equation 5-4), respectively.

$$\text{TEX}_{86} = \frac{\text{iGDGT-2} + \text{iGDGT-3} + \text{cren}'}{\text{iGDGT-1} + \text{iGDGT-2} + \text{iGDGT-3} + \text{cren}'} \quad (5-3)$$

$$\text{BIT} = \frac{\text{bGDGT-I} + \text{bGDGT-II} + \text{bGDGT-III}}{\text{bGDGT-I} + \text{bGDGT-II} + \text{bGDGT-III} + \text{cren}} \quad (5-4)$$

$\text{TEX}_{86}$  values were converted to SST estimates using the calibrations (Equations 5-5 and 5-6) proposed by Kim et al. (2010) for high temperatures (from 5 to 30 °C):

$$\text{TEX}_{86}^{\text{H}} = \log(\text{TEX}_{86}) \quad (5-5)$$

$$T \text{ (}^\circ\text{C)} = 38.6 + 68.4 (\text{TEX}_{86}^{\text{H}}) \quad (5-6)$$

### 5.3.6. Long-chain diol analysis and LDI index

The identification of the long-chain diols was conducted on a GC-TOF-MS system consisting of a Leco Pegasus III (Leco Corp., St. Joseph, MI) interfaced to an Agilent model 6890 GC, equipped with a Restek Rtx-1MS column (10 m x 0.25 mm x 0.14  $\mu\text{m}$ ) with a 5 m integrated pre-column, using the conditions described by Hefter (2008), as follows: (i) He as carrier gas at a flow rate of 0.8  $\text{mL min}^{-1}$ ; (ii) GC oven initially held at 60 °C for 1 min, and then heated at a temperature ramp of 50  $^\circ\text{C min}^{-1}$  up to 250 °C and then of 30  $^\circ\text{C min}^{-1}$  up to 310 °C, with a final hold of 2 min at this temperature, resulting in an analysis time of 8.8 min. The electron impact ion source is operated at a temperature of 220 °C and is connected to the GC by a heated transfer line set to 280 °C. The pressure in the flight tube of the TOF-MS was  $2 \times 10^{-7}$  Torr. The compounds were identified using characteristic fragment ions (Versteegh et al., 1997):  $m/z$  299 ( $\text{C}_{28:0}$  1,14-diol), 313 ( $\text{C}_{28:0}$  1,13- and  $\text{C}_{30:0}$  1,15-diols), 327 ( $\text{C}_{28:0}$  1,12-,  $\text{C}_{30:1}$  and  $\text{C}_{30:0}$  1,14-diols) and 341 ( $\text{C}_{30:0}$  1,13-diol). The relative abundance among the diols was determined by integration of the chromatographic peaks. Since no specific internal standard was added, the long chain diols results were only used in the temperature reconstruction.

The LDI index was calculated (Equation 5-7) and converted to SST (Equation 5-8) using the calibration described by Rampen et al. (2012).

$$\text{LDI} = \frac{(\text{C}_{30:0} 1,15\text{-diol})}{(\text{C}_{30:0} 1,15\text{-diol}) + (\text{C}_{28:0} 1,13\text{-diol}) + (\text{C}_{30:0} 1,13\text{-diol})} \quad (5-7)$$

$$\text{SST (}^\circ\text{C)} = \frac{\text{LDI} - 0.095}{0.033} \quad (5-8)$$

## 5.4. Results

### 5.4.1. Core RJ13-01C, off Rio de Janeiro shelf

Figure 5.2 presents the variation of the dataset obtained for the core RJ13-01C, covering the last 14.5 cal kyr BP. In this figure, three depositional periods as proposed by Lazzari et al. (2018) can be seen.

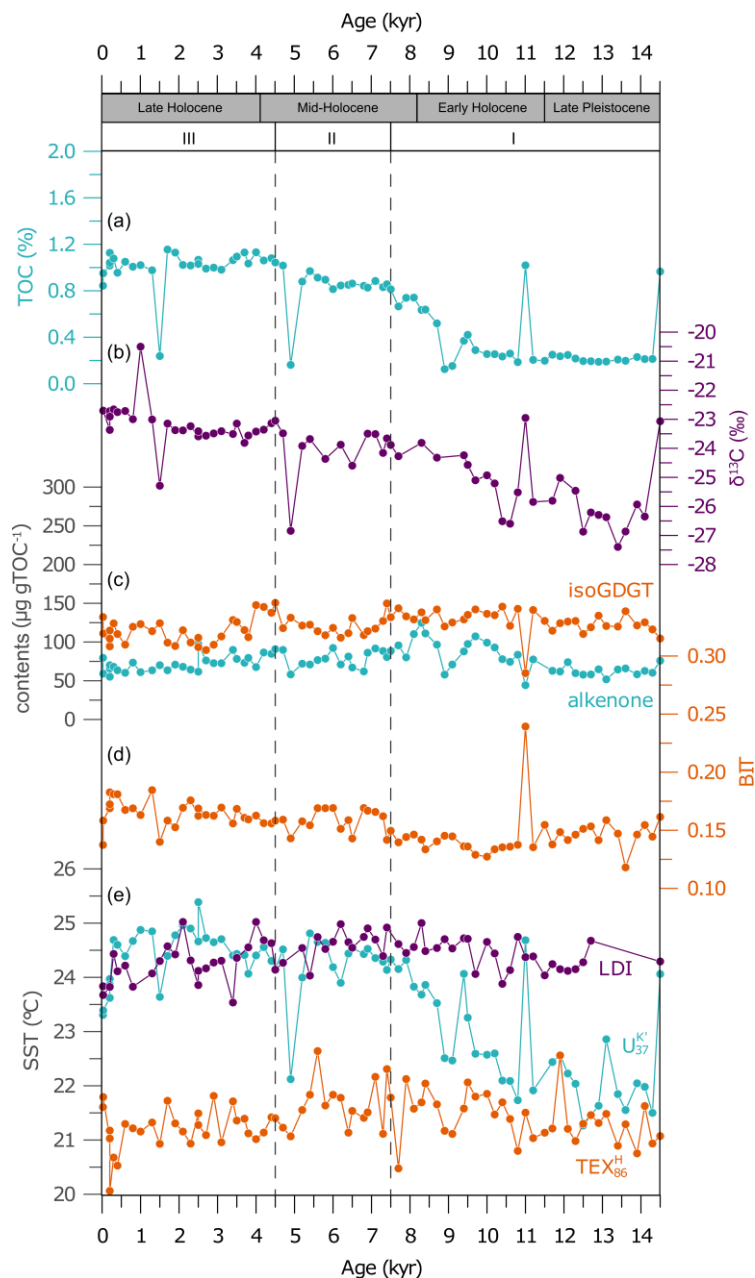


Figure 5.2: Variation in the (a) TOC (%); (b) bulk  $\delta^{13}\text{C}$  (‰); (c) total isoGDGT and total alkenone contents ( $\mu\text{g gTOC}^{-1}$ ); (d) BIT index; and (e) temperature estimates based on  $U_{37}^K$ ,  $TEX_{86}^H$  and LDI ( $^{\circ}\text{C}$ ) along the RJ13-01C core. The vertical dashed lines represent the depositional phases as proposed by Lazzari et al. (2018), based on sedimentary processes, geochemical and geophysical properties.

#### 5.4.1.1. Total organic carbon and bulk $\delta^{13}\text{C}$

The TOC averaged  $0.70 \pm 0.36$  %, with a range from 0.13 % to 1.15 %. The TOC profile is marked by relatively constant TOC of  $\sim 0.2$  % from 14.3 to 11.2 kyr BP, followed by a rise up to 1.13 % TOC at 4.0 kyr BP, with a stabilization at these level until the present (Figure 5.2a). Abrupt changes in the TOC profile can also be seen, like the rise at 11.0 cal kyr BP and three drops at 8.9-9.1 cal kyr BP, 4.9 cal kyr BP and 1.5 cal kyr BP.

The profile of  $\delta^{13}\text{C}$  (Figure 5.2b) in this core is marked by a narrow range of values from  $-25.0$  to  $-27.4$  ‰ in the period from 14.3 to 11.2 cal kyr BP, matching with the period of low and constant values of TOC (see above). After 10.8 cal kyr BP, the  $\delta^{13}\text{C}$  constantly increased to more positive values, around  $-23$  ‰ in the late Holocene. Finally, the  $\delta^{13}\text{C}$  profile also exhibited abrupt changes, with values 2 or 3 ‰ above or below the general trend. As will be discussed in detail later, most of these abrupt changes in the  $\delta^{13}\text{C}$  are coincident with the TOC changes.

#### 5.4.1.2. Alkenone contents and $U_{37}^{K'}$ temperature estimates

The TOC-normalized contents of total alkenones (sum of  $C_{37:2}$  and  $C_{37:3}$ ) ranged from 44 to 125  $\mu\text{g gTOC}^{-1}$ , with a mean of  $75 \pm 15$   $\mu\text{g gTOC}^{-1}$  (Figure 5.2c). The maximum and minimum values in the alkenone profile were measured in abrupt 'events', in the same dates as mentioned for the TOC and  $\delta^{13}\text{C}$  distributions in 11.0 cal kyr BP, 8.9 cal kyr BP and 4.9 cal kyr BP. The highest contents of 107 and 125  $\mu\text{g gTOC}^{-1}$  are found in early Holocene, at 9.7 cal kyr BP and 8.3 cal kyr BP, respectively.

The calculated  $U_{37}^{K'}$  values resulted in estimated temperatures ranging from 21.3 °C to 25.4 °C (Figure 5.2e). During the late Pleistocene and early Holocene (14.3 to  $\sim 8.0$  kyr BP), the SST- $U_{37}^{K'}$  increased from 21.5 °C to around 24.5 °C. In the late Holocene (4.2 kyr BP to the present), the mean SST- $U_{37}^{K'}$  averaged above 24.5 °C. All over the profile of SST- $U_{37}^{K'}$ , several temperature excursions to positive values before 10.0 cal kyr BP and three abrupt cooling events at 9.1 cal kyr BP, 4.9 cal kyr BP and 1.5 cal kyr BP, can be observed.

### 5.4.1.3.

#### GDGT contents, $\text{TEX}_{86}^{\text{H}}$ temperature estimates and BIT index

The TOC-normalized total contents of isoGDGTs varied from 60 to 151  $\mu\text{g gTOC}^{-1}$ , with a mean of  $121 \pm 16 \mu\text{g gTOC}^{-1}$  (Figure 5.2c). Overall, this profile resembles that of the total alkenones, including an abrupt drop to  $60 \mu\text{g gTOC}^{-1}$  observed at 11.0 cal kyr BP.

The BIT index varied from 0.12 to 0.24, with an average of  $0.15 \pm 0.02$  (Figure 5.2d). These values suggest a relatively low contribution of soil OM over the entire core that may be considered not to interfere with the  $\text{TEX}_{86}^{\text{H}}$  marine signal (Hopmans et al., 2004). The variation is very slight over the entire period analyzed, except for a decrease at 13.6 cal kyr BP and a relatively high value found at 11.0 cal kyr BP.

The depth profile of  $\text{TEX}_{86}^{\text{H}}$ -based temperature estimates varied from 20.1 to 22.6 °C, a much smaller range than the  $\text{SST-U}_{37}^{\text{K}'}$  (Figure 5.2e). Highest  $\text{TEX}_{86}^{\text{H}}$  are found at 11.9 cal kyr BP and 5.6 cal kyr BP. The lowest values are found at 7.7 cal kyr BP and 0.2 cal kyr BP.  $\text{Temp-TEX}_{86}^{\text{H}}$  are very similar to  $\text{U}_{37}^{\text{K}'}$  estimates during the late Pleistocene and the early Holocene, but the values didn't follow the  $\text{U}_{37}^{\text{K}'}$  increase starting in the mid Holocene to the present, and an up to 4.1 °C lower  $\text{TEX}_{86}^{\text{H}}$  than  $\text{U}_{37}^{\text{K}'}$  estimates were obtained.

### 5.4.1.4.

#### LDI temperature estimates

From the 78 samples from core RJ13-01C, 65 contained sufficient long chain diols that allowed obtaining a LDI-based temperature estimate (Supplementary Table S5.2). The  $\text{SST-LDI}$  varied from 23.5 to 25.0 °C, with a mean of  $24.4 \pm 0.3 \text{ °C}$  (Figure 5.2e). The LDI values are consistently higher than the  $\text{U}_{37}^{\text{K}'}$  before 8.0 ky BP and at least 2-3 °C higher than the  $\text{TEX}_{86}^{\text{H}}$  over the period covered by the core RJ13-01C.

## 5.4.2. Core CF10-09A, off Cabo Frio shelf

Figure 5.3 presents the variation of the dataset obtained for the core CF10-09A, covering the period from 7.1 to 1.1 cal kyr BP. In this figure, four depositional periods as proposed by Lessa et al. (2016) can be seen.

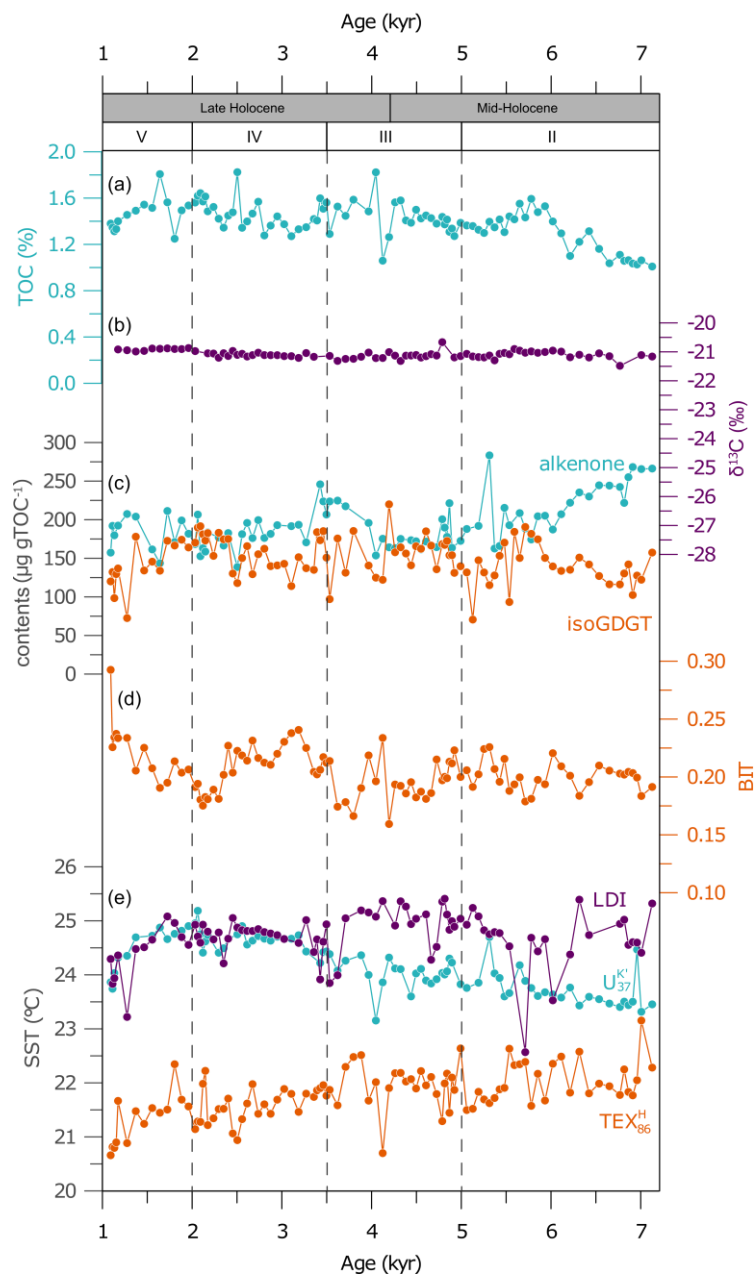


Figure 5.3: Variation in the (a) TOC (%); (b) bulk  $\delta^{13}\text{C}$  (‰) (Ana L. S. Albuquerque, personal communication); (c) total isoGDGT and total alkenone contents ( $\mu\text{g gTOC}^{-1}$ ); (d) BIT index; and (e) temperature estimates based on  $U_{37}^K$ ,  $\text{TEX}_{86}^H$  and LDI ( $^{\circ}\text{C}$ ) along the CF10-09A core. The vertical dashed lines represent the depositional phases as proposed by Lessa et al. (2016) based on planktonic foraminifera.

#### 5.4.2.1. Total organic carbon and bulk $\delta^{13}\text{C}$

The TOC contents of the core CF10-09A varied from 1.01 % to 1.82 %, with a mean of  $1.40 \pm 0.17$  % (Figure 5.3a). The TOC contents in this core, located in the core of the Cabo Frio upwelling system, were higher than those measured off

Rio de Janeiro (Figure 5.2a). An increase in the TOC contents between 7.1 and ~6 cal kyr BP was observed during Unit II in this core, reaching values around 1.5 %, and a slight decrease to 1.3% was measured in the most recent sediment layers. Finally, superimposed on the general trend at least two abrupt changes in TOC contents during the late Holocene are evident.

The  $\delta^{13}\text{C}$  of the bulk OM ranges between  $-21.5$  and  $-20.7$  ‰ in the core CF10-09A (Figure 5.3b). Therefore, the shelf sediments in the Cabo Frio region are enriched in  $^{13}\text{C}$  compared to those off Rio, core RJ13-01C (Figure 5.2b).

#### 5.4.2.2.

#### **Alkenones contents and $U_{37}^{K'}$ temperature estimates**

The total alkenones varied from 139 to 283  $\mu\text{g gTOC}^{-1}$ . The highest contents are observed between 7.1 and ~6 cal kyr BP, with values around 250  $\mu\text{g gTOC}^{-1}$  (Figure 5.3c). The total alkenones gradually decrease until around 4 cal kyr BP, with an abrupt change in 5.31 cal kyr BP. In the period between 4.0 and 3.4 cal kyr BP there is an increase in the total alkenone content, but after that there is little variation up to the present.

The  $U_{37}^{K'}$ -based temperature estimates ranged from 23.1 °C to 25.2 °C. From 7.1 cal kyr BP to 5.2 cal kyr BP, the SST- $U_{37}^{K'}$  variation is very similar to the total contents of alkenones (Figure 5.3e). An abrupt decrease to 23.1 °C can be later observed at 4.0 cal kyr BP. In general, the SST- $U_{37}^{K'}$  seems to increase until its maximum in the late Holocene (2.1 cal kyr BP), followed by a gradual decrease toward the present day.

#### 5.4.2.3.

#### **GDGT contents, $\text{TEX}_{86}^{\text{H}}$ temperature estimates and BIT index**

Total isoGDGTs contents in the core CF10-09A varied between 71 and 220  $\mu\text{g gTOC}^{-1}$ . Although in the same range of contents, the depth-distribution of total isoGDGTs seems to mirror that of the alkenones, particularly in the periods of 7.1-6.0 cal kyr BP and 4.0-3.4 cal kyr BP (Figure 5.3c).

The calculated BIT values ranged from 0.16 to 0.29, with an average of  $0.20 \pm 0.02$  (Figure 5.3d). Along the core, oscillations with positive BIT values during the middle of section IV (3.5 to 2.0 cal kyr BP) and in the sediments deposited in the upper layers of the core (1.5-1.0 cal kyr BP) can be identified. Notwithstanding these features, the BIT values are typically in the range

suggesting low input of terrigenous OM (Hopmans et al., 2004), which is consistent with observations in the core RJ13-01C (this study) and in core-top sediment samples regionally collected in the Campos Basin (Ceccopieri et al., 2018).

The  $\text{TEX}_{86}^{\text{H}}$  temperature estimates ranged from 20.7 to 23.1 °C, with a general trend of decreasing values towards modern sediments (Figure 5.3e). The offset between estimated temperature by  $\text{TEX}_{86}^{\text{H}}$  and  $\text{U}_{37}^{\text{K}'}$  proxies are relatively lower in the mid-Holocene (~1 °C; 7.0 to 5.5 cal kyr BP), but in the sector V of this core (2.0 to 1.0 cal kyr BP) the difference increase. A negative offset of 3.9 °C is reached during the late-Holocene, a period with the lowest estimated temp- $\text{TEX}_{86}^{\text{H}}$  values.

#### 5.4.2.4. LDI temperature estimates

From a total of 96 samples analyzed from CF10-09A core, 83 contained sufficient long chain diols for quantification and further LDI-based temperature estimate (Supplementary Table S5.4). The SST-LDI ranged from 22.6 to 25.4 °C, with a depth-profile variation in the estimated temperature that is distinct from those based on isoGDGTs and alkenones (Figure 5.3e). With the exception of some samples in the period 6.0-5.5 cal kyr BP, all the LDI-estimated temperatures in the sections II and III of this core are above the other estimates, but after 3.5 cal kyr BP (sections IV and V), the LDI and  $\text{U}_{37}^{\text{K}'}$ -based temperatures are similar, around 24.5 °C, and decrease to the core-top. In general, SST-LDI values are up to 4.7 °C higher than temp- $\text{TEX}_{86}^{\text{H}}$ .

### 5.5. Discussion

The data obtained by organic paleotemperature proxies are usually considered to reflect the annual mean SST, but a number of factors can influence the proxy's performance and cause bias in the estimates provided by each group of molecules (Huguet et al., 2006b; Lopes dos Santos et al., 2013; Smith et al., 2013; Becker et al., 2015; Jonas et al., 2017). Factors other than water temperature where the organisms thrive – the rationale common to all temperature proxy – have been suggested to cause inconsistencies in proxy estimates, including seasonal production and preferential depth habitats of the source organisms (Sikes et al., 1997; Prah et al., 2001; Herfort et al., 2006a; Popp et al., 2006; Huguet et al.,

2007a; Lee et al., 2008), lateral transport (Benthien and Müller, 2000; Mollenhauer et al., 2007; Kim et al., 2009), influence of nutrients and light (Epstein et al., 1998; Versteegh et al., 2001; Prahl et al., 2003) and selective degradation under oxic conditions (Conte et al., 1992; Hoefs et al., 1998; Gong and Hollander, 1999; Huguet et al., 2009). Differences between the proxies' estimates may also be related to the calibration associated errors of  $\pm 1.0$  °C for  $U_{37}^{K'}$  (Müller et al., 1998),  $\pm 2.5$  °C for  $TEX_{86}^H$  (Kim et al., 2010) and  $\pm 2$  °C for LDI (Rampen et al., 2012), and have to be taken in account.

In the following sections we will initially evaluate the consistency of the temperature data set obtained by the proxies considered and, in the following, the implication of these results to reconstruct the oceanographic and sedimentary conditions over the Holocene in a shelf region under the influence of a non-conventional westerly upwelling system.

### 5.5.1.

#### Influence of seasonal factors and water depth on temperature estimates

To investigate possible bias of the organic proxies considered in the present study towards a specific season or water depth temperature, we compared the SST estimated for the uppermost core sample with the recent depth profiles of water temperature (0-100 m) taken from the WOA13. As can be seen from Figure 5.4, the observed modern annual mean SST (WOA13) in the region of the two cores are very similar, around 23.2 (off Rio de Janeiro) and 23.4 °C (off Cabo Frio).

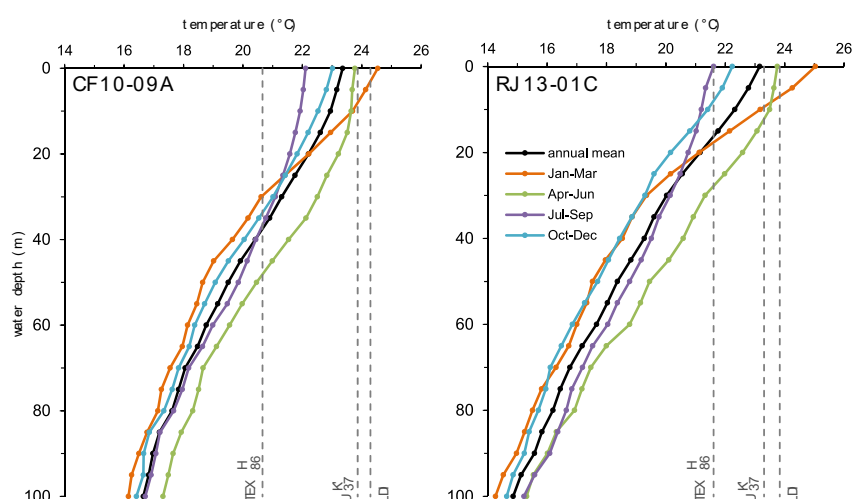


Figure 5.4: Annual mean and seasonal depth profiles of water temperature (1955-2012) corresponding to the nearest interpolated  $0.25^\circ$  grid box taken from the World Ocean Atlas 2013. Dashed grey lines correspond to the proxy-estimated temperatures for the core-top sample from the present work.

The upper sample of the Cabo Frio sediment core, dated to 1.09 cal kyr BP, showed proxy-based temperatures of 23.9 °C for  $U_{37}^{K'}$ , 20.7 °C for  $TEX_{86}^H$  and 24.3 °C for LDI. When compared to the observed annual mean SST, the estimated temperature values for the SST- $U_{37}^{K'}$  show a warm bias of 0.50 °C, which is within the calibration error of this proxy (Müller et al., 1998). The single value for the alkenone-based estimate is consistent with previous data of core-tops along the CFUS shelf and its associated muddy deposit (Cordeiro et al., 2014; Lourenço et al., 2017b, 2017a; Ceccopieri et al., 2018). Overall, there is consensus that the alkenone-based temperatures for the muddy deposit where the core CF10-09A is located is not significantly biased by non-temperature effects. Regarding the LDI-estimated temperatures, our data are the first reported for the south-eastern Brazilian continental margin. In the top sample of the Cabo Frio core, the SST-LDI was 24.3 °C and a warm bias of 0.93 °C relative to the annual mean SST was observed, also within the error of the calibration model. The similarity between the diol- and alkenone-based temperatures – at least in the last 3.5 cal kyr BP (see later) – are attributed to the fact that they are both produced by photosynthetic eukaryotes thriving in the euphotic zone (Prahl and Wakeham, 1987; Rampen et al., 2012).

The  $TEX_{86}^H$ -based temperature estimates for the top sample of core CF10-09A revealed a negative bias of 2.7 °C when compared to the annual mean SST-WOA13. In fact, the  $TEX_{86}^H$  estimates seem to reflect the temperature of waters at 30-40 m (Figure 5.4). The same bias in the GDGTs-based temperature estimates was measure in surface sediment (0-2 cm) samples in the same region (Ceccopieri et al., 2018), and was attributed to a possible preferential habitat for the Thaumarchaeota at ca. 35 m depth and/or a maximum export of GDGTs during upwelling events. Moreover, the BIT values  $<0.3$  measured in our samples exclude any relevant influence of soil-derived isoGDGTs that may cause bias on  $TEX_{86}^H$  estimates (Weijers et al., 2006b).

The core-top off Rio de Janeiro, located ca 200 km to the west of CFUS, has an age of 0.024 cal kyr BP and showed proxy-based temperatures of 23.3 °C for  $U_{37}^{K'}$ , 21.6 °C for  $TEX_{86}^H$  and 23.4 °C for LDI. Compared to the annual mean SST-WOA13 (Figure 5.4), the Rio de Janeiro estimates were slightly warmer for SST- $U_{37}^{K'}$  and SST-LDI ( $\Delta T = 0.15$  °C and 0.68 °C, respectively) but colder for temp- $TEX_{86}^H$  ( $\Delta T = -1.5$  °C). Contrary to the observations at Cabo Frio, here the differences between the proxies' estimates for alkenones and long-chain diols are subtle and for GDGTs is within the calibration error. It is noteworthy the SST- $TEX_{86}^H$

of the core-top at the Rio de Janeiro is equivalent to the WOA13 annual mean temperature at around 20 m water depth. If here the  $\text{TEX}_{86}^{\text{H}}$  signal also represent temperature of sub-surface waters, like in the CFUS, the shallow thermocline off Rio de Janeiro might suggest a gradient of environmental conditions with distance from the main area of the upwelling events in the shelf.

### 5.5.2.

#### **Environmental changes registered in the Rio de Janeiro and Cabo Frio shelves**

In the Rio de Janeiro core, from the Late Pleistocene to the mid-Holocene (14.3 to 7.5 cal kyr BP), lower values and a gradual increase in  $\text{SST-U}_{37}^{\text{K}'}$ , TOC and  $\delta^{13}\text{C}$  is observed. This period coincides with phase I (Figure 5.2), characterized by Lazzari et al. (2018) as a period marked by low sea level conditions, low continental input, medium to coarse sediments, high %Si and %Ca and predominance of dry climate. During the transition from the Pleistocene to the Holocene, the relative sea level in the Rio de Janeiro coast was about 4.5 m below the current level. After the transition, the sea level rose relatively fast reaching the contemporary level at about 7.5 cal kyr BP (Castro et al., 2014). In this core, the sand contents changed from 60 % to 0.25 % from the core bottom upwards (14.5 cal kyr BP to ~3.3 cal kyr BP), in a strong correlation with the sea level variation (Lazzari et al., 2018). Consistent with the predominance of sandy sediments, the low TOC contents during phase I of the Rio de Janeiro core could be ascribed to a stronger hydrodynamic system that preclude TOC accumulation and/or to a lower productivity regime at lower sea levels (Nagai et al., 2009). The relatively constant TOC-normalized contents of alkenones and isoGDGTs throughout the core (Figure 5.2c) are noteworthy, suggesting the low stands of sea level during phase I did not change the general pattern of organic matter production, only its rate of accumulation in the sediment.

The lower  $\text{SST-U}_{37}^{\text{K}'}$  in the Rio de Janeiro core during the period of low sea level might be related to an intensified AMOC and a weaker BC during the early Holocene (Lessa et al., 2016 and references therein). Also, the low sea-level conditions may promote an offshore displacement of the BC, favoring the presence of colder water over the shelf (Mahiques et al., 2007). The gradual increase in  $\text{SST-U}_{37}^{\text{K}'}$  along phase I and the relative stability during phases II and III (Figure 5.2e) could be related to a return of the BC flow over the shelf with the rising of the sea level. Contrary to the alkenone-based temperature estimates, the  $\text{TEX}_{86}^{\text{H}}$  and LDI

did not exhibit significant variation during phase I in the Rio de Janeiro core, but the reasons for this behavior are not clear with the available information. A possible hypothesis for the difference between  $U_{37}^{K'}$ ,  $TEX_{86}^H$  and LDI will be discussed in the next section.

The core CF10-09A represents the sedimentation of the last 7.1 cal kyr BP (Figure 5.3), and therefore did not register the sea level low stand during the Pleistocene-Holocene transition, as observed for the core RJ13-01C. Moreover, the sedimentation phases from the mid-Holocene up to 1.0 cal kyr BP (core-top sample) present at Cabo Frio, proposed by Lessa et al. (2016) based on planktonic foraminifera, differ from those proposed by Lazzari et al. (2018) for the core off Rio de Janeiro.

The mid-Holocene is characterized by changes in the circulation of the AMOC because of a weakening in the NADW in the subpolar North Atlantic (Hall et al., 2004; Hoogakker et al., 2011). In the Cabo Frio region, between 7.0 to 5.0 cal kyr BP, multiple proxies (foraminifera,  $\delta^{18}O$  of carbonate shells, alkenones) suggested the gradual approach of the BC over the shelf with low intensity, a relatively stronger local oceanic circulation and high productivity linked to the mid-shelf upwelling of the cold and nutrient enriched SACW (Nagai et al., 2009; Lessa et al., 2016). Accordingly, in our core a trend of increasing SST- $U_{37}^{K'}$  mirrored by a decreasing of temp- $TEX_{86}^H$  can be observed, which may be the result from a combination between SST warming caused by the increasing TW influence on the shelf with deepening of the mixed layer caused by the subsurface upwelling. The period between 7.1 and 4.0 presented lower SST- $U_{37}^{K'}$  values for Cabo Frio than Rio de Janeiro, which may be related to the combination of BC instabilities and bottom topography that would favor upwelling of nutrient rich and cold SACW in Cabo Frio, whereas a prevalence of warmer waters occurs in the Rio de Janeiro shelf (Pivel et al., 2013; Lessa et al., 2016).

At the end of the mid-Holocene, at 4.9 cal kyr BP, an abrupt decrease in TOC,  $\delta^{13}C$  and SST- $U_{37}^{K'}$  is observed in the Rio de Janeiro core (Figure 5.2a,b,e). Temp- $TEX_{86}^H$  and alkenone content also decreases, but at a smaller scale. Changes at ca 5 cal kyr BP were previously observed at Cabo Frio (Lessa et al., 2016) and in other paleoclimate records in the South America (Mahiques et al., 2002; Scheel-Ybert et al., 2003; Cruz et al., 2009; Nagai et al., 2009; Lazzari et al., 2018), and are usually attributed to changes in the hydrological regime. Even though the displacement of ITCZ may act as an indirect cause for increasing humidity in southeast Brazil (Sifeddine et al., 2001; Cruz et al., 2009), it does not

explain our minimum TOC value at this period when an opposite trend would be expected. According to the sea level curve of the Rio de Janeiro coast, a maximum transgression occurred between 4.8 and 4.5 kyr BP (Castro et al., 2014). However, it is also not clear how a higher sea level would bring SST- $U_{37}^{K'}$ , TOC and  $\delta^{13}C$  to expressively lower values at 4.9 cal kyr BP, especially considering that low values are observed during Phase I, when the lowest sea level is established. Besides that, this punctual abrupt variation is not observed in the Cabo Frio record.

The transition from middle to late Holocene is clearly marked in the Cabo Frio core by abrupt variations in TOC,  $\delta^{13}C$ , BIT, SST- $U_{37}^{K'}$  and temp- $TEX_{86}^H$  from 4.2 to 3.8 cal kyr BP. From 5.13 to 3.71 cal kyr BP, higher SST-LDI temperatures and an increase in SST- $U_{37}^{K'}$  are observed, except for the above mentioned rapid decrease around 4 cal kyr BP. Lessa et al. (2016) observed a transition phase between 5.0 and 3.5 cal kyr BP, which the authors defined as the period when the BC became more intense because of a less intense AMOC, especially between 5.0 and 4.0 cal kyr BP, resulting in higher reconstructed SST. In fact, a compilation of globally distributed records described the period from 4.2 to 3.8 cal kyr BP as having a weak NADW production and ITCZ southward migration (Mayewski et al., 2004 and references therein). In this period, the temp- $TEX_{86}^H$  kept the cooling trend opposite to the  $U_{37}^{K'}$  signal, probably caused by the return of cold waters from the SACW in subsurface after 4.0 cal kyr BP in the Cabo Frio region (Mahiques et al., 2005; Nagai et al., 2009, 2016; Lessa et al., 2016). In the Rio de Janeiro core, this transition is marked by an increase in isoGDGTs and alkenones contents between 4.5 and 3.4 cal kyr BP, which agrees with findings of high productivity events during the same period reported by Lazzari et al. (2018).

BIT values increased between 3.8 and 3.1 cal kyr BP, and again after 1.8 cal kyr BP in the Cabo Frio record. A higher BIT may be indicative of a more humid period, with more precipitation leading to a higher input of soil organic material to the shelf. According to Lessa et al. (2016), the climate in the Cabo Frio region became more humid after 4.5 cal kyr BP. The seasonal displacement of the ITCZ promote the intensification of the SAMS and the consequent expansion of the tropical rainforest vegetation, conveying humidity to the southeast of Brazil trough the intensification of the SACZ (Gan et al., 2004; Marengo et al., 2004; Chiessi et al., 2009; Cruz et al., 2009; Ledru et al., 2009). Variations between dry and humid climate during the late Holocene were previously observed in South America and attributed to the SAMS fluctuations (Cruz et al., 2009; Bernal et al., 2016). The increase in BIT co-occurs with decrease in TOC, alkenones and isoGDGTs

contents, indicating a decrease in local productivity and possibly a less intense upwelling, which corroborates the weakening in coastal and mid-shelf upwelling observed by Lessa et al. (2016) between 3.5 and 2.5 cal kyr BP. Alternatively, variations in the terrestrial input of brGDGTs may be irrelevant and the BIT ratio is more affected by the crenarchaeol contents, varying in function of the autochthone production only (Ceccopieri et al., 2018).

At Cabo Frio, from 3.6 to 2.1 cal kyr BP, both SST- $U_{37}^{K'}$  and SST-LDI increased until SST- $U_{37}^{K'}$  achieved its highest temperature of the Holocene (25.2 °C). The warmest SST- $U_{37}^{K'}$  in Rio de Janeiro (25.4 °C) is observed around the same period, at 2.5 cal kyr BP. From 3.5 to 2.5 kyr B.P, Ingólfsson et al. (1998) observed conditions warmer than today in discontinuous lake sediment records from Antarctica and attributed them to increased southern summer insolation.

In the Cabo Frio core, from 2.1 to 1.1 cal kyr BP, SST- $U_{37}^{K'}$  and SST-LDI decreased to temperatures more similar to the present-day SST. Temp- $TEX_{86}^H$ , however, maintained its general cooling pattern, but presented more expressive oscillations. According to Lessa et al. (2016), the BC reached its modern dynamics after 3.5 cal kyr BP, with intense flow offshore, and the interval 2.5–0.8 cal kyr BP (Phase V, Figure 5.3) is marked by the establishment of the current CFUS oceanographic condition. Evidences of stronger hydrodynamic and higher productivity related to an upwelling enhancement during this period has been recorded by other previous studies in the Cabo Frio region (Mahiques et al., 2005; Nagai et al., 2009, 2016). Thus, the overall cooling trend registered by all three-organic geochemical paleotemperature proxies after 2.1 cal kyr BP is another strong evidence of the return of cold water from the SACW to the region. Because the BC strength and position became stable, the temperature oscillations after 3.5 cal kyr BP are probably related to local action of NE winds (Lessa et al., 2016). In the core off Rio de Janeiro, a decreasing pattern in SST- $U_{37}^{K'}$  and SST-LDI was also observed after 2.5 cal kyr BP and again after 400 cal yr BP, which may be an evidence that, even though less pronounced, the upwelling also intensified in this region in the same period.

Overall, the differences between the two cores are likely related to the different oceanographic features of each area. For instance, while the BC instabilities near de CFUS region favors mid-shelf and coastal SACW upwelling, more stable hydrodynamics are observed on the Rio de Janeiro shelf (Lessa et al., 2016). Apart from the above-mentioned events, the distinct characteristics in terms of local productivity between the two regions is evident. For instance, the  $\delta^{13}C$

values vary from  $-21.5$  to  $-20.7$  ‰ at Cabo Frio, which means that the organic carbon comes mainly from primary production. Off Rio de Janeiro, a higher amplitude is observed ( $-27.4$  to  $-20.5$  ‰) and values achieve a minimum of  $-26.8$  ‰ within the same period covered by the Cabo Frio core ( $7.1$  cal kyr BP), pointing to a more significant terrestrial influence in this area, especially at lower sea level conditions.

As the paleotemperature proxies are based on lipid compounds produced by primary producers, differences in the provenance of autochthone and allochthone material can be intimately connected to the organism's production. In fact, the contents of alkenones in Cabo Frio (mean value of  $194 \pm 30$   $\mu\text{g gTOC}^{-1}$ ) are almost three times higher than in Rio de Janeiro (mean value of  $75 \pm 15$   $\mu\text{g gTOC}^{-1}$ ), which may be related to the local more eutrophic conditions caused by SACW upwelling. In contrast, contents of isoGDGTs are on the same order for the two regions, suggesting that Thaumarchaeota production is less affected by the BC instabilities in the Cabo Frio region, while *Emiliana huxleyi* production might be favored.

### 5.5.3.

#### Comparison between $U_{37}^{K'}$ , $TEX_{86}^H$ and LDI records

Differences between  $U_{37}^{K'}$ ,  $TEX_{86}^H$  and LDI are evident in both sediment cores throughout the entire Holocene period and possibly resulted from the physiological differences of the source organisms and how each of them responds to the local environmental changes (Lopes dos Santos et al., 2013; Becker et al., 2015; Rodrigo-Gámiz et al., 2015; Jonas et al., 2017). For some periods, the difference between the SST estimates are within the calibration errors of the proxies (Müller et al., 1998; Kim et al., 2010; Rampen et al., 2012). However, the discrepancies between the proxies are not always systematic, as they vary differently along the analyzed period, and sometimes are higher than the calibration error, which suggest they may also result from the local water column structure or seasonality of the source organisms.

Because  $TEX_{86}^H$  probably reflect subsurface water temperatures instead of SST (e.g. Huguet et al., 2007a; Lee et al., 2008; Lopes dos Santos et al., 2010; Kim et al., 2012; Chen et al., 2014), temp- $TEX_{86}^H$  is lower than SST- $U_{37}^{K'}$  and SST-LDI during the entire Holocene period in both cores. In the Rio de Janeiro shelf waters, temp- $TEX_{86}^H$  can be up to  $4.1$  °C colder than SST- $U_{37}^{K'}$  and SST-LDI. At Cabo Frio, temp- $TEX_{86}^H$  can be up to  $3.9$  °C colder than SST- $U_{37}^{K'}$  and up to  $4.7$  °C

colder than SST-LDI. Oscillations in temp-TEX<sub>86</sub><sup>H</sup> are possibly related to variations in the thermocline position and the consequent vertical migration of Thaumarchaeota (Lopes dos Santos et al., 2013; Jonas et al., 2017).

The difference between U<sub>37</sub><sup>K'</sup> and TEX<sub>86</sub><sup>H</sup> signals is small in the late Pleistocene and gradually increases until ca 7.5 cal kyr BP in Rio de Janeiro. The same happens at Cabo Frio from 7.1 to ca 3.5 cal kyr BP. The earlier compatibility between the two proxies could be ascribed to a possible upward migration of pelagic Thaumarchaeota to habitat depths closer to the phototrophic haptophytes caused by a thermocline shoaling combined to a weaker and more offshore BC and a consequent reduction in export of warm surface waters to the study region (Jonas et al., 2017). A subsequent gradual approximation of the BC to the coast may have increased the TW influence and, consequently, the local SST, which may explain the SST-U<sub>37</sub><sup>K'</sup> becoming warmer, whereas the temp-TEX<sub>86</sub><sup>H</sup> remained colder because of a preferential depth habitats of Thaumarchaeota below the thermocline (Huguet et al., 2007a; Lee et al., 2008; Lopes dos Santos et al., 2010; Kim et al., 2012; Chen et al., 2014).

SST-LDI were warmer and less variable throughout the entire Holocene, except for two periods of abrupt cooling at 6.0 and 5.7 cal kyr BP at Cabo Frio. The expressive disagreement between SST-U<sub>37</sub><sup>K'</sup> and SST-LDI before 7.5 cal kyr BP off Rio de Janeiro and before 3.5 cal kyr BP at Cabo Frio is probably related to differences in the seasonality of production of haptophytes and eustigmatophytes (Lopes dos Santos et al., 2013; Becker et al., 2015; Rodrigo-Gámiz et al., 2015; Jonas et al., 2017). Warm bias in SST-LDI was also observed in previous studies (Lopes dos Santos et al., 2013; Becker et al., 2015; Rodrigo-Gámiz et al., 2015; Jonas et al., 2017) and the authors related this to a maximum productivity of eustigmatophytes algae during summer. In fact, when analyzing globally distributed core-top sediments, Rampen et al. (2012) observed a higher correlation between LDI and late summer and early autumn temperatures, suggesting a preferential production of the source organisms during the warmest months. Notwithstanding, the correlation between LDI and temperature, the exact biological source and its physiology still requires further investigation (Rampen et al., 2012).

U<sub>37</sub><sup>K'</sup> seems to be the only organic paleotemperature proxy that responds to changes in upper water column hydrography triggered by changes in sea level in our study area. It is also the one that better correlates with the SST reconstructed from *Globigerinoides ruber* Mg/Ca on the outer shelf of Cabo Frio (Lessa et al., 2016). From a global compilation of sediment trap data, Rosell-Melé and Prahl

(2013) observed that the  $U_{37}^{K'}$  in some locations may be seasonally biased, but sedimentary  $U_{37}^{K'}$  most significantly correspond to the annual mean SST. This may suggest that, even though all three proxies are providing valuable information about the local processes,  $U_{37}^{K'}$  may be the more reliable in reconstructing the local annual mean SST.

## 5.6. Conclusions

The core-top estimates of SST- $U_{37}^{K'}$  and SST-LDI agree with the modern annual mean SST in both Cabo Frio and Rio de Janeiro records. Temp- $TEX_{86}^H$ , however, presented colder bias, especially at Cabo Frio, probably reflecting the peak upwelling events and/or a preferential subsurface habitat for Thaumarchaeota.

The reconstructed paleotemperature from  $U_{37}^{K'}$ ,  $TEX_{86}^H$  and LDI proxies in the Rio de Janeiro and Cabo Frio shelves presented variations that agree with previous paleoclimate studies in the region. A distinct period from the Late Pleistocene to 7.5 cal kyr BP is observed on the Rio de Janeiro shelf, where lower values of SST- $U_{37}^{K'}$ , TOC and  $\delta^{13}C$  are found and gradually increase, influenced by the gradual increase in sea level and the approach of the BC. In the Cabo Frio shelf, the transition between mid- and late Holocene is well marked by the proxy-based reconstructed temperatures. After ca 4.0 cal kyr BP, warmer SST- $U_{37}^{K'}$  in both cores coincides with a more intense BC activity. A decrease in  $U_{37}^{K'}$ -SST and SST-LDI after ca 2.5 cal kyr BP is possibly related to the return of cold water from the SACW to the region and the establishment of the current CFUS oceanographic condition.

Differences between Rio de Janeiro and Cabo Frio are probably related to the local BC instabilities near de CFUS region, which favors SACW upwelling, while more stable hydrodynamics are observed on the Rio de Janeiro shelf. But, overall, for the entire covered period in both cores, SST-LDI was warmer, SST- $TEX_{86}^H$  was clearly biased towards subsurface temperatures and SST- $U_{37}^{K'}$  was more affected by the sea level variation and/or the BC flow over the shelf. Oscillations in  $TEX_{86}^H$  are possibly be related to variations in the thermocline depth. The differences between the three SST proxies are derived from a combination of thermal and non-thermal parameters, which provided more insights about the local paleoceanographic changes, such as variation in the sea level, thermocline depth,

BC flow and upwelling enhancement during the Holocene period in the southeastern Brazilian margin.

### **Acknowledgements**

This study is funded in part by the Coordenação de Aperfeiçoamento de Pessoal de Nível Superior – Brasil (CAPES) – Finance Code 001. M. Ceccopieri thanks the National Council for Scientific and Technological Development (CNPq, grant 142451/2015-0), CAPES (grant PDSE 88881.134877/2016-01) and the German Academic Exchange Service (DAAD, short-term grant 2015/91591964) for her PhD scholarships. R. S. Carreira was supported by research fellowships from CNPq (grant 309347/2017-3) and CAPES (grant 88881.121009/2016-01). The research was partially funded by CNPq (process 402459/2012-1). Our thanks to Prof. Alberto Figueiredo and João R. dos Santos Filho for the study area map.

## Chapter 6

### Conclusions

The application of three-existing organic-geochemical SST proxies was investigated in modern and past marine sediments from the south-eastern Brazilian continental margin. When testing the applicability of alkenone- and GDGT-based temperature proxies in the Campos Basin, our results showed a strong correlation between the  $U_{37}^{K'}$  and  $TEX_{86}^H$  with annual mean SST. In more detail, the temp- $TEX_{86}^H$  using the surface calibration (Kim et al., 2010) reflects the surface mixed layer, while the subsurface temp- $TEX_{86}^H$  using the depth-integrated calibration for 0-200 m (Kim et al., 2012) agrees with the observed depth-integrated temperatures at 100-200 m. In relation to the alkenone's seasonal calibrations, SST- $U_{37}^{K'}$  shows a better agreement with SST-WOA13 for winter, which may be related to a higher production of haptophytes in the region during this period. However, both  $TEX_{86}^H$  and  $U_{37}^{K'}$  proxies can be biased towards colder temperatures inside or near the CFUS region. The first occurs on the inner shelf and is probably caused by the coastal upwelling that increases the fertilization and primary production leading to a maximum export and/or a predominant subsurface habitat of Thaumarchaeota in comparison to the oligotrophic adjacent waters. The second occurs in the mid and outer shelf and may be caused by pre- or post-depositional lateral transport, but further investigation regarding the advected material's origin is needed. These biases must be considered when applying  $TEX_{86}^H$  and  $U_{37}^{K'}$  in sediment records in the same study area.

Higher contents of soil brGDGTs were observed in the inner shelf, with a gradual decrease towards the open ocean, which confirms the Paraíba do Sul River as the main terrigenous source to the Campos Basin. However, no trend in the BIT index from coast to open ocean was observed, which possibly indicates that the proxy is more influenced by crenarchaeol contents rather than the brGDGTs content in the region. The spatial distribution of the brGDGTs points to the occurrence of selective degradation and *in situ* production that compromise the use of brGDGTs to reconstruct the soil pH and MAAT of the nearby land area. The selective degradation increases with distance from the coast and seems to affect the MAAT more strongly than the pH estimates. The *in situ* production of brGDGTs

is less clear, but seems to occur in the mid and outer shelf overestimating both pH and MAAT. For a better evaluation of the possible *in situ* production, the separation of the 5 and 6-methyl isomers should be pursued. Notwithstanding, these results agree with previous observation that the MBT/CBT proxy should only be applied in marine sediments with a relatively high contribution of terrigenous OM. Analyses of soil samples from the main source river's catchment could improve the understanding of the brGDGTs sources and distribution in the studied region.

The paleotemperature reconstructed from  $U_{37}^{K'}$ ,  $TEX_{86}^H$  and LDI and the bulk parameters analyzed in the Cabo Frio and Rio de Janeiro shelves for the past 14.5 kyrs agreed with several paleoclimatic events described in the region. In the Rio de Janeiro shelf, a distinct phase where SST- $U_{37}^{K'}$ , TOC and  $\delta^{13}C$  values gradually increase from Late Pleistocene to 7.5 cal kyr BP is consistent with the gradual increase of sea level within the same period. In the Cabo Frio shelf, the transition between mid- and late Holocene is well marked by warmer SST- $U_{37}^{K'}$  and SST-LDI that coincides with a more intense BC activity. A decrease in reconstructed temperatures after ca 2.5 cal kyr BP on both the Cabo Frio and Rio de Janeiro shelves is probably related to a well established upwelling enhancement during this period.

Differences between Rio de Janeiro and Cabo Frio are probably related to the local BC instabilities near de CFUS region, while more stable hydrodynamics are observed on the Rio de Janeiro shelf. The differences among the SST proxies within a single core were also clearly observed. In general, SST-LDI was warmer, SST- $TEX_{86}^H$  was colder and SST- $U_{37}^{K'}$  gradually increase throughout the Holocene, which means that the  $U_{37}^{K'}$  is probably more affected by the oceanographic changes during the Holocene period, such as sea level variations and BC approach over the shelf. These discrepancies between the SST proxies' are attributed to local oceanographic parameters other than temperature combined with the seasonality and depth habitat of the source organisms.

In summary, our surface sediments data provide information on the applicability of  $U_{37}^{K'}$  and  $TEX_{86}^H$  proxies in the Campos Basin and the limitations that must be considered in future research studies in the region, and our downcore records emphasizes the relevance of a multi-proxy approach ( $U_{37}^{K'}$ ,  $TEX_{86}^H$  and LDI) to bring more insights about local environmental changes in two distinct oceanographic settings, leading to a better understanding of the paleoclimatic changes during the Holocene in the south-eastern Brazilian margin.

## References

- ALBUQUERQUE, A. L. S.; BELÉM, A. L.; ZULUAGA, F. J. B.; et al. Particle fluxes and bulk geochemical characterization of the Cabo Frio Upwelling System in Southeastern Brazil: Sediment trap experiments between spring 2010 and summer 2012. **Anais da Academia Brasileira de Ciências**, v. 86, n. 2, p. 601–619, 2014.
- ALLEY, R. B.; MAYEWSKI, P. A.; SOWERS, T.; et al. Holocene climatic instability: A prominent, widespread event 8200 yr ago. **Geology**, v. 25, n. 6, p. 483–486, 1997.
- DE ALMEIDA, A. G.; KOWSMANN, R. O. Geomorphology of the Continental Slope and São Paulo Plateau. **Geology and Geomorphology - Regional Environmental Characterization of the Campos Basin, Southwest Atlantic**. p.33–66, 2016.
- ANGULO, R. J.; DE SOUZA, M. C.; REIMER, P. J.; SASAOKA, S. K. Reservoir Effect of the Southern and Southeastern Brazilian Coast. **Radiocarbon**, v. 47, n. 01, p. 67–73, 2005.
- ARAUJO, B. F.; HINTELMANN, H.; DIMOCK, B.; ALMEIDA, M. G.; REZENDE, C. E. Concentrations and isotope ratios of mercury in sediments from shelf and continental slope at Campos Basin near Rio de Janeiro, Brazil. **Chemosphere**, v. 178, n. Supplement C, p. 42–50, 2017.
- ARZ, H. W.; PÄTZOLD, J.; WEFER, G. The deglacial history of the western tropical Atlantic as inferred from high resolution stable isotope records off northeastern Brazil. **Earth and Planetary Science Letters**, v. 167, n. 1, p. 105–117, 1999.
- BARD, E. Comparison of alkenone estimates with other paleotemperature proxies. **Geochemistry Geophysics Geosystems**, v. 2, n. 1, p. 12, 2001.
- BARKER, S.; GREAVES, M.; ELDERFIELD, H. A study of cleaning procedures used for foraminiferal Mg/Ca paleothermometry. **Geochemistry, Geophysics, Geosystems**, v. 4, n. 9, 2003.
- BASSE, A.; ZHU, C.; VERSTEEGH, G. J. M.; et al. Distribution of intact and core

- tetraether lipids in water column profiles of suspended particulate matter off Cape Blanc, NW Africa. **Organic Geochemistry**, v. 72, p. 1–13, 2014.
- BECKER, K. W.; LIPP, J. S.; VERSTEEGH, G. J. M.; WÖRMER, L.; HINRICHS, K. U. Rapid and simultaneous analysis of three molecular sea surface temperature proxies and application to sediments from the Sea of Marmara. **Organic Geochemistry**, v. 85, p. 42–53, 2015.
- BELEM, A. L.; CASTELAO, R. M.; ALBUQUERQUE, A. L. Controls of subsurface temperature variability in a western boundary upwelling system. **Geophysical Research Letters**, v. 40, n. 7, p. 1362–1366, 2013.
- BEMAN, J. M.; SACHDEVA, R.; FUHRMAN, J. A. Population ecology of nitrifying Archaea and Bacteria in the Southern California Bight. **Environmental Microbiology**, v. 12, n. 5, p. 1282–1292, 2010.
- BENDER, V. B.; HANEBUTH, T. J. J.; CHIESSI, C. M. Holocene shifts of the Subtropical Shelf Front off southeastern South America controlled by high and low latitude atmospheric forcings. **Paleoceanography**, v. 28, n. 3, p. 481–490, 2013.
- BENTHIEN, A.; MÜLLER, P. J. Anomalously low alkenone temperatures caused by lateral particle and sediment transport in the Malvinas Current region, western Argentine Basin. **Deep-Sea Research Part I: Oceanographic Research Papers**, v. 47, n. 12, p. 2369–2393, 2000.
- BERNAL, J. P.; CRUZ, F. W.; STRÍKIS, N. M.; et al. High-resolution Holocene South American monsoon history recorded by a speleothem from Botuverá Cave, Brazil. **Earth and Planetary Science Letters**, v. 450, p. 186–196, 2016.
- BLAAUW, M. Methods and code for ‘classical’ age-modelling of radiocarbon sequences. **Quaternary Geochronology**, v. 5, n. 5, p. 512–518, 2010.
- BLAGA, C. I.; REICHART, G.-J.; HEIRI, O.; SINNINGHE DAMSTÉ, J. S. Tetraether membrane lipid distributions in water-column particulate matter and sediments: a study of 47 European lakes along a north–south transect. **Journal of Paleolimnology**, v. 41, n. 3, p. 523–540, 2009.
- BLUMENBERG, M.; SEIFERT, R.; REITNER, J.; PAPE, T.; MICHAELIS, W. Membrane lipid patterns typify distinct anaerobic methanotrophic consortia. **Proceedings of the National Academy of Sciences of the United States of America**, v. 101, n. 30, p. 11111–11116, 2004.
- BOEBEL, O.; DAVIS, E. R.; OLLITRAULT, M.; et al. The intermediate depth

- circulation of the western South Atlantic. **Geophysical Research Letters**, v. 26, n. 21, p. 3329–3332, 1999. Wiley-Blackwell.
- BOND, G. A Pervasive Millennial-Scale Cycle in North Atlantic Holocene and Glacial Climates. **Science**, v. 278, n. 5341, p. 1257–1266, 1997.
- BOND, G. Persistent Solar Influence on North Atlantic Climate During the Holocene. **Science**, v. 294, n. 5549, p. 2130–2136, 2001.
- BOON, J. J.; VAN DER MEER, F. W.; SCHUYL, P. J. W.; LEEUW, J. W.; SCHENCK, P. A. Organic geochemical analyses of core samples from Site 362, Walvis Ridge, DSDP Leg 40. **Initial Reports of the Deep Sea Drilling Project**, v. 38–41, p. 627–637, 1978.
- BOYER, T. P.; ANTONOV, J. I.; BARANOVA, O. K.; et al. World Ocean Database 2013. In: S. Levitus; A. Mishonov (Orgs.); **NOAA Atlas NESDIS**. v. 72, p.209, 2013.
- BRANDINI, F. P.; NOGUEIRA, M.; SIMIÃO, M.; CARLOS UGAZ CODINA, J.; ALMEIDA NOERNBERG, M. Deep chlorophyll maximum and plankton community response to oceanic bottom intrusions on the continental shelf in the South Brazilian Bight. **Continental Shelf Research**, v. 89, p. 61–75, 2014.
- BRANDINI, F. P.; TURA, P. M.; SANTOS, P. P. G. M. Ecosystem responses to biogeochemical fronts in the South Brazil Bight. **Progress in Oceanography**, v. 164, p. 52–62, 2018.
- BRASSELL, S. C.; EGLINTON, G.; MARLOWE, I. T.; PFLAUMANN, U.; SARNTHEIN, M. Molecular stratigraphy: a new tool for climatic assessment. **Nature**, v. 320, n. 6058, p. 129–133, 1986.
- BREHME, I. Vales submarinos entre o banco de abrolhos e Cabo Frio. **Anuário do Instituto de Geociências**, v. 16, p. 68, 1993.
- BROWN, C. W.; PODESTÁ, G. P. Remote sensing of coccolithophore blooms in the Western South atlantic ocean. **Remote Sensing of Environment**, v. 60, n. 1, p. 83–91, 1997.
- BUCKLEY, M. W.; MARSHALL, J. Observations, inferences, and mechanisms of the Atlantic Meridional Overturning Circulation: A review. **Reviews of Geophysics**, v. 54, n. 1, p. 5–63, 2016.
- CALADO, L.; DA SILVEIRA, I. C. A.; GANGOPADHYAY, A.; DE CASTRO, B. M. Eddy-induced upwelling off Cape São Tomé (22°S, Brazil). **Continental Shelf Research**, v. 30, n. 10, p. 1181–1188, 2010.

- CAMPOS, E. J. D.; VELHOTE, D.; SILVEIRA, I. C. A. Shelf break upwelling driven by Brazil current cyclonic meanders. **Geophysical Research Letters**, v. 27, n. 6, p. 751–754, 2000.
- CARMINATTI, M.; SCARTON, J. C. Sequence stratigraphy of the Oligocene turbidite complex of the Campos Basin, offshore Brazil; an overview. In: P. Weimer; M. Link (Orgs.); **Seismic facies and sedimentary processes of submarine fans and turbidite systems**. p.241–246, 1991. Springer New York.
- CARREIRA, R. DA S.; CANUEL, E. A.; MACKO, S. A.; et al. On the accumulation of organic matter on the southeastern Brazilian continental shelf: a case study based on a sediment core from the shelf off Rio de Janeiro. **Brazilian Journal of Oceanography**, v. 60, n. 1, p. 75–87, 2012.
- CARREIRA, R. S.; ARAÚJO, M. P.; COSTA, T. L. F.; ANSARI, N. R.; PIRES, L. C. M. Lipid biomarkers in deep sea sediments from the Campos Basin, SE Brazilian continental margin. **Organic Geochemistry**, v. 41, n. 9, p. 879–884, 2010.
- CARREIRA, R. S.; CORDEIRO, L. G. M. S.; OLIVEIRA, D. R. P.; BAÊTA, A.; WAGENER, A. L. R. Source and distribution of organic matter in sediments in the SE Brazilian continental shelf influenced by river discharges: An approach using stable isotopes and molecular markers. **Journal of Marine Systems**, v. 141, p. 80–89, 2015.
- CARVALHO, C. E. V.; SALOMÃO, M. S. M. B.; MOLISANI, M. M.; REZENDE, C. E.; LACERDA, L. D. Contribution of a medium-sized tropical river to the particulate heavy-metal load for the South Atlantic Ocean. **Science of the Total Environment**, v. 284, n. 1–3, p. 85–93, 2002.
- CARVALHO, C.; TORRES, J. P. M. The Ecohydrology of the Paraíba do Sul River, Southeast Brazil. In: M. McClain (Org.); **The Ecohydrology of South America Rivers and Wetlands**. p.179–191, 2002. International Association of Hydrological Sciences.
- CARVALHO, L. M. V.; JONES, C.; LIEBMANN, B. The South Atlantic convergence zone: Intensity, form, persistence, and relationships with intraseasonal to interannual activity and extreme rainfall. **Journal of Climate**, v. 17, n. 1, p. 88–108, 2004.
- CASTELAO, R. M.; BARTH, J. A. Upwelling around Cabo Frio, Brazil: The importance of wind stress curl. **Geophysical Research Letters**, v. 33, n. 3,

p. L03602, doi:10.1029/2005GL025182, 2006.

CASTRO FILHO, B. M.; PEREIRA, A. F.; DE CAROLI, A.; et al. Currents and water masses over the continental shelf. In: R. P. Martins; G. S. Grossmann-Matheson (Orgs.); **Meteorology and Oceanography - Regional Environmental Characterization of the Campos Basin, Southwest Atlantic**, 2017. Rio de Janeiro: Elsevier. Habitats, v. 2, p. 189-254.

CASTRO, J. W. A.; SUGUIO, K.; SEOANE, J. C. S.; CUNHA, A. M. D. A.; DIAS, F. F. Sea-level fluctuations and coastal evolution in the state of Rio de Janeiro, southeastern Brazil. **Anais da Academia Brasileira de Ciências**, 2014.

CECCOPIERI, M.; CARREIRA, R. S.; WAGENER, A. L. R.; HEFTER, J. H.; MOLLENHAUER, G. On the application of alkenone- and GDGT-based temperature proxies in the south-eastern Brazilian continental margin. **Organic Geochemistry**, v. 126, p. 43–56, 2018.

CERDA, C.; CASTRO, B. M. Hydrographic climatology of South Brazil Bight shelf waters between Sao Sebastiao (24°S) and Cabo Sao Tome (22°S). **Continental Shelf Research**, v. 89, p. 5–14, 2014.

CHAVES, R. R.; NOBRE, P. Interactions between sea surface temperature over the South Atlantic Ocean and the South Atlantic Convergence Zone. **Geophysical Research Letters**, v. 31, p. L03204, doi:10.1029/2003GL018647, 2004.

CHEN, W.; MOHTADI, M.; SCHEFUSS, E.; MOLLENHAUER, G. Organic-geochemical proxies of sea surface temperature in surface sediments of the tropical eastern Indian Ocean. **Deep Sea Research Part I: Oceanographic Research Papers**, v. 88, n. 0, p. 17–29, 2014.

CHEN, W.; MOHTADI, M.; SCHEFUSS, E.; MOLLENHAUER, G. Concentrations and abundance ratios of long-chain alkenones and glycerol dialkyl glycerol tetraethers in sinking particles south of Java. **Deep Sea Research Part I: Oceanographic Research Papers**, v. 112, p. 14–24, 2016.

CHIESSI, C. M.; MULITZA, S.; GROENEVELD, J.; et al. Variability of the Brazil Current during the late Holocene. **Palaeogeography, Palaeoclimatology, Palaeoecology**, v. 415, n. 0, p. 28–36, 2014.

CHIESSI, C. M.; MULITZA, S.; MOLLENHAUER, G.; et al. Thermal evolution of the western South Atlantic and the adjacent continent during Termination 1. **Clim. Past**, v. 11, n. 6, p. 915–929, 2015.

- CHIESSI, C. M.; STEFAN, M.; JÜRGEN, P.; GEROLD, W.; MARENGO, J. A. Possible impact of the Atlantic Multidecadal Oscillation on the South American summer monsoon. **Geophysical Research Letters**, v. 36, n. 21, 2009.
- COELHO-SOUZA, S. A.; PEREIRA, G. C.; LOPEZ, M. S.; GUIMARAES, J. R. D.; COUTINHO, R. Seasonal sources of carbon to the Brazilian upwelling system. **Estuarine, Coastal and Shelf Science**, v. 194, n. Supplement C, p. 162–171, 2017.
- COHEN, K.; FINNEY, S.; GIBBARD, P.; FAN, J. The ICS International Chronostratigraphic Chart. **Episodes**, v. 36, p. 199-204, 2013.
- CONTE, M. H.; EGLINTON, G. Alkenone and alkenoate distributions within the euphotic zone of the eastern North Atlantic: correlation with production temperature. **Deep-Sea Research Part I**, v. 40, n. 10, p. 1935–1961, 1993.
- CONTE, M. H.; EGLINTON, G.; MADUREIRA, L. A. S. Long-chain alkenones and alkyl alkenoates as palaeotemperature indicators: their production, flux and early sedimentary diagenesis in the Eastern North Atlantic. **Organic Geochemistry**, v. 19, n. 1, p. 287–298, 1992.
- CONTE, M. H.; SICRE, M.-A.; RÜHLEMANN, C.; et al. Global temperature calibration of the alkenone unsaturation index ( $U_{37}^{K'}$ ) in surface waters and comparison with surface sediments. **Geochemistry, Geophysics, Geosystems**, v. 7, n. 2, p. Q02005, doi:10.1029/2005GC001054, 2006.
- CORDEIRO, L. G. M. S.; BELEM, A. L.; BOULOUBASSI, I.; et al. Reconstruction of southwestern Atlantic sea surface temperatures during the last Century: Cabo Frio continental shelf (Brazil). **Palaeogeography, Palaeoclimatology, Palaeoecology**, v. 415, p. 225–232, 2014.
- CORDEIRO, L. G. M. S.; WAGENER, A. L. R.; CARREIRA, R. S. Organic matter in sediments of a tropical and upwelling influenced region of the Brazilian continental margin (Campos Basin, Rio de Janeiro). **Organic Geochemistry**, v. 120, p. 86–98, 2018.
- CORDEIRO, R. C.; TURCQ, B.; SUGUIO, K.; et al. Holocene fires in East Amazonia (Carajás), new evidences, chronology and relation with paleoclimate. **Global and Planetary Change**, v. 61, n. 1–2, p. 49–62, 2008.
- CRIVELLARI, S.; CHIESSI, C. M.; KUHNERT, H.; et al. Increased Amazon freshwater discharge during late Heinrich Stadial 1. **Quaternary Science Reviews**, v. 181, p. 144–155, 2018.
- CROWLEY, T. J. Causes of Climate Change Over the Past 1000 Years. **Science**,

- v. 289, n. 5477, p. 270 LP-277, 2000.
- CRUZ, A. P. S.; BARBOSA, C. F.; AYRES-NETO, A.; ALBUQUERQUE, A. L. S. Physical and geochemical properties of centennial marine sediments of the continental shelf of southeast Brazil. **Geochimica Brasiliensis**, v. 27, n. 1, p. 1–12, 2013.
- CRUZ, F. W.; BURNS, S. J.; KARMANN, I.; et al. Insolation-driven changes in atmospheric circulation over the past 116,000 years in subtropical Brazil. **Nature**, v. 434, p. 63, 2005.
- CRUZ, F. W.; VUILLE, M.; BURNS, S. J.; et al. Orbitally driven east–west antiphasing of South American precipitation. **Nature Geoscience**, v. 2, p. 210, 2009.
- DAMSTÉ, J. S. S.; OSSEBAAR, J.; ABBAS, B.; SCHOUTEN, S.; VERSCHUREN, D. Fluxes and distribution of tetraether lipids in an equatorial African lake: Constraints on the application of the TEX<sub>86</sub> palaeothermometer and BIT index in lacustrine settings. **Geochimica et Cosmochimica Acta**, v. 73, n. 14, p. 4232–4249, 2009.
- DELONG, E. F. Archaea in coastal marine environments. **Proceedings of the National Academy of Sciences**, v. 89, n. 12, p. 5685–5689, 1992.
- DIAZ, H. F.; TRIGO, R.; HUGHES, M. K.; et al. Spatial and Temporal Characteristics of Climate in Medieval Times Revisited. **Bulletin of the American Meteorological Society**, v. 92, n. 11, p. 1487–1500, 2011.
- DITTMAR, T.; REZENDE, C. E.; MANECKI, M.; et al. Continuous flux of dissolved black carbon from a vanished tropical forest biome. **Nature Geoscience**, v. 5, p. 618, 2012.
- ELLING, F. J.; KÖNNEKE, M.; MUSSMANN, M.; GREVE, A.; HINRICHS, K.-U. Influence of temperature, pH, and salinity on membrane lipid composition and TEX<sub>86</sub> of marine planktonic thaumarchaeal isolates. **Geochimica et Cosmochimica Acta**, v. 171, p. 238–255, 2015.
- EMEIS, K.-C.; STRUCK, U.; SCHULZ, H.-M.; et al. Temperature and salinity variations of Mediterranean Sea surface waters over the last 16,000 years from records of planktonic stable oxygen isotopes and alkenone unsaturation ratios. **Palaeogeography, Palaeoclimatology, Palaeoecology**, v. 158, n. 3, p. 259–280, 2000.
- EPSTEIN, B. L.; D'HONDT, S.; QUINN, J. G.; ZHANG, J.; HARGRAVES, P. E. An effect of dissolved nutrient concentrations on alkenone-based temperature

- estimates. **Paleoceanography**, v. 13, n. 2, p. 122–126, 1998.
- EREZ, J.; LUZ, B. Experimental paleotemperature equation for planktonic foraminifera. **Geochimica et Cosmochimica Acta**, v. 47, n. 6, p. 1025–1031, 1983.
- EVANGELISTA, H.; GURGEL, M.; SIFEDDINE, A.; RIGOZO, N. R.; BOUSSAFIR, M. South Tropical Atlantic anti-phase response to Holocene Bond Events. **Palaeogeography, Palaeoclimatology, Palaeoecology**, v. 415, p. 21–27, 2014.
- FALCÃO, A. P. C.; CURBELO-FERNANDEZ, M. P.; BORGES, A. L. N.; et al. Importância ecológica e econômica da Bacia de Campos: ambiente transicional na margem continental do Oceano Atlântico Sudoeste. In: M. P. Curbelo-Fernandez; A. C. Braga (Orgs.); **Ambiente Bentônico: caracterização ambiental regional da Bacia de Campos, Atlântico Sudoeste.**, 2017. Rio de Janeiro: Elsevier. Habitats, v. 3, p. 1-13.
- FAO/IIASA/ISRIC/ISS-CAS/JRC. Harmonized World Soil Database (version 1.2). FAO, Rome, Italy and IIASA, Laxenburg, Austria, 2012.
- FICK, S.; HIJMANS, R. WorldClim 2: New 1-km spatial resolution climate surfaces for global land areas. **International Journal of Climatology**, v. 37, n. 12, p. 4302–4315, 2017.
- FIETZ, S.; MARTÍNEZ-GARCIA, A.; HUGUET, C.; RUEDA, G.; ROSELL-MELÉ, A. Constraints in the application of the Branched and Isoprenoid Tetraether index as a terrestrial input proxy. **Journal of Geophysical Research: Oceans**, v. 116, n. C10, p. n/a-n/a, 2011.
- FIGUEIREDO JR., A. G.; PACHECO, C. E. P.; DE VASCONCELOS, S. C.; DA SILVA, F. T. Continental Shelf Geomorphology and Sedimentology. **Geology and Geomorphology - Regional Environmental Characterization of the Campos Basin, Southwest Atlantic**. p.13–31, 2016. Rio de Janeiro: Elsevier Editora Ltda.
- FIGUEIREDO, R.; OVALLE, A.; REZENDE, C.; MARTINELLI, L. Carbon and Nitrogen in the Lower Basin of the Paraíba do Sul River, Southeastern Brazil: Element fluxes and biogeochemical processes. **Ambiente & Água - An Interdisciplinary Journal of Applied Science**, v. 6, p. 7–37, 2011.
- FRANCHITO, S. H.; ODA, T. O.; RAO, V. B.; KAYANO, M. T. Interaction between coastal upwelling and local winds at Cabo Frio, Brazil: An observational study. **Journal of Applied Meteorology and Climatology**, v. 47, n. 6, p. 1590–

1598, 2008.

FREYMOND, C. V.; PETERSE, F.; FISCHER, L. V.; et al. Branched GDGT signals in fluvial sediments of the Danube River basin: Method comparison and longitudinal evolution. **Organic Geochemistry**, v. 103, p. 88–96, 2017.

GAN, M. A.; KOUSKY, V. E.; ROPELEWSKI, C. F. The South America Monsoon Circulation and Its Relationship to Rainfall over West-Central Brazil. **Journal of Climate**, v. 17, n. 1, p. 47–66, 2004.

GANACHAUD, A.; WUNSCH, C. Large-Scale Ocean Heat and Freshwater Transports during the World Ocean Circulation Experiment. **Journal of Climate**, v. 16, n. 4, p. 696–705, 2003.

GELIN, F.; BOOGERS, I.; NOORDELOOS, A. A. M.; et al. Resistant biomacromolecules in marine microalgae of the classes eustigmatophyceae and chlorophyceae: Geochemical implications. **Organic Geochemistry**, v. 26, n. 11–12, p. 659–675, 1997.

GLIOZZI, A.; PAOLI, G.; DE ROSA, M.; GAMBACORTA, A. Effect of isoprenoid cyclization on the transition temperature of lipids in thermophilic archaeobacteria. **BBA - Biomembranes**, v. 735, n. 2, p. 234–242, 1983.

GONG, C.; HOLLANDER, D. J. Evidence for differential degradation of alkenones under contrasting bottom water oxygen conditions: implication for paleotemperature reconstruction. **Geochimica et Cosmochimica Acta**, v. 63, n. 3, p. 405–411, 1999.

GONZALEZ-RODRIGUEZ, E.; VALENTIN, J. L.; ANDRÉ, D. L.; JACOB, S. A. Upwelling and downwelling at Cabo Frio (Brazil): comparison of biomass and primary production responses. **Journal of Plankton Research**, v. 14, n. 2, p. 289–306, 1992.

GYLLENCREUTZ, R.; MAHIQUES, M. M.; ALVES, D. V. P.; WAINER, I. K. C. Mid- to late-Holocene paleoceanographic changes on the southeastern Brazilian shelf based on grain size records. **The Holocene**, v. 20, n. 6, p. 863–875, 2010.

HALL, I. R.; BIANCHI, G. G.; EVANS, J. R. Centennial to millennial scale Holocene climate-deep water linkage in the North Atlantic. **Quaternary Science Reviews**, v. 23, n. 14, p. 1529–1536, 2004.

HARADA, N.; SATO, M.; SHIRAIISHI, A.; HONDA, M. C. Characteristics of alkenone distributions in suspended and sinking particles in the northwestern North Pacific. **Geochimica et Cosmochimica Acta**, v. 70, n. 8, p. 2045–

2062, 2006.

HEFTER, J. Analysis of Alkenone Unsaturation Indices with Fast Gas Chromatography/Time-of-Flight Mass Spectrometry. **Analytical Chemistry**, v. 80, n. 6, p. 2161–2170, 2008.

HENDERIKS, J.; WINTER, A.; ELBRÄCHTER, M.; et al. Environmental controls on *Emiliania huxleyi* morphotypes in the Benguela coastal upwelling system (SE Atlantic). **Marine Ecology Progress Series**, v. 448, p. 51–66, 2012.

HERFORT, L.; SCHOUTEN, S.; BOON, J. P.; WOLTERING, M.; et al. Characterization of transport and deposition of terrestrial organic matter in the southern North Sea using the BIT index. **Limnology and Oceanography**, v. 51, n. 5, p. 2196–2205, 2006.

HERFORT, L.; SCHOUTEN, S.; BOON, J. P.; SINNINGHE DAMSTÉ, J. S. Application of the TEX<sub>86</sub> temperature proxy to the southern North Sea. **Organic Geochemistry**, v. 37, n. 12, p. 1715–1726, 2006.

HOEFS, M. J. L.; SCHOUTEN, S.; DE LEEUW, J. W.; et al. Ether lipids of planktonic archaea in the marine water column? **Applied and Environmental Microbiology**, v. 63, n. 8, p. 3090–3095, 1997.

HOEFS, M. J. L.; VERSTEEGH, G. J. M.; RIJPSTRA, W. I. C.; LEEUW, J. W.; SINNINGHE-DAMSTÉ JAAP S. Postdepositional oxic degradation of alkenones: Implications for the measurement of palaeo sea surface temperatures. **Paleoceanography**, v. 13, n. 1, p. 42–49, 1998.

HOOGAKKER, B. A. A.; CHAPMAN, M. R.; MCCAVE, I. N.; et al. Dynamics of North Atlantic Deep Water masses during the Holocene. **Paleoceanography**, v. 26, n. 4, 2011.

HOPMANS, E. C.; SCHOUTEN, S.; PANCOST, R. D.; VAN DER MEER, M. T.; SINNINGHE DAMSTÉ, J. S. Analysis of intact tetraether lipids in archaeal cell material and sediments by high performance liquid chromatography/atmospheric pressure chemical ionization mass spectrometry. **Rapid Commun Mass Spectrom**, v. 14, n. 7, p. 585–589, 2000.

HOPMANS, E. C.; SCHOUTEN, S.; SINNINGHE DAMSTÉ, J. S. The effect of improved chromatography on GDGT-based palaeoproxies. **Organic Geochemistry**, v. 93, p. 1–6, 2016.

HOPMANS, E. C.; WEIJERS, J. W. H.; SCHEFUSS, E.; et al. A novel proxy for terrestrial organic matter in sediments based on branched and isoprenoid

- tetraether lipids. **Earth and Planetary Science Letters**, v. 224, n. 1–2, p. 107–116, 2004.
- HU, J.; MEYERS, P. A.; CHEN, G.; PENG, P.; YANG, Q. Archaeal and bacterial glycerol dialkyl glycerol tetraethers in sediments from the Eastern Lau Spreading Center, South Pacific Ocean. **Organic Geochemistry**, v. 43, n. 0, p. 162–167, 2012.
- HUGUET, C.; CARTES, J. E.; SINNINGHE DAMSTÉ, J. S.; SCHOUTEN, S. Marine crenarchaeotal membrane lipids in decapods: Implications for the TEX<sub>86</sub> paleothermometer. **Geochemistry, Geophysics, Geosystems**, v. 7, n. 11, p. Q11010, doi:10.1029/2006GC001305, 2006.
- HUGUET, C.; KIM, J.-H.; DE LANGE, G. J.; SINNINGHE DAMSTÉ, J. S.; SCHOUTEN, S. Effects of long term oxic degradation on the U<sub>37</sub><sup>K'</sup>, TEX<sub>86</sub> and BIT organic proxies. **Organic Geochemistry**, v. 40, n. 12, p. 1188–1194, 2009.
- HUGUET, C.; KIM, J. H.; SINNINGHE DAMSTÉ, J. S.; SCHOUTEN, S. Reconstruction of sea surface temperature variations in the Arabian Sea over the last 23 kyr using organic proxies (TEX<sub>86</sub> and U<sub>37</sub><sup>K'</sup>). **Paleoceanography**, v. 21, n. 3, p. PA3003, doi:10.1029/2005PA001215, 2006.
- HUGUET, C.; SCHIMMELMANN, A.; THUNELL, R.; et al. A study of the TEX<sub>86</sub> paleothermometer in the water column and sediments of the Santa Barbara Basin, California. **Paleoceanography**, v. 22, n. 3, p. PA3203, doi:10.1029/2006PA001310, 2007.
- HUGUET, C.; SMITTENBERG, R. H.; BOER, W.; SINNINGHE DAMSTÉ, J. S.; SCHOUTEN, S. Twentieth century proxy records of temperature and soil organic matter input in the Drammensfjord, southern Norway. **Organic Geochemistry**, v. 38, n. 11, p. 1838–1849, 2007.
- HURLEY, S. J.; ELLING, F. J.; KÖNNEKE, M.; et al. Influence of ammonia oxidation rate on thaumarchaeal lipid composition and the TEX<sub>86</sub> temperature proxy. **Proceedings of the National Academy of Sciences**, v. 113, n. 28, p. 7762 LP-7767, 2016.
- INGÓLFSSON, Ó.; HJORT, C.; BERKMAN, P. A.; et al. Antarctic glacial history since the Last Glacial Maximum: an overview of the record on land. **Antarctic Science**, v. 10, n. 3, p. 326–344, 1998.
- IPCC. **Climate Change 2007: The physical science basis. Contribution of working group I to the fourth assessment report of the intergovernmental**

**panel on climate change.** Cambridge, United Kingdom and New York, NY, USA, 2007.

IPCC. **Climate Change 2013: The physical science basis. Contribution of working group I to the fifth assessment report of the intergovernmental panel on climate change.** Cambridge, United Kingdom and New York, NY, USA, 2013.

JONAS, A.-S.; SCHWARK, L.; BAUERSACHS, T. Late Quaternary water temperature variations of the Northwest Pacific based on the lipid paleothermometers  $\text{TEX}_{86}^{\text{H}}$ ,  $\text{U}_{37}^{\text{K}'}$  and LDI. **Deep Sea Research Part I: Oceanographic Research Papers**, v. 125, p. 81–93, 2017.

DE JONGE, C.; HOPMANS, E. C.; STADNITSKAIA, A.; et al. Identification of novel penta- and hexamethylated branched glycerol dialkyl glycerol tetraethers in peat using HPLC–MS2, GC–MS and GC–SMB-MS. **Organic Geochemistry**, v. 54, p. 78–82, 2013.

DE JONGE, C.; HOPMANS, E. C.; ZELL, C. I.; et al. Occurrence and abundance of 6-methyl branched glycerol dialkyl glycerol tetraethers in soils: Implications for palaeoclimate reconstruction. **Geochimica et Cosmochimica Acta**, v. 141, p. 97–112, 2014.

DE JONGE, C.; STADNITSKAIA, A.; CHERKASHOV, G.; SINNINGHE DAMSTÉ, J. S. Branched glycerol dialkyl glycerol tetraethers and crenarchaeol record post-glacial sea level rise and shift in source of terrigenous brGDGTs in the Kara Sea (Arctic Ocean). **Organic Geochemistry**, v. 92, p. 42–54, 2016.

DE JONGE, C.; STADNITSKAIA, A.; HOPMANS, E. C.; et al. In situ produced branched glycerol dialkyl glycerol tetraethers in suspended particulate matter from the Yenisei River, Eastern Siberia. **Geochimica et Cosmochimica Acta**, v. 125, p. 476–491, 2014.

KARNER, M. B.; DELONG, E. F.; KARL, D. M. Archaeal dominance in the mesopelagic zone of the Pacific Ocean. **Nature**, v. 409, n. 6819, p. 507–510, 2001.

KATES, M.; SASTRY, P. S.; YENGOYAN, L. S. Isolation and characterization of a diether analog of phosphatidylglyceophosphate from *Halobacterium cutirubrum*. **Biochim. Biophys. Acta**, v. 70, p. 705–707, 1963.

KIM, J.-H.; RIMBU, N.; LORENZ, S. J.; et al. North Pacific and North Atlantic sea-surface temperature variability during the Holocene. **Quaternary Science Reviews**, v. 23, n. 20–22, p. 2141–2154, 2004.

- KIM, J.-H.; SCHOUTEN, S.; BUSCAIL, R.; et al. Origin and distribution of terrestrial organic matter in the NW Mediterranean (Gulf of Lions): Exploring the newly developed BIT index. **Geochemistry, Geophysics, Geosystems**, v. 7, n. 11, p. DOI: 10.1029/2006GC001306, 2006.
- KIM, J. H.; CROSTA, X.; MICHEL, E.; et al. Impact of lateral transport on organic proxies in the Southern Ocean. **Quaternary Research**, v. 71, n. 2, p. 246–250, 2009.
- KIM, J. H.; VAN DER MEER, J.; SCHOUTEN, S.; et al. New indices and calibrations derived from the distribution of crenarchaeal isoprenoid tetraether lipids: Implications for past sea surface temperature reconstructions. **Geochimica et Cosmochimica Acta**, v. 74, n. 16, p. 4639–4654, 2010.
- KIM, J. H.; SCHOUTEN, S.; HOPMANS, E. C.; DONNER, B.; SINNINGHE DAMSTÉ, J. S. Global sediment core-top calibration of the TEX<sub>86</sub> paleothermometer in the ocean. **Geochimica et Cosmochimica Acta**, v. 72, n. 4, p. 1154–1173, 2008.
- KIM, J.; ROMERO, O. E.; LOHMANN, G.; et al. Pronounced subsurface cooling of North Atlantic waters off Northwest Africa during Dansgaard – Oeschger interstadials. **Earth and Planetary Science Letters**, v. 340, n. 0, p. 95–102, 2012.
- KOGA, Y.; AKAGAWA-MATSUSHITA, M.; OHGA, M.; NISHIHARA, M. Taxonomic Significance of the Distribution of Component Parts of Polar Ether Lipids in Methanogens. **Systematic and Applied Microbiology**, v. 16, n. 3, p. 342–351, 1993.
- KOGA, Y.; NISHIHARA, M.; MORII, H.; AKAGAWA-MATSUSHITA, M. Ether polar lipids of methanogenic bacteria: structures, comparative aspects, and biosyntheses. **Microbiological reviews**, v. 57, n. 1, p. 164–182, 1993.
- KÖNNEKE, M.; BERNHARD, A.; DE LA TORRE, J.; et al. Isolation of an autotrophic ammonia-oxidizing marine archaeon. **Nature**, v. 437, p. 543–546, 2005.
- KOWSMANN, R.; COSTA, M. **Sedimentação quaternária da margem continental brasileira e das áreas oceânicas adjacentes - In: Projeto REMAC - Reconhecimento Global da Margem Continental Brasileira**. v. 8, p. 1–55, 1979. Rio de Janeiro, Petrobrás, Cenpes, Dintep.
- LACERDA, L. D.; CARVALHO, C. E. V.; REZENDE, C. E.; PFEIFFER, W. C. Mercury in sediments from the Paraíba do Sul River continental shelf, S.E.

- Brazil. **Marine Pollution Bulletin**, v. 26, n. 4, p. 220–222, 1993.
- LANGWORTHY, T. A. Long-chain diglycerol tetraethers from *Thermoplasma acidophilum*. **Biochimica et Biophysica Acta (BBA)/Lipids and Lipid Metabolism**, v. 487, n. 1, p. 37–50, 1977.
- LAZZARI, L.; WAGENER, A. L. R.; CARREIRA, R. S.; et al. Climate variability and sea level change during the Holocene: Insights from an inorganic multi-proxy approach in the SE Brazilian continental shelf. **Quaternary International**, 2018.
- LEDRU, M.-P.; MOURGUIART, P.; RICCOMINI, C. Related changes in biodiversity, insolation and climate in the Atlantic rainforest since the last interglacial. **Palaeogeography, Palaeoclimatology, Palaeoecology**, v. 271, n. 1, p. 140–152, 2009.
- LEDUC, G.; SCHNEIDER, R.; KIM, J.-H.; LOHMANN, G. Holocene and Eemian sea surface temperature trends as revealed by alkenone and Mg/Ca paleothermometry. **Quaternary Science Reviews**, v. 29, n. 7, p. 989–1004, 2010.
- LEE, K. E.; KIM, J.-H.; WILKE, I.; HELMKE, P.; SCHOUTEN, S. A study of the alkenone, TEX<sub>86</sub>, and planktonic foraminifera in the Benguela Upwelling System: Implications for past sea surface temperature estimates. **Geochemistry Geophysics Geosystems**, v. 9, p. Q10019, doi:10.1029/2008GC002056, 2008.
- DE LEEUW, J. W.; RIJPSTRA, W. I. C.; SCHENCK, P. A. The occurrence and identification of C<sub>30</sub>, C<sub>31</sub> and C<sub>32</sub> alkan-1,15-diols and alkan-15-one-1-ols in unit-I and unit-II Black Sea sediments. **Geochimica Et Cosmochimica Acta**, v. 45, n. 11, p. 2281–2285, 1981.
- LEEUW, J. W.; VAN DER MEER, F. W.; RIJPSTRA, I.; SCHENCK, P. A. On the occurrence and structural identification of long chain unsaturated ketones and hydrocarbons in sediments. **Physics and Chemistry of The Earth**, v. 12, p. 211–217, 1980.
- LEIDER, A.; HINRICHS, K. U.; MOLLENHAUER, G.; VERSTEEGH, G. J. M. Core-top calibration of the lipid-based U<sub>37</sub><sup>K'</sup> and TEX<sub>86</sub> temperature proxies on the southern Italian shelf (SW Adriatic Sea, Gulf of Taranto). **Earth and Planetary Science Letters**, v. 300, n. 1–2, p. 112–124, 2010.
- LESSA, D. V. O.; RAMOS, R. P.; BARBOSA, C. F.; et al. Planktonic foraminifera in the sediment of a western boundary upwelling system off Cabo Frio, Brazil.

- Marine Micropaleontology**, v. 106, p. 55–68, 2014.
- LESSA, D. V. O.; VENANCIO, I. M.; DOS SANTOS, T. P.; et al. Holocene oscillations of Southwest Atlantic shelf circulation based on planktonic foraminifera from an upwelling system (off Cabo Frio, Southeastern Brazil). **The Holocene**, v. 26, n. 8, p. 1175–1187, 2016.
- LIEBMANN, B.; MARENGO, J. A. Interannual variability of the rainy season and rainfall in the Brazilian Amazon Basin. **Journal of Climate**, v. 14, n. 22, p. 4308–4318, 2001. American Meteorological Society.
- LIMA, I. D.; GARCIA, C. A. E.; MOLLER, O. O. Ocean surface processes on the southern Brazilian shelf: Characterization and seasonal variability. **Cont. Shelf Res.**, v. 16, n. 10, p. 1307–1317, 1996.
- LIU, Z.; PAGANI, M.; ZINNIKER, D.; et al. Global Cooling During the Eocene-Oligocene Climate Transition. **Science**, v. 323, n. 5918, p. 1187–1190, 2009.
- LOCARNINI, R. A.; MISHONOV, A. V.; ANTONOV, J. I.; et al. **World Ocean Atlas 2013, Volume 1: Temperature**. NOAA Atlas NESDIS, 2013.
- LOPES DOS SANTOS, R. A.; SPOONER, M. I.; BARROWS, T. T.; et al. Comparison of organic ( $U_{37}^{K'}$ ,  $TEX_{86}^H$ , LDI) and faunal proxies (foraminiferal assemblages) for reconstruction of late Quaternary sea surface temperature variability from offshore southeastern Australia. **Paleoceanography**, v. 28, n. 3, p. 377–387, 2013.
- LOPES DOS SANTOS, R.; PRANGE, M.; CASTAÑEDA, I.; et al. Glacial–interglacial variability in Atlantic meridional overturning circulation and thermocline adjustments in the tropical North Atlantic. **Earth and Planetary Science Letters**, v. 300, n. 3–4, p. 407–414, 2010.
- LORENZZETTI, J. A.; GAETA, S. The Cape Frio upwelling effect over the South Brazil Bight northern sector shelf waters: a study using AVHRR images. **International Archives of Photogrammetry and Remote Sensing**, v. XXXI, n. Part B7, p. 448–453, 1996.
- LOURENÇO, R. A.; MAGALHÃES, C. A.; MAHIQUES, M. M.; TANIGUCHI, S.; BÍCEGO, M. C. Distribution of terrigenous and marine material along the Southeastern Brazilian continental margin. **Regional Studies in Marine Science**, v. 14, p. 118–125, 2017.
- LOURENÇO, R. A.; MARTINS, C. C.; TANIGUCHI, S.; et al. Distribution and evolution of sterols and aliphatic hydrocarbons in dated marine sediment cores from the Cabo Frio upwelling region, SW Atlantic, Brazil.

- Environmental Science and Pollution Research**, v. 24, n. 24, p. 19888–19901, 2017.
- LÜ, X.; YANG, H.; SONG, J.; et al. Sources and distribution of isoprenoid glycerol dialkyl glycerol tetraethers (GDGTs) in sediments from the east coastal sea of China: Application of GDGT-based paleothermometry to a shallow marginal sea. **Organic Geochemistry**, v. 75, n. 0, p. 24–35, 2014.
- MACARIO, K. D.; SOUZA, R. C. C. L.; AGUILERA, O. A.; et al. Marine reservoir effect on the Southeastern coast of Brazil: results from the Tarioba shellmound paired samples. **Journal of Environmental Radioactivity**, v. 143, p. 14–19, 2015.
- MAGALHÃES, C. A. **Reconstrução paleoceanográfica de alta resolução baseada em marcadores geoquímicos orgânicos região de Cabo Frio**Instituto Oceanográfico, 2010. São Paulo: USP.
- MAHIQUES, M. M.; FUKUMOTO, M. M.; SILVEIRA, I. C. A.; FIGUEIRA, R. C. L.; MELLO-E-SOUSA, S. H. Sedimentary changes on the Southeastern Brazilian upper slope during the last 35,000 years. **Anais Da Academia Brasileira De Ciencias**, v. 79, p. 171–181, 2007.
- MAHIQUES, M. M.; MISHIMA, Y.; RODRIGUES, M. Characteristics of the sedimentary organic matter on the inner and middle continental shelf between Guanabara Bay and Sao Francisco do Sul, southeastern Brazilian margin. **Continental Shelf Research**, v. 19, n. 6, p. 775–798, 1999.
- MAHIQUES, M. M.; SILVEIRA, I. C. A.; DE MELLO E SOUSA, S. H.; RODRIGUES, M. Post-LGM sedimentation on the outer shelf-upper slope of the northernmost part of the São Paulo Bight, southeastern Brazil. **Marine Geology**, v. 181, n. 4, p. 387–400, 2002.
- MAHIQUES, M. M.; SILVEIRA, I. C. A.; SOUSA, S. H. M.; FUKUMOTO, M. M. Modern sedimentation in the Cabo Frio upwelling system. **Anais da Academia Brasileira de Ciências**, v. 77, p. 535–548, 2005.
- MAHIQUES, M. M.; TESSLER, M. G.; MARIA CIOTTI, A.; et al. Hydrodynamically driven patterns of recent sedimentation in the shelf and upper slope off Southeast Brazil. **Continental Shelf Research**, v. 24, n. 15, p. 1685–1697, 2004.
- MANN, M. E.; BRADLEY, R. S.; HUGHES, M. K. Global-scale temperature patterns and climate forcing over the past six centuries. **Nature**, v. 392, p. 779, 1998.

- MANN, M. E.; ZHANG, Z.; RUTHERFORD, S.; et al. Global Signatures and Dynamical Origins of the Little Ice Age and Medieval Climate Anomaly. **Science**, v. 326, n. 5957, p. 1256 LP-1260, 2009.
- MARENCO, J. A.; SOARES, W. R.; SAULO, C.; NICOLINI, M. Climatology of the Low-Level Jet East of the Andes as Derived from the NCEP–NCAR Reanalyses: Characteristics and Temporal Variability. **Journal of Climate**, v. 17, n. 12, p. 2261–2280, 2004. American Meteorological Society.
- MARONE, E.; KNOPPERS, B. A.; SOUZA, W. F. L.; SILVEIRA, I. C. A.; GODOI, S. S. The Brazil current: physical-biogeochemical domains. In: L. Kon-Kee; L. Atkinson; R. Quinones (Orgs.); **Carbon and nutrient fluxes in continental margins: a global synthesis**. p.153–170, 2010. Berlin: Springer Verlag.
- MATSUURA, Y. A probable cause of recruitment failure of the Brazilian sardine, *Sardinella aurita*, population during 1974/75 spawning season. **South African Journal of Marine Science**, v. 17, n. 1, p. 29–35, 1996.
- MAYEWSKI, P.; ROHLING, E.; CURTSTAGER, J.; et al. Holocene climate variability. **Quaternary Research**, v. 62, n. 3, p. 243–255, 2004.
- MCCAVE, I. N. Size spectra and aggregation of suspended particles in the deep ocean. **Deep Sea Research Part A. Oceanographic Research Papers**, v. 31, n. 4, p. 329–352, 1984.
- MCGREGOR, H. V.; EVANS, M. N.; GOOSSE, H.; et al. Robust global ocean cooling trend for the pre-industrial Common Era. **Nature Geoscience**, v. 8, p. 671, 2015.
- MÉJANELLE, L.; SANCHEZ-GARGALLO, A.; BENTALEB, I.; GRIMALT, J. O. Long chain n-alkyl diols, hydroxy ketones and sterols in a marine eustigmatophyte, *Nannochloropsis gaditana*, and in *Brachionus plicatilis* feeding on the algae. **Organic Geochemistry**, v. 34, n. 4, p. 527–538, 2003.
- MENARY, M. B.; PARK, W.; LOHMANN, K.; et al. A multimodel comparison of centennial Atlantic meridional overturning circulation variability. **Climate Dynamics**, v. 38, n. 11–12, p. 2377–2388, 2012.
- MENDOZA, U.; NETO, A. A.; ABUCHACRA, R. C.; et al. Geoacoustic character, sedimentology and chronology of a cross-shelf holocene sediment deposit off cabo frio, Brazil (southwest Atlantic Ocean). **Geo-Marine Letters**, v. 34, n. 4, p. 297–314, 2014.
- METZLER, P. M.; GLIBERT, P. M.; GAETA, S. A.; LUDLAM, J. M. New and regenerated production in the South Atlantic off Brazil. **Deep Sea Research**

**Part I: Oceanographic Research Papers**, v. 44, n. 3, p. 363–384, 1997.

MEYERS, P. A. Organic geochemical proxies of paleoceanographic, plaeolimnologic, and plaeoclimatic processes. **Organic Geochemistry**, v. 27, n. 5, p. 213–250, 1997.

MEYERS, P. A. Applications of organic geochemistry to paleolimnological reconstructions: a summary of examples from the Laurentian Great Lakes. **Organic Geochemistry**, v. 34, n. 2, p. 261–289, 2003.

MOLLENHAUER, G.; BASSE, A.; KIM, J.; SINNINGHE, J. S.; FISCHER, G. A four-year record of  $U_{37}^K$  and  $TEX_{86}$  derived sea surface temperature estimates from sinking particles in the filamentous upwelling region off Cape Blanc, Mauritania. **Deep-Sea Research Part I**, v. 97, n. 0, p. 67–79, 2015.

MOLLENHAUER, G.; INTHORN, M.; VOGT, T.; et al. Aging of marine organic matter during cross-shelf lateral transport in the Benguela upwelling system revealed by compound-specific radiocarbon dating. **Geochemistry, Geophysics, Geosystems**, v. 8, n. 9, p. Q09004, doi:10.1029/2007GC001603, 2007.

MÜLLER, P. J.; FISCHER, G. Global core-top calibration of  $U_{37}^K$  (update), 9. set. 2004. PANGAEA. Disponível em: <<https://doi.org/10.1594/PANGAEA.126662>>.

MÜLLER, P. J.; KIRST, G.; RUHLAND, G.; VON STORCH, I.; ROSELL-MELE, A. Calibration of the alkenone paleotemperature index  $U_{37}^K$  based on core-tops from the eastern South Atlantic and the global ocean (60 degrees N-60 degrees S). **Geochimica Et Cosmochimica Acta**, v. 62, n. 10, p. 1757–1772, 1998.

MURRAY, A. E.; PRESTON, C. M.; MASSANA, R.; et al. Seasonal and Spatial Variability of Bacterial and Archaeal Assemblages in the Coastal Waters near Anvers Island, Antarctica. **Applied and Environmental Microbiology**, v. 64, n. 7, p. 2585–2595, 1998.

NAGAI, R. H.; SOUSA, S. H. M.; BURONE, L.; MAHIQUES, M. M. Paleoproductivity changes during the Holocene in the inner shelf of Cabo Frio, southeastern Brazilian continental margin: Benthic foraminifera and sedimentological proxies. **Quaternary International**, v. 206, n. 1, p. 62–71, 2009.

NAGAI, R.; MARTINS, V.; BURONE, L.; et al. In-phase inter-hemispheric changes in two upwelling regions: the Southeast Brazilian and and NW Iberian

- margins. **Journal of Sedimentary Environments**, v. 1, p. 43–67, 2016.
- NÜRNBERG, D.; BIJMA, J.; HEMLEBEN, C. Assessing the reliability of magnesium in foraminiferal calcite as a proxy for water mass temperatures. **Geochimica et Cosmochimica Acta**, v. 60, n. 5, p. 803–814, 1996.
- O'BRIEN, S. R.; MAYEWSKI, P. A.; MEEKER, L. D.; et al. Complexity of Holocene Climate as Reconstructed from a Greenland Ice Core. **Science**, v. 270, n. 5244, p. 1962–1964, 1995.
- OLIVEIRA, D. R. P.; CORDEIRO, L. G. M. S.; CARREIRA, R. S. Characterization of organic matter in cross-margin sediment transects of an upwelling region in the Campos Basin (SW Atlantic, Brazil) using lipid biomarkers. **Biogeochemistry**, v. 112, n. 1, p. 311–327, 2013.
- OSHIMA, M.; MIYAGAWA, A. Comparative studies on the fatty acid composition of moderately and extremely thermophilic bacteria. **Lipids**, v. 9, n. 7, p. 476–480, 1974.
- OVALLE, A. R. C.; SILVA, C. F.; REZENDE, C. E.; et al. Long-term trends in hydrochemistry in the Paraíba do Sul River, southeastern Brazil. **Journal of Hydrology**, v. 481, p. 191–203, 2013.
- PANCOST, R. D.; HOPMANS, E. C.; SINNINGHE DAMSTÉ, J. S. Archaeal lipids in Mediterranean cold seeps: molecular proxies for anaerobic methane oxidation. **Geochimica et Cosmochimica Acta**, v. 65, n. 10, p. 1611–1627, 2001.
- PANCOST, R. D.; SINNINGHE DAMSTÉ, J. S. Carbon isotopic compositions of prokaryotic lipids as tracers of carbon cycling in diverse settings. **Chemical Geology**, v. 195, n. 1, p. 29–58, 2003.
- PARK, E.; HEFTER, J.; FISCHER, G.; MOLLENHAUER, G. TEX<sub>86</sub> in sinking particles in three eastern Atlantic upwelling regimes. **Organic Geochemistry**, v. 124, p. 151–163, 2018.
- PEARSON, E. J.; JUGGINS, S.; TALBOT, H. M.; et al. A lacustrine GDGT-temperature calibration from the Scandinavian Arctic to Antarctic: Renewed potential for the application of GDGT-paleothermometry in lakes. **Geochimica et Cosmochimica Acta**, v. 75, n. 20, p. 6225–6238, 2011.
- PETERS, K. E.; WALTERS, C. C.; MOLDOWAN, J. M. **The Biomarker Guide: Volume 1: Biomarkers and Isotopes in the Environment and Human History**. 2<sup>o</sup> ed. Cambridge: Cambridge University Press, 2004.
- PETERSE, F.; KIM, J.; SCHOUTEN, S.; et al. Constraints on the application of the

- MBT/CBT palaeothermometer at high latitude environments (Svalbard, Norway). **Organic Geochemistry**, v. 40, n. 6, p. 692–699, 2009.
- PETERSE, F.; VAN DER MEER, J.; SCHOUTEN, S.; et al. Revised calibration of the MBT-CBT paleotemperature proxy based on branched tetraether membrane lipids in surface soils. **Geochimica et Cosmochimica Acta**, v. 96, p. 215–229, 2012.
- PETERSON, R. G.; STRAMMA, L. Upper level circulation in the South Atlantic Ocean. **Prog. Oceanogr.**, v. 26, n. 26, p. 1–73, 1991.
- PITCHER, A.; VILLANUEVA, L.; C HOPMANS, E.; et al. Niche segregation of ammonia-oxidizing archaea and anammox bacteria in the Arabian Sea oxygen minimum zone. **ISME Journal**, v. 5, p. 1896–1904, 2011.
- PITCHER, A.; WUCHTER, C.; SIEDENBERG, K.; SCHOUTEN, S.; SINNINGHE DAMSTÉ, J. S. Crenarchaeol tracks winter blooms of ammonia-oxidizing Thaumarchaeota in the coastal North Sea. **Limnology and Oceanography**, v. 56, n. 6, p. 2308–2318, 2011.
- PIVEL, M. A. G.; SANTAROSA, A. C. A.; TOLEDO, F. A. L.; COSTA, K. B. The Holocene onset in the southwestern South Atlantic. **Palaeogeography, Palaeoclimatology, Palaeoecology**, v. 374, p. 164–172, 2013.
- POPP, B. N.; PRAHL, F. G.; WALLSGROVE, R. J.; JAMIE, T. Seasonal patterns of alkenone production in the subtropical oligotrophic North Pacific. **Paleoceanography**, v. 21, n. 1, 2006.
- PRADO, L. F.; WAINER, I.; CHIESSI, C. M. Mid-Holocene PMIP3/CMIP5 model results: Intercomparison for the South American Monsoon System. **The Holocene**, v. 23, n. 12, p. 1915–1920, 2013.
- PRADO, L. F.; WAINER, I.; CHIESSI, C. M.; LEDRU, M. P.; TURCQ, B. A mid-Holocene climate reconstruction for eastern South America. **Climate of the Past**, v. 9, n. 5, p. 2117–2133, 2013.
- PRAHL, F. G.; COLLIER, R. B.; DYMOND, J.; LYLE, M.; SPARROW, M. A. A biomarker perspective on prymnesiophyte in the northeast Pacific Ocean. **Deep-Sea Research I**, v. 40, n. 10, p. 2061–2076, 1993.
- PRAHL, F. G.; MUEHLHAUSEN, L. A.; ZAHNLE, D. L. Further evaluation of long-chain alkenones as indicators of paleoceanographic conditions. **Geochimica et Cosmochimica Acta**, v. 52, n. 9, p. 2303–2310, 1988.
- PRAHL, F. G.; PILSKALN, C. H.; SPARROW, M. A. Seasonal record for alkenones in sedimentary particles from the Gulf of Maine. **Deep Sea Research Part I:**

- Oceanographic Research Papers**, v. 48, n. 2, p. 515–528, 2001.
- PRAHL, F. G.; RONTANI, J. F.; ZABETI, N.; WALINSKY, S. E.; SPARROW, M. A. Systematic pattern in  $U_{37}^{K'}$  - Temperature residuals for surface sediments from high latitude and other oceanographic settings. **Geochimica et Cosmochimica Acta**, v. 74, n. 1, p. 131–143, 2010.
- PRAHL, F. G.; SPARROW, M. A.; WOLFE, G. V. Physiological impacts on alkenone paleothermometry. **Paleoceanography**, v. 18, n. 2, 2003.
- PRAHL, F. G.; WAKEHAM, S. G. Calibration of unsaturation patterns in long-chain ketone compositions for palaeotemperature assessment. **Nature**, v. 330, n. 6146, p. 367–369, 1987.
- QIAN, P.-Y.; WANG, Y.; LEE, O. O.; et al. Vertical stratification of microbial communities in the Red Sea revealed by 16S rDNA pyrosequencing. **The Isme Journal**, v. 5, p. 507, 2010.
- RAHMSTORF, S. Ocean circulation and climate during the past 120,000 years. **Nature**, v. 419, n. 6903, p. 207–214, 2002.
- RAHMSTORF, S.; FEULNER, G. Chapter 2 - Paleoclimatic Ocean Circulation and Sea-Level Changes. In: G. Siedler; S. M. Griffies; J. Gould; J. A. B. T.-I. G. Church (Orgs.); **Ocean Circulation and Climate**. v. 103, p.31–56, 2013. Academic Press.
- RAMPEN, S. W.; SCHOUTEN, S.; KONING, E.; BRUMMER, G. J. A.; SINNINGHE DAMSTÉ, J. S. A 90 kyr upwelling record from the northwestern Indian Ocean using a novel long-chain diol index. **Earth and Planetary Science Letters**, v. 276, n. 1–2, p. 207–213, 2008.
- RAMPEN, S. W.; SCHOUTEN, S.; SCHEFUSS, E.; SINNINGHE DAMSTÉ, J. S. Impact of temperature on long chain diol and mid-chain hydroxy methyl alkanoate composition in Proboscia diatoms: Results from culture and field studies. **Organic Geochemistry**, v. 40, n. 11, p. 1124–1131, 2009.
- RAMPEN, S. W.; WILLMOTT, V.; KIM, J. H.; et al. Long chain 1,13- and 1,15-diols as a potential proxy for palaeotemperature reconstruction. **Geochimica et Cosmochimica Acta**, v. 84, p. 204–216, 2012.
- RAMSEY, C. B.; LEE, S. Recent and planned developments of the program OxCal. **Radiocarbon**, v. 55, n. 2–3, p. 720–730, 2013.
- RAY, P. H.; WHITE, D. C.; BROCK, T. D. Effect of Temperature on the Fatty Acid Composition of *Thermus aquaticus*. **Journal of Bacteriology**, v. 106, n. 1, p. 25–30, 1971.

- RAZIK, S.; CHIESSI, C. M.; ROMERO, O. E.; VON DOBENECK, T. Interaction of the South American Monsoon System and the Southern Westerly Wind Belt during the last 14kyr. **Palaeogeography, Palaeoclimatology, Palaeoecology**, v. 374, p. 28–40, 2013.
- RAZIK, S.; GOVIN, A.; CHIESSI, C. M.; VON DOBENECK, T. Depositional provinces, dispersal, and origin of terrigenous sediments along the SE South American continental margin. **Marine Geology**, v. 363, p. 261–272, 2015.
- REID, J. L. On the total geostrophic circulation of the South Atlantic Ocean: Flow patterns, tracers, and transports. **Progress in Oceanography**, v. 23, n. 3, p. 149–244, 1989.
- REIMER, P. J.; BAILLIE, M. G. L.; BARD, E.; et al. IntCal09 and Marine09 Radiocarbon Age Calibration Curves, 0-50,000 Years cal BP. **Radiocarbon**, v. 51, n. 4, p. 1111–1150, 2009.
- REIMER, P. J.; BARD, E.; BAYLISS, A.; et al. IntCal13 and Marine13 radiocarbon age calibration curves 0–50,000 years cal BP. **Radiocarbon**, v. 55, n. 4, p. 1869–1887, 2013.
- ROBERTSON, A.; MECHOSO, C. Interannual and interdecadal variability of the South Atlantic Convergence Zone. **Monthly weather review**, v. 128, n. 8, p. 2947–2957, 2000.
- RODRIGO-GÁMIZ, M.; RAMPEN, S. W.; HAAS, H. DE; et al. Constraints on the applicability of the organic temperature proxies  $U_{37}^{K'}$ ,  $TEX_{86}$  and LDI in the subpolar region around Iceland. **Biogeosciences**, v. 12, p. 6573–6590, 2015.
- RODRIGUES, R. R.; LORENZZETTI, J. A numerical study of the effects of bottom topography and coastline geometry on the Southeast Brazilian coastal upwelling. **Continental Shelf Research**2, v. 21, p. 371–394, 2001.
- RODRIGUES, S. V.; MARINHO, M. M.; CUBAS JONCK, C. C.; et al. Phytoplankton community structures in shelf and oceanic waters off southeast Brazil (20°–25°S), as determined by pigment signatures. **Deep Sea Research Part I: Oceanographic Research Papers**, v. 88, n. Supplement C, p. 47–62, 2014.
- ROHLING, E.; MAYEWSKI, P.; ABU-ZIED, R.; CASFORD, J.; HAYES, A. Holocene atmosphere-ocean interactions: Records from Greenland and the Aegean sea. **Climate Dynamics**, v. 18, n. 7, p. 587–594, 2002.
- ROSELL-MELÉ, A.; EGLINTON, G.; PFLAUMANN, U.; SARNTHEIN, M. Atlantic core-top calibration of the  $U_{37}^K$  index as a sea-surface palaeotemperature indicator. **Geochimica et Cosmochimica Acta**, v. 59, n. 15, p. 3099–3107,

- 1995.
- ROSELL-MELÉ, A.; EGLINTON, G.; PFLAUMANN, U.; SARNTHEIN, M. Atlantic core-top calibration of the  $U_{37}^K$  index as a sea-surface paleotemperature indicator. **Geochimica et Cosmochimica Acta**, v. 59, n. 15, p. 3099–3107, 1995.
- ROSELL-MELÉ, A.; PRAHL, F. G. Seasonality of  $U_{37}^{K'}$  temperature estimates as inferred from sediment trap data. **Quaternary Science Reviews**, v. 72, p. 128–136, 2013.
- RUEDA, G.; ROSELL-MELÉ, A.; ESCALA, M.; GYLLENCREUTZ, R.; BACKMAN, J. Comparison of instrumental and GDGT-based estimates of sea surface and air temperatures from the Skagerrak. **Organic Geochemistry**, v. 40, n. 2, p. 287–291, 2009.
- RÜHLEMANN, C.; BUTZIN, M. Alkenone temperature anomalies in the Brazil-Malvinas confluence area caused by lateral advection of suspended particulate material. **Geochemistry, Geophysics, Geosystems**, v. 7, n. 10, p. Q10015, DOI: 10.1029/2006GC001251, 2006.
- SANDERS, C. J.; CALDEIRA, P. P.; SMOAK, J. M.; et al. Recent organic carbon accumulation (similar to 100 years) along the Cabo Frio, Brazil upwelling region. **Continental Shelf Research**, v. 75, p. 68–75, 2014.
- SANTOS, T. P.; BELEM, A. L.; BARBOSA, C. F.; DOKKEN, T.; ALBUQUERQUE, A. L. S. Paleoceanographic reconstruction of the western equatorial Atlantic during the last 40 kyr. **Palaeogeography, Palaeoclimatology, Palaeoecology**, v. 415, n. 0, p. 14–20, 2014.
- SCHEEL-YBERT, R.; GOUVEIA, S. E. M.; PESSENDA, L. C. R.; et al. Holocene palaeoenvironmental evolution in the São Paulo State (Brazil), based on anthracology and soil  $\delta^{13}C$  analysis. **The Holocene**, v. 13, n. 1, p. 73–81, 2003.
- SCHIEBEL, R.; ZELTNER, A.; F. TREPPKE, U.; et al. Distribution of diatoms, coccolithophores and planktic foraminifers along a trophic gradient during SW monsoon in the Arabian Sea. **Marine Micropaleontology**, v. 51, p. 345–371, 2004.
- SCHILMAN, B.; BAR-MATTHEWS, M.; ALMOGI-LABIN, A. Global climate instability reflected by Eastern Mediterranean marine records during the late Holocene. **Palaeogeography, Palaeoclimatology, Palaeoecology**, v. 176, n. 1–4, p. 151–176, 2001.

- SCHMID, C.; SIEDLER, G.; ZENK, W. Dynamics of Intermediate Water Circulation in the Subtropical South Atlantic. **Journal of Physical Oceanography**, v. 30, n. 12, p. 3191–3211, 2000.
- SCHMIDT, F.; HINRICHS, K.-U.; ELVERT, M. Sources, transport, and partitioning of organic matter at a highly dynamic continental margin. **Marine Chemistry**, v. 118, n. 1, p. 37–55, 2010.
- SCHOUTEN, S.; HOPMANS, E. C.; VAN DER MEER, J.; et al. An interlaboratory study of TEX<sub>86</sub> and BIT analysis using high-performance liquid chromatography–mass spectrometry. **Geochemistry, Geophysics, Geosystems**, v. 10, n. 3, 2009.
- SCHOUTEN, S.; HOPMANS, E. C.; PANCOST, R. D.; SINNINGHE DAMSTÉ, J. S. Widespread occurrence of structurally diverse tetraether membrane lipids: Evidence for the ubiquitous presence of low-temperature relatives of hyperthermophiles. **Proceedings of the National Academy of Sciences**, v. 97, n. 26, p. 14421–14426, 2000.
- SCHOUTEN, S.; HOPMANS, E. C.; ROSELL-MELÉ, A.; et al. An interlaboratory study of TEX<sub>86</sub> and BIT analysis of sediments, extracts, and standard mixtures. **Geochemistry, Geophysics, Geosystems**, v. 14, n. 12, p. 5263–5285, 2013.
- SCHOUTEN, S.; HOPMANS, E. C.; SCHEFUSS, E.; SINNINGHE DAMSTÉ, J. S. Distributional variations in marine crenarchaeol membrane lipids: a new tool for reconstructing ancient sea water temperatures? **Earth and Planetary Science Letters**, v. 204, n. 1–2, p. 265–274, 2002.
- SCHOUTEN, S.; HOPMANS, E. C.; SINNINGHE DAMSTÉ, J. S. The organic geochemistry of glycerol dialkyl glycerol tetraether lipids: A review. **Organic Geochemistry**, v. 54, n. 0, p. 19–61, 2013.
- SCHOUTEN, S.; HUGUET, C.; HOPMANS, E. C.; KIENHUIS, M. V. M.; SINNINGHE DAMSTÉ, J. S. Analytical Methodology for TEX<sub>86</sub> Paleothermometry by High-Performance Liquid Chromatography/Atmospheric Pressure Chemical Ionization-Mass Spectrometry. **Analytical Chemistry**, v. 79, n. 7, p. 2940–2944, 2007.
- SCHOUTEN, S.; VAN DER MEER, M. T. J.; HOPMANS, E. C.; et al. Archaeal and bacterial glycerol dialkyl glycerol tetraether lipids in hot springs of Yellowstone National Park. **Applied and Environmental Microbiology**, v. 73, n. 19, p. 6181–6191, 2007.

- SCHOUTEN, S.; PITCHER, A.; HOPMANS, E. C.; et al. Intact polar and core glycerol dibiphytanyl glycerol tetraether lipids in the Arabian Sea oxygen minimum zone: I. Selective preservation and degradation in the water column and consequences for the TEX<sub>86</sub>. **Geochimica et Cosmochimica Acta**, v. 98, p. 228–243, 2012.
- SHAH, S. R.; MOLLENHAUER, G.; OHKOUCHI, N.; EGLINTON, T. I.; PEARSON, A. Origins of archaeal tetraether lipids in sediments: Insights from radiocarbon analysis. **Geochimica et Cosmochimica Acta**, v. 72, n. 18, p. 4577–4594, 2008.
- SIFEDDINE, A.; MARTIN, L.; TURCQ, B.; et al. Variations of the Amazonian rainforest environment: a sedimentological record covering 30,000 years. **Palaeogeography, Palaeoclimatology, Palaeoecology**, v. 168, n. 3, p. 221–235, 2001.
- SIKES, E. L.; FARRINGTON, J. W.; KEIGWIN, L. D. Use of the alkenone unsaturation ratio  $U_{37}^K$  to determine past sea surface temperatures: core-top SST calibrations and methodology considerations. **Earth and Planetary Science Letters**, v. 104, n. 1, p. 36–47, 1991.
- SIKES, E. L.; VOLKMAN, J. K. Calibration of alkenone unsaturation ratios ( $U_{37}^{K'}$ ) for paleotemperature estimation in cold polar waters. **Geochimica et Cosmochimica Acta**, v. 57, n. 8, p. 1883–1889, 1993.
- SIKES, E. L.; VOLKMAN, J. K.; ROBERTSON, L. G.; PICHON, J. J. Alkenones and alkenes in surface waters and sediments of the Southern Ocean: Implications for paleotemperature estimation in polar regions. **Geochimica et Cosmochimica Acta**, v. 61, n. 7, p. 1495–1505, 1997.
- SILVEIRA, I. C. A.; FOLONI NETO, H.; COSTA, T. P.; et al. Physical oceanography of Campos Basin continental slope and ocean region. In: R. P. Martins; G. S. Grossmann-Matheson (Orgs.); **Meteorology and Oceanography: regional environmental characterization of the Campos Basin, Southwest Atlantic**, 2017. Rio de Janeiro: Elsevier. Habitats, v. 2, p. 135-90.
- SILVEIRA, I. C. A.; SCHMIDT, A. C. K.; CAMPOS, E. J. D.; GODOI, S. S. DE; IKEDA, Y. A corrente do Brasil ao largo da costa leste brasileira. **Brazilian Journal of Oceanography**, v. 48, n. 2, p. 171–183, 2000.
- SINNINGHE DAMSTÉ, J. S. Spatial heterogeneity of sources of branched tetraethers in shelf systems: The geochemistry of tetraethers in the Berau

- River delta (Kalimantan, Indonesia). **Geochimica et Cosmochimica Acta**, v. 186, p. 13–31, 2016.
- SINNINGHE DAMSTÉ, J. S.; HOPMANS, E. C.; PANCOST, R. D.; SCHOUTEN, S.; GEENEVASEN, J. A. J. Newly discovered non-isoprenoid glycerol dialkyl glycerol tetraether lipids in sediments. **Chemical Communications**, , n. 17, p. 1683–1684, 2000.
- SINNINGHE DAMSTÉ, J. S.; RIJPSTRA, W. I. C.; HOPMANS, E. C.; et al. 13,16-Dimethyl octacosanedioic acid (iso-Diabolic Acid), a common membrane-spanning lipid of Acidobacteria subdivisions 1 and 3. **Applied and Environmental Microbiology**, v. 77, n. 12, p. 4147–4154, 2011.
- SINNINGHE DAMSTÉ, J. S.; RIJPSTRA, W. I. C.; HOPMANS, E. C.; et al. Intact polar and core glycerol dibiphytanyl glycerol tetraether lipids of group I.1a and I.1b Thaumarchaeota in soil. **Applied and Environmental Microbiology**, v. 78, n. 19, p. 6866–6874, 2012.
- SINNINGHE DAMSTÉ, J. S.; RIJPSTRA, W. I. C.; HOPMANS, E. C.; et al. Ether- and Ester-Bound iso-Diabolic Acid and Other Lipids in Members of Acidobacteria Subdivision 4. (K. E. Wommack, Org.) **Applied and Environmental Microbiology**, v. 80, n. 17, p. 5207 LP-5218, 2014.
- SINNINGHE DAMSTÉ, J. S.; SCHOUTEN, S.; C HOPMANS, E.; VAN DUIN, A.; A J GEENEVASEN, J. Crenarchaeol: The characteristic core glycerol dibiphytanyl glycerol tetraether membrane lipid of cosmopolitan pelagic crenarchaeota. **Journal of lipid research**, v. 43, p. 1641-1651, 2002.
- SMITH, M.; DE DECKKER, P.; ROGERS, J.; et al. Comparison of  $U_{37}^{K'}$ ,  $TEX_{86}^H$  and LDI temperature proxies for reconstruction of south-east Australian ocean temperatures. **Organic Geochemistry**, v. 64, p. 94–104, 2013.
- SMITH, R. W.; BIANCHI, T. S.; LI, X. A re-evaluation of the use of branched GDGTs as terrestrial biomarkers: Implications for the BIT Index. **Geochimica et Cosmochimica Acta**, v. 80, p. 14–29, 2012.
- SONZOGNI, C.; BARD, E.; ROSTEK, F.; et al. Core-top calibrations of the alkenone index vs sea surface temperature in the Indian Ocean. **Deep Sea Research II**, v. 44, n. 6–7, p. 1445–1460, 1997.
- SOUTO, D. D.; LESSA, D. V. O.; ALBUQUERQUE, A. L. S.; et al. Marine sediments from southeastern Brazilian continental shelf: A 1200 year record of upwelling productivity. **Palaeogeography, Palaeoclimatology, Palaeoecology**, v. 299, n. 1, p. 49–55, 2011.

- SOUZA, T. A.; GODOY, J. M.; GODOY, M. L. D. P.; et al. Use of multitracers for the study of water mixing in the Paraíba do Sul River estuary. **Journal of Environmental Radioactivity**, v. 101, n. 7, p. 564–570, 2010.
- SOUZA, W. F. L.; KNOPPERS, B. A. Fluxos de água e sedimentos a costa leste do Brasil: relações entre a tipologia e as pressões antrópicas. **Geochimica Brasiliensis**, v. 17, n. 1, p. 57–74, 2003.
- SOUZA, W.; MARONE, E.; KNOPPERS, B. The Brazil current: typology and physical biogeochemical domains. **Carbon and Nutrient Fluxes in Continental Margins: A Global Synthesis**. p.153–170, 2011. Berlin: Springer.
- SPERO, H. J.; BIJMA, J.; LEA, D. W.; BEMIS, B. E. Effect of seawater carbonate concentration on foraminiferal carbon and oxygen isotopes. **Nature**, v. 390, n. 6659, p. 497–500, 1997. Macmillan Magazines Ltd.
- STRAMMA, L.; ENGLAND, M. On the water masses and mean circulation of the South Atlantic Ocean. **Journal of Geophysical Research: Oceans**, v. 104, n. C9, p. 20863–20883, 1999.
- SUZUKI, M. S.; REZENDE, C. E.; PARANHOS, R.; FALCÃO, A. P. Spatial distribution (vertical and horizontal) and partitioning of dissolved and particulate nutrients (C, N and P) in the Campos Basin, Southern Brazil. **Estuarine, Coastal and Shelf Science**, v. 166, p. 1–9, 2015.
- TERNOIS, Y.; SICRE, M. A.; BOIREAU, A.; CONTE, M. H.; EGLINTON, G. Evaluation of long-chain nikenones as paleo-temperature indicators in the mediterranean sea. **Deep-Sea Research Part I: Oceanographic Research Papers**, v. 44, n. 2, p. 271–286, 1997.
- TIERNEY, J. E.; RUSSELL, J. M.; EGGERMONT, H.; et al. Environmental controls on branched tetraether lipid distributions in tropical East African lake sediments. **Geochimica et Cosmochimica Acta**, v. 74, n. 17, p. 4902–4918, 2010.
- TIERNEY, J. E.; TINGLEY, M. P. A Bayesian, spatially-varying calibration model for the TEX<sub>86</sub> proxy. **Geochimica et Cosmochimica Acta**, v. 127, p. 83–106, 2014.
- TIERNEY, J. E.; TINGLEY, M. P. BAYSPLINE: A New Calibration for the Alkenone Paleothermometer. **Paleoceanography and Paleoclimatology**, v. 33, n. 3, p. 281–301, 2018.
- TROMMER, G.; SICCHA, M.; VAN DER MEER, M. T. J.; et al. Distribution of

- Crenarchaeota tetraether membrane lipids in surface sediments from the Red Sea. **Organic Geochemistry**, v. 40, n. 6, p. 724–731, 2009.
- TURICH, C.; SCHOUTEN, S.; THUNELL, R.; et al. Comparison of TEX<sub>86</sub> and U<sub>37</sub><sup>K'</sup> temperature proxies in sinking particles in the Cariaco Basin. **Deep Sea Research Part I: Oceanographic Research**, v. 78, p. 115–133, 2013.
- UREY, H. C. The thermodynamic properties of isotopic substances. **Journal of the Chemical Society (Resumed)**, n. 582, p. 562, 1947.
- VALENTIN, J. L. Spatial structure of the zooplankton community in the Cabo Frio region (Brazil) influenced by coastal upwelling. **Hydrobiologia**, v. 113, n. 1, p. 183–199, 1984a.
- VALENTIN, J. L. Analyse des paramètres hydrobiologiques dans la remontée de Cabo Frio (Brésil). **Marine Biology**, v. 82, n. 3, p. 259–276, 1984b.
- VALENTIN, J. L.; ANDRE, D. L.; JACOB, S. A. Hydrobiology in the Cabo Frio (Brazil) upwelling: two-dimensional structure and variability during a wind cycle. **Continental Shelf Research**, v. 7, n. 1, p. 77–88, 1987.
- VALENTIN, J. L.; MONTEIRO-RIBAS, W. M. Zooplankton community structure on the east-southeast Brazilian continental shelf (18–23°S latitude). **Continental Shelf Research**, v. 13, n. 4, p. 407–424, 1993.
- VALENTIN, J. L.; MOREIRA, A. P. A matéria orgânica de origem zooplanctônica nas águas de ressurgência de Cabo Frio (Brasil). **Anais da Academia Brasileira de Ciências**, v. 50, p. 103–112, 1978.
- VERSTEEGH, G. J. M.; BOSCH, H. J.; DE LEEUW, J. W. Potential palaeoenvironmental information of C<sub>24</sub> to C<sub>36</sub> mid-chain diols, keto-ols and mid-chain hydroxy fatty acids; a critical review. **Organic Geochemistry**, v. 27, n. 1–2, p. 1–15, 1997.
- VERSTEEGH, G. J. M.; JANSEN, J. H. F.; DE LEEUW, J. W.; SCHNEIDER, R. R. Mid-chain diols and keto-ols in SE Atlantic sediments: A new tool for tracing past sea surface water masses? **Geochimica et Cosmochimica Acta**, v. 64, n. 11, p. 1879–1892, 2000.
- VERSTEEGH, G.; RIEGMAN, R.; LEEUW, J. W.; JANSEN, F. U<sub>37</sub><sup>K'</sup> values for *Isochrysis galbana* as a function of culture temperature, light intensity and nutrient concentrations. **Organic Geochemistry**, v. 32, p. 785–794, 2001.
- VIANA, A. R.; FAUGERES, J. C.; KOWSMANN, R. O.; et al. Hydrology, morphology and sedimentology of the Campos continental margin, offshore Brazil. **Sedimentary Geology**, v. 115, n. 1–4, p. 133–157, 1998.

- VOLKMAN, J. K.; BARRETT, S. M.; BLACKBURN, S. I. Eustigmatophyte microalgae are potential sources of C<sub>29</sub> sterols, C<sub>22</sub>–C<sub>28</sub> n-alcohols and C<sub>28</sub>–C<sub>32</sub> n-alkyl diols in freshwater environments. **Organic Geochemistry**, v. 30, n. 5, p. 307–318, 1999.
- VOLKMAN, J. K.; BARRETT, S. M.; BLACKBURN, S. I.; SIKES, E. L. Alkenones in *Gephyrocapsa Oceanica* - Implications for Studies of Paleoclimate. **Geochimica et Cosmochimica Acta**, v. 59, n. 3, p. 513–520, 1995.
- VOLKMAN, J. K.; BARRETT, S. M.; DUNSTAN, G. A.; JEFFREY, S. W. C<sub>30</sub>C<sub>32</sub> alkyl diols and unsaturated alcohols in microalgae of the class Eustigmatophyceae. **Organic Geochemistry**, v. 18, n. 1, p. 131–138, 1992.
- VOLKMAN, J. K.; EGLINTON, G.; CORNER, E. D. S.; FORSBERG, T. E. V. Long chain alkenes and alkenones in the coccolithophorid *Emiliana huxleyi*. **Phytochemistry**, v. 19, n. 12, p. 2619–2622, 1980.
- WAINER, I.; PRADO, L. F.; KHODRI, M.; OTTO-BLIESNER, B. Reconstruction of the South Atlantic Subtropical Dipole index for the past 12,000 years from surface temperature proxy. **Scientific Reports**, v. 4, p. 5291, 2014.
- WALSH, E. M.; INGALLS, A. E.; KEIL, R. G. Sources and transport of terrestrial organic matter in Vancouver Island fjords and the Vancouver-Washington Margin: A multiproxy approach using δ<sup>13</sup>C<sub>org</sub>, lignin phenols, and the ether lipid BIT index. **Limnology and Oceanography**, v. 53, n. 3, p. 1054–1063, 2008.
- WANNER, H.; SOLOMINA, O.; GROSJEAN, M.; RITZ, S. P.; JETEL, M. Structure and origin of Holocene cold events. **Quaternary Science Reviews**, v. 30, n. 21, p. 3109–3123, 2011.
- WARD, J. H. Hierarchical Grouping to Optimize an Objective Function. **Journal of the American Statistical Association**, v. 58, n. 301, p. 236–244, 1963.
- WEIJERS, J. W. H.; PANOTO, E.; VAN BLEIJSWIJK, J.; et al. Constraints on the Biological Source(s) of the Orphan Branched Tetraether Membrane Lipids. **Geomicrobiology Journal**, v. 26, n. 6, p. 402–414, 2009.
- WEIJERS, J. W. H.; SCHEFUSS, E.; SCHOUTEN, S.; SINNINGHE DAMSTÉ, J. S. Coupled Thermal and Hydrological Evolution of Tropical Africa over the Last Deglaciation. **Science**, v. 315, n. 5819, p. 1701–1704, 2007.
- WEIJERS, J. W. H.; SCHOUTEN, S.; VAN DEN DONKER, J. C.; HOPMANS, E. C.; SINNINGHE DAMSTÉ, J. S. Environmental controls on bacterial tetraether membrane lipid distribution in soils. **Geochimica et**

- Cosmochimica Acta**, v. 71, n. 3, p. 703–713, 2007.
- WEIJERS, J. W. H.; SCHOUTEN, S.; HOPMANS, E. C.; et al. Membrane lipids of mesophilic anaerobic bacteria thriving in peats have typical archaeal traits. **Environmental Microbiology**, v. 8, n. 4, p. 648–657, 2006.
- WEIJERS, J. W. H.; SCHOUTEN, S.; SPAARGAREN, O. C.; SINNINGHE DAMSTÉ, J. S. Occurrence and distribution of tetraether membrane lipids in soils: implications for the use of the TEX<sub>86</sub> proxy and the BIT index. **Organic Geochemistry**, v. 37, n. 12, p. 1680–1693, 2006.
- WIBERG, K. B. The Concept of Strain in Organic Chemistry. **Angewandte Chemie International Edition in English**, v. 25, n. 4, p. 312–322, 1986.
- WUCHTER, C.; ABBAS, B.; COOLEN, M. J. L.; et al. Archaeal nitrification in the ocean. **Proceedings of the National Academy of Sciences of the United States of America**, v. 103, n. 33, p. 12317–12322, 2006.
- WUCHTER, C.; SCHOUTEN, S.; COOLEN, M. J. L.; SINNINGHE DAMSTÉ, J. S. Temperature-dependent variation in the distribution of tetraether membrane lipids of marine Crenarchaeota: Implications for TEX<sub>86</sub> paleothermometry. **Paleoceanography**, v. 19, n. 4, p. 1–10, 2004.
- WUCHTER, C.; SCHOUTEN, S.; WAKEHAM, S. G.; SINNINGHE DAMSTÉ, J. S. Temporal and spatial variation in tetraether membrane lipids of marine Crenarchaeota in particulate organic matter: Implications for TEX<sub>86</sub> paleothermometry. **Paleoceanography**, v. 20, n. 3, p. PA3013, doi:10.1029/2004PA001110, 2005.
- YAMAMOTO, M.; SHIMAMOTO, A.; FUKUHARA, T.; et al. Seasonal and depth variations in molecular and isotopic alkenone composition of sinking particles from the western North Pacific. **Deep Sea Research Part I: Oceanographic Research Papers**, v. 54, n. 9, p. 1571–1592, 2007.
- YAMAMOTO, M.; SHIMAMOTO, A.; FUKUHARA, T.; TANAKA, Y.; ISHIZAKA, J. Glycerol dialkyl glycerol tetraethers and TEX<sub>86</sub> index in sinking particles in the western North Pacific. **Organic Geochemistry**, v. 53, p. 52–62, 2012.
- YANG, G.; ZHANG, C. L.; XIE, S.; et al. Microbial glycerol dialkyl glycerol tetraethers from river water and soil near the Three Gorges Dam on the Yangtze River. **Organic Geochemistry**, v. 56, p. 40–50, 2013.
- YOSHINAGA, M.; SUMIDA, P.; WAKEHAM, S. G. Lipid biomarkers in surface sediments from an unusual coastal upwelling area from the SW Atlantic Ocean. **Organic Geochemistry**, v. 39, n. 10, p. 1385–1399, 2008.

- ZELL, C.; KIM, J.-H.; ABRIL, G.; et al. Impact of seasonal hydrological variation on the distributions of tetraether lipids along the Amazon River in the central Amazon basin: implications for the MBT/CBT paleothermometer and the BIT index. **Frontiers in Microbiology**, v. 4, p. 228, 2013.
- ZELL, C.; KIM, J.-H.; FERNANDES, M. J.; et al. Transport of branched tetraether lipids from the Tagus River basin to the coastal ocean of the Portuguese margin: consequences for the interpretation of the MBT/CBT paleothermometer. **Biogeosciences**, v. 11, p. 5637–5655, 2014.
- ZELL, C.; KIM, J.-H.; MOREIRA-TURCQ, P.; et al. Disentangling the origins of branched tetraether lipids and crenarchaeol in the lower Amazon River: Implications for GDGT-based proxies. **Limnology and Oceanography**, v. 58, n. 1, p. 343–353, 2013.
- ZELL, C.; KIM, J. H.; HOLLANDER, D.; et al. Sources and distributions of branched and isoprenoid tetraether lipids on the Amazon shelf and fan: Implications for the use of GDGT-based proxies in marine sediments. **Geochimica et Cosmochimica Acta**, v. 139, n. 0, p. 293–312, 2014.
- ZEMBRUSCKI, S. G. Geomorfologia da margem continental sul brasileira e das bacias oceânicas adjacentes. **Reconhecimento global da margem continental brasileira geomorfologia da margem continental brasileira e das áreas oceânicas adjacentes (Relatório final)**, v. 7, p. 129–177, 1979.
- ZHANG, R.; DELWORTH, T. L. Simulated Tropical Response to a Substantial Weakening of the Atlantic Thermohaline Circulation. **Journal of Climate**, v. 18, n. 12, p. 1853–1860, 2005.
- ZHANG, Y. G.; PAGANI, M.; WANG, Z. Ring Index: A new strategy to evaluate the integrity of TEX<sub>86</sub> paleothermometry. **Paleoceanography**, v. 31, n. 2, p. 220–232, 2015.
- ZHANG, Y. G.; ZHANG, C. L.; LIU, X.-L.; et al. Methane Index: A tetraether archaeal lipid biomarker indicator for detecting the instability of marine gas hydrates. **Earth and Planetary Science Letters**, v. 307, n. 3, p. 525–534, 2011.
- ZHOU, J.; LAU, K. M. Does a monsoon climate exist over South America? **Journal of Climate**, v. 11, n. 5, p. 1020–1040, 1998.
- ZHU, C.; WEIJERS, J. W. H.; WAGNER, T.; et al. Sources and distributions of tetraether lipids in surface sediments across a large river-dominated continental margin. **Organic Geochemistry**, v. 42, n. 4, p. 376–386, 2011.

## Supplementary data

Table S3.1: Results of each analyzed isoGDGT and alkenone per gram of TOC ( $\mu\text{g gTOC}^{-1}$ ) in the sediment core RJ13-01C (n.d. = not determined).

Station (0-2 cm)	GDGT-0	GDGT-1	GDGT-2	GDGT-3	cren	cren'	C37:2	C37:3
A01	82.44	12.27	7.16	3.01	105.50	1.94	77.13	14.66
A02	82.23	14.98	9.18	3.03	95.45	2.76	95.16	15.90
A03	50.33	10.52	6.75	2.02	63.27	2.17	111.35	18.08
A04	68.53	13.67	8.60	3.59	84.26	4.42	119.79	19.64
A05	38.77	11.14	9.98	2.54	59.85	3.41	281.16	38.36
A06	69.39	17.87	16.11	3.92	100.27	7.53	172.96	20.17
A07	50.11	11.78	12.76	2.35	73.42	6.30	175.40	27.21
A08	53.92	12.89	13.00	2.91	76.81	6.91	122.53	14.08
A09	34.64	8.96	9.15	1.62	47.53	3.97	193.84	19.76
A10	26.78	7.06	7.50	1.25	35.34	3.37	54.42	5.29
A11	31.31	8.55	9.37	1.38	40.11	4.10	42.42	4.43
A12	33.79	10.17	11.12	1.32	41.61	4.77	40.48	3.48
B1	45.51	8.51	5.07	1.86	63.92	1.24	n.d.	n.d.
B2	88.28	16.53	11.21	3.39	106.72	2.84	n.d.	n.d.
B3	45.28	10.24	7.99	2.27	70.39	3.07	n.d.	n.d.
B4	18.49	5.62	5.58	1.66	33.96	1.96	n.d.	n.d.
B5	17.07	5.33	5.49	1.67	32.10	1.83	n.d.	n.d.
B6	34.49	8.83	8.57	2.15	53.52	3.48	n.d.	n.d.
B7	35.86	8.78	8.34	2.01	53.15	3.65	n.d.	n.d.
B8	41.39	10.59	11.07	2.40	60.96	4.74	n.d.	n.d.
B9	30.63	8.11	9.26	1.76	43.88	3.96	n.d.	n.d.
B10	14.36	3.62	4.34	0.68	20.90	1.95	n.d.	n.d.
B11	22.66	5.45	7.34	1.08	33.58	3.37	n.d.	n.d.
B12	25.16	6.40	8.91	1.04	38.42	3.91	n.d.	n.d.
G03	43.82	14.14	12.64	3.86	78.31	4.06	69.75	5.32
G04	43.64	14.43	13.17	3.93	70.90	4.54	n.d.	n.d.
G05	33.85	11.17	9.95	3.07	56.07	3.78	70.36	5.68
G07	42.92	11.27	10.22	2.36	59.67	4.22	180.42	17.26
G08	36.88	9.37	9.92	1.99	50.35	4.73	91.34	10.21
G09	32.16	7.62	7.76	1.44	42.19	3.41	115.95	10.95
G10	16.00	4.60	4.64	0.81	25.66	2.10	80.96	7.51
G11	25.78	5.99	8.16	1.04	33.27	3.38	26.72	1.90
G12	31.35	6.84	5.76	0.81	39.71	3.24	14.40	0.96
H1 <sup>a</sup>	n.d.	n.d.	n.d.	n.d.	n.d.	n.d.	n.d.	n.d.

Station (0-2 cm)	GDGT-0	GDGT-1	GDGT-2	GDGT-3	cren	cren'	C37:2	C37:3
H2	94.41	24.42	27.62	5.16	153.37	13.69	n.d.	n.d.
H3	24.52	7.58	7.03	2.21	53.25	2.44	n.d.	n.d.
H4	20.49	5.88	6.10	1.93	42.25	2.04	n.d.	n.d.
H5	26.41	6.92	6.87	2.08	51.58	2.56	n.d.	n.d.
H6	27.28	7.25	7.77	1.95	48.66	3.39	n.d.	n.d.
H7	23.74	5.72	6.73	1.45	38.85	3.12	n.d.	n.d.
H10	13.62	3.47	4.06	0.60	20.85	1.86	n.d.	n.d.
H11	14.95	3.69	5.09	0.70	22.51	2.20	n.d.	n.d.
H12	1.52	0.55	0.59	0.17	4.39	0.16	n.d.	n.d.
I02	26.06	7.35	6.79	2.94	53.05	2.33	43.14	3.07
I04	23.69	6.46	6.60	2.32	46.67	2.28	41.89	3.14
I05	34.58	9.44	9.12	3.12	69.07	3.40	83.61	7.60
I06	46.37	14.46	12.12	3.61	69.28	5.14	90.99	7.23
I07	42.82	9.98	9.93	2.59	57.59	4.39	134.80	10.78
I08	35.16	8.88	9.37	1.70	54.48	4.31	117.31	11.80
I09	30.30	7.46	7.25	1.46	40.92	3.70	91.00	8.72
I10	18.47	4.70	5.46	0.78	26.17	2.46	48.29	4.11
I11	33.65	9.18	10.78	1.49	44.68	4.66	35.80	2.26
I12	64.01	14.77	17.07	1.91	85.53	5.68	27.63	1.57

<sup>a</sup>The isoGDGTs normalized by the TOC were not determined in sample H1 because the TOC content of this sample was below quantification limit.

Table S3.2 : Instrumental annual mean and seasonal temperatures (from 1955 to 2012) corresponding to the nearest interpolated 0.25° gridbox obtained from the WOA13 (n.a. = not available).

Station	annual mean SST (°C)	summer SST (°C)	autumn SST (°C)	winter SST (°C)	spring SST (°C)	annual mean	annual mean	annual mean
						depth-integrated (0-200 m, °C)	depth-integrated (100-150 m, °C)	depth-integrated (100-200 m, °C)
A01	22.93	23.96	23.34	21.88	22.55	19.95	n.a.	n.a.
A02	22.93	23.96	23.34	21.88	22.55	19.95	n.a.	n.a.
A03	23.36	24.54	23.77	22.11	23.02	19.78	16.65	16.65
A04	23.36	24.54	23.77	22.11	23.02	19.78	16.65	16.65
A05	24.24	25.74	24.75	22.67	23.81	20.93	18.71	18.71
A06	24.24	25.74	24.75	22.67	23.81	20.93	18.71	18.71
A07	24.24	25.74	24.75	22.67	23.81	20.93	18.71	18.71
A08	24.24	25.74	24.75	22.67	23.81	20.93	18.71	18.71
A09	24.43	26.00	24.94	22.80	23.97	20.42	19.27	18.33
A10	24.57	26.26	25.13	22.84	24.07	20.84	19.71	18.73
A11	24.79	26.72	25.35	22.90	24.17	21.48	20.46	19.41
A12	24.88	27.15	25.36	22.90	24.10	21.97	21.07	19.97
B1	22.69	23.60	23.09	21.80	22.27	21.20	n.a.	n.a.
B2	22.69	23.60	23.09	21.80	22.27	21.20	n.a.	n.a.
B3	23.37	24.48	23.80	22.24	22.96	20.59	n.a.	n.a.
B4	24.03	25.35	24.52	22.66	23.59	21.41	18.90	18.90
B5	24.03	25.35	24.52	22.66	23.59	21.41	18.90	18.90
B6	24.33	25.74	24.84	22.90	23.84	20.50	19.54	18.71
B7	24.33	25.74	24.84	22.90	23.84	20.50	19.54	18.71
B8	24.33	25.74	24.84	22.90	23.84	20.50	19.54	18.71

Station	annual mean SST (°C)	summer SST (°C)	autumn SST (°C)	winter SST (°C)	spring SST (°C)	annual mean	annual mean	annual mean
						depth-integrated (0-200 m, °C)	depth-integrated (100-150 m, °C)	depth-integrated (100-200 m, °C)
B9	24.49	26.03	25.01	22.92	24.00	20.65	19.59	18.68
B10	24.49	26.03	25.01	22.92	24.00	20.65	19.59	18.68
B11	24.70	26.34	25.24	23.07	24.15	21.11	20.04	19.11
B12	25.02	27.12	25.59	23.08	24.29	22.02	21.12	20.01
G03	24.87	26.39	25.46	23.57	24.06	23.25	19.82	19.82
G04	24.87	26.39	25.46	23.57	24.06	23.25	19.82	19.82
G05	24.87	26.39	25.46	23.57	24.06	23.25	19.82	19.82
G07	25.08	26.72	25.71	23.66	24.26	21.94	21.09	20.00
G08	25.08	26.72	25.71	23.66	24.26	21.94	21.09	20.00
G09	25.08	26.72	25.71	23.66	24.26	21.94	21.09	20.00
G10	25.25	27.00	25.91	23.73	24.36	22.13	21.27	20.10
G11	25.47	27.37	26.20	23.76	24.56	22.58	21.78	20.58
G12	25.56	27.54	26.33	23.71	24.68	22.83	22.09	20.90
H1	24.38	25.69	24.86	23.39	23.59	23.95	n.a.	n.a.
H2	24.68	26.14	25.18	23.53	23.86	24.28	n.a.	n.a.
H3	24.94	26.52	25.45	23.66	24.14	21.47	20.82	19.56
H4	24.94	26.52	25.45	23.66	24.14	21.47	20.82	19.56
H5	24.94	26.52	25.45	23.66	24.14	21.47	20.82	19.56
H6	24.94	26.52	25.45	23.66	24.14	21.47	20.82	19.56
H7	24.94	26.52	25.45	23.66	24.14	21.47	20.82	19.56
H10	25.33	27.09	25.93	23.84	24.46	21.99	21.09	19.83
H11	25.54	27.41	26.20	23.89	24.67	22.47	21.57	20.32

Station	annual mean SST (°C)	summer SST (°C)	autumn SST (°C)	winter SST (°C)	spring SST (°C)	annual mean depth-integrated (0-200 m, °C)	annual mean depth-integrated (100-150 m, °C)	annual mean depth-integrated (100-200 m, °C)
I02	24.76	26.29	25.25	23.57	23.92	24.47	n.a.	n.a.
I04	24.90	26.50	25.38	23.64	24.07	24.63	n.a.	n.a.
I05	24.76	26.29	25.25	23.57	23.92	24.47	n.a.	n.a.
I06	24.90	26.50	25.38	23.64	24.07	24.63	n.a.	n.a.
I07	25.14	26.80	25.63	23.77	24.35	21.45	20.63	19.43
I08	25.14	26.80	25.63	23.77	24.35	21.45	20.63	19.43
I09	25.14	26.80	25.63	23.77	24.35	21.45	20.63	19.43
I10	25.47	27.22	25.99	23.96	24.70	21.80	20.66	19.36
I11	25.65	27.45	26.27	24.02	24.86	22.24	21.16	19.86
I12	25.72	27.53	26.43	23.95	24.98	22.61	21.72	20.41

Table S3.3: SST- $U_{37}^K$  and temp- $TEX_{86}^H$  estimates (n.d. = not determined).

Station	SST- $U_{37}^K$					Temp- $TEX_{86}^H$	
	annual mean South Atlantic (0 m, °C) <sup>a</sup>	summer South Atlantic (0-10 m, °C) <sup>a</sup>	autumn South Atlantic (0-10 m, °C) <sup>a</sup>	winter South Atlantic (0-10 m, °C) <sup>a</sup>	spring South Atlantic (0-10 m, °C) <sup>a</sup>	global calibration (0m, °C) <sup>b</sup>	global calibration (0-200 m, °C) <sup>c</sup>
A01	23.37	25.30	24.53	20.92	22.46	17.82	14.08
A02	23.87	25.83	25.06	21.41	22.96	18.00	14.23
A03	23.98	25.95	25.17	21.51	23.07	18.58	14.69
A04	23.94	25.91	25.13	21.47	23.03	20.75	16.43
A05	24.57	26.58	25.80	22.09	23.66	22.84	18.10
A06	25.05	27.08	26.31	22.55	24.14	23.76	18.83
A07	24.14	26.12	25.35	21.67	23.23	25.57	20.28
A08	25.09	27.13	26.35	22.59	24.18	25.29	20.06
A09	25.41	27.47	26.69	22.90	24.50	24.49	19.42
A10	25.53	27.59	26.82	23.01	24.62	24.96	19.79
A11	25.35	27.40	26.63	22.84	24.44	25.10	19.90
A12	25.81	27.90	27.12	23.29	24.90	24.81	19.67
B1	21.74	23.56	22.79	19.34	20.83	17.41	13.75
B2	n.d.	n.d.	n.d.	n.d.	n.d.	18.80	14.87
B3	20.90	22.67	21.89	18.52	19.99	21.66	17.15
B4	21.92	23.76	22.98	19.52	21.02	24.45	19.38
B5	19.95	21.66	20.89	17.60	19.04	24.76	19.63
B6	21.55	23.36	22.59	19.15	20.64	24.24	19.21
B7	23.23	25.15	24.38	20.79	22.32	24.15	19.14
B8	23.26	25.18	24.40	20.81	22.35	24.99	19.82
B9	22.40	24.26	23.49	19.97	21.49	25.74	20.42

Station	SST-U <sup>K</sup> <sub>37</sub>					Temp-TEX <sub>86</sub> <sup>H</sup>	
	annual mean South Atlantic (0 m, °C) <sup>a</sup>	summer South Atlantic (0-10 m, °C) <sup>a</sup>	autumn South Atlantic (0-10 m, °C) <sup>a</sup>	winter South Atlantic (0-10 m, °C) <sup>a</sup>	spring South Atlantic (0-10 m, °C) <sup>a</sup>	global calibration (0m, °C) <sup>b</sup>	global calibration (0-200 m, °C) <sup>c</sup>
	B10	19.19	20.85	20.07	16.86	18.28	26.18
B11	25.00	27.04	26.26	22.50	24.09	27.31	21.67
B12	n.d.	n.d.	n.d.	n.d.	n.d.	27.33	21.69
G03	26.07	28.17	27.39	23.53	25.16	23.06	18.27
G04	n.d.	n.d.	n.d.	n.d.	n.d.	23.42	18.56
G05	25.95	28.04	27.27	23.42	25.04	23.45	18.58
G07	25.57	27.64	26.86	23.05	24.66	23.35	18.50
G08	25.16	27.21	26.43	22.66	24.25	25.33	20.09
G09	25.60	27.67	26.89	23.08	24.69	24.56	19.47
G10	25.64	27.71	26.94	23.12	24.73	24.47	19.40
G11	26.20	28.31	27.53	23.66	25.29	27.03	21.45
G12	26.32	28.44	27.67	23.78	25.41	22.88	18.13
H1	24.98	27.01	26.24	22.48	24.07	25.79	20.46
H2	25.03	27.07	26.29	22.53	24.12	26.05	20.67
H3	24.04	26.01	25.23	21.57	23.13	23.74	18.82
H4	23.69	25.64	24.86	21.23	22.78	24.93	19.77
H5	24.81	26.83	26.06	22.32	23.90	24.62	19.52
H6	25.21	27.26	26.49	22.71	24.31	25.52	20.24
H7	25.17	27.21	26.44	22.66	24.26	26.43	20.96
H10	25.48	27.54	26.77	22.97	24.57	25.93	20.57
H11	25.67	27.75	26.97	23.15	24.76	27.34	21.70
I02	26.20	28.31	27.53	23.66	25.29	24.47	19.40

Station	SST-U <sub>37</sub> <sup>K</sup>					Temp-TEX <sub>86</sub> <sup>H</sup>	
	annual mean South Atlantic (0 m, °C) <sup>a</sup>	summer South Atlantic (0-10 m, °C) <sup>a</sup>	autumn South Atlantic (0-10 m, °C) <sup>a</sup>	winter South Atlantic (0-10 m, °C) <sup>a</sup>	spring South Atlantic (0-10 m, °C) <sup>a</sup>	global calibration (0m, °C) <sup>b</sup>	global calibration (0-200 m, °C) <sup>c</sup>
I04	26.10	28.20	27.43	23.57	25.19	25.07	19.88
I05	25.69	27.76	26.99	23.17	24.78	24.56	19.47
I06	25.98	28.08	27.30	23.45	25.07	22.97	18.20
I07	25.97	28.06	27.29	23.44	25.06	24.82	19.68
I08	25.44	27.50	26.73	22.93	24.53	25.07	19.88
I09	25.56	27.63	26.86	23.05	24.65	24.61	19.51
I10	25.84	27.92	27.15	23.31	24.93	25.77	20.44
I11	26.41	28.54	27.76	23.87	25.51	25.73	20.41
I12	26.59	28.72	27.95	24.04	25.68	24.66	19.55

<sup>a</sup> SST-U<sub>37</sub><sup>K</sup> calculated with the calibrations of Müller et al. (1998).

<sup>b</sup> Temp-TEX<sub>86</sub><sup>H</sup> calculated with the surface calibration of Kim et al. (2010).

<sup>c</sup> Temp-TEX<sub>86</sub><sup>H</sup> calculated with the subsurface calibration of Kim et al. (2012).

Table S3.4: SST- $U_{37}^K$  and temp- $TEX_{86}^H$  estimates minus instrumental temperatures from the WOA13 (nd = not determined).

Station	SST- $U_{37}^K$ minus SST-WOA13 <sup>a</sup>					Temp- $TEX_{86}^H$ minus temp-WOA13 <sup>b</sup>			
	annual mean	summer South	autumn South	winter South	spring South	global	global calibration	global calibration	global calibration
	South Atlantic	Atlantic (0-10	Atlantic (0-10	Atlantic (0-10	Atlantic (0-10	calibration	(0-200 m) minus	(0-200 m) minus	(0-200 m) minus
	(0 m) minus	m) minus	m) minus	m) minus	m) minus	(0m) minus	annual mean	annual mean	annual mean
annual mean	summer SST	autumn SST	winter SST	spring SST	annual mean	depth integrated	depth integrated	depth integrated	
SST (°C)	(°C)	(°C)	(°C)	(°C)	SST (°C)	(0-200 m, °C)	(100-150 m, °C)	(100-200 m, °C)	
A01	0.44	1.34	1.19	-0.96	-0.09	-5.12	-5.87	n.d.	n.d.
A02	0.94	1.87	1.72	-0.47	0.41	-4.93	-5.72	n.d.	n.d.
A03	0.62	1.40	1.40	-0.60	0.05	-4.78	-5.09	-1.95	-1.95
A04	0.58	1.37	1.36	-0.64	0.02	-2.61	-3.35	-0.22	-0.22
A05	0.34	0.84	1.06	-0.58	-0.14	-1.40	-2.83	-0.61	-0.61
A06	0.81	1.35	1.56	-0.12	0.33	-0.48	-2.10	0.12	0.12
A07	-0.10	0.39	0.60	-1.00	-0.57	1.34	-0.65	1.57	1.57
A08	0.85	1.39	1.61	-0.08	0.37	1.05	-0.88	1.35	1.35
A09	0.98	1.46	1.75	0.10	0.53	0.07	-1.01	0.14	1.09
A10	0.95	1.33	1.69	0.18	0.55	0.39	-1.05	0.08	1.06
A11	0.56	0.68	1.28	-0.07	0.27	0.31	-1.58	-0.56	0.49
A12	0.93	0.75	1.76	0.38	0.80	-0.07	-2.30	-1.40	-0.30
B1	-0.95	-0.04	-0.31	-2.47	-1.44	-5.28	-7.45	n.d.	n.d.
B2	n.d.	n.d.	n.d.	n.d.	n.d.	-3.89	-6.34	n.d.	n.d.
B3	-2.47	-1.81	-1.91	-3.73	-2.97	-1.71	-3.43	n.d.	n.d.
B4	-2.10	-1.59	-1.53	-3.14	-2.57	0.42	-2.03	0.48	0.48
B5	-4.07	-3.69	-3.63	-5.06	-4.54	0.73	-1.78	0.73	0.73
B6	-2.78	-2.37	-2.25	-3.74	-3.19	-0.09	-1.28	-0.33	0.50

Station	SST-U <sup>K</sup> <sub>37</sub> minus SST-WOA13 <sup>a</sup>					Temp-TEX <sub>86</sub> <sup>H</sup> minus temp-WOA13 <sup>b</sup>			
	annual mean	summer South	autumn South	winter South	spring South	global	global calibration	global calibration	global calibration
	South Atlantic	Atlantic (0-10	Atlantic (0-10	Atlantic (0-10	Atlantic (0-10	calibration	(0-200 m) minus	(0-200 m) minus	(0-200 m) minus
	(0 m) minus	m) minus	m) minus	m) minus	m) minus	(0m) minus	annual mean	annual mean	annual mean
annual mean	summer SST	autumn SST	winter SST	spring SST	annual mean	depth integrated	depth integrated	depth integrated	
SST (°C)	(°C)	(°C)	(°C)	(°C)	SST (°C)	(0-200 m, °C)	(100-150 m, °C)	(100-200 m, °C)	
B7	-1.09	-0.58	-0.46	-2.11	-1.51	-0.18	-1.36	-0.40	0.43
B8	-1.07	-0.56	-0.44	-2.09	-1.49	0.66	-0.68	0.27	1.10
B9	-2.09	-1.77	-1.52	-2.94	-2.51	1.25	-0.23	0.83	1.73
B10	-5.30	-5.18	-4.94	-6.06	-5.71	1.69	0.12	1.18	2.09
B11	0.30	0.69	1.02	-0.56	-0.06	2.61	0.57	1.63	2.57
B12	n.d.	n.d.	n.d.	n.d.	n.d.	2.31	-0.33	0.57	1.68
G03	1.19	1.78	1.93	-0.04	1.10	-1.81	-4.98	-1.55	-1.55
G04	n.d.	n.d.	n.d.	n.d.	n.d.	-1.45	-4.68	-1.26	-1.26
G05	1.08	1.65	1.81	-0.15	0.98	-1.42	-4.67	-1.24	-1.24
G07	0.48	0.92	1.16	-0.61	0.40	-1.74	-3.44	-2.59	-1.50
G08	0.08	0.49	0.73	-1.00	0.00	0.25	-1.85	-1.00	0.09
G09	0.51	0.95	1.19	-0.58	0.43	-0.52	-2.47	-1.62	-0.53
G10	0.39	0.71	1.03	-0.61	0.37	-0.78	-2.72	-1.87	-0.70
G11	0.73	0.94	1.33	-0.10	0.73	1.56	-1.13	-0.33	0.87
G12	0.76	0.90	1.34	0.07	0.73	-2.68	-4.69	-3.96	-2.77
H1	0.60	1.32	1.38	-0.91	0.48	1.41	-3.49	n.d.	n.d.
H2	0.36	0.93	1.11	-1.00	0.26	1.38	-3.61	n.d.	n.d.
H3	-0.90	-0.51	-0.22	-2.09	-1.01	-1.20	-2.65	-2.00	-0.74
H4	-1.25	-0.88	-0.59	-2.43	-1.36	-0.01	-1.69	-1.04	0.21

Station	SST-U <sub>37</sub> <sup>K'</sup> minus SST-WOA13 <sup>a</sup>					Temp-TEX <sub>86</sub> <sup>H</sup> minus temp-WOA13 <sup>b</sup>			
	annual mean	summer South	autumn South	winter South	spring South	global	global calibration	global calibration	global calibration
	South Atlantic	Atlantic (0-10	Atlantic (0-10	Atlantic (0-10	Atlantic (0-10	calibration	(0-200 m) minus	(0-200 m) minus	(0-200 m) minus
	(0 m) minus	m) minus	m) minus	m) minus	m) minus	(0m) minus	annual mean	annual mean	annual mean
annual mean	summer SST	autumn SST	winter SST	spring SST	annual mean	depth integrated	depth integrated	depth integrated	
SST (°C)	(°C)	(°C)	(°C)	(°C)	SST (°C)	(0-200 m, °C)	(100-150 m, °C)	(100-200 m, °C)	
H5	-0.13	0.31	0.60	-1.34	-0.24	-0.32	-1.94	-1.29	-0.04
H6	0.27	0.74	1.03	-0.95	0.17	0.57	-1.23	-0.58	0.68
H7	0.23	0.70	0.99	-0.99	0.12	1.49	-0.50	0.15	1.40
H10	0.15	0.45	0.84	-0.87	0.11	0.60	-1.43	-0.52	0.73
H11	0.13	0.33	0.77	-0.74	0.10	1.80	-0.77	0.13	1.37
I02	1.44	2.02	2.29	0.10	1.37	-0.29	-5.07	n.d.	n.d.
I04	1.20	1.70	2.04	-0.07	1.12	0.18	-4.74	n.d.	n.d.
I05	0.93	1.47	1.74	-0.40	0.86	-0.19	-5.00	n.d.	n.d.
I06	1.08	1.58	1.92	-0.19	1.01	-1.93	-6.43	n.d.	n.d.
I07	0.83	1.27	1.66	-0.33	0.71	-0.32	-1.76	-0.95	0.25
I08	0.30	0.71	1.10	-0.84	0.18	-0.07	-1.57	-0.75	0.45
I09	0.43	0.84	1.23	-0.73	0.30	-0.53	-1.93	-1.12	0.08
I10	0.37	0.70	1.16	-0.64	0.23	0.30	-1.36	-0.22	1.08
I11	0.76	1.09	1.49	-0.14	0.64	0.08	-1.83	-0.76	0.54
I12	0.86	1.19	1.51	0.09	0.69	-1.06	-3.06	-2.17	-0.86

<sup>a</sup> SST-U<sub>37</sub><sup>K'</sup> calculated with the calibrations of Müller et al. (1998).

<sup>b</sup> Temp-TEX<sub>86</sub><sup>H</sup> calculated with the surface calibration of Kim et al. (2010) and subsurface calibration of Kim et al. (2012).

Table S3.5: Alkenone- and GDGT-based estimates from different calibrations minus instrumental temperatures from the WOA13 (n.d. = not determined).

Station	Alkenone-based estimates minus annual mean SST-WOA13				GDGT-based estimates minus annual mean SST-WOA13					
	Muller et al. (1998) – Southeastern Atlantic	Muller et al. (1998) – Global	Conte et al. (2006)	Tierney and Tingley (2018)	Schouten et al. (2002)	Kim et al. (2008)	Liu et al. (2009)	Kim et al. (2010) -TEX <sub>86</sub> <sup>H</sup>	Kim et al. (2010) -TEX <sub>86</sub> <sup>L</sup>	Tierney and Tingley (2014)
A01	0.44	1.20	0.84	-0.95	-8.48	-5.80	-5.81	-5.12	-9.50	-7.75
A02	0.94	1.70	1.33	-0.38	-8.28	-5.62	-5.60	-4.93	-7.86	-7.56
A03	0.62	1.38	1.01	-0.70	-8.04	-5.49	-5.39	-4.78	-7.24	-7.38
A04	0.58	1.34	0.97	-0.73	-5.47	-3.32	-3.14	-2.61	-8.75	-5.25
A05	0.34	1.09	0.72	-0.88	-3.68	-1.95	-2.00	-1.40	-2.64	-3.74
A06	0.81	1.57	1.18	-0.34	-2.46	-0.92	-1.15	-0.48	-2.41	-2.56
A07	-0.10	0.66	0.29	-1.38	0.10	1.23	0.44	1.34	0.81	-0.38
A08	0.85	1.61	1.22	-0.27	-0.31	0.89	0.20	1.05	-0.67	-0.69
A09	0.98	1.74	1.35	-0.05	-1.63	-0.25	-0.68	0.07	-0.05	-1.88
A10	0.95	1.71	1.32	-0.08	-1.12	0.15	-0.42	0.39	0.47	-1.50
A11	0.56	1.32	0.93	-0.49	-1.14	0.10	-0.52	0.31	0.93	-1.48
A12	0.93	1.69	1.30	-0.01	-1.64	-0.33	-0.86	-0.07	1.23	-1.93
B1	-0.95	-0.19	-0.53	-2.37	-8.69	-5.94	-6.02	-5.28	-8.43	-7.84
B2	n.d.	n.d.	n.d.	n.d.	-7.12	-4.61	-4.49	-3.89	-5.73	-6.53
B3	-2.47	-1.72	-2.04	-3.90	-4.34	-2.37	-2.25	-1.71	-4.10	-4.11
B4	-2.10	-1.34	-1.68	-3.54	-1.29	0.09	-0.32	0.42	-1.59	-1.51
B5	-4.07	-3.32	-3.63	-5.50	-0.86	0.46	-0.05	0.73	-1.25	-1.29
B6	-2.78	-2.02	-2.35	-4.18	-1.89	-0.45	-0.81	-0.09	-1.61	-2.09
B7	-1.09	-0.34	-0.69	-2.49	-2.01	-0.56	-0.89	-0.18	-1.76	-2.20
B8	-1.07	-0.31	-0.67	-2.46	-0.83	0.44	-0.15	0.66	-0.18	-1.12

Station	Alkenone-based estimates minus annual mean SST-WOA13				GDGT-based estimates minus anual mean SST-WOA13					
	Muller et al. (1998) – Southeastern Atlantic	Muller et al. (1998) – Global	Conte et al. (2006)	Tierney and Tingley (2018)	Schouten et al. (2002)	Kim et al. (2008)	Liu et al. (2009)	Kim et al. (2010) -TEX <sub>86</sub> <sup>H</sup>	Kim et al. (2010) -TEX <sub>86</sub> <sup>L</sup>	Tierney and Tingley (2014)
	B9	-2.09	-1.33	-1.68	-3.50	0.09	1.19	0.34	1.25	1.13
B10	-5.30	-4.54	-4.84	-6.74	0.73	1.73	0.71	1.69	2.22	0.24
B11	0.30	1.06	0.68	-0.82	2.23	2.95	1.42	2.61	3.56	1.50
B12	n.d.	n.d.	n.d.	n.d.	1.93	2.66	1.12	2.31	4.09	2.40
G03	1.19	1.95	1.56	0.35	-4.03	-2.35	-2.43	-1.81	-3.92	-4.00
G04	n.d.	n.d.	n.d.	n.d.	-3.54	-1.93	-2.09	-1.45	-3.56	-3.53
G05	1.08	1.84	1.44	0.22	-3.51	-1.91	-2.07	-1.42	-4.02	-3.53
G07	0.48	1.24	0.85	-0.51	-3.86	-2.23	-2.37	-1.74	-3.04	-2.79
G08	0.08	0.84	0.45	-1.02	-1.10	0.09	-0.61	0.25	-0.56	-0.27
G09	0.51	1.27	0.88	-0.46	-2.19	-0.83	-1.28	-0.52	-0.86	-1.36
G10	0.39	1.15	0.76	-0.58	-2.48	-1.10	-1.52	-0.78	-1.02	-1.78
G11	0.73	1.48	1.08	-0.10	1.02	1.81	0.42	1.56	3.21	1.50
G12	0.76	1.52	1.12	0.00	-4.96	-3.24	-3.28	-2.68	-3.44	-3.86
H1	0.60	1.36	0.97	-0.54	0.27	1.35	0.49	1.41	0.87	-0.22
H2	0.36	1.11	0.73	-0.79	0.36	1.38	0.41	1.38	0.88	-0.11
H3	-0.90	-0.14	-0.51	-2.22	-3.18	-1.64	-1.87	-1.20	-3.62	-3.26
H4	-1.25	-0.49	-0.86	-2.64	-1.52	-0.24	-0.81	-0.01	-2.19	-1.83
H5	-0.13	0.63	0.25	-1.30	-1.96	-0.61	-1.08	-0.32	-2.59	-2.23
H6	0.27	1.03	0.65	-0.84	-0.69	0.46	-0.31	0.57	-0.96	-1.03
H7	0.23	0.99	0.60	-0.88	0.64	1.58	0.46	1.49	0.69	0.16
H10	0.15	0.91	0.52	-0.90	-0.48	0.58	-0.35	0.60	1.23	0.19

Station	Alkenone-based estimates minus annual mean SST-WOA13				GDGT-based estimates minus anual mean SST-WOA13					
	Muller et al. (1998) – Southeastern Atlantic	Muller et al. (1998) – Global	Conte et al. (2006)	Tierney and Tingley (2018)	Schouten et al. (2002)	Kim et al. (2008)	Liu et al. (2009)	Kim et al. (2010) -TEX <sub>86</sub> <sup>H</sup>	Kim et al. (2010) -TEX <sub>86</sub> <sup>L</sup>	Tierney and Tingley (2014)
H11	0.13	0.88	0.49	-0.84	1.42	2.15	0.60	1.80	3.14	1.94
I02	1.44	2.20	1.80	0.62	-1.99	-0.61	-1.03	-0.29	-4.89	-2.22
I04	1.20	1.96	1.56	0.34	-1.28	-0.03	-0.65	0.18	-2.80	-1.58
I05	0.93	1.69	1.30	-0.03	-1.86	-0.50	-0.95	-0.19	-3.24	-2.03
I06	1.08	1.84	1.44	0.22	-4.18	-2.47	-2.54	-1.93	-4.75	-4.12
I07	0.83	1.59	1.19	-0.04	-1.88	-0.57	-1.10	-0.32	-2.21	-2.07
I08	0.30	1.06	0.67	-0.74	-1.53	-0.28	-0.89	-0.07	-0.39	-1.77
I09	0.43	1.18	0.79	-0.56	-2.18	-0.83	-1.29	-0.53	-1.75	-2.40
I10	0.37	1.13	0.73	-0.57	-0.85	0.24	-0.62	0.30	1.04	-0.13
I11	0.76	1.52	1.12	0.04	-1.09	0.01	-0.83	0.08	1.09	-0.34
I12	0.86	1.62	1.22	0.24	-2.69	-1.35	-1.83	-1.06	1.20	-1.80

Table S4.1: Results of total brGDGT and crenarchaeol contents; and the brGDGT-based proxies and the estimated pH and MAAT in the Campos Basin surface sediments (n.d. = not determined).

Station (0-2 cm)	$\Sigma$ brGDGT (ng g <sup>-1</sup> )	$\Sigma$ brGDGT ( $\mu$ g gTOC <sup>-1</sup> )	Crenarchaeol (ng g <sup>-1</sup> )	Crenarchaeol ( $\mu$ g gTOC <sup>-1</sup> )	CBT <sup>a</sup>	MBT <sup>b</sup>	pH <sup>b</sup>	MAAT <sup>b</sup> (°C)
A01	17.03	25.06	71.67	105.50	0.15	0.48	7.60	14.79
A02	39.72	23.64	160.38	95.45	0.26	0.47	7.39	13.89
A03	221.33	16.89	829.01	63.27	0.22	0.47	7.47	14.24
A04	309.37	22.68	1149.27	84.26	0.17	0.45	7.57	13.80
A05	43.93	11.00	238.94	59.85	0.01	0.49	7.87	15.77
A06	91.32	17.63	519.29	100.27	0.05	0.43	7.80	13.93
A07	147.62	11.68	927.83	73.42	0.16	0.44	7.58	13.47
A08	95.65	9.46	776.49	76.81	0.27	0.47	7.36	13.86
A09	42.94	6.69	304.91	47.53	0.34	0.45	7.24	12.89
A10	39.46	5.79	240.86	35.34	0.45	0.42	7.01	11.36
A11	33.76	7.45	181.81	40.11	0.55	0.37	6.82	9.24
A12	25.30	8.88	118.60	41.61	0.69	0.30	6.53	6.32
B1	315.68	25.04	805.80	63.92	0.30	0.57	7.31	16.83
B2	54.08	24.55	235.05	106.72	0.19	0.48	7.53	14.62
B3	35.35	19.41	128.22	70.39	0.13	0.46	7.64	14.22
B4	52.50	11.93	149.50	33.96	0.01	0.52	7.89	16.81
B5	48.47	11.93	130.44	32.10	-0.04	0.54	7.97	17.85
B6	242.45	14.82	875.74	53.52	0.15	0.45	7.61	13.97
B7	220.54	14.06	833.92	53.15	0.18	0.48	7.54	14.72
B8	239.97	14.69	995.96	60.96	0.16	0.46	7.59	14.24
B9	126.41	10.92	507.92	43.88	0.23	0.48	7.45	14.29
B10	39.49	5.52	149.43	20.90	0.46	0.42	7.00	11.31
B11	33.22	8.53	130.77	33.58	0.54	0.37	6.83	9.05
B12	16.03	7.70	80.03	38.42	0.70	0.34	6.52	7.40
G03	59.62	25.20	185.31	78.31	-0.05	0.57	8.01	18.85
G04	73.15	25.72	201.64	70.90	-0.02	0.54	7.93	17.70
G05	32.77	16.59	110.72	56.07	-0.12	0.55	8.13	18.46
G07	38.75	11.36	203.54	59.67	0.30	0.51	7.30	14.78
G08	63.71	8.05	398.44	50.35	0.12	0.57	7.67	17.82
G09	38.69	6.80	239.89	42.19	0.38	0.48	7.16	13.43
G10	31.04	5.22	152.58	25.66	0.51	0.47	6.89	12.38
G11	21.77	5.66	127.96	33.27	0.70	0.37	6.51	8.39
G12	7.43	5.99	49.26	39.71	0.78	0.28	6.36	5.04
H1	89.77	n.d. <sup>c</sup>	415.74	n.d. <sup>c</sup>	0.34	0.51	7.23	14.55
H2	80.06	29.65	414.11	153.37	0.35	0.48	7.21	13.61
H3	94.13	25.54	196.27	53.25	-0.05	0.60	8.01	19.86
H4	65.38	20.64	133.85	42.25	-0.07	0.58	8.03	19.09
H5	78.24	24.14	167.15	51.58	0.06	0.50	7.79	15.87
H6	124.18	18.87	320.27	48.66	0.07	0.45	7.77	14.46

Station (0-2 cm)	$\Sigma$ brGDGT (ng g <sup>-1</sup> )	$\Sigma$ brGDGT ( $\mu$ g gTOC <sup>-1</sup> )	Crenarchaeol (ng g <sup>-1</sup> )	Crenarchaeol ( $\mu$ g gTOC <sup>-1</sup> )	CBT <sup>a</sup>	MBT <sup>b</sup>	pH <sup>b</sup>	MAAT <sup>b</sup> (°C)
H7	104.51	11.38	356.97	38.85	0.27	0.50	7.38	14.79
H10	30.08	5.61	111.90	20.85	0.53	0.44	6.85	11.41
H11	15.19	5.77	59.29	22.51	0.66	0.38	6.61	8.88
I02	72.06	21.43	178.35	53.05	0.01	0.60	7.88	19.40
I04	78.22	17.69	206.29	46.67	0.11	0.54	7.68	16.99
I05	127.97	20.94	422.09	69.07	0.14	0.53	7.62	16.46
I06	289.59	21.24	944.59	69.28	0.20	0.52	7.51	15.72
I07	214.19	18.98	649.84	57.59	0.18	0.50	7.55	15.33
I08	116.05	11.35	556.84	54.48	0.33	0.53	7.25	15.52
I09	68.95	7.93	355.59	40.92	0.39	0.50	7.14	14.17
I10	27.33	5.80	123.40	26.17	0.58	0.45	6.76	11.40
I11	15.71	6.44	108.95	44.68	0.67	0.41	6.57	9.71

<sup>a</sup> CBT calculated with the calibration of Weijers et al. (2007)

<sup>b</sup> MBT<sup>c</sup>, pH an.d. MAAT calculated with the calibrations of Peterse et al. (2012)

<sup>c</sup> The total brGDGT an.d. crenarchaeol normalized by the TOC were not determined in sample H11 because the TOC content of this sample was below quantification limit.

Table S4.2: Results of each analyzed brGDGT per gram of TOC ( $\mu\text{g gTOC}^{-1}$ ) in the Campos Basin surface sediments (n.d. = not determined).

Station (0-2 cm)	GDGT- Ia	GDGT- Ib	GDGT- Ic	GDGT- IIa	GDGT- IIb	GDGT- IIc	GDGT- IIIa	GDGT- IIIb	GDGT- IIIc
A01	4.93	3.94	2.96	5.44	3.33	1.08	3.02	0.26	0.09
A02	5.34	3.35	2.29	5.84	2.78	0.84	2.94	0.22	0.05
A03	3.57	2.56	1.75	4.03	2.07	0.61	2.07	0.19	0.05
A04	4.32	3.34	2.40	5.23	3.14	1.04	2.90	0.26	0.06
A05	2.08	1.79	1.36	1.81	1.97	0.67	1.11	0.17	0.06
A06	3.28	2.51	1.66	3.05	3.13	1.29	2.31	0.30	0.09
A07	2.57	1.42	0.99	2.12	1.83	0.62	1.82	0.23	0.08
A08	2.49	1.13	0.72	1.90	1.22	0.37	1.40	0.17	0.06
A09	1.78	0.70	0.45	1.39	0.76	0.22	1.19	0.16	0.04
A10	1.59	0.49	0.30	1.20	0.49	0.13	1.42	0.14	0.03
A11	1.95	0.48	0.26	1.45	0.47	0.13	2.47	0.20	0.03
A12	2.08	0.34	0.19	1.58	0.41	0.10	3.88	0.26	0.05
B1	8.09	3.73	2.34	4.98	2.82	0.89	1.93	0.20	0.06
B2	5.07	3.79	2.74	5.41	3.04	0.92	3.23	0.25	0.09
B3	3.67	2.95	2.10	4.17	2.81	1.05	2.33	0.22	0.10
B4	1.99	2.21	1.88	2.02	1.74	0.63	1.27	0.13	0.05
B5	2.04	2.42	1.92	1.79	1.74	0.67	1.16	0.14	0.05
B6	2.93	2.15	1.47	2.97	2.06	0.70	2.23	0.21	0.09
B7	3.18	2.10	1.38	2.83	1.86	0.65	1.82	0.17	0.07
B8	3.09	2.14	1.42	2.78	1.95	0.68	2.33	0.20	0.09
B9	2.69	1.47	0.94	2.15	1.38	0.43	1.62	0.18	0.06
B10	1.53	0.46	0.28	1.17	0.48	0.11	1.34	0.12	0.03
B11	2.17	0.54	0.30	1.68	0.56	0.13	2.85	0.29	0.02
B12	2.07	0.28	0.17	1.39	0.40	0.10	3.00	0.24	0.05
G03	4.08	5.50	4.68	3.86	3.49	1.46	1.86	0.20	0.06
G04	4.19	5.33	4.25	4.32	3.52	1.43	2.39	0.22	0.07
G05	2.66	3.44	2.84	2.07	2.77	1.16	1.38	0.22	0.07
G07	3.42	1.38	0.82	2.23	1.43	0.44	1.40	0.18	0.05
G08	2.62	1.16	0.69	0.48	1.20	0.42	1.27	0.14	0.06
G09	2.02	0.70	0.44	1.36	0.72	0.21	1.18	0.14	0.03
G10	1.69	0.42	0.24	1.06	0.42	0.11	1.09	0.16	0.03
G11	1.62	0.26	0.15	1.05	0.27	0.08	2.00	0.21	0.03
G12	1.36	0.18	0.09	1.11	0.23	0.08	2.78	0.13	0.03
H1 <sup>a</sup>	n.d.	n.d.	n.d.	n.d.	n.d.	n.d.	n.d.	n.d.	n.d.
H2	8.56	3.22	2.03	6.01	3.28	0.98	4.88	0.55	0.13
H3	4.66	5.76	4.92	3.40	3.36	1.47	1.78	0.09	0.08
H4	3.48	4.23	4.06	2.73	3.00	1.36	1.51	0.21	0.06
H5	4.48	4.14	3.14	4.04	3.36	1.50	3.05	0.32	0.12
H6	3.90	2.69	1.76	3.08	3.28	1.37	2.37	0.31	0.11
H7	3.30	1.42	0.84	2.15	1.53	0.48	1.40	0.19	0.05

Station (0-2 cm)	GDGT- Ia	GDGT- Ib	GDGT- Ic	GDGT- IIa	GDGT- IIb	GDGT- IIc	GDGT- IIIa	GDGT- IIIb	GDGT- IIIc
H10	1.76	0.39	0.22	1.10	0.45	0.11	1.36	0.18	0.03
H11	1.69	0.27	0.13	1.06	0.33	0.07	1.94	0.24	0.03
I02	17.15	19.41	17.53	14.30	11.25	4.70	5.57	0.67	0.25
I04	4.88	4.26	3.33	4.37	2.88	1.23	2.03	0.22	0.06
I05	6.66	5.12	3.42	5.50	3.65	1.30	2.98	0.23	0.08
I06	12.09	7.62	4.49	9.33	5.96	1.96	5.33	0.46	0.15
I07	4.13	2.19	1.36	2.69	2.32	0.76	1.88	0.27	0.11
I08	3.35	1.31	0.74	1.97	1.19	0.35	1.18	0.14	0.04
I09	2.12	0.73	0.45	1.37	0.71	0.20	1.00	0.14	0.03
I10	1.04	0.20	0.11	0.63	0.24	0.05	0.73	0.12	0.02
I11	1.04	0.18	0.10	0.63	0.18	0.05	1.04	0.11	0.01

<sup>a</sup>The brGDGTs normalized by the TOC were not determined in sample H1 because the TOC content of this sample was below quantification limit.

Table S5.1: Results of each analyzed GDGT and alkenone per gram of TOC ( $\mu\text{g gTOC}^{-1}$ ) in the sediment core RJ13-01C.

Sample	GDGT-0	GDGT-1	GDGT-2	GDGT-3	cren	cren'	GDGT-Ia	GDGT-IIa	GDGT-IIIa	C37:2	C37:3
S004LE_0114	45.55	10.12	7.14	2.26	63.85	3.72	3.28	3.59	3.30	66.67	12.88
S005LE_0114	40.02	9.04	6.15	1.93	50.80	3.80	3.08	3.39	3.09	49.95	9.21
S006LE_0114	33.35	7.62	5.14	1.61	43.76	2.70	2.94	3.05	2.92	55.92	9.98
S007LE_0114	38.11	8.34	5.63	1.74	47.37	3.09	3.17	3.56	3.14	60.19	9.80
S009LE_0114	43.55	9.55	6.07	1.94	50.13	3.13	3.62	4.02	3.55	47.26	7.92
S011LE_0114	48.04	9.94	6.25	2.00	54.00	3.74	3.81	4.26	3.88	60.10	7.91
S013LE_0114	41.25	8.68	5.74	1.81	49.35	2.81	3.46	3.94	3.52	55.93	7.57
S015LE_0114	35.95	7.64	5.07	1.59	43.41	3.00	2.93	3.11	2.70	52.67	7.60
S017LE_0114	45.56	9.69	6.69	2.09	51.99	3.41	3.64	3.67	3.27	64.82	8.58
S019LE_0114	46.66	9.66	6.54	2.06	54.58	3.48	3.62	3.57	3.46	54.35	6.73
S021LE_0114	42.19	9.19	6.39	2.00	50.53	3.26	3.74	3.92	3.79	56.40	7.04
S023LE_0114	47.85	9.23	5.99	2.06	55.89	3.31	3.22	3.19	2.70	56.09	13.99
S025LE_0114	37.87	7.68	5.28	1.64	43.82	3.12	2.91	2.78	2.55	55.49	8.00
S027LE_0114	35.63	7.26	4.89	1.55	42.79	2.75	2.78	2.73	2.20	62.76	8.03
S029LE_0114	42.76	8.88	5.81	1.85	52.39	3.46	3.54	3.69	3.46	60.73	7.29
S031LE_0114	37.07	7.88	5.22	1.63	44.38	2.84	3.19	3.26	3.03	57.32	7.03
S033LE_0114	38.53	8.51	5.91	1.77	47.64	3.25	3.12	3.11	3.02	54.48	7.23
S035LE_0114	34.91	7.60	5.13	1.65	41.30	2.82	2.82	2.84	2.73	88.24	9.07
S037LE_0114	33.85	7.28	4.96	1.56	39.36	2.55	2.60	2.58	2.50	67.46	8.77
S039LE_0114	36.21	7.64	5.30	1.59	42.84	3.17	2.88	2.79	2.65	64.12	8.55
S041LE_0114	40.74	8.80	5.92	1.86	46.59	3.07	3.28	3.21	3.03	64.21	8.41
S044LE_0114	47.29	10.44	7.63	2.31	57.17	3.70	3.56	3.58	3.42	78.53	11.29

Sample	GDGT-0	GDGT-1	GDGT-2	GDGT-3	cren	cren'	GDGT-Ia	GDGT-IIa	GDGT-IIIa	C37:2	C37:3
S045LE_0114	48.04	10.75	7.35	2.26	53.89	4.06	3.53	3.87	3.52	68.41	9.75
S047LE_0114	43.23	10.05	6.73	2.10	50.10	3.98	3.15	3.27	3.18	63.98	9.17
S049LE_0114	40.27	8.57	5.89	1.81	46.65	3.00	3.04	3.13	2.69	68.62	10.87
S051LE_0114	55.48	13.19	8.98	2.70	63.44	4.65	3.88	4.49	3.95	59.14	8.50
S053LE_0114	52.93	12.71	8.64	2.72	64.45	4.52	3.79	4.30	3.84	76.06	10.43
S055LE_0114	52.03	11.63	8.15	2.44	59.93	4.27	3.56	3.74	3.77	73.82	10.94
S056LE_0114	55.72	12.96	9.04	2.75	66.08	4.65	3.97	4.20	3.94	78.69	12.17
S058LE_0114	43.74	10.00	6.76	2.09	52.20	3.73	3.12	3.60	3.16	78.85	10.95
S060LE_0114	51.79	9.21	5.79	2.07	58.64	3.59	3.90	3.27	2.64	46.46	11.69
S063LE_0114	45.70	10.25	7.21	2.21	52.64	3.81	3.21	3.42	3.24	61.95	10.01
S065LE_0114	46.15	10.23	7.38	2.23	53.20	3.88	3.14	3.34	3.23	62.95	7.96
S067LE_0114	43.40	9.67	6.69	2.13	48.67	4.78	3.37	3.42	3.12	67.68	9.01
S069LE_0114	40.75	8.89	6.25	1.93	47.78	3.36	3.19	3.39	3.15	69.28	9.26
S071LE_0114	44.98	9.68	6.83	2.13	51.20	3.80	3.47	3.60	3.36	80.05	12.26
S073LE_0114	38.58	8.30	5.74	1.79	47.99	3.36	3.12	2.87	2.56	60.87	10.10
S075LE_0114	41.28	9.63	6.54	2.02	48.76	3.47	3.15	3.16	2.90	71.11	10.11
S077LE_0114	49.07	10.58	7.49	2.31	58.20	3.83	3.26	3.38	3.08	58.92	8.11
S080LE_0114	41.70	9.64	6.60	2.04	45.94	3.66	3.01	3.28	3.07	54.29	7.74
S081LE_0114	42.96	10.09	7.10	2.15	48.48	3.73	3.19	3.35	3.18	75.67	10.48
S083LE_0114	44.98	10.49	7.53	2.31	48.79	4.35	3.18	3.42	3.10	80.00	11.66
S085LE_0114	48.87	11.61	7.93	2.52	52.90	4.04	3.36	3.67	3.22	76.92	11.44
S086LE_0114	56.49	12.99	8.86	2.86	65.11	6.06	3.53	3.83	3.40	69.71	10.83
S087LE_0114	49.78	11.87	8.29	2.60	56.18	4.70	3.26	3.44	3.19	77.08	11.33

Sample	GDGT-0	GDGT-1	GDGT-2	GDGT-3	cren	cren'	GDGT-Ia	GDGT-IIa	GDGT-IIIa	C37:2	C37:3
S089LE_0114	56.71	12.88	8.94	2.64	59.18	3.74	3.19	3.13	3.29	82.83	12.81
S091LE_0114	51.65	11.29	8.20	2.65	56.31	4.38	3.03	3.39	3.07	69.87	10.30
S093LE_0114	51.48	11.27	7.78	2.42	53.32	4.36	2.87	3.29	2.98	94.32	15.95
S095LE_0114	54.96	11.76	8.28	2.52	57.73	4.54	3.04	3.43	3.08	106.11	18.65
S096LE_0114	49.75	11.02	7.57	2.39	54.79	4.82	2.69	3.07	2.69	95.14	15.96
S099LE_0114	56.10	11.95	8.24	2.65	59.83	4.65	3.24	3.55	2.99	81.64	14.94
S101LE_0114	46.88	9.06	5.86	1.94	53.05	3.55	3.32	3.10	2.61	47.04	10.90
S104LE_0114	49.48	9.85	6.29	2.07	54.38	3.92	3.13	3.12	2.96	57.45	13.44
S107LE_0114	50.52	10.72	7.28	2.34	55.50	4.18	2.82	3.07	2.78	75.82	12.03
S108LE_0114	51.78	11.19	7.52	2.47	59.04	5.03	3.04	3.25	3.01	81.49	15.93
S110LE_0114	55.09	10.89	7.33	2.46	63.30	4.53	2.98	3.40	3.00	87.38	19.90
S113LE_0114	52.15	10.36	6.53	2.24	62.11	4.90	3.00	3.19	2.87	80.71	18.46
S115LE_0114	53.56	9.72	6.21	2.11	59.98	4.13	3.06	3.29	2.91	75.71	17.22
S117LE_0114	58.36	10.19	6.68	2.40	64.50	4.21	3.52	3.49	3.09	62.12	15.71
S119LE_0114	47.74	8.48	5.51	1.94	54.38	3.35	2.89	3.09	2.58	59.36	15.03
S121LE_0114	56.69	10.36	6.53	2.23	63.47	3.87	3.58	3.53	3.01	65.70	17.87
S123LE_0114	22.92	5.18	3.53	1.12	24.54	2.00	2.56	2.63	2.54	39.10	5.15
S125LE_0114	55.52	9.92	6.27	2.15	64.06	3.90	3.43	3.60	3.01	61.39	16.10
S128LE_0114	50.25	9.86	6.12	2.15	55.26	4.05	3.57	3.57	2.98	19.31	1.95
S130LE_0114	45.17	8.41	5.55	1.81	50.85	3.21	2.79	2.88	2.46	50.85	11.97
S133LE_0114	49.92	8.85	5.91	2.01	54.10	4.45	3.50	3.11	2.83	50.38	11.53
S135LE_0114	49.62	9.05	5.85	1.96	56.64	3.56	3.25	3.31	2.79	59.34	14.61
S137LE_0114	50.92	9.40	5.82	2.03	55.53	3.77	3.47	3.29	2.76	47.57	12.18

Sample	GDGT-0	GDGT-1	GDGT-2	GDGT-3	cren	cren'	GDGT-Ia	GDGT-IIa	GDGT-IIIa	C37:2	C37:3
S139LE_0114	43.13	7.94	5.05	1.64	49.33	3.36	3.30	2.93	2.57	44.58	13.26
S141LE_0114	46.79	8.59	5.38	1.84	52.89	3.78	3.53	3.28	2.78	45.16	12.96
S143LE_0114	53.78	9.54	6.19	2.05	58.83	3.84	3.61	3.27	2.82	50.69	14.06
S145LE_0114	48.74	9.35	5.70	1.98	51.41	4.31	3.49	3.35	2.87	43.35	8.48
S148LE_0114	47.21	9.04	5.50	1.93	52.98	3.67	3.30	3.26	2.59	50.97	13.55
S150LE_0114	54.16	9.02	5.59	1.93	65.72	3.89	3.28	2.91	2.60	51.40	14.48
S153LE_0114	47.67	9.00	5.61	1.93	53.74	3.40	3.49	3.07	2.65	46.43	11.86
S155LE_0114	50.45	9.32	5.95	2.01	54.03	4.14	3.66	3.41	2.81	49.79	12.89
S157LE_0114	45.51	8.85	5.45	1.90	51.25	3.55	3.30	2.89	2.48	46.96	13.36
S160LE_0114	39.00	8.63	5.80	1.81	46.35	3.14	2.94	3.14	2.92	65.43	10.38

Table S5.2: Bulk analyses and results of alkenone, GDGT and long chain diols from the sediment core RJ13-01C (n.d. = not determined).

Sample	Depth (cm)	Age (cal kyr BP) <sup>a</sup>	TOC (%)	$\delta^{13}\text{C}$ (‰)	$\Sigma$ alkenones ( $\mu\text{g gTOC}^{-1}$ )	$\Sigma$ isoGDGT ( $\mu\text{g gTOC}^{-1}$ )	BIT index	$U^{K_{37}}$	SST- $U^{K_{37}b}$ ( $^{\circ}\text{C}$ )	TEX <sub>86</sub>	Temp-TEX <sub>86</sub> <sup>Hc</sup> ( $^{\circ}\text{C}$ )	LDI	SST-LDI <sup>d</sup>
S004LE_0114	-4	0.024	0.84	-22.70	79.54	132.19	0.14	0.84	23.31	0.56	21.61	0.88	23.84
S005LE_0114	-5	0.029	0.95	-22.70	59.16	111.02	0.16	0.84	23.39	0.57	21.79	0.88	23.67
S006LE_0114	-6	0.2	1.02	-23.37	65.90	94.41	0.17	0.85	23.62	0.55	21.03	0.88	23.82
S007LE_0114	-7	0.2	1.04	-22.72	69.99	104.37	0.17	0.86	23.97	0.56	21.18	n.d.	n.d.
S009LE_0114	-9	0.2	1.13	-22.91	55.18	114.87	0.18	0.86	23.86	0.54	20.06	n.d.	n.d.
S011LE_0114	-11	0.3	1.08	-22.66	68.01	124.04	0.18	0.88	24.69	0.55	20.68	0.90	24.43
S013LE_0114	-13	0.4	0.96	-22.75	63.50	110.28	0.18	0.88	24.60	0.54	20.53	0.89	24.11
S015LE_0114	-15	0.6	1.05	-22.72	60.27	96.59	0.17	0.87	24.39	0.56	21.30	0.89	24.22
S017LE_0114	-17	0.8	1.01	-23.00	73.40	119.65	0.17	0.88	24.67	0.56	21.22	0.88	23.83
S019LE_0114	-19	1	1.02	-20.50	61.08	123.12	0.16	0.89	24.87	0.56	21.16	n.d.	n.d.
S021LE_0114	-21	1.1	0.98	-23.01	63.44	114.04	0.18	0.89	24.85	0.56	21.32	0.89	24.07
S023LE_0114	-23	1.3	0.24	-25.29	70.08	124.24	0.14	0.80	23.64	0.55	20.93	0.90	24.30
S025LE_0114	-25	1.5	1.15	-23.15	63.49	99.20	0.16	0.87	24.39	0.57	21.72	0.91	24.57
S027LE_0114	-27	1.7	1.13	-23.38	70.79	94.89	0.15	0.89	24.78	0.56	21.31	0.90	24.42
S029LE_0114	-29	1.9	1.02	-23.38	68.02	115.22	0.17	0.89	24.96	0.56	21.16	0.92	25.02
S031LE_0114	-31	2.1	1.02	-23.24	64.35	99.37	0.18	0.89	24.90	0.55	20.93	0.90	24.31
S033LE_0114	-33	2.3	1.07	-23.59	61.70	105.48	0.16	0.88	24.66	0.56	21.49	0.88	23.86
S035LE_0114	-35	2.5	1.03	-23.41	97.31	93.42	0.17	0.91	25.39	0.56	21.28	0.89	24.12
S037LE_0114	-37	2.7	0.99	-23.57	76.23	89.61	0.16	0.88	24.73	0.55	21.09	0.89	24.17
S039LE_0114	-39	2.9	1.00	-23.49	72.67	96.47	0.16	0.88	24.65	0.57	21.81	0.90	24.27
S041LE_0114	-41	3.1	0.98	-23.41	72.61	107.17	0.17	0.88	24.70	0.55	20.96	0.90	24.31
S044LE_0114	-44	3.4	1.06	-23.51	89.82	128.40	0.16	0.87	24.40	0.57	21.71	0.87	23.54
S045LE_0114	-45	3.5	1.09	-23.15	78.16	125.83	0.17	0.88	24.43	0.56	21.36	0.90	24.36
S047LE_0114	-47	3.7	1.13	-23.81	73.15	115.37	0.16	0.87	24.41	0.56	21.39	n.d.	n.d.
S049LE_0114	-49	3.8	1.03	-23.56	79.50	106.23	0.16	0.86	24.07	0.56	21.12	0.91	24.55
S051LE_0114	-51	4	1.13	-23.42	67.64	147.67	0.16	0.87	24.40	0.55	21.02	0.92	25.02
S053LE_0114	-53	4.2	1.06	-23.36	86.49	145.24	0.16	0.88	24.56	0.56	21.14	0.91	24.68

Sample	Depth (cm)	Age (cal kyr BP) <sup>a</sup>	TOC (%)	$\delta^{13}\text{C}$ (‰)	$\Sigma$ alkenones ( $\mu\text{g gTOC}^{-1}$ )	$\Sigma$ isoGDGT ( $\mu\text{g gTOC}^{-1}$ )	BIT index	$U^{K}_{37}$	SST- $U^{K}_{37}$ <sup>b</sup> (°C)	TEX <sub>86</sub>	Temp-TEX <sub>86</sub> <sup>H c</sup> (°C)	LDI	SST-LDI <sup>d</sup>
S055LE_0114	-55	4.4	1.08	-23.14	84.76	137.75	0.16	0.87	24.30	0.56	21.42	0.91	24.63
S056LE_0114	-56	4.5	1.04	-23.05	90.86	150.53	0.16	0.87	24.15	0.56	21.40	0.89	24.14
S058LE_0114	-58	4.7	1.02	-23.49	89.80	117.91	0.16	0.88	24.52	0.56	21.23	0.90	24.27
S060LE_0114	-60	4.9	0.16	-26.84	58.15	131.39	0.14	0.80	22.12	0.55	21.07	n.d.	n.d.
S063LE_0114	-63	5.2	0.88	-23.92	71.97	121.22	0.16	0.86	24.00	0.56	21.55	0.90	24.54
S065LE_0114	-65	5.4	0.97	-23.68	70.91	122.34	0.15	0.89	24.81	0.57	21.83	0.89	24.03
S067LE_0114	-67	5.6	0.91	n.d.	76.69	113.93	0.17	0.88	24.65	0.58	22.64	0.91	24.74
S069LE_0114	-69	5.8	0.90	-24.36	78.54	108.79	0.17	0.88	24.64	0.56	21.64	0.90	24.52
S071LE_0114	-71	6	0.81	n.d.	92.31	118.30	0.17	0.87	24.19	0.57	21.83	0.91	24.66
S073LE_0114	-73	6.2	0.85	-23.88	70.98	105.53	0.15	0.86	23.90	0.57	21.78	0.92	24.98
S075LE_0114	-75	6.4	0.85	n.d.	81.22	111.38	0.16	0.88	24.44	0.56	21.14	0.91	24.65
S077LE_0114	-77	6.5	0.86	-24.60	67.04	130.92	0.14	0.88	24.54	0.56	21.54	0.91	24.55
S080LE_0114	-80	6.8	0.84	n.d.	62.04	108.94	0.17	0.88	24.43	0.56	21.41	0.91	24.75
S081LE_0114	-81	6.9	0.83	-23.50	86.15	113.97	0.17	0.88	24.53	0.56	21.51	0.92	24.90
S083LE_0114	-83	7.1	0.88	-23.51	91.66	117.29	0.17	0.87	24.36	0.58	22.16	0.91	24.70
S085LE_0114	-85	7.3	0.83	-24.16	88.36	127.19	0.16	0.87	24.29	0.56	21.11	0.90	24.39
S086LE_0114	-86	7.4	0.86	-23.66	80.54	149.83	0.14	0.87	24.14	0.58	22.31	0.92	24.92
S087LE_0114	-87	7.5	0.81	-23.89	88.42	131.99	0.15	0.87	24.33	0.57	21.78	n.d.	n.d.
S089LE_0114	-89	7.7	0.67	-24.27	95.64	143.54	0.14	0.87	24.15	0.54	20.48	0.91	24.61
S091LE_0114	-91	7.9	0.74	n.d.	80.17	133.13	0.14	0.87	24.32	0.57	22.12	0.90	24.45
S093LE_0114	-93	8.1	0.74	n.d.	110.28	129.15	0.15	0.86	23.83	0.56	21.58	0.91	24.56
S095LE_0114	-95	8.3	0.63	-23.81	124.76	138.30	0.14	0.85	23.68	0.57	21.69	0.92	25.00
S096LE_0114	-96	8.4	0.64	n.d.	111.10	128.21	0.13	0.86	23.86	0.57	22.04	0.90	24.48
S099LE_0114	-99	8.7	0.52	-24.32	96.58	142.01	0.14	0.85	23.52	0.57	21.66	0.90	24.54
S101LE_0114	-101	8.9	0.13	n.d.	57.95	120.11	0.15	0.81	22.51	0.56	21.17	0.91	24.70
S104LE_0114	-104	9.1	0.15	n.d.	70.90	125.21	0.14	0.81	22.47	0.56	21.11	0.90	24.53
S107LE_0114	-107	9.4	0.37	-24.24	87.85	129.18	0.14	0.86	24.06	0.56	21.58	0.91	24.72
S108LE_0114	-108	9.5	0.42	-24.57	97.42	135.03	0.14	0.84	23.26	0.57	22.06	0.91	24.71
S110LE_0114	-110	9.7	0.29	-25.10	107.28	142.05	0.13	0.81	22.59	0.57	21.80	0.89	24.06

Sample	Depth (cm)	Age (cal kyr BP) <sup>a</sup>	TOC (%)	$\delta^{13}\text{C}$ (‰)	$\Sigma$ alkenones ( $\mu\text{g gTOC}^{-1}$ )	$\Sigma$ isoGDGT ( $\mu\text{g gTOC}^{-1}$ )	BIT index	$U^{K_{37}}$	SST- $U^{K_{37}}$ <sup>b</sup> (°C)	TEX <sub>86</sub>	Temp-TEX <sub>86</sub> <sup>H c</sup> (°C)	LDI	SST-LDI <sup>d</sup>
S113LE_0114	-113	10	0.26	-24.93	99.17	136.39	0.13	0.81	22.57	0.57	21.85	0.91	24.65
S115LE_0114	-115	10.2	0.25	-25.21	92.92	134.64	0.13	0.81	22.60	0.56	21.47	0.90	24.44
S117LE_0114	-117	10.4	0.23	-26.51	77.83	145.65	0.14	0.80	22.10	0.57	21.70	0.88	23.88
S119LE_0114	-119	10.6	0.26	-26.60	74.39	120.93	0.14	0.80	22.09	0.56	21.39	0.89	24.13
S121LE_0114	-121	10.8	0.19	-25.52	83.56	142.86	0.14	0.79	21.73	0.55	20.80	0.91	24.75
S123LE_0114	-123	11	1.02	-22.95	44.25	59.85	0.24	0.88	24.68	0.56	21.50	0.90	24.37
S125LE_0114	-125	11.2	0.21	-25.85	77.49	141.35	0.14	0.79	21.91	0.55	21.04	0.90	24.39
S128LE_0114	-128	11.5	0.20	n.d.	n.d.	127.20	0.15	n.d.	n.d.	0.56	21.13	0.89	24.04
S130LE_0114	-130	11.7	0.25	-25.81	62.82	114.58	0.14	0.81	22.44	0.56	21.21	0.90	24.24
S133LE_0114	-133	11.9	0.24	-25.02	61.91	124.28	0.15	0.81	22.57	0.58	22.56	0.89	24.15
S135LE_0114	-135	12.1	0.25	n.d.	73.95	126.37	0.14	0.80	22.23	0.56	21.21	0.89	24.12
S137LE_0114	-137	12.3	0.22	-25.46	59.75	127.16	0.15	0.80	22.04	0.55	20.98	0.89	24.15
S139LE_0114	-139	12.5	0.19	-26.87	57.83	110.38	0.15	0.77	21.27	0.56	21.30	0.90	24.28
S141LE_0114	-141	12.7	0.19	-26.21	58.12	119.03	0.15	0.78	21.46	0.56	21.46	0.91	24.68
S143LE_0114	-143	12.9	0.19	-26.29	64.75	134.00	0.14	0.78	21.63	0.56	21.31	n.d.	n.d.
S145LE_0114	-145	13.1	0.19	-26.37	51.83	120.67	0.16	0.84	22.86	0.56	21.48	n.d.	n.d.
S148LE_0114	-148	13.4	0.21	-27.40	64.53	119.95	0.15	0.79	21.85	0.55	20.89	n.d.	n.d.
S150LE_0114	-150	13.6	0.20	-26.86	65.88	139.70	0.12	0.78	21.55	0.56	21.29	n.d.	n.d.
S153LE_0114	-153	13.9	0.23	-25.93	58.29	121.44	0.15	0.80	22.05	0.55	20.75	n.d.	n.d.
S155LE_0114	-155	14.1	0.21	-26.35	62.68	125.42	0.15	0.79	21.98	0.56	21.63	n.d.	n.d.
S157LE_0114	-157	14.3	0.21	n.d.	60.32	116.24	0.14	0.78	21.50	0.55	20.94	n.d.	n.d.
S160LE_0114	-160	14.5	0.97	-23.07	75.81	104.52	0.16	0.86	24.06	0.55	21.07	0.90	24.29
S004LE_0114	-4	0.024	0.84	-22.70	79.54	132.19	0.14	0.84	23.31	0.56	21.61	0.88	23.84
S005LE_0114	-5	0.029	0.95	-22.70	59.16	111.02	0.16	0.84	23.39	0.57	21.79	0.88	23.67

<sup>a</sup>Age model developed by Lazzari et al. (2018).

<sup>b</sup> SST- $U^{K_{37}}$  calculated with the calibration of Müller et al. (1998).

<sup>c</sup> Temp-TEX<sub>86</sub><sup>H</sup> calculated with the calibration of Kim et al. (2010).

<sup>d</sup> SST-LDI calculated with the calibration of (Rampen et al., 2012).

Table S5.3: Results of each analyzed GDGT and alkenone per gram of TOC ( $\mu\text{g gTOC}^{-1}$ ) in the sediment core CF10-09A (n.d. = not determined).

Sample	GDGT-0	GDGT-1	GDGT-2	GDGT-3	cren	cren'	GDGT-Ia	GDGT-IIa	GDGT-IIIa	C37:2	C37:3
S044MC_0816	31.77	7.38	5.09	1.60	31.51	2.21	4.30	4.49	4.27	209.31	35.07
S045MC_0816	48.40	11.90	7.89	2.62	57.38	4.00	5.44	5.61	5.70	163.70	28.32
S046MC_0816	38.08	8.71	5.99	1.87	40.95	2.76	4.07	4.15	4.32	154.96	24.80
S047MC_0816	49.63	11.59	8.00	2.60	54.14	3.63	5.30	5.73	5.84	n.d.	n.d.
S048MC_0816	53.21	11.59	8.33	2.66	56.94	4.10	5.67	6.04	5.67	167.64	24.71
S049MC_0816	28.04	6.40	4.37	1.41	30.24	2.07	3.01	3.15	3.08	180.97	26.42
S050MC_0816	67.27	16.62	12.04	3.94	72.39	5.68	6.55	6.47	5.37	180.28	23.68
S051MC_0816	50.24	12.00	8.52	2.73	56.83	3.86	5.68	6.08	4.78	n.d.	n.d.
S052MC_0816	55.10	12.82	9.16	2.98	61.16	4.37	6.00	5.25	4.77	142.90	18.59
S053MC_0816	49.58	11.64	8.17	2.64	57.78	4.08	4.89	4.61	4.11	127.80	15.82
S054MC_0816	64.87	14.86	10.61	3.41	73.78	5.08	6.54	6.05	5.30	186.55	24.76
S055MC_0816	62.38	13.77	10.24	3.21	71.46	5.46	6.69	6.87	5.86	151.56	19.49
S056MC_0816	65.52	15.05	10.98	3.43	73.90	5.21	6.70	6.28	5.94	176.72	22.30
S057MC_0816	63.08	14.50	10.41	3.35	67.72	4.96	6.30	6.00	5.34	161.96	19.86
S058MC_0816	64.46	15.59	11.44	3.73	70.03	5.05	5.83	5.51	4.85	150.29	18.11
S059MC_0816	72.69	17.06	12.14	3.81	78.43	5.61	6.76	6.50	5.64	186.00	20.64
S060MC_0816	72.53	16.81	11.90	3.84	80.96	5.49	6.50	6.11	5.21	135.25	17.43
S061MC_0816	68.16	15.37	11.44	3.59	77.03	5.47	5.80	5.66	4.91	142.60	20.46
S062MC_0816	65.51	14.59	10.79	3.47	73.08	5.58	5.85	5.57	4.93	139.82	18.82
S063MC_0816	68.16	15.76	11.11	3.54	78.91	5.17	6.24	6.02	5.17	162.53	21.05
S064MC_0816	57.45	12.71	8.95	2.83	66.84	4.36	5.50	5.33	4.76	n.d.	n.d.
S065MC_0816	68.37	15.27	10.99	3.55	79.75	5.10	6.20	5.98	5.47	154.82	22.22

Sample	GDGT-0	GDGT-1	GDGT-2	GDGT-3	cren	cren'	GDGT-Ia	GDGT-IIa	GDGT-IIIa	C37:2	C37:3
S066MC_0816	66.51	14.38	10.30	3.31	75.18	4.89	6.47	6.47	6.09	146.03	20.43
S067MC_0816	65.09	16.24	11.60	3.80	72.47	5.81	7.06	7.41	6.83	161.26	21.40
S068MC_0816	49.35	10.55	7.47	2.41	57.25	3.23	5.15	4.76	4.75	n.d.	n.d.
S069MC_0816	44.91	9.26	6.54	2.02	52.32	2.83	4.77	5.62	4.61	122.84	15.85
S070MC_0816	56.96	12.30	8.66	2.78	65.44	4.16	5.99	6.42	5.92	161.46	19.80
S071MC_0816	62.19	14.13	10.14	3.26	71.08	4.92	6.27	6.71	6.41	172.22	23.60
S072MC_0816	48.84	10.59	7.77	2.47	55.84	3.88	5.46	6.28	5.09	155.38	20.81
S073MC_0816	59.27	13.59	9.74	3.05	65.05	4.58	5.84	6.39	5.74	176.48	23.00
S074MC_0816	61.14	13.55	9.62	3.07	70.12	4.86	6.42	6.40	6.11	155.76	20.62
S075MC_0816	52.42	11.30	7.99	2.54	61.63	3.92	5.54	5.52	5.39	160.17	21.45
S076MC_0816	51.79	11.94	8.65	2.78	61.49	4.14	5.87	5.92	5.57	170.59	22.32
S077MC_0816	53.16	12.35	9.02	2.87	61.00	4.47	6.34	6.40	5.54	n.d.	n.d.
S078MC_0816	42.96	9.55	7.10	2.24	48.93	3.22	5.66	5.20	4.43	169.24	22.41
S079MC_0816	57.45	12.92	9.24	2.96	64.45	4.36	7.04	7.05	6.36	171.20	22.21
S080MC_0816	51.74	11.61	8.63	2.76	58.54	3.88	5.96	5.89	5.17	149.32	21.29
S081MC_0816	50.24	11.04	7.97	2.52	59.30	3.97	5.55	5.05	4.65	n.d.	n.d.
S082MC_0816	66.56	15.90	11.62	3.75	80.37	5.64	7.19	7.08	6.12	n.d.	n.d.
S083MC_0816	65.19	15.26	11.30	3.72	72.57	5.37	6.70	6.83	5.96	213.42	32.39
S084MC_0816	69.45	16.87	12.49	3.93	76.45	6.04	7.29	7.27	6.67	195.73	28.00
S085MC_0816	57.46	13.30	9.74	3.12	62.65	4.58	5.87	5.92	5.10	180.93	25.78
S086MC_0816	36.32	8.68	6.33	2.08	40.55	3.08	3.79	3.76	3.50	195.43	28.26
S087MC_0816	65.08	14.77	10.74	3.48	76.72	4.88	6.00	5.11	5.09	194.09	30.66
S088MC_0816	47.93	10.24	7.78	2.53	59.15	3.70	4.09	4.65	4.10	189.07	28.35

Sample	GDGT-0	GDGT-1	GDGT-2	GDGT-3	cren	cren'	GDGT-Ia	GDGT-IIa	GDGT-IIIa	C37:2	C37:3
S089MC_0816	66.65	15.97	12.23	3.88	80.63	6.05	5.61	5.50	4.97	n.d.	n.d.
S090MC_0816	n.d.	n.d.	n.d.	n.d.	n.d.	n.d.	n.d.	n.d.	n.d.	n.d.	n.d.
S091MC_0816	51.46	11.58	8.44	2.69	62.48	3.95	6.09	6.29	5.13	168.58	27.23
S092MC_0816	45.61	10.46	7.80	2.46	54.84	3.73	4.48	5.02	3.90	127.99	25.64
S093MC_0816	29.20	6.09	4.32	1.32	33.86	1.73	3.70	3.57	3.09	104.95	17.60
S094MC_0816	76.62	15.42	11.33	3.60	107.46	5.52	6.88	7.00	6.49	143.12	21.09
S095MC_0816	57.62	13.71	10.36	3.31	67.91	4.91	5.61	5.72	4.97	141.10	22.04
S096MC_0816	60.27	14.22	10.50	3.33	70.46	5.45	6.05	5.77	4.96	151.40	23.74
S097MC_0816	58.15	13.04	9.53	3.02	67.56	4.91	5.55	5.34	4.53	n.d.	n.d.
S098MC_0816	51.86	12.04	8.88	2.86	60.81	4.44	5.14	5.06	4.59	147.01	26.39
S099MC_0816	61.30	14.21	10.34	3.24	71.23	5.25	5.54	5.47	4.88	148.26	23.76
S100MC_0816	59.60	14.63	10.90	3.54	68.23	5.45	5.46	5.32	4.96	139.62	21.86
S101MC_0816	68.79	16.66	12.39	3.94	77.32	5.85	5.88	5.92	5.31	147.25	24.46
S102MC_0816	60.39	15.08	11.12	3.52	70.73	5.63	5.76	5.79	5.32	141.99	23.94
S103MC_0816	50.48	11.96	8.79	2.86	57.63	4.06	5.36	5.44	5.01	141.15	23.30
S104MC_0816	62.66	15.19	10.85	3.39	71.30	4.97	6.04	6.04	5.43	172.94	27.65
S105MC_0816	61.92	15.32	11.25	3.66	69.68	5.54	6.07	6.00	5.38	163.41	26.34
S106MC_0816	63.95	15.62	11.65	3.73	71.71	5.77	6.30	6.00	5.52	153.45	24.33
S107MC_0816	57.22	13.95	10.36	3.38	64.87	4.11	6.02	6.07	5.50	192.82	28.58
S108MC_0816	57.41	13.59	10.10	3.12	64.72	5.08	5.75	6.08	5.57	142.07	21.52
S109MC_0816	49.52	11.36	8.41	2.64	55.23	3.97	5.33	5.45	5.10	n.d.	n.d.
S110MC_0816	52.84	11.56	8.93	2.84	59.04	4.48	5.31	5.06	4.41	147.57	24.98
S111MC_0816	49.92	11.45	8.30	2.62	55.65	3.79	5.27	4.85	4.32	160.33	27.63

Sample	GDGT-0	GDGT-1	GDGT-2	GDGT-3	cren	cren'	GDGT-Ia	GDGT-IIa	GDGT-IIIa	C37:2	C37:3
S112MC_0816	26.23	5.76	4.17	1.30	31.19	1.94	2.69	2.42	2.29	n.d.	n.d.
S113MC_0816	53.92	12.19	8.91	2.79	65.23	4.37	5.53	5.62	5.41	164.36	27.61
S114MC_0816	49.07	10.37	7.69	2.37	58.68	3.48	5.50	5.72	5.76	n.d.	n.d.
S115MC_0816	43.58	9.08	6.64	2.07	50.76	3.06	4.69	4.94	5.20	250.52	32.85
S116MC_0816	47.46	10.51	7.64	2.41	56.10	3.69	4.84	5.16	4.65	140.20	22.47
S117MC_0816	56.77	12.50	9.26	2.93	67.47	4.36	5.46	5.74	5.24	142.59	23.39
S118MC_0816	63.62	14.24	10.51	3.35	73.55	5.03	5.98	7.94	6.33	182.61	32.78
S119MC_0816	34.43	8.14	6.19	2.00	39.30	3.25	3.09	3.05	2.96	163.90	28.96
S120MC_0816	69.22	15.60	11.52	3.76	78.06	6.12	6.03	6.42	6.30	n.d.	n.d.
S121MC_0816	56.68	12.73	9.40	3.06	63.54	5.03	5.21	5.43	5.23	180.77	27.76
S122MC_0816	70.24	15.48	11.61	3.67	83.53	6.04	6.05	6.17	5.98	161.79	26.93
S123MC_0816	69.31	14.91	10.85	3.50	78.21	4.92	5.64	6.23	5.44	148.74	25.64
S124MC_0816	66.50	14.77	10.87	3.52	73.35	5.60	5.84	6.26	5.96	173.36	31.05
S125MC_0816	57.95	12.86	9.35	3.00	62.91	4.39	5.03	5.10	4.99	174.46	30.70
S126MC_0816	53.11	11.72	8.71	2.81	58.54	4.58	5.46	5.78	5.34	159.01	28.28
S127MC_0816	50.08	10.98	8.24	2.63	57.36	4.39	4.96	5.09	5.14	175.42	31.66
S128MC_0816	51.43	10.50	7.76	2.47	59.40	3.60	4.86	5.08	5.03	189.40	32.59
S129MC_0816	55.54	12.23	9.46	3.02	66.04	4.63	4.97	5.04	4.88	198.17	37.11
S130MC_0816	55.05	12.19	9.03	2.95	58.69	4.06	4.57	4.97	4.75	194.99	35.07
S131MC_0816	48.52	10.31	7.76	2.51	54.45	3.49	4.60	4.84	5.05	206.94	37.64
S132MC_0816	44.90	9.48	7.16	2.25	49.29	3.19	4.18	4.38	4.21	205.99	38.23
S133MC_0816	44.23	9.59	7.12	2.29	49.71	3.18	4.15	4.38	4.14	203.97	38.46
S134MC_0816	49.77	10.70	8.05	2.54	55.35	3.95	4.56	4.80	4.62	187.33	34.46

Sample	GDGT-0	GDGT-1	GDGT-2	GDGT-3	cren	cren'	GDGT-Ia	GDGT-IIa	GDGT-IIIa	C37:2	C37:3
S135MC_0816	54.06	11.95	8.92	2.87	60.29	3.97	5.05	5.34	5.11	214.92	40.18
S136MC_0816	39.03	7.92	5.95	1.87	45.07	2.58	3.66	4.02	3.85	226.56	41.70
S137MC_0816	48.54	10.24	7.76	2.47	55.10	3.50	4.39	4.77	4.59	n.d.	n.d.
S138MC_0816	46.10	9.37	7.23	2.25	53.02	4.26	3.85	3.98	4.11	222.71	42.92
S139MC_0816	58.22	12.32	8.97	2.82	70.06	5.04	5.47	5.58	5.56	224.48	41.82

Table S5.4: Bulk analyses and results of alkenone, GDGT and long chain diols from the sediment core CF10-09A (n.d. = not determined).

Sample	Depth (cm)	Age (cal kyr BP) <sup>a</sup>	TOC (%)	$\delta^{13}\text{C}^b$ (‰)	$\Sigma$ alkenones ( $\mu\text{g gTOC}^{-1}$ )	$\Sigma$ isoGDGT ( $\mu\text{g gTOC}^{-1}$ )	BIT index	$U^{K}_{37}$	SST- $U^{K}_{37}^c$ (°C)	TEX <sub>86</sub>	Temp-TEX <sub>86</sub> <sup>H d</sup> (°C)	LDI	SST-LDI <sup>e</sup>
S044MC_0816	-1	1.09	1.38	n.d.	157.35	120.07	0.29	0.86	23.86	0.55	20.66	0.90	24.29
S045MC_0816	-2	1.11	1.35	n.d.	192.02	132.18	0.23	0.85	23.74	0.55	20.81	0.88	23.83
S046MC_0816	-3	1.13	1.31	n.d.	179.76	98.36	0.23	0.86	24.03	0.55	20.80	0.88	23.94
S047MC_0816	-4	1.15	1.33	n.d.	n.d.	129.59	0.24	n.d.	n.d.	0.55	20.90	n.d.	n.d.
S048MC_0816	-5	1.17	1.40	-20.92	192.35	136.83	0.23	0.87	24.32	0.57	21.67	0.90	24.36
S049MC_0816	-10	1.28	1.46	-20.94	207.39	72.53	0.23	0.87	24.35	0.55	20.88	0.86	23.22
S050MC_0816	-15	1.37	1.49	-20.99	203.96	177.96	0.21	0.88	24.69	0.57	21.48	0.90	24.48
S051MC_0816	-20	1.47	1.54	-20.97	n.d.	134.18	0.23	n.d.	n.d.	0.56	21.24	0.90	24.51
S052MC_0816	-25	1.56	1.52	-20.89	161.49	145.60	0.21	0.88	24.72	0.56	21.53	0.91	24.65
S053MC_0816	-30	1.64	1.81	-20.89	143.62	133.89	0.19	0.89	24.87	0.56	21.45	n.d.	n.d.
S054MC_0816	-35	1.72	1.56	-20.88	211.31	172.61	0.20	0.88	24.66	0.56	21.51	0.92	25.08
S055MC_0816	-40	1.81	1.25	-20.90	171.06	166.52	0.21	0.89	24.76	0.58	22.34	0.92	24.96
S056MC_0816	-45	1.88	1.49	-20.90	199.02	174.08	0.20	0.89	24.82	0.57	21.69	0.91	24.70
S057MC_0816	-50	1.96	1.54	-20.87	181.81	164.03	0.21	0.89	24.90	0.56	21.56	0.91	24.55
S058MC_0816	-55	2.03	1.56	-20.97	168.40	170.30	0.19	0.89	24.95	0.56	21.14	0.92	24.93
S059MC_0816	-57	2.06	1.62	n.d.	206.65	189.73	0.19	0.90	25.19	0.56	21.29	0.91	24.71
S060MC_0816	-59	2.09	1.64	n.d.	152.68	191.54	0.18	0.89	24.75	0.56	21.28	0.91	24.59
S061MC_0816	-61	2.12	1.57	n.d.	163.06	181.07	0.18	0.87	24.41	0.57	21.98	0.92	24.93
S062MC_0816	-63	2.15	1.61	n.d.	158.64	173.03	0.18	0.88	24.62	0.58	22.22	n.d.	n.d.
S063MC_0816	-65	2.17	1.49	-21.05	183.57	182.65	0.18	0.89	24.74	0.56	21.22	0.91	24.80
S064MC_0816	-70	2.24	1.52	-21.06	n.d.	153.14	0.19	n.d.	n.d.	0.56	21.34	0.91	24.66
S065MC_0816	-75	2.30	1.42	-21.20	177.04	183.04	0.18	0.87	24.41	0.56	21.52	0.91	24.78
S066MC_0816	-80	2.35	1.34	-21.05	166.46	174.57	0.20	0.88	24.49	0.56	21.52	0.89	24.21
S067MC_0816	-85	2.40	1.45	-21.14	182.66	175.01	0.23	0.88	24.66	0.57	21.71	0.91	24.67
S068MC_0816	-90	2.45	1.48	-20.97	n.d.	130.25	0.20	n.d.	n.d.	0.55	21.06	0.92	25.05
S069MC_0816	-95	2.50	1.82	-21.11	138.69	117.88	0.22	0.89	24.75	0.55	20.94	0.92	24.88
S070MC_0816	-100	2.56	1.34	-21.07	181.26	150.29	0.22	0.89	24.90	0.56	21.33	0.91	24.83

Sample	Depth (cm)	Age (cal kyr BP) <sup>a</sup>	TOC (%)	$\delta^{13}\text{C}^b$ (‰)	$\Sigma$ alkenones ( $\mu\text{g gTOC}^{-1}$ )	$\Sigma$ isoGDGT ( $\mu\text{g gTOC}^{-1}$ )	BIT index	$U^{K}_{37}$	SST- $U^{K}_{37}{}^c$ ( $^{\circ}\text{C}$ )	TEX <sub>86</sub>	Temp-TEX <sub>86</sub> <sup>H d</sup> ( $^{\circ}\text{C}$ )	LDI	SST-LDI <sup>e</sup>
S071MC_0816	-105	2.61	1.40	-21.16	195.82	165.72	0.21	0.88	24.56	0.56	21.62	0.91	24.81
S072MC_0816	-110	2.67	1.47	-21.11	176.19	129.38	0.23	0.88	24.63	0.57	21.98	0.91	24.81
S073MC_0816	-115	2.74	1.57	-21.03	199.48	155.27	0.22	0.88	24.72	0.56	21.43	0.91	24.85
S074MC_0816	-120	2.81	1.28	-21.11	176.38	162.36	0.21	0.88	24.67	0.56	21.60	0.91	24.79
S075MC_0816	-125	2.88	1.36	-21.12	181.62	139.80	0.21	0.88	24.63	0.56	21.43	0.91	24.77
S076MC_0816	-130	2.95	1.44	-21.12	192.91	140.79	0.22	0.88	24.71	0.57	21.69	0.91	24.73
S077MC_0816	-135	3.03	1.37	-21.15	n.d.	142.86	0.23	n.d.	n.d.	0.57	21.89	0.91	24.66
S078MC_0816	-140	3.11	1.27	-21.15	191.65	114.00	0.24	0.88	24.67	0.57	21.80	n.d.	n.d.
S079MC_0816	-145	3.19	1.33	-21.21	193.41	151.38	0.24	0.89	24.73	0.56	21.46	0.91	24.59
S080MC_0816	-150	3.27	1.35	-21.04	170.61	137.16	0.23	0.88	24.43	0.57	21.80	0.92	25.01
S081MC_0816	-155	3.36	1.42	-21.17	n.d.	135.03	0.20	n.d.	n.d.	0.57	21.74	0.90	24.42
S082MC_0816	-157	3.39	1.41	n.d.	n.d.	183.84	0.20	n.d.	n.d.	0.57	21.86	0.91	24.66
S083MC_0816	-159	3.43	1.60	n.d.	245.81	173.41	0.21	0.87	24.22	0.57	21.90	0.88	23.92
S084MC_0816	-161	3.46	1.51	n.d.	223.73	185.22	0.22	0.87	24.42	0.57	21.96	0.91	24.61
S085MC_0816	-163	3.50	1.56	n.d.	206.72	150.84	0.21	0.88	24.43	0.57	21.76	0.92	24.93
S086MC_0816	-165	3.53	1.29	-21.14	223.70	97.03	0.21	0.87	24.38	0.57	21.87	0.88	23.85
S087MC_0816	-170	3.62	1.53	-21.31	224.76	175.67	0.17	0.86	24.08	0.56	21.58	0.89	23.99
S088MC_0816	-175	3.71	1.45	-21.24	217.42	131.34	0.18	0.87	24.26	0.58	22.30	0.92	25.05
S089MC_0816	-180	3.80	1.59	-21.24	n.d.	185.41	0.17	n.d.	n.d.	0.58	22.48	n.d.	n.d.
S090MC_0816	-185	3.88	n.d.	-21.17	n.d.	n.d.	0.19	0.87	24.36	0.58	22.51	0.93	25.19
S091MC_0816	-190	3.97	1.48	-21.03	195.81	140.60	0.22	0.86	24.00	0.57	21.67	0.93	25.15
S092MC_0816	-195	4.05	1.82	-21.22	153.63	124.90	0.20	0.83	23.15	0.57	22.01	0.92	25.08
S093MC_0816	-200	4.12	1.06	-21.21	175.33	122.12	0.23	0.86	23.86	0.55	20.70	0.93	25.36
S094MC_0816	-205	4.20	1.26	-21.01	164.21	219.95	0.16	0.87	24.32	0.57	21.90	n.d.	n.d.
S095MC_0816	-210	4.26	1.56	-21.13	163.14	157.82	0.19	0.86	24.12	0.58	22.18	0.92	24.91
S096MC_0816	-215	4.32	1.58	-21.31	175.14	164.22	0.19	0.86	24.11	0.58	22.18	0.93	25.36
S097MC_0816	-220	4.38	1.41	-21.13	n.d.	156.22	0.19	n.d.	n.d.	0.57	22.02	0.93	25.26
S098MC_0816	-225	4.44	1.39	-21.13	173.40	140.88	0.20	0.85	23.60	0.57	22.07	0.92	24.94
S099MC_0816	-230	4.50	1.50	-21.11	172.03	165.57	0.18	0.86	24.03	0.57	21.90	0.92	25.04

Sample	Depth (cm)	Age (cal kyr BP) <sup>a</sup>	TOC (%)	$\delta^{13}\text{C}^b$ (‰)	$\Sigma$ alkenones ( $\mu\text{g gTOC}^{-1}$ )	$\Sigma$ isoGDGT ( $\mu\text{g gTOC}^{-1}$ )	BIT index	$U^{K}_{37}$	SST- $U^{K}_{37}{}^c$ (°C)	TEX <sub>86</sub>	Temp-TEX <sub>86</sub> <sup>H d</sup> (°C)	LDI	SST-LDI <sup>e</sup>
S100MC_0816	-235	4.55	1.42	-21.20	161.48	162.34	0.19	0.86	24.11	0.58	22.22	n.d.	n.d.
S101MC_0816	-240	4.61	1.45	-21.15	171.72	184.95	0.18	0.86	23.90	0.57	21.95	0.92	25.12
S102MC_0816	-245	4.66	1.43	-21.08	165.93	166.48	0.19	0.86	23.84	0.57	22.11	0.90	24.28
S103MC_0816	-250	4.73	1.38	-21.13	164.45	135.78	0.22	0.86	23.92	0.57	21.79	0.90	24.52
S104MC_0816	-255	4.79	1.44	-20.67	200.59	168.36	0.20	0.86	24.04	0.56	21.29	0.93	25.35
S105MC_0816	-257	4.82	1.37	n.d.	189.75	167.38	0.20	0.86	24.01	0.57	21.99	0.93	25.41
S106MC_0816	-259	4.84	1.41	n.d.	177.78	172.44	0.20	0.86	24.06	0.58	22.17	0.92	25.12
S107MC_0816	-261	4.87	1.31	n.d.	221.39	153.90	0.21	0.87	24.30	0.56	21.45	0.91	24.83
S108MC_0816	-263	4.90	1.34	n.d.	163.59	154.01	0.21	0.87	24.23	0.57	22.10	0.92	24.99
S109MC_0816	-265	4.92	1.27	-21.19	n.d.	131.12	0.22	n.d.	n.d.	0.57	21.87	0.92	24.89
S110MC_0816	-270	4.99	1.39	-21.15	172.55	139.70	0.20	0.86	23.83	0.58	22.64	0.92	25.04
S111MC_0816	-275	5.06	1.36	-21.07	187.96	131.73	0.21	0.85	23.76	0.56	21.50	0.92	24.93
S112MC_0816	-280	5.13	1.36	-21.16	n.d.	70.60	0.19	n.d.	n.d.	0.56	21.52	0.93	25.24
S113MC_0816	-285	5.19	1.33	-21.18	191.98	147.43	0.20	0.86	23.85	0.57	21.83	0.92	25.08
S114MC_0816	-290	5.25	1.30	-21.19	n.d.	131.65	0.22	n.d.	n.d.	0.57	21.69	0.91	24.83
S115MC_0816	-295	5.31	1.40	-21.13	283.36	115.19	0.23	0.88	24.70	0.56	21.62	0.91	24.75
S116MC_0816	-300	5.37	1.35	-21.29	162.67	127.81	0.21	0.86	24.03	0.57	21.72	0.91	24.79
S117MC_0816	-305	5.43	1.42	-21.07	165.98	153.28	0.20	0.86	23.94	0.57	21.88	0.91	24.77
S118MC_0816	-310	5.48	1.31	-21.04	215.38	170.29	0.22	0.85	23.60	0.57	21.91	n.d.	n.d.
S119MC_0816	-315	5.54	1.44	-21.08	192.86	93.32	0.19	0.85	23.66	0.58	22.63	0.90	24.53
S120MC_0816	-320	5.59	1.42	-20.90	n.d.	184.28	0.19	n.d.	n.d.	0.58	22.33	n.d.	n.d.
S121MC_0816	-325	5.65	1.55	-20.96	208.54	150.43	0.20	0.87	24.18	0.58	22.34	n.d.	n.d.
S122MC_0816	-330	5.71	1.43	-21.03	188.73	190.57	0.18	0.86	23.89	0.58	22.39	0.84	22.57
S123MC_0816	-335	5.78	1.59	-20.98	174.37	181.69	0.18	0.85	23.76	0.56	21.57	0.91	24.69
S124MC_0816	-340	5.85	1.48	-21.03	204.41	174.61	0.20	0.85	23.61	0.58	22.17	0.90	24.43
S125MC_0816	-345	5.93	1.53	-21.01	205.16	150.46	0.19	0.85	23.68	0.57	21.67	0.91	24.66
S126MC_0816	-350	6.02	1.40	-20.96	187.29	139.47	0.22	0.85	23.64	0.58	22.35	0.87	23.53
S127MC_0816	-355	6.11	1.30	-20.99	207.08	133.68	0.21	0.85	23.58	0.58	22.49	n.d.	n.d.
S128MC_0816	-360	6.21	1.10	-21.19	221.98	135.15	0.20	0.85	23.76	0.57	21.82	0.90	24.38

Sample	Depth (cm)	Age (cal kyr BP) <sup>a</sup>	TOC (%)	$\delta^{13}\text{C}^b$ (‰)	$\Sigma$ alkenones ( $\mu\text{g gTOC}^{-1}$ )	$\Sigma$ isoGDGT ( $\mu\text{g gTOC}^{-1}$ )	BIT index	$U^{K}_{37}$	SST- $U^{K}_{37}{}^c$ (°C)	TEX <sub>86</sub>	Temp-TEX <sub>86</sub> <sup>H d</sup> (°C)	LDI	SST-LDI <sup>e</sup>
S129MC_0816	-365	6.32	1.22	-21.10	235.29	150.92	0.18	0.84	23.43	0.58	22.58	0.93	25.39
S130MC_0816	-370	6.42	1.31	-21.20	230.06	141.97	0.20	0.85	23.59	0.57	21.81	0.91	24.74
S131MC_0816	-375	6.54	1.16	-21.05	244.58	127.05	0.21	0.85	23.55	0.57	21.99	n.d.	n.d.
S132MC_0816	-380	6.65	1.04	-21.15	244.22	116.26	0.21	0.84	23.47	0.57	21.94	n.d.	n.d.
S133MC_0816	-385	6.77	1.11	-21.48	242.44	116.11	0.20	0.84	23.40	0.57	21.78	0.92	24.94
S134MC_0816	-387	6.82	1.06	n.d.	221.79	130.37	0.20	0.84	23.50	0.58	22.25	0.92	25.02
S135MC_0816	-389	6.86	1.06	n.d.	255.09	142.06	0.20	0.84	23.44	0.57	21.83	0.91	24.55
S136MC_0816	-391	6.91	1.03	n.d.	268.26	102.42	0.20	0.84	23.50	0.57	21.77	0.91	24.60
S137MC_0816	-393	6.96	1.03	n.d.	n.d.	127.62	0.20	0.88	24.47	0.57	22.05	0.91	24.60
S138MC_0816	-395	7.01	1.06	-21.11	265.63	122.22	0.18	0.84	23.32	0.59	23.15	0.90	24.41
S139MC_0816	-400	7.13	1.01	-21.16	266.30	157.42	0.19	0.84	23.45	0.58	22.28	0.93	25.32
S044MC_0816	-1	1.09	1.38	n.d.	157.35	120.07	0.29	0.86	23.86	0.55	20.66	0.90	24.29
S045MC_0816	-2	1.11	1.35	n.d.	192.02	132.18	0.23	0.85	23.74	0.55	20.81	0.88	23.83
S046MC_0816	-3	1.13	1.31	n.d.	179.76	98.36	0.23	0.86	24.03	0.55	20.80	0.88	23.94
S047MC_0816	-4	1.15	1.33	n.d.	n.d.	129.59	0.24	n.d.	n.d.	0.55	20.90	n.d.	n.d.
S048MC_0816	-5	1.17	1.40	-20.92	192.35	136.83	0.23	0.87	24.32	0.57	21.67	0.90	24.36
S049MC_0816	-10	1.28	1.46	-20.94	207.39	72.53	0.23	0.87	24.35	0.55	20.88	0.86	23.22

<sup>a</sup>Age model developed by (Lessa et al., 2016)

<sup>b</sup>  $\delta^{13}\text{C}$  data given by Ana L. S. Albuquerque (personal communication).

<sup>c</sup> SST- $U^{K}_{37}$  calculated with the calibration of Müller et al. (1998).

<sup>d</sup> Temp-TEX<sub>86</sub><sup>H</sup> calculated with the calibration of Kim et al. (2010).

<sup>e</sup> SST-LDI calculated with the calibration of (Rampen et al., 2012).